UNIVERSIDADE FEDERAL DE PERNAMBUCO
CENTRO DE CIÊNCIAS EXATAS E DA NATUREZA
DEPARTAMENTO DE FÍSICA
PROGRAMA DE PÓS-GRADUAÇÃO EM FÍSICA

Wilmer Yecid Córdoba Camacho

Vortex Matter in Intertype Superconductivity Regime

Recife
2018

WILMER YECID CÓRDOBA CAMACHO

VORTEX MATTER IN INTERTYPE SUPERCONDUCTIVITY REGIME

Tese apresentada ao Programa de Pós-Graduação em Física Departamento de Física da Universidade Federal de Pernambuco como parte dos requisitos para obtenção do título de Doutor em Física.

Área de Concentração:
Física de Matéria Condensada e Materiais, Superconductividade

Orientador:
Prof. José Albino Oliveira de Aguiar

Recife
2018

Catalogação na fonte
Bibliotecária Elaine Freitas CRB4-1790

C172v Camacho, Wilmer Yecid Córdoba
Vortex Matter in Intertype Superconductivity Regime / Wilmer Yecid Córdoba Camacho. – 2018.
177f. : fig.

Orientador: José Albino Oliveira de Aguiar
Tese (Doutorado) – Universidade Federal de Pernambuco. CCEN. Física. Recife, 2018.
Inclui referências e apêndices.

1. Supercondutividade 2. Configuração exóticas de vórtices 3. Ponto de Bogomolnyi I. Aguiar, José Albino Oliveira de (Orientador). II. Título.

537.623 CDD (22. ed.) UFPE-FQ 2018-65

WILMER YECID CÓRDOBA CAMACHO

VORTEX MATTER IN INTERTYPE SUPERCONDUCTIVITY REGIME

Tese apresentada ao Programa de Pós-Graduação em Física da Universidade Federal de Pernambuco, como requisito parcial para a obtenção do título de Doutor em Física.

Aprovada em: 31/08/2018.

BANCA EXAMINADORA

Prof. Dr. José Albino Oliveira de Aguiar
Orientador
Universidade Federal de Pernambuco

Prof. Dr. Ernesto Carneiro Pessoa Raposo
Examinador Interno
Universidade Federal de Pernambuco

Prof. Dr. Marcelo Andrade de Filgueiras Gomes
Examinador Interno
Universidade Federal de Pernambuco

Prof. Dr. Andrey Chaves
Examinador Externo
Universidade Federal do Ceará

Prof. Dr. Mauro Melchiades Doria
Examinador Externo
Universidade Federal do Rio de Janeiro

A meus pais Ana E. Camacho e José A. Córdoba por seu grande apoio nesta caminhada, a minha lindinha, Mirela por seu amor e companhia

Acknowledgments

Agradeço, primeiramente, ao professor *José Albino Aguiar*, por ser mais que um orientador, por ter me presenteado com seu apoio, confiança e em especial, por ter acreditado neste trabalho.

Agradeço a *Rogeiro Mendes da Silva*, por compartilhado sua experiência e seus conhecimentos em física e, em especial, por ter-me mostrado e ensinado diversas ferramentas matemáticas e métodos computacionais que foram extremamente úteis para o desenvolvimento deste trabalho.

Ao professor *Arkady Shanenko*, pela oportunidade de aprender em suas aulas e de poder trabalhar com ele em alguns estudos do meu doutorado.

A *Alexei Vagov*, por seu acolhimento e recepção em Bayreuth e por dar-me a oportunidade de absorver um pouco de seu conhecimento e fazer parte de sua pesquisa.

Ao Departamento de Física da UFPE, professores e estudantes, por me permetir fazer parte desta família e aos meus colegas de laboratório do SuperLab. Ao grupo Theoretische Physik III do Professor V. Martin Axt da Universität Bayreuth-Alemanha, por me aceitar no período de doutorado sanduíche no exterior.

Aos meus colegas Colombianos que tive a oportunidade de conhecer e compartilhar aqui no Recife. Em especial, agradeço a meu colega *Alejandro* pelos bons momentos e experiencias compartidas.

Agradeço a meus familiares. Meus pais, *José A. Córdoba* e *Ana E. Camacho*, que são os responsáveis por eu estar onde estou. Sem o incentivo e o apoio que sempre recebi deles, tudo seria mais difícil para mim. Aos meus Irmãos, tios, primos e sobrinhos por terem me apoiado nos estudos, desde a época da minha graduação.

Em especial eu quero agradecer a minha lindinha *Mirela Ricarte*, por seu amor e companhia nesta jornada, por estar sempre de meu lado e querer continuar crescendo juntos.

Aos membros da banca, pela leitura, avaliação e sugestões desta tese.

Finalmente, agradeço ao apoio financeiro dado pela CAPES e pelo CNPq durante meu doutorado no Brasil e no exterior.

Abstract

Based on the Ginzburg-Landau (GL) theory, superconducting materials are classified as ideally diamagnetic type-I or type-II, where the magnetic field penetrates the superconducting condensate as a regular lattice of Abrikosov single-quantum vortices, depending on the Ginzburg-Landau parameter κ. However, this simple classification applies only for materials deep in type-I ($\kappa < 1/\sqrt{2}$) or in deep type-II ($\kappa > 1/\sqrt{2}$). Superconducting materials with κ in the vicinity of $\kappa_0 \approx 1/\sqrt{2}$ reveals non-standard properties that cannot be described within the conventional type-I/type-II dichotomy. These materials are broadly referred as presenting *intertype* (IT) superconductivity. IT superconductivity appears in a finite interval between types-I and -II amending the standard classification. The existence of the IT superconductivity is a general property of the BCS pairing mechanism and is related to the infinite degeneracy of the Bogomolnyi point. By lowering the temperature or introducing or impurities and/or defects this degeneracy is removed, leading to many unconventional properties of the superconducting mixed state, which are characteristic to the IT superconductivity. The magnetic properties of IT superconductivity cannot be described as a mixture of those in type-I or -II superconductors. In this work we present results on the vortex matter in the IT regime, and discuss the perspective of observing it in films, wires and bilayers superconductors. We use Ginzburg-Landau theory, the Lawrence-Doniach model and Extended Ginzburg Landau formalism to calculate the vortices configurations on these systems. Our calculations reveal exotic flux distribution that are indeed in IT regime, they can be classified into typical patterns which are not found in type-I and type-II superconductors, like: giant vortices and vortex clusters, vortex chains, vortex stripes, superconducting islands separated by vortex chains in the films superconductors. These vortex configurations in IT superconductors depend on the vortex-vortex interaction type. Analysis of the vortex-vortex interactions in the IT domain reveals that they have a considerable many-body (many-vortex) contribution. Such many-body interactions play a crucial role in the formation of the vortex matter in the mixed state, e.g., stabilizing multi-vortex clusters. The properties of the vortex-vortex interactions depend strongly on the number of vortices in a cluster and on the material (κ value). The interaction can be monotonically attractive, monotonically repulsive or, in the major cases, non-monotonic, this being is more noticeable near to the boundary of the IT regime. This observation demonstrates an existence of a special type of vortex matter shaped by many-vortex interactions. Our findings shed a new light on the problem of the interchange between types-I and -II, breaking the grounds of understanding the magnetic response and of superconductors and raise questioning on the completeness of the conventional classification of superconductors materials types.

Keywords: Intertype superconductors. Exotic vortex configuration. Bogomolnyi point. Nanowires. Thin film superconductor. Bilayer superconductor.

Resumo

Com base na teoria de Ginzburg-Landau (GL), os materiais supercondutores são classificados como idealmente diamagnéticos tipo-I ou tipo-II, onde o campo magnético penetra no supercondutor como uma rede regular de vórtices com um único quantum de fluxo (rede de Abrikosov), dependendo do parâmetro de Ginzburg-Landau κ. No entanto, essa classificação simples aplica-se apenas a materiais fortemente tipo-I ($\kappa < 1/\sqrt{2}$) ou tipo-II ($\kappa > 1/\sqrt{2}$). Materiais supercondutores com κ nas proximidades de $\kappa_0 \approx 1/\sqrt{2}$ revelam propriedades magnéticas não-convencionais que não podem ser descritas dentro da dicotomia convencional de materiais tipo-I/tipo-II. Estes materiais são amplamente referidos como supercondutividade *intertipo* (IT). A supercondutividade IT aparece em um intervalo finito entre os tipo-I e -II que alteram a classificação padrão. A existência da supercondutividade IT é uma propriedade geral do mecanismo de pareamento BCS e está relacionada ao fato do ponto de Bogomolnyi (κ_0, T_c) possuir infinitos estados degenerados. Baixando a temperatura ou introduzindo-se impurezas e/ou defeitos no material, essa degenerecência é removida, levando a muitas propriedades não convencionais do estado misto supercondutor, que são característicos da supercondutividade IT. As propriedades magnéticas da supercondutividade IT não podem ser descritas como uma mistura daquelas dos supercondutores tipo-I ou tipo-II. Neste trabalho apresenta-se resultados sobre a materia de vórtices no regime IT, e discutimos a perspectiva de observá-lo em filmes finos, fios e bicamada supercondutores. Usamos a teoria de Ginzburg-Landau, o modelo de Lawrence-Doniach e o formalismo Extendido de Ginzburg Landau, para calcular as configurações de vórtices nesses sistemas. Nossos cálculos revelam a existência de fluxos exóticos, característicos do regime IT, que não são encontrados em supercondutores tipo-I ou tipo-II, tais como: vórtices gigantes, aglomerados de vórtices, cadeias de vórtices, faixas de vórtices, ilhas supercondutoras separadas por cadeias de vórtices. Essas configurações de vórtice em supercondutores IT dependem do tipo da interação vórtice-vórtice. A Análise das interações de vórtices no domínio IT revela uma considerável contribução de muitos corpos (muitos vórtices). Tais interações de muitos corpos desempenham um papel crucial na formação da matéria de vórtices no estado misto, por exemplo, estabilização de aglomerados de múltiplos vórtices. As propriedades das interações vórtice-vórtice dependem fortemente do número de vórtices em um cluster e de κ. A interação pode ser monotonicamente atrativa, monotonicamente repulsiva ou, nos casos principais nãomonotônica, sendo este comportamento mais perceptível perto do limite do regime IT. Esta observação demonstra a existência de um tipo especial de matéria de vórtices moldada pelas interações de muitos vórtices. Nossas descobertas leva um novo olhar sobre o problema da mudança entre os materias tipos I e II, rompendo os fundamentos da compreensão da resposta magnética de supercondutores e levantando questionamentos sobre a completeza da classificação convencional dos tipos de materiais dos supercondutores.

Palavras-chaves: Superconductividade Intertipo. Configuração exóticas de vórtices. Ponto de Bogomolnyi. Fios supercondutores. Filmes finos superconductorores. Bicamadas superconductoras.

Resumen

Con base en la teoría de Ginzburg-Landau (GL), los materiales superconductores se clasifican como idealmente diamagnéticos tipo-I o tipo-II, donde el campo magnético penetra el superconductor en forma de una red regular de vórtices con un único cuanto de flujo (red de Abrikosov), según el parámetro Ginzburg-Landau κ. Sin embargo, esta simple clasificación se aplica unicamente a los materiales fuertemente tipo-I ($\kappa < 1/\sqrt{2}$) o tipo-II ($\kappa > 1/\sqrt{2}$). Materiales superconductores con valores de κ proximos de $\kappa_0 = 1/\sqrt{2}$ revelan propiedades magnéticas no estándar que no se pueden describir dentro de la dicotomía convencional de materiales tipo-I/tipo-II. Estos materiales son apliamente referidos como superconductividad *intertipo* (IT). La superconductividad IT aparece en un intervalo finito entre tipo-I y tipo-II que modifica la clasificación estándar. La existencia del régimen de superconductividad IT es una propiedad general del mecanismo de emparejamiento BCS y está relacionada de hecho con el punto de Bogomolnyi (κ_0, T_c) poseer infinitos estados degenerados. Disminuyendo la temperatura o introduciendo impurezas y/o defectos, la degenerecencia es removida, llevando a muchas propiedades no convencionales del estado mixto de los superconductores, que son caracteristicos de la superconductividad IT. Las propiedades magnéticas de la superconductividad intertipo no se pueden describir como una convinación de superconductores convensionales tipo-I o tipo-II. En este trabajo presentamos resultados sobre la materia de vórtices en el régimen IT, discutimos la perspectiva de observarlo en: filmes finos, hilos y bicamada supercondutoras. Utilizamos la teoría de Ginzburg-Landau, el modelo Lawrence-Doniach y el formalismo Extendido de Ginzburg Landau (EGL) para calcular las configuraciones de vórtices en estos sistemas. Nuestros cálculos revelan distribuciones de flujos exóticos, característicos de el régimen IT, que no son encuentran en superconductores tipo-I o tipo-II, tales como: vórtices gigantes, aglomerados de vórtices, cadenas vórices, islas superconductoras separados por cadenas vórtices. Estas configuraciones de vortices en superconductores IT dependen del tipo de interacción vórtice-vórtice. El análisis de las interacciones de vórtices en el dominio IT revela una considerable contribución de muchos cuerpos (muchos vórtices). Tales interacciones de muchos cuerpos desempeñan un papel crucial en la formación de la materia de vórtices en el estado mixto, por ejemplo, estabilizando de aglomeradosde multiple-vórtices. Las propiedades de las interacciones vórtice-vórtice dependen en gran medida del número de vórtices dentro del clúster y del valor de κ. La interacción puede ser monótonamente atractivo, monótonamente creciente repulsiva, o, en los casos principales no-monótonica, siendo este comportamiento más perceptible cerca del límite del régimen IT Esta observación demuestra la existencia de un tipo especial de materia de vórtices que es moldeada por las interacciones de muchos vórtices. Nuestros hallazgos llevan a una nueva visión sobre el problema de cambio entre los materiales tipo-I y tipo-II, rompiendo las bases de la comprensión de la respuesta magnética de superconductores y elevar cuestionamientos sobre la integridad de la clasificación convencional de los tipos de materiales superconductores.

Palabras claves: Superconductores Intertipo. Configuraciones exóticas de vórtices. Punto de Bogomolnyi. Hilos supercondutores. Filmes finos superconductorores. Bicamadas superconductoras.

Content

1 General Introduction

For over a 100 years there has been intense research of the physics of superconductors and their applications. One important characteristic of superconductors is their peculiar behavior in an applied magnetic field, which has been the focus of a great deal of experimental and theoretical research. Into technology, superconducting materials are today widely used for a large variety of applications ranging from energy and management, medical diagnostics, the production of superconducting quantum interference devices which in turn can be used to measure low magnetic fields, and the utilization of superconducting properties to produce highly sensitive particle detectors. For a long time the application of superconductivity was hampered by its low transition temperature Tc that required cooling down to liquid He temperature at 4.2 K. As a consequence, superconductive solutions were considered and developed in the past only if classical solutions were not feasible, making practical superconducting devices just a dream due the need for expensive liquid helium and the engineering complications that come from retaining such a low temperature. However a marvelous breakthrough has been made in the last 30 years in the discovery of high temperature superconductors. As is the case of magnesium diboride (MgB_2), that possess superconducting properties at temperatures at 39K. It also seems that the highest critical temperature found increases every year, giving promise to the hope of room temperature superconductors.

The last decade has been marked by the fast development of the nanotechnology and low-dimensional materials. For example, new properties of low-dimensional materials are revealed and these materials can be used as fundamental building blocks for nanoscale science and technology, ranging from chemical and biological sensors, field effect transistors to logic circuits. Also, the recent application is the employment of superconducting nanowires to detect single photons [1]. Another important characteristic is the new properties of nano-size as the quantum size fluctuations in nanosize superconductors, induced by a geometrical quantization of the single particle states, first investigated by Blatt and Thomson [2]. This effect is notable for sample sizes of the order of few nanometers. However, geometry-induced changes can be important also for sample with much larger dimensions, where the quantization-related effects are negligible. Such changes can appear, for instance, due to interactions between superconducting condensate and sample boundaries [3] or due to coupling with stray magnetic fields outside the superconducting sample. Both interactions modify the free energy of the sample which can lead to substantial changes in its magnetic properties. It is also clear that their contribution to the energy grows with the decreasing system size. This opens a possibility to control and manipulate properties of artificially created inhomogeneous superconductors by changing their geometry and dimensions. For example, magnetic properties of a superconducting film, made of type I material, becomes that of type II, when the film thickness is comparable to several superconducting coherence lengths, ξ [4–6], chapter5.

Returning to another of the highlights mentioned above. The discovery of the intermetallic compound superconductor MgB_2 stirred up intense research to investigate the novel properties of this material. The compound MgB_2, the temperature dependences are seen in the material that are not seen in more traditional superconductors. This has caused some to theorize that these materials may possess multiple electron bands that participate in superconductivity. The so called Two-Band Ginzburg Landau model was derived to handle such materials. This gave physicists and mathematicians a better grip on these new phenomena. Other odd behaviors such as anisotropies in the crystal structure of the material have also been found in these materials, and recently there has been increased interest in superconductors with several superconducting components. The main situations where multiple superconducting components arise are, multiband superconductor and artificially fabricated superconducting layers.

In this endeavor to create new technology, numerical simulations to model such technology are a must. Any engineer would prefer to have some reliable computational simulations to make predictions about a new technology before diving in and building the actual device. Computer simulations form a bridge between theory and experiments: on the one hand computational models are based on certain assumptions which simplify the true situation, but on the other hand computations can be performed for systems which are much more complex and closer to reality than can be described by analytical theory. In this respect computer simulations play an important role in assessing the appropriateness of theoretical models. As is the case of the superconductivity, where until today many works have been developed in this area and produced excellent results that can be verified by experimental dates.

With all this in mind and choosing some topics, I develop my doctoral work and as a final product, this thesis was produced.

The thesis will be organized as follows:

In **Chapter 2**, presents a brief overview of the key historic events related to superconductivity. Further, different theoretical frameworks are presented, starting with London brother's phenomenological models, Ginzburg-Landau (GL) theory, the Lawrence-Doniach model for layered superconductors and finally, present the Bardeen-Cooper-Schrieffer (BCS) theory.

In **Chapter 3** the Extended GL formalism (EGL) derived based on Gor'kov formalism for a clean s-wave superconductor, is presented. The GL equation and EGL formalism for a single band superconductor in the absence of the magnetic field is obtained.

In **Chapter 4** presents the numerical methods for solving the Ginzburg-Landau model and Extendent Ginzburg-Landau. In the first part for this chapter, we found the explains for the TDGL model of superconductivity and introduce the equations of the TDGL. The TDGL equations are written in their dimensionless form, with the characteristics of the material, as well as, the universal constants, are included in the dimensionless variables, making them easier for analysis and computations, Also we describes the popular $U-\psi$ method used in the most numerical computation work on superconductivity. In the second part, presents a brief summary of the Monte Carlo method used to solve Extendent Ginzburg-Landau formalism in the problem of vortex interaction, chapter 8.

A comprehensive analysis of flux configurations in a thin film superconducting in an applied perpendicular magnetic field is present in **Chapter 5**. It is investigated how those configurations depend on the system parameters, in particular, on the field magnitude, GL parameter κ, film thickness w and the temperature. It is demonstrated explicitly that there is a thickness interval, where the flux patterns are qualitatively different from those typical for the standard types I and II. Among them are giant vortices and vortex clusters, stripes of vortices, and lattices of superconducting islands separated by vortex chains.

Chapter 6 reports the results on the mixed and intermediates states in a thin superconducting wire, made of a type I material, subject to a perpendicular magnetic field. It is shown that superconducting wires like thin films change from type I to type II superconductivity with decreasing thickness. Despite the 1D geometry of the mixed state and a strong influence of the wire boundaries and the stray fields, the field/condensate configurations reveal clear signatures of the IT superconductivity, such as vortex clustering and giant vortices. These can be traced in the magnetization curve that undergoes qualitative changes, when the IT domain is crossed.

In the **Chapter 7** we studied a mechanism for superconducting bilayer which can mimic two-band superconductors, where each layer can be corresponds to each band. The theoretical description which we used is a variant of the famous Lawrence-Doniach model for high-temperature cuprates emphasizing the layered aspect of the structure. In the results we show that the complexity of the patterns obtained in the penetration of the magnetic field comes from the changes in the interaction of short and medium range between the vortices (non-monotonic interaction), where these patterns implicitly depends on parameters such as the coupling between layers and temperature.

Chapter 8 presents the results on the vortex-vortex interaction dependence on the sample thickness, and the influence of stray field on different vortex cluster configuration, in special we are the focus in the analysis of the vortex-vortex interactions in the intertype (IT) domain. The results reveal that the, IT domain interaction, have a considerable many-body (many-vortex) contribution. Such many-body interactions play a crucial role in the formation of the vortex matter in the mixed state stabilizing multi-vortex clusters. Properties of the vortex-vortex interactions depend strongly on the number of vortices in a cluster.

In the **Chapter 9** present the summary for each work presented in this thesis and future works.

Finally, the **Appendix** contains different calculation that are explicit in the thesis: Time-dependent delta function, the integrals which appearing in the EGL formalism and derivation of Bogomolnyi equations and the scientific Works Produced During my Ph.D. Course.

2 Superconductivity: Phenomena and Theories

In this chapter a review of the important phenomenological and mycroscopic theories that were successful in explaining some features of superconductivity will be presented.

2.1 Fundamental properties of Superconductors

The phenomenon of superconductivity was discovered in 1911 by H. Kamerlingh Onnes, whose "factory" for producing liquid helium had provided a considerable advance in experimental low temperatures physics. In his quest for the intrinsic resistance of metals, he surprisingly observed that the electrical resistance of mercury drops abruptly to zero around 4.2 K [7–9], Fig. **2-1**.

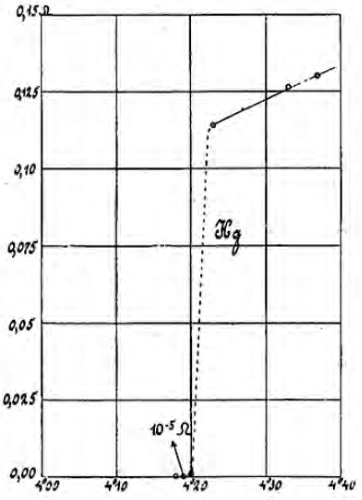

Figure 2-1 : Resistivity of mercury as a function of temperature. Figure take from [7].

He called this unexpected feature superconductivity, as a special and unknown way of carrying electric currents below that critical temperature. This was the beginning one of the most exciting adventures in physics throughout the 20th century, having seen the award of numerous Nobel prizes.

For the next decades, several other metals and compounds were shown to exhibit superconductivity under very low temperatures, always below 30 K. Soon after his discovery, H.K. Onnes noticed that superconductivity was influenced by an external magnetic field, bringing back a sample to its normal resistive state at sufficiently high values. A superconductor was thus characterised by a spectacular feature "the total loss of resistivity" and two critical parameters: a temperature and a magnetic field.

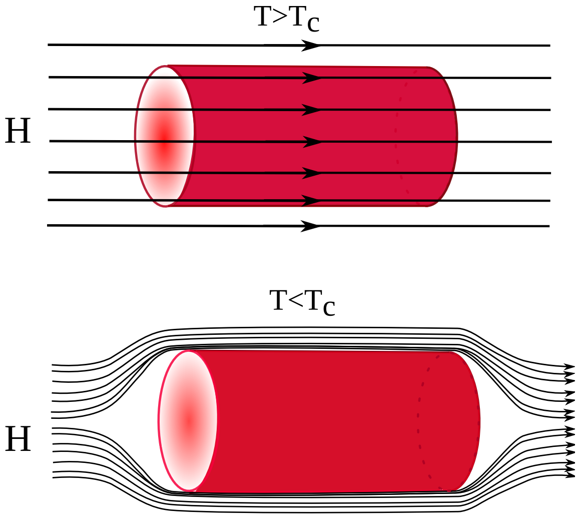

Figure 2-2 : The Meissner effect for a superconducting sample.

In 1933, W. Meissner and R. Oschenfeld discovered that superconductors also have the property of expelling a magnetic field. Together they devised an experiment which made use of a very small coil to measure the magnetic field between two solid, current-carrying, single-crystal cylinders, made of tin. The result was unexpected: even when the tin cylinders were not carrying any current, the magnetic field between them increased when they were cooled into superconducting state, as if there was something forcing the magnetic field to be expelled out of the superconducting cylinders [see Fig. **2-2**]. It was clear that this effect of expulsion of applied flux is not some dynamical consequence of perfect conductivity, meaning that superconductors also exhibit perfect diamagnetism as a fundamental property [10]. In fact, now it is well known that this Meissner-Ochsenfeld effect arises because of the flow of internal currents (the so-called Meissner-Ochsenfeld currents) which generate a magnetic field inside a superconductor, equal in magnitude to the applied field, but with opposite direction so that total field is canceled out. Superconductors can remain in the state of perfect diamagnetism only up to a certain applied field, above which magnetic flux penetrates the material, and suppresses superconductivity.

The first sucessful microscopic description of superconductivity was proposed by Bardeen, Cooper, and Schrieffer in their seminal BCS theory in 1957. Before the BCS theory, various theories were proposed, including the London equations in 1935, and the Ginzburg-Landau macroscopic theory in 1950. The Ginzburg-Landau (GL) theory was not appreciated until, in 1959, Gorkov proved that the GL theory is actually a limiting case of the BCS theory. The GL theory is now since then commonly accepted as a successful phenomenological model for superconductivity.

Also in 1957, Abrikosov, based on the Ginzburg-Landau theory, predicted that superconductors are divided into two categories, i.e., Type I and Type II. For their work, Abrikosov and Ginzburg won the 2003 Nobel Prize.

In 1962, on the basis of BCS theory, Josephson predicted that a supercurrent can flow between two pieces of superconducting material separated by a thin layer of insulating material [11]. This phenomenon is called the Josephson effect and it is exploited by some important superconducting electronic devices such as superconducting quantum interference devices (SQUIDs) which are used for measuring extremely weak signals. For this work, Josephson was awarded the Nobel Prize in 1973.

2.2 Summary of Theories for Superconductivity

2.2.1 London theory

The first theory which could account for the existence of the Meissner-Ochsenfeld effect was developed by the two brothers, F. London and H. London, in 1935 [12]. Their theory was originally motivated by two-fluid model. They assumed that all free electrons in a superconducting material can be a divided into two groups: superconducting electrons of density n_s and normal electrons of density n_n. The total density of free electrons is $n = n_s + n_n$. As the temperature increases from 0 to T_c, the density n_s decreases from n to 0. They also considered that both the electric field , $\boldsymbol{E}$, and the magnetic field, $\boldsymbol{H}$, are so weak that they do not have any appreciable influence on n_s (n_s = constant everywhere) and the supercurrent is homogeneous.

The equation of motion for n_s electrons in an electric field $\boldsymbol{E}$ is

$$n_s m \frac{d\boldsymbol{v}_s}{dt} = n_s e\boldsymbol{E}, \tag{2.1}$$

where m is the electron mass, e is the electron charge, $\boldsymbol{v}_s$ is the superfluid velocity. Visualizing the currents as a flow of the superconducting electrons of number density n_s (per unit volume), charge and mass moving with the superfluid velocity $\boldsymbol{v}_s(\boldsymbol{r})$, one can calculate the supercurrent density as $\boldsymbol{j}_s = n_s e \boldsymbol{v}_s(\boldsymbol{r})$, then the above equation becomes

$$\boldsymbol{E} = \frac{d}{dt}(\Lambda \boldsymbol{j}_s). \tag{2.2}$$

This is the first London equation, where $\Lambda = m/n_s e^2$. It denotes the perfect conductivity: when $d/dt(\boldsymbol{j}_s) = 0$ the electric field inside the superconductor is absent.

The total free energy of the superconductor can be written as:

$$\mathcal{F} = \int f_s d^3\boldsymbol{r} + \mathcal{F}_{\text{kin}} + \mathcal{F}_{\text{mag}}, \tag{2.3}$$

where f_s is the superconductor energy density, $\mathcal{F}_{\text{kin}}$ the kinetic energy of the electric currents, and $\mathcal{F}_{\text{mag}} = \int \boldsymbol{H}^2/8\pi d^3\boldsymbol{r}$ the energy of the magnetic field $\boldsymbol{H}^2$. The total kinetic energy of such flow of particles is then

$$\mathcal{F}_{\text{kin}} = \int \frac{1}{2} n_s m v_s^2 d^3\boldsymbol{r}. \tag{2.4}$$

Moreover, the currents must obey the Maxwell equation $\boldsymbol{\nabla} \times \boldsymbol{H} = \frac{4\pi}{c}\boldsymbol{j}_s$. Substituting this information into Eq. (2.3) we obtain

$$\mathcal{F} = \mathcal{F}_0 + \frac{1}{8\pi}\int [\boldsymbol{H}^2 + \lambda_L^2 |\boldsymbol{\nabla} \times \boldsymbol{H}|^2] d^3\boldsymbol{r}, \tag{2.5}$$

where we denoted $\mathcal{F}_0 = \int f_s d^3\boldsymbol{r}$ and the London penetration depth λ_L is defined as

$$\lambda_L = \left[\frac{mc^2}{4\pi n_s e^2}\right]^{\frac{1}{2}}. \tag{2.6}$$

Now we look for the configuration of the local magnetic field $\boldsymbol{H}(\boldsymbol{r})$ which minimizes the above energy, by searching for a variational fixed point of energy $\mathcal{F}$ with respect to small variation $\delta\boldsymbol{H}(\boldsymbol{r})$

$$\begin{aligned} \delta\mathcal{F} =& \frac{1}{4\pi}\int [\boldsymbol{H} \cdot \delta\boldsymbol{H} + \lambda_L (\boldsymbol{\nabla} \times \boldsymbol{H}) \cdot (\boldsymbol{\nabla} \times \delta\boldsymbol{H})] d^3\boldsymbol{r} \\ =& \frac{1}{4\pi}\int [\boldsymbol{H} + \lambda_L (\boldsymbol{\nabla} \times \boldsymbol{\nabla} \times \boldsymbol{H})] \cdot \delta\boldsymbol{H} d^3\boldsymbol{r}, \end{aligned} \tag{2.7}$$

where the final expression has been obtained by integration by parts. For $\delta\mathcal{F} = 0$ (stationary condition), we must have

$$\boldsymbol{H} + \lambda_L (\boldsymbol{\nabla} \times \boldsymbol{\nabla} \times \boldsymbol{H}) = 0. \tag{2.8}$$

Additional use of the vectorial identity $\boldsymbol{\nabla} \times \boldsymbol{\nabla} \times \boldsymbol{H} = \boldsymbol{\nabla}(\boldsymbol{\nabla} \cdot \boldsymbol{H}) - \nabla^2 \boldsymbol{H}$ and the Maxwell equation $\boldsymbol{\nabla} \cdot \boldsymbol{H} = 0$ finally leads us to:

$$\nabla^2 \boldsymbol{H} = \frac{\boldsymbol{H}}{\lambda_L}, \tag{2.9}$$

where ∇^2 is the Laplace operator. This equation is the second London equation, and together with the Maxwell equation, it allows one to calculate the spatial distribution of the magnetic fields and currents.

The simplest situation to consider is a semi-infinite superconductor filling the half-space $x > 0$, and a normal material filling the half-space $x < 0$, where the surface coincides with $x = 0$ plane, with applied homogeneous external field H_0 parallel to the surface. We solve Eq. (2.9) with the boundary conditions $H(0) = H_0$ and $H(\infty) = 0$, where we want to calculate the field profile inside the superconductor. It is trivial to see that the appropriate solution is $H(x) = H_0 e^{-x/\lambda_L}$, meaning that the magnetic field decays inside a superconductor with a characteristic length scale given by London penetration depth λ_L which is analog of the skin depth in a metal. A visual representation of λ_L is given in Fig. **2-3**. Following the two fluid model, λ_L is also temperature dependent, as

$$\lambda_L(T) = \frac{\lambda_L(0)}{[1 - (T/T_c)^4]^{\frac{1}{2}}} \tag{2.10}$$

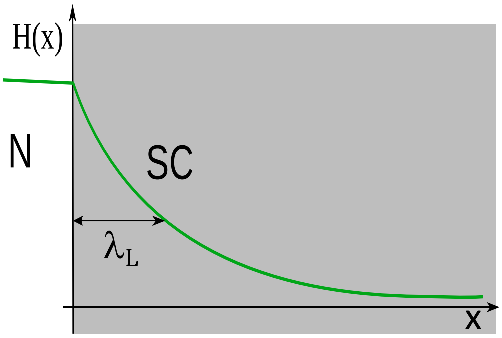

Figure 2-3 : A normal/superconductor boundary in the presence of an applied external magnetic field. The field decays into the superconductor over characteristic lengthscale λ_L.

2.2.2 Phenomenological Ginzburg-Landau (GL) Theory

In 1950, L. Landau and V. Ginzburg applied this successful framework and achieved a powerful phenomenological theory that could explain superconductivity as a second order phase transition [13][a].

The theory relies on a space dependent order parameter Ψ which is supposed to vanish in the normal state, but to take some finite value below the critical temperature; it is usually normalized to the density of supercharge carriers n_s already introduced in the London theory:

$$\Psi(\boldsymbol{r}) = \sqrt{n_s(\boldsymbol{r})}e^{i\theta(\boldsymbol{r})}. \tag{2.11}$$

It is further assumed that the thermodynamic free energy $\mathcal{G}$ of the system is an analytic function of n_s, so that its value $\mathcal{G}_s$ in the superconducting state can be expanded in power series around its value in the normal state $\mathcal{G}_n$, close to the critical temperature

$$\mathcal{G}_s = \mathcal{G}_n + \alpha n_s + \frac{\beta}{2} n_s + \cdots . \tag{2.12}$$

It follows that the Ginzburg-Landau (GL) theory is strictly valid only close to the critical temperature. A dynamical approach requires the introduction of gradients of the order parameter, which are combined with the electromagnetic field in such way that local U(1) gauge invariance is preserved. Finally, the free energy of the normal state can involve different definitions, and may always be shifted by a constant, so that in general one is interested in the condensation energy $\mathcal{G}_s - \mathcal{G}_n$:

$$\mathcal{G}_s - \mathcal{G}_n = \alpha|\Psi|^2 + \frac{\beta}{2}|\Psi|^4 + \frac{1}{2m}\left|\left(-i\hbar\boldsymbol{\nabla} - \frac{e^*}{\boldsymbol{c}}\boldsymbol{A}\right)\right|^2 + \frac{(\boldsymbol{H}-\boldsymbol{H}_0)^2}{2\mu_0}, \tag{2.13}$$

where $\boldsymbol{A}$ is the electromagnetic vector potential. It is now admitted that superconductivity involves paired electrons, so that we may identify the electric charge $e^* = 2e = -2|e| < 0$ in the term accompanying the gradient. For the same reason, one generally considers $m^* = 2m$ as the mass of one pair of electrons. Assuming the superconducting state to be energetically more favourable than the normal state below the critical temperature, this energy difference must be kept negative. The quantities α and β are phenomenological parameters whose signs are fixed by analysis of the power expansion: β must be positive, otherwise the minimal energy would be obtained for arbitrary large values of the order parameter, and the only way to get a nontrivial value of the order parameter which minimizes the energy is to assume that α is negative [see Fig. **2-4**]. In principle both parameters are temperature dependent: one can show that α varies as $1-t$, with $t = T/T_c$, close to the critical temperature, and β as $(1-t^2)^{-2}$ and is usually taken to be constant [14].

- Ginzburg-Landau Equations

---

[a] In second order transitions, one phase evolves into the other so that both phases never coexist. Their first derivatives are continuous, and second derivatives are discontinuous.

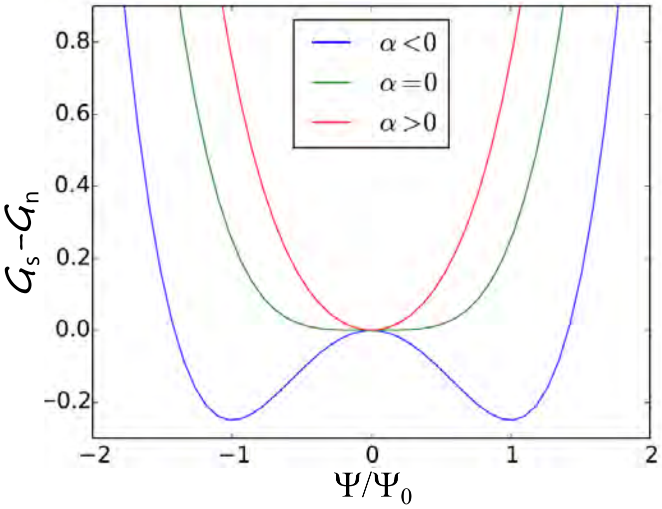

Figure 2-4 : Ginzburg-Landau free-energy functions for describing spontaneous symmetry breaking through a second order phase transition.

The total energy of the superconducting system can be obtained from the volume integration of Eq. (2.13), and the equilibrium state is reached when the variations of this total energy with respect to Ψ^* and $\boldsymbol{A}$ become zero.

The former $\delta_{\Psi^*}\mathcal{G}_s$ can be written as

$$\int \left\{ \alpha\Psi\delta\Psi^* + \frac{1}{2m^*}\left[(-i\hbar\boldsymbol{\nabla} - \frac{e^*}{c}\boldsymbol{A})\Psi(-i\hbar\boldsymbol{\nabla} - \frac{e^*}{c}\boldsymbol{A})\delta\Psi^*\right] + \beta|\Psi|^2\delta\Psi \right\} d^3\boldsymbol{r} = 0. \qquad (2.14)$$

Let $\varphi = (-i\hbar\boldsymbol{\nabla} - \frac{e^*}{c}\boldsymbol{A})\Psi$, by using relationship $\boldsymbol{\nabla}\cdot(d\nu) - \nu\cdot\boldsymbol{\nabla}d + d\boldsymbol{\nabla}\cdot\nu$ where d is a scalar, the second term in Eq. (2.14) can be written as

$$\frac{1}{2m^*}\varphi(-i\hbar - \frac{e^*}{\boldsymbol{c}}\boldsymbol{A})\delta\Psi^* = \frac{1}{2m^*}i\hbar\left[\boldsymbol{\nabla}\cdot(\delta\Psi^*\varphi) - \delta\Psi^*\boldsymbol{\nabla}\cdot\varphi\right] - \frac{1}{2m^*}\varphi\frac{e^*}{\boldsymbol{c}}\boldsymbol{A}\delta\Psi. \qquad (2.15)$$

Following Gauss theorem $\int \boldsymbol{\nabla T}d^3\boldsymbol{r} = \oint \boldsymbol{n}\cdot\boldsymbol{T}d^2\boldsymbol{r}$,

$$\int \frac{1}{2m^*}(-i\hbar\boldsymbol{\nabla} - \frac{e^*}{c}\boldsymbol{A})\delta\Psi^* d^2\boldsymbol{r} = \int \frac{1}{2m^*}i\hbar\left[\boldsymbol{\nabla}\cdot(\delta\Psi^*\varphi) - \delta\Psi^*\boldsymbol{\nabla}\cdot\varphi\right]d^3\boldsymbol{r} - \frac{1}{2m^*}\oint_s i\hbar\boldsymbol{n}\cdot\varphi\delta\Psi d^2\boldsymbol{r}. \qquad (2.16)$$

Eq. (2.16) can only be satisfied if

$$\alpha\Psi + \frac{\beta}{2}|\Psi|^2\Psi - \frac{1}{2m^*}\left(-i\hbar\boldsymbol{\nabla} - \frac{e^*}{c}\boldsymbol{A}\right)^2\Psi = 0, \qquad (2.17)$$

with the additional boundary condition

$$\oint \boldsymbol{n}\cdot\left[\frac{1}{2m^*}\left(-i\hbar\boldsymbol{\nabla}-\frac{e^*}{c}\boldsymbol{A}\right)\Psi\delta\Psi^*\right]d^2\boldsymbol{r}=0\Rightarrow\left(-i\hbar\boldsymbol{\nabla}-\frac{e^*}{c}\boldsymbol{A}\right)\Psi\bigg|_{\partial\Omega}=0. \tag{2.18}$$

Which are the first Ginzburg-Landau equation and the boundary condition (valid for a superconductor vacuum interface), respectively, where the subscript $\partial\Omega$ refers to the component normal to the sample surface. The first relation is recognized as the Schrodinger equation for the superconducting carriers; the second generalizes London's constitutive relation including possible spatial variation of Ψ.

The variation of Eq. (2.13) with respect to the vector potential $\boldsymbol{A}$ is

$$\begin{aligned}&\int\left\{\left(-i\hbar\boldsymbol{\nabla}-\frac{e^*}{c}\boldsymbol{A}\right)\Psi\frac{-e^*}{c}\delta\boldsymbol{A}\Psi^*+\frac{-e^*}{c}\delta\boldsymbol{A}\Psi\left(-i\hbar\boldsymbol{\nabla}-\frac{e^*}{c}\boldsymbol{A}\right)\Psi^*\right\}d^3\boldsymbol{r}+\\&+\frac{1}{4\pi}\int(\boldsymbol{\nabla}\times\boldsymbol{A}-\boldsymbol{H})\cdot\boldsymbol{\nabla}\times\delta\boldsymbol{A}d^3\boldsymbol{r}=0.\end{aligned} \tag{2.19}$$

The first integral can be written as

$$\int\left[\frac{i\hbar e}{m^*c}(\Psi^*\boldsymbol{\nabla}\Psi-\Psi\boldsymbol{\nabla}\Psi^*)+\frac{4e^2}{m^*c^2}|\Psi|^2\boldsymbol{A}\right]\cdot\delta\boldsymbol{A}d^3\boldsymbol{r}=0. \tag{2.20}$$

By using vector identity $\boldsymbol{\nabla}\cdot(\boldsymbol{a}\times\boldsymbol{b})=\boldsymbol{b}\cdot(\boldsymbol{\nabla}\times\boldsymbol{a})-a\cdot(\boldsymbol{\nabla}\times\boldsymbol{b})$, the second integral becomes

$$\frac{1}{4\pi}\int\left\{\delta\boldsymbol{A}\cdot\boldsymbol{\nabla}\times\boldsymbol{\nabla}\times\boldsymbol{A}+\boldsymbol{\nabla}\cdot[\delta\boldsymbol{A}\times(\boldsymbol{\nabla}\times\boldsymbol{A}-\boldsymbol{H}_0)]\right\}d^3\boldsymbol{r}=0. \tag{2.21}$$

By using Gauss's theorem

$$\int\boldsymbol{\nabla}\cdot[\delta\boldsymbol{A}\times(\boldsymbol{\nabla}\times\boldsymbol{A}-\boldsymbol{H}_0)]d^3\boldsymbol{r}=\oint_s[\delta\boldsymbol{A}\times(\boldsymbol{\nabla}\times\boldsymbol{A}-\boldsymbol{H}_0)]d^2\boldsymbol{r}, \tag{2.22}$$

with turns out to be zero if one chooses the integral surface to be far from the superconductor, where $\boldsymbol{A}=\boldsymbol{A}_0$. Eq. (2.19) finally takes the form

$$\int\left[\frac{i\hbar e}{m^*c}(\Psi^*\boldsymbol{\nabla}\Psi-\Psi\boldsymbol{\nabla}\Psi^*)+\frac{4e^2}{m^*c^2}|\Psi|^2\boldsymbol{A}+\frac{1}{4\pi}\boldsymbol{\nabla}\times\boldsymbol{\nabla}\boldsymbol{A}\right]\cdot\delta\boldsymbol{A}dV=0, \tag{2.23}$$

which combined with the Maxwell equation (Ampere's law)

$$\boldsymbol{j}_s=\frac{\boldsymbol{c}}{4\pi}\boldsymbol{\nabla}\times\boldsymbol{A}, \tag{2.24}$$

gives the second GL equation as

$$\boldsymbol{j}_s = \frac{i\hbar e}{m^*}(\Psi^* \boldsymbol{\nabla} \Psi - \Psi \boldsymbol{\nabla} \Psi^*) + \frac{4e^2}{m^* \boldsymbol{c}^2} |\Psi|^2 \boldsymbol{A}. \tag{2.25}$$

For a superconductor-normal metal interface the boundary condition must be modified, the more general expression, which assures that no supercurrent passes perpendicular to the sample boundary, can be written as [14].

$$\left(-i\hbar \boldsymbol{\nabla} - \frac{e^*}{c} \boldsymbol{A} \right) \Psi \bigg|_{\partial\Omega} = \frac{i\hbar}{b} \Psi \bigg|_{\partial\Omega}, \tag{2.26}$$

with b the extrapolation length (de Gennes extrapolation length) over which the order parameter becomes zero in the normal metal by extrapolation [see Fig. **2-5**]. Notice that for a superconductor-normal metal interface b is positive.

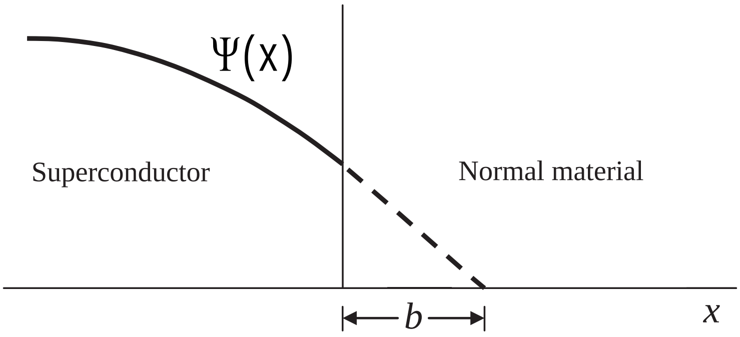

Figure 2-5 : Schematic diagram illustrating the boundary condition (2-26) at an superconductor/normal material interface characterized by an extrapolation length b. Taken from [14].

The value of the extrapolation length is determined by the medium adjacent to the superconductor:

- for vacuum or insulator: $b \rightarrow \infty$,
- for normal metals: $b > 0$, and for ferromagnets or disordered materials: $b \rightarrow 0$,
- for a superconducting layer material with a higher T_c: $b < 0$.

Validity of the Ginzburg-Landau theory

A few points need to be discussed in relation to the validity of the GL equations ref [15]:

- Landau assumes in his theory of second order transitions that the free energy can be expanded in powers of $|\Psi|$ [16]. This is not generally valid, but Gor'kov showed theoretically that the Landau expansion is valid in the case of superconductors [17].
- Ψ must be a slowly varying function over distances of the order of ξ_0. A necessary condition for the validity of the theory is, therefore, $\xi(T) \gg \xi_0$ or

  $$\frac{T_c - T}{T_c} \ll 1 \tag{2.27}$$

  i.e. the temperature must be close to T_c, the critical temperature in zero field.
- The local electrodynamic approximation will be valid only if $\boldsymbol{H}$ and $\boldsymbol{A}$ are slowly varying functions over distances of the order of ξ_0. Therefore, it is necessary that $\lambda(T) \gg \xi_0$ or

  $$\frac{T_c - T}{T_c} \ll \left[\frac{\lambda(0)}{\xi_0}\right]^2, \tag{2.28}$$

  which expresses again the temperature must be close to T_c

2.2.3 Characteristic Length Scales

From the GL equations some meaningful quantities can be defined. For a bulk superconductor in the absence of a magnetic field, Eq. (2.17) in one dimension reduce to

$$\alpha\Psi + \beta\Psi^3 - \frac{\hbar^2}{2m}\frac{\partial^2\Psi}{\partial x^2} = 0, \tag{2.29}$$

where we chose a gauge in which the order parameter is real. This has as non-trivial solution $|\Psi| = \Psi_0 = \sqrt{-\alpha/\beta}$, the value of the order parameter far away from inhomogeneities. By expressing the order parameter in Ψ_0 by defining $\psi = \Psi/\Psi_0$, the GL equation reduces to

$$-\psi + \psi^3 - \frac{\hbar^2}{2m|\alpha|}\frac{\partial^2\psi}{\partial x^2} = 0, \tag{2.30}$$

and a characteristic length scale for variation of ψ emerges,

$$\xi^2 = \frac{\hbar^2}{2m|\alpha|}, \tag{2.31}$$

over which changes of ψ are expected happen. This fundamental length scale is called the coherence length. When we consider a normal metal-superconductor boundary at $x = 0$, the meaning of ξ becomes clear. We then have $\psi = 0$ at $x = 0$ and $\psi = 1$ at $x \to \infty$ as boundary condition. The solution of Eq. (2.29) becomes

$$\psi = \tanh\left(\frac{x}{\sqrt{2}\xi}\right), \tag{2.32}$$

i.e. ξ represents the length over which the order parameter heals.

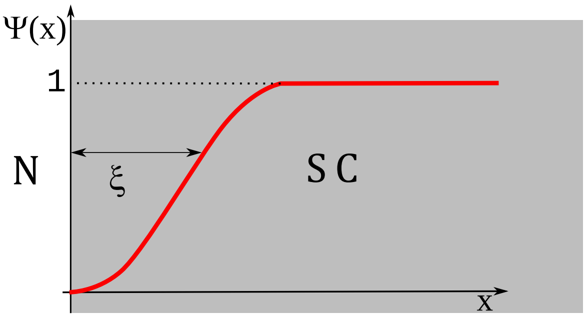

Figure 2-6 : The density of superconducting charge carriers within a superconducting material can vary over a characteristic length scale (ξ) called the coherence length. ξ emerges from the Ginzburg-Landau theory and is defined in Eq. 2.31.

Figure **2-6** offers a visual representation of how ψ varies at a superconducting/normal boundary. It is now clear that GL theory achieves what it set out to do: characterise the spatial variation of ψ within a superconductor.

Since α depends on the temperature as $\alpha \propto (T - T_c)$, the coherence length varies as a function of the temperature as

$$\xi(T) \propto (1 - T/T_c)^{-1/2}. \tag{2.33}$$

Notice that this is certainly not the same length as the BCS coherence length [14, 18]. Near T_c the relation between $\xi(T)$ and ξ_0 depends on the material purity, defined by elastic mean free path l_{el}:

$$\xi(T) = 0.74\xi_0(1 - T/T_c)^{-1/2} \quad \text{when} \quad l_{el} \gg \xi_0(\text{pure}), \tag{2.34}$$

$$\xi(T) = \sqrt{\xi_0 l_{el}}(1 - T/T_c)^{-1/2} \quad \text{when} \quad l_{el} \ll \xi_0\text{dirty}). \tag{2.35}$$

Notice further that the coherence length $\xi(T)$ diverges at the critical temperature T_c.

Another fundamental length scale emerges when considering the second GL equation. In a weak magnetic field the order parameter can be assumed constant and equal to Ψ_0 and in that case Eq. (2.25) reduces to

$$\boldsymbol{j}_s = -\frac{4e^2}{mc}|\Psi_0|^2\boldsymbol{A}, \tag{2.36}$$

which is simply the second London Eq. (2.24-2.25) describing that a magnetic field cannot penetrate a superconductor beyond a layer of thickness λ. After taking the curl of both sides, gives:

$$\lambda^2 = \frac{mc^2}{16|\Psi_0|^2\pi e^2} = \frac{mc^2}{8\pi e^2 n_s} = \frac{mc^2\beta}{16\pi|\alpha|e^2} \tag{2.37}$$

where the density of superconducting electrons $n_s = 2|\Psi_0|^2 = 2|\alpha|/\beta$. Also the penetration depth $\lambda(T)$ varies as a function of the temperature as

$$\lambda(T) \propto /(1 - T/T_{c0})^{-1/2}, \tag{2.38}$$

since $|\Psi_0|^2 \propto |\alpha| \propto (T_{c0} - T)$. The relation between the temperature dependent penetration depth $\lambda(T)$ and the London penetration depth $\lambda_L(0)$ at absolute zero temperature differs for pure and dirty materials [14]

$$\lambda(T) = \frac{\lambda(T)}{\sqrt{2}}(1 - T/T_{c0})^{-1/2} \qquad \text{when} \qquad l_{el} \gg \xi_0(\text{pure}), \tag{2.39}$$

$$\lambda(T) = \frac{\lambda(T)}{\sqrt{2}}\sqrt{\frac{\xi_0}{1.33 l_{el}}}(1 - T/T_{c0})^{-1/2} \qquad \text{when} \qquad l_{el} \ll \xi_0(\text{dirty}) \tag{2.40}$$

Notice that the penetration depth $\lambda(T)$ diverges at the critical temperature T_c

2.2.4 Types of Superconductors

A classification of superconductors can be made depending on their behavior in an external applied magnetic field. This division is based on the fact that the surface energy σ_s which is proportional to the difference $(\xi - \lambda)$, of a boundary between a normal and superconducting (S/N) has different sing depending on the value of the GL parameter $\kappa = \lambda/\xi$. In fact for $T = T_c$ it changes sign at $\kappa_0 = 1/\sqrt{2}$ [19, 20]. If $\kappa < \kappa_0$(type-I superconductor), the energy of the interface $\sigma_s > 0$, i. e., the system tends to minimize the normal-superconducting interface; if $\kappa > \kappa_0$ (type-II superconductor), the energy of the interface $\sigma_{ns} < 0$, i. e., the system tends to maximize the normal superconducting interface. This favors formation of superconductor-normal boundaries and the flux penetration in small tubes (vortices) each one carrying a quantized amount of flux, or superconducting flux quantum $\Phi_0 = hc/2e = 2.7 \times 10^{-15} Tm^2$. Therefore, two types of superconductors are distinguished by κ. This behavior of type-I and type-II materials at an SN interface is illustrated in Fig. **2-7**.

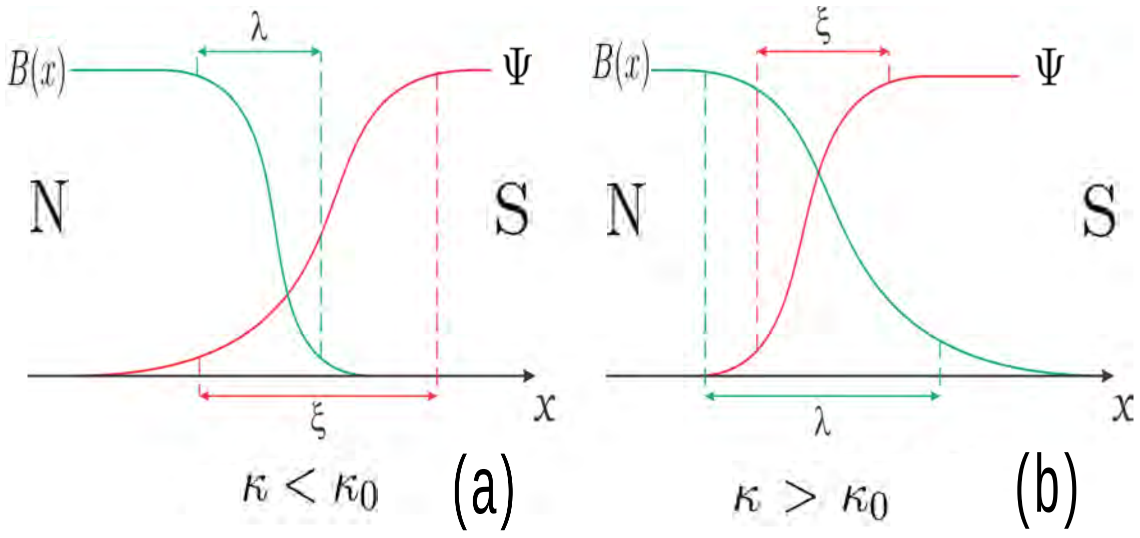

Figure 2-7 : Spatial variation of the magnetic induction $B(x)$ and the order parameter $\Psi(x)$ in type-I and type-II superconductor. (a) type-I superconductor $\kappa < \kappa_0$, (b) type-II superconductor, $\kappa > \kappa_0$.

All critical fields can be expressed in terms of the fundamental length scales of the GL theory. The field at which a type-I superconductor abruptly loses superconductivity,

$$H_c(T) = \frac{\Phi_0}{2\sqrt{2}\lambda(T)\xi(T)}, \tag{2.41}$$

is called the thermodynamic critical field, as it corresponds to an energy density equal to the condensation energy density of the superconducting state in te absence of a magnetic field.

A bulk type-II superconductor is in the Meissner state until the first critical field $H_{c1} < H_c$ is reached,

$$H_{c1}(T) = \frac{\Phi_0}{4\pi\lambda^2(T)} \ln(k) = \frac{H_c(T)\ln(\kappa)}{\sqrt{2}\kappa}. \tag{2.42}$$

After this field the magnetic induction is allowed to penetrate the sample stepwise by means of vortices, each carrying one magnetic flux quantum. The vortices arrange themselves in an Abrikosov lattice. By further increasing the field, vortices keep entering the sample, the mean Cooper pair density gradually decreases, eventually leading to the loss of superconductivity at the second critical field

$$H_{c2} = \frac{\Phi_0}{2\pi\xi^2(T)} = \sqrt{2}\kappa H_c. \tag{2.43}$$

In the region $H_{c2} < H < H_{c3}$, superconductivity only exists at a thin layer of thickness $\xi(T)$ near the sample edge, while the inner side of the sample is in the normal state. For bulk type-II superconductors, which an applied magnetic parallel to sample surface, the third critical field H_{c3} is $H_{c3} \approx 1.69H_{c2}$ [18]. In obtaining the latter expression it was assumed that the medium has flat boundary and it is semi-infinite, which allows one to ignore all other surfaces. In general the coefficient for H_{c3} is geometry dependent. For example, for a thin field in a parallel field the critical field for bulk superconductivity, i.e $H_{c3} = 2H_{c2}$ [14]. If the surface of a superconductor is covered with a layer of normal metal, it causes a reduction of H_{c3} to a value very close to H_{c2}.

The critical fields H_c, H_{c1}, H_{c2} and H_{c3} depend on temperature. The $H-T$ phase diagram for type-I and type-II bulk superconductors are shown in the Fig. **2-8**.

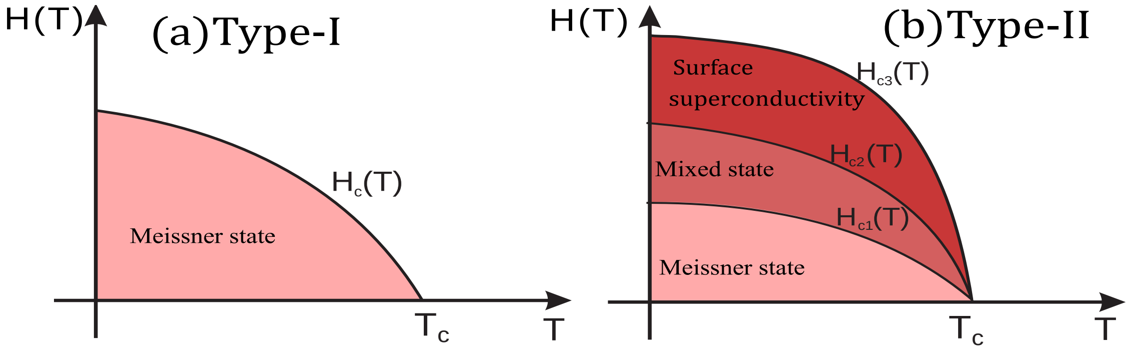

Figure 2-8 : Schematic $H-T$ phase diagram for a type-I (a) and a type-II (b) bulk superconductor.

The different phases (Meissner, mixed and normal) can be easily identified by the equilibrium magnetization:

$$\boldsymbol{M} = \frac{1}{4\pi}(\boldsymbol{B} - \boldsymbol{H}_0), \tag{2.44}$$

where the magnetic induction $\boldsymbol{B} = \langle \boldsymbol{H} \rangle$ and $\boldsymbol{H}_0$ is the applied magnetic field.

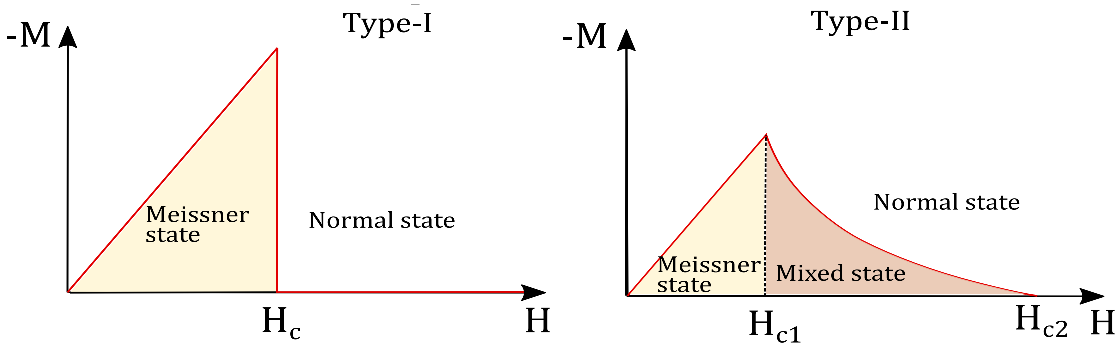

Figure 2-9 : The magnetization as a function of the applied magnetic field for bulk type-I and type-II superconductor.

Fig. **2-9** shows the negative of the magnetization $-M$ plotted as a function of the applied field H for bulk type-I and type-II superconductors. In the Meissner state all magnetic flux is expelled ($B = 0$) from the interior of the sample and therefore $M = -H/4\pi$. For absolute values of the field $H > H_{c1}$, type-II superconductors are in the mixed state. The incoming magnetic flux causes a smooth decrease of the magnetization $|M|$ down to zero at the second critical field H_{c2}, where superconductivity is suppressed. Some examples of critical fields are given in Table **2-1** .

Table 2-1 : Experimental values of superconducting parameters for some materials: T_c is the critical temperature, expressed in Kelvin, κ GL-parameter, H_c, H_c1, H_{c2} critical magnetic fields expressed in Tesla.

Metal	κ	H_c	H_c1	H_{c2}	T_c
Al	0.07	0.11			1.2
Sn	0.15	0.030			3.7
Pb	0.45	0.076			7.2
Nb	1.03	0.157	0.003	0.223	9.3
Nb_3Sn	22	1.95	0.12	29	18
YBCO($\|c$)	560	1.1	0.01	130	92

2.3 Vortices in Superconductors

2.3.1 Flux quantization

The distinguishing property of type-II superconductors is the existence of an intermediate state between the Meissner and the normal phase where vortices appear due to the negative energy of the superconducting-normal interface. Using the second GL equation, let us calculate the magnetic flux inside area S of a type-II superconductor enclosed by a path C. Writing the order parameter in the polar form of complex numbers, i.e. $\Psi = |\Psi|e^{i\varphi}$. Eq (2.25) becomes

$$\boldsymbol{j}_s = \frac{2e\hbar}{m}|\Psi|^2\boldsymbol{\nabla}\varphi - \frac{4e^2}{mc}|\Psi|^2\boldsymbol{A}. \tag{2.45}$$

Consider a contour C enclosing the flux inside the superconductor, as show in Fig. **2-10**, where the supercurrent $j_s = 0$ everywhere on C. The contour integral of vector potential along C can be calculated as

$$\oint_C \boldsymbol{A} \cdot d\boldsymbol{l} = \frac{c\hbar}{2e}\oint_C \boldsymbol{\nabla}\varphi \cdot d\boldsymbol{l}. \tag{2.46}$$

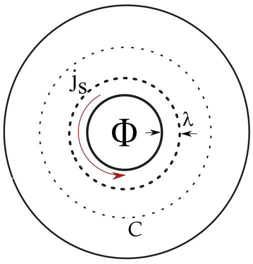

Figure 2-10 : Flux quantization

From Eq. (2.46), one can see that φ is a multiple-valued function. However the wavefunction Ψ must be single-valued. Therefore, we have to stipulate that the change in φ after each turn around the hole containing the magnetic flux must be an integral multiple of 2π. Indeed, the addition of $2\pi n$ where $n = 0, 1, 2, \cdots$ to φ does not change the function $\Psi(\boldsymbol{r}) = \psi(\boldsymbol{r})e^{i\varphi}$ since $e^{i2\pi n} = 1$. Therefore $\oint_C \boldsymbol{\nabla}\varphi \cdot d\boldsymbol{l} = 2\pi n$ and Eq. (2.46) can finally be written as

$$\Phi = n\Phi_0, \qquad \text{where} \qquad \Phi_0 = \frac{\hbar c}{2e}. \tag{2.47}$$

This shows that the magnetic flux enclosed can only assume values which are integer multiples of the minimal possible magnetic flux, the magnetic flux quantum Φ_0. The value of Φ_0 is defined above and equals to 2.7×10^{-15}T m^2. The generalized expression of Eq. (2.47) to the case of any contour (even with non-zero current) is

$$\Phi = n\Phi_0 - \frac{mc}{4e^2}\oint_C \frac{\boldsymbol{j}_s}{|\psi^2|} \cdot d\boldsymbol{l}. \tag{2.48}$$

2.3.2 Vortex state

In section 2.2.3 we defined two regimens based in considerations of the overall system energy at the superconducting/normal (SN) interface. In type-I bulk superconductor, the system exhibits the Meissner-Ochsenfeld effect until superconductivity is destroyed by the applied magnetic field. In the type-II superconductor, the SN boundary has negative sing and so nature acts to maximise the surface area of the interface by admitting flux (normal regions) into the samples where they coexist alongside Meissner screened areas of superconductivity. In light of the results discussed in the previous section it is now clear that in order to minimise the total system energy (maximise the SN surface area), flux penetration will occur in the form of flux tubes containing quantised packets of flux Φ_0 known as superconducting vortices. Within the framework of GL the structure of vortex is characterized by two fundamental length scales: the magnetic penetration depth λ and the coherence length ξ, where $\lambda > \xi$. The flux tubes can be described as a cylindrical normal core with radius ξ and a superconducting current circulating around it at a radius λ.

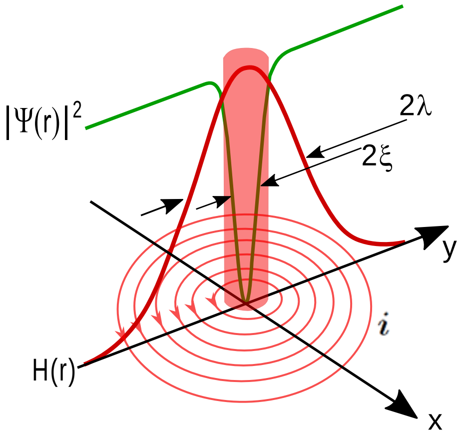

Figure 2-11 : The magnetic flux density and the magnitude of the order parameter, $\Psi(r)$, for a isolated vortex. The magnetic flux density decreases from the maximum value at the vortex centre to zero in the superconductor with a characteristic length λ. The order parameter grows from zero to maximum value in the superconductor with a characteristic lenth ξ.

The structure of a vortex is depicted in Fig. **2-11**. A maximum of the magnetic flux density occurs in the centre of the vortex and at large distance from the core decays roughly exponentially with the penetration depth λ. The order parameter $\Psi(\boldsymbol{r})$ is reduced in a small core region with radius of the order of the coherence length ξ, therefore the vortex core can be represented as a region of normal phase of an area $\sim \pi\xi^2$.

Abrikosov predicted theoretically, that the most energetically favorable configuration for a vortex lattice in the absence of any impurity in the superconducting material is the square array. His prediction for the square lattice had a small numerical error which was later rectified by Kleiner [21] and showed that the hexagonal configuration is most favorable situation for all possible periodic [see Fig. **2-12**].

This state of a superconductor is referred to as the mixed state because it is characterized by a partial penetration of the magnetic field in the interior of the specimen so that the sample contains interrelated superconductivity and normal regions. The existence of the mixed state in type-II superconductor has been verified by experiments, where the first experimental demonstration was done via Bitter decoration by Essmann and Trauble in 1967 [23] and other experimental works with different techniques as: Magneto-optical imaging, scacnning SQUID microscopy, scanning Hall probe microscopy, transmission electron microscopy (TEM) are cited in the references [24–30].

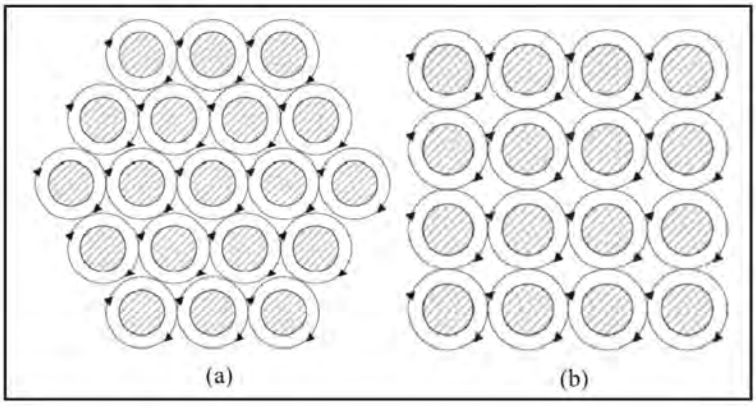

Figure 2-12 : Mixed state of a type II superconductor. Vortices form a regular triangular (hexagonal) (a) or square (b) lattice. Vortex cores (dashed regions) are normal. Taken from [22].

2.3.3 Isolated Vortex

As a long as the separation between vortices is large compared to λ, there will negligible overlap or interaction between vortices. In this limit, each vortex can be treated as isolated. We consider the case of a typical type-II superconductor, where limit $\kappa = \lambda/\xi \gg 1$, and $|\Psi|^2 = 1$ a distance $r \gg \xi$, the currents and field can be calculated by using London's equation Eq. (2.8) or from the second GL equation (Eq. 2.24) where we took the curl of both sides, we obtain

$$\boldsymbol{H} + \lambda \boldsymbol{\nabla} \times \boldsymbol{\nabla} \times \boldsymbol{H} = \frac{\Phi_0}{2\pi} \boldsymbol{\nabla} \times \boldsymbol{\nabla}\theta. \tag{2.49}$$

Around the vortex core, we have the following relationship

$$\int \boldsymbol{\nabla} \times \boldsymbol{\nabla}\theta \cdot d\boldsymbol{S} = \oint \boldsymbol{\nabla}\theta \cdot d\boldsymbol{l} = 2\pi, \tag{2.50}$$

so that

$$\boldsymbol{\nabla} \times \boldsymbol{\nabla}\theta = 2\pi\delta(r)\boldsymbol{e}_\nu, \tag{2.51}$$

where $\boldsymbol{e}_\nu$ is the unit vector along the vortex. As a result, the solution of Eq. (2.49) subjected to the boundary condition $H(\infty) = 0$ is

$$H = \frac{\Phi_0}{2\pi\lambda^2} K_0(r/\lambda), \tag{2.52}$$

where K_0 is the Bessel function with imaginary argument. By setting a cut-off at $r = \xi \ll \lambda$, one obtains an approximate field in the center of a vortex as

$$H(0) \approx \frac{\Phi_0}{2\pi\lambda} \ln\kappa \tag{2.53}$$

2.3.4 Vortex Interactions

When two vortices are far apart, the resulting current distribution can be approximated as a superposition of the individual current distribution. Then the vortex-vortex interaction can be calculated analytically. For a bulk superconductor the result is [14, 18, 31]

$$U_{vv} = \frac{\Phi_0^2}{8\pi^2\lambda} K_0\left(\frac{r}{\lambda}\right). \tag{2.54}$$

It decays exponentially for $r > \lambda$, thus it is a short range interaction. In a thin superconducting film the interaction energy is [5].

$$U_{vv} = \frac{\Phi_0^2}{4\pi^2} \frac{1}{r}. \tag{2.55}$$

It has been shown in [32] that for large distances the interaction energy between two vortices is

$$U_{vv} = \frac{\Phi_0^2}{8\pi^2\lambda} \left[K_0\left(\frac{r}{\lambda}\right) - K_0\left(\frac{r}{\xi/\sqrt{2}}\right) \right], \tag{2.56}$$

the first term is the repulsive electromagnetic interaction and the second term is the core-core attraction. When $\kappa > 1/\sqrt{2}$, i.e., for type-II superconductors, $U_{vv} > 0$ so there is an repulsive pairwise interaction. When $\kappa < 1/\sqrt{2}$, i.e., for type-I superconductors, $U_{vv} < 0$ so there is an attractive pairwise interaction.

A very special case can be found in the close vicinity to the crossover point $\kappa \approx 1/\sqrt{2}$, where Meissner (typical type-I) and vortex states (typical type-II) can co-exist in te same sample [see Fig. **2-13**] [33, 34]. This state is called in text books as "intermediate-mixed state" [35, 36]. The intermediate state is formed in type-I superconducting samples when the actual magnetic field at the sample's edge exceeds the critical field, H_c. Direct visualization of the intermediate state is ordinarily carried out on samples with flat surfaces, usually slabs or disks. There is an ongoing discussion on the effects of this nonellipsoidal geometry, with no consensus yet achieved. The thermodynamics of the intermediate state has been the subject of many works [37]. The conventional approach is to assume some geometrical pattern of the intermediate state, and then minimize its free energy by varying the geometrical parameters. The typical and most used structure is the Landau laminar pattern of alternating normal and superconducting regions. Experimental works in which the intermediate state patterns are directly observed and are shown in Fig. **2-14** [38]. In such cases, the system can present a variety of patterns, not only the reticular phases of Meissner and Abrikosov and the magnetic response exhibit discontinuity in the first critical field.

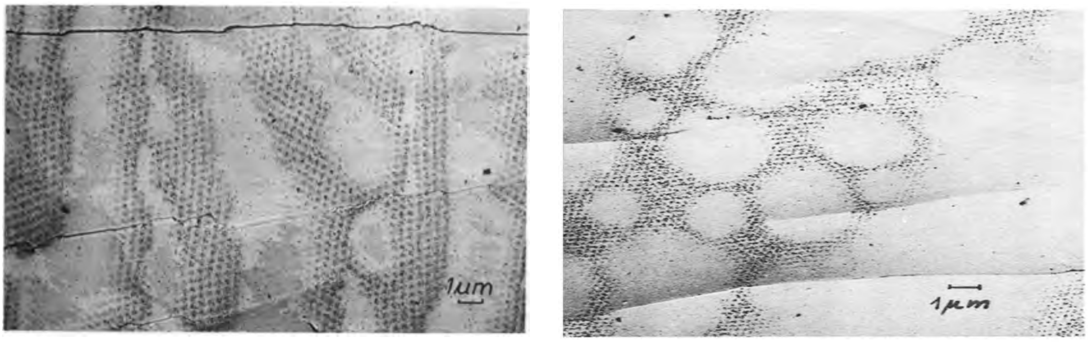

Figure 2-13 : Intermediate state ofat a Pb-1.89% TL disc (κ=0.73 at 1.2 K), with diameter 5 mm and thickness 1 mm for H_{ext} = 365 Oe. Abrikosov vortex lattice (black regions) and Meissner phase (white regions) are seen. Take from [33].

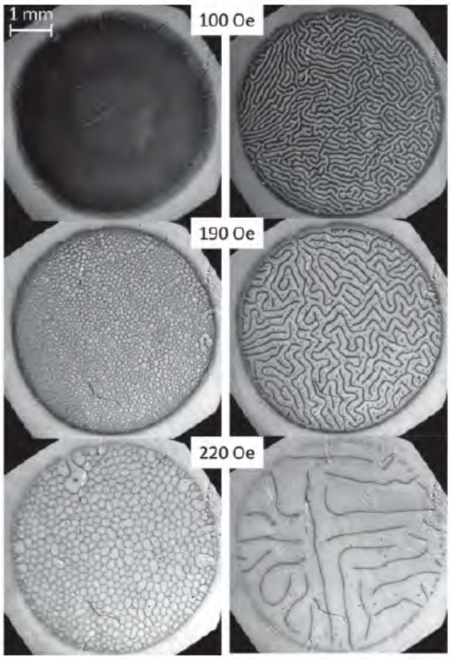

Figure 2-14 : Structure of the intermediate state in a disc-shaped Pb single crystal at 5 K. Left column-increasing magnetic field after ZFC. Right column decreasing magnetic field, Taken from [38].

Already in 1970's it was observed that type-I to type-II transition occurs at finite interval of $\kappa \approx 1/\sqrt{2}$. An experimental study of the $\kappa-$regime, in which the interaction between vortex is attractive, has been performed by Auer and Ullmaier [39] using magnetization measurements. For obtaining sufficient accuracy, such measurements required samples with high reversibility, i.e., vanishing influence of flux pinning, and a careful control of the Ginzburg-Landau parameter. Both requirements could be achieved by doping polycrystalline wires of hight-purity tantalum and niobium with nitrogen. Figure **2-15** shows a series of magnetization curves for a TaN ($\kappa = 0.665$) at different temperatures. We see that the material exhibits type-I behavior for hight-temperature curves and type-II behavior for lower-temperature curves with a discontinuity at H_{c1}. They demonstrated that between pure type-I and pure type-II (there called type-II/2) there exists a region of type-II/1 superconductivity, with a particular magnetic response, namely, with a first order transition at H_{c1}. indicating the κ-range, with attractive vortex interaction (and first order transition at H_{c1}), as function of temperature. In this phase diagram we see that vortex attraction occurs in a narrow $\kappa-$range near $\kappa = 1/\sqrt{2}$, this range becoming large with decreasing temperature.

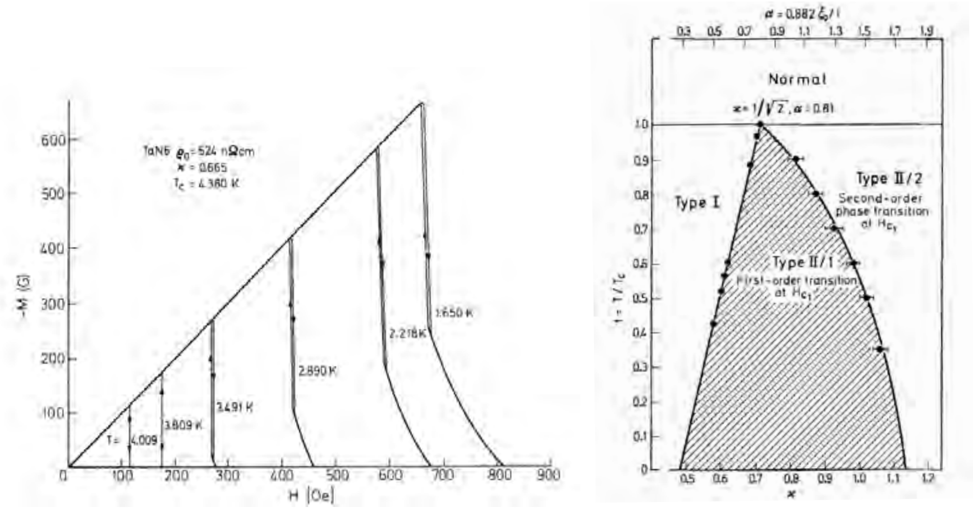

Figure 2-15 : One the left, highly reversible magnetization curves for tantalum sample doped with nitrogen, with $\kappa = 0.665$ and exhibiting the type-I behavior at the high temperatures, and type-II/1 behavior at lower temperature. On the right, phase diagram of the magnetic behavior for TaN system. Both the Ginzburg-Landau parameter κ (lower abscissa) and the impurity parameter α (upper abscissa) are proportional to the amount of dissolved nitrogen. Taken from Ref. [39].

From the theoretical point of view, $\kappa_0 = 1/\sqrt{2}$ is the Bogomolnyi point of the GL theory [19]. It has an number infinite degenerate solutions for the superconducting state, as each vorticity has the same energy at κ_0. Within Ginzburg-Landau theory, κ is temperature independent and therefore it predicts $\kappa_0 = 1/\sqrt{2}$ as universal dividing value at all temperatures, regardless of whether one considers the sign of the normal metal-superconductor interface energy, $H_c = H_{c1}, H_c = H_{c2}$ or the long-range vortex asymptotics.

2.4 The Josephson Effect

One of the archetypal consequences of the quantum behavior of electrons is their ability to tunnel through potential barriers. Similarly, the tunneling of Cooper pairs between two superconductors separated by a thin insulating or metallic layer has provided one of the hallmarks of the quantum nature of the Cooper pairs. However, the fact that the Cooper pairs form a highly coherent condensate, unlike electrons in a conduction band, allows the stabilization of an persistent flow between two weakly connected superconductors without any external drive (the Josephson effect) [11]. This effect, named after the theoretical prediction of Brian David Josephson in 1962, is one of the most successfully applied features of superconductivity in technology. In order to explain this effect, let us consider a junction where a thin layer separates two superconductors such as shown in Fig. **2-16**.

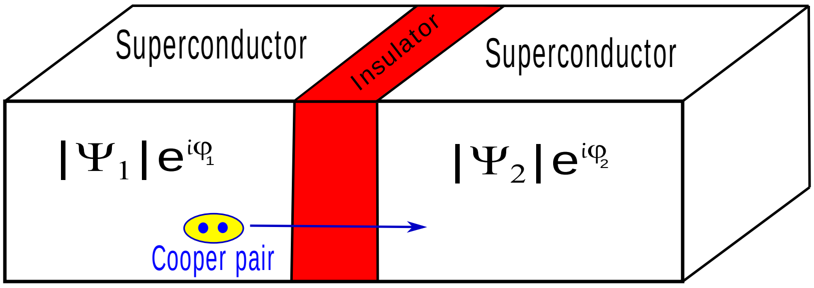

Figure 2-16 : The sketch of a Josephson junction. Taken from [40].

Moreover, consider the following appropriate boundary conditions for the junction [31].

$$\frac{\partial \Psi_1}{\partial x} - \frac{ie^*}{\hbar c} A_x \Psi_1 = \frac{\Psi_2}{\zeta}, \qquad \text{and} \qquad \frac{\partial \Psi_2}{\partial x} - \frac{ie^*}{\hbar c} A_x \Psi_2 = \frac{\Psi_1}{\zeta} \tag{2.57}$$

where ζ is a phenomenological parameter associated to the insulating layer. Substituing the junction boundary condition in the x component of the superconducting current density given by Eq. (2.25), one obtains

$$\boldsymbol{j}_x = \frac{e^*\hbar}{2m^*} \left[\Psi_1^* \left(\frac{\Psi_2}{\zeta} + \frac{ie^*}{\hbar c} A_x \Psi_1 \right) - \Psi_1 \left(\frac{\Psi_2^*}{\zeta} - \frac{ie^*}{\hbar c} A_x \Psi_1^* \right) \right]. \tag{2.58}$$

In the last equation, where the time reversal invariance of the order parameter an the vector potential was assumed, the boundary coefficient ζ become real, along with the vector potential leading to the following simple form

$$\boldsymbol{j}_x = \frac{e^* \hbar}{m^* \zeta} |\Psi_1||\Psi_2| \sin(\varphi_2 - \varphi_1), \tag{2.59}$$

where the polar expression of the superconducting order parameters have been used. If the two superconductors are the same material, the expression for this tunneling current becomes

$$\boldsymbol{j}_x = \boldsymbol{j}_m \sin \Phi_{21}, \tag{2.60}$$

where $\boldsymbol{j}_m = \frac{e^* \hbar |\Psi|^2}{m^* \zeta}$ is the maximal value of the Josephson current and $\Phi_{21} = \varphi_2 - \varphi_1$ is the phase difference between the two superconductor. Eq. (2.60) then tells us that due to tunneling of Cooper pairs between two weakly connected superconductors, a nonzero current density can appear on the junction provided that there exists an imbalance in phase between the two sides of the junction. Such imbalance can be achieved by e.g. applying a voltage to the junction or an external magnetic field.

2.5 The Lawrence-Doniach Model for Layered Superconductors

The Lawrence-Doniach (LD) model [41] can be understood as a modification of the anisotropic Ginzburg-Landau theory for the extremely anisotropic (layered) materials, where the discrete superconducting layers are only weakly coupled in the perpendicular direction. It is widely applied to the high-Tc cuprate superconductors as it is able to capture their highly anisotropic behavior which in some cases even becomes effectively two-dimensional (as expected from a stack of decoupled superconducting film planes). We will refer to this model in Chapter 7, where we will use its modification to study a superconducting bilayer composed of two layers superconductors.

In the LD model the layered superconductors are viewed as a stacked array of two-dimensional superconductors. Within each layer the GL order parameter $\Psi_n(x, y)$is a 2D function. The layers are coupled together by Josephson tunneling between adjacent layers. When the superconducting coherence length ξ is much larger than the distance between the layers, as is for example always the case close to Tc, the effective behavior is three-dimensional and the Lawrence-Doniach model gives essentially the same results as the anisotropic GL theory. If the coherence length is insufficient to “bridge” the layers, the effective behavior becomes two-dimensional. Let us take the layers to be in the *ab* plane, while the perpendicular direction will be denoted c as usual in crystallography. The Cartesian coordinates x and y then lie in the *ab* plane, while the z axis is along the c direction. The perpendicular distance between the layers is denoted by s. Then in the absence of the magnetic field we can write the free energy of the Lawrence-Doniach model as

$$\mathcal{F} = \sum_n s \int \left[\alpha|\Psi_n|^2 + \frac{1}{2}\beta|\Psi_n|^4 + \frac{\hbar^2}{2m_{ab}} \left(\left|\frac{\partial \Psi_n}{\partial x}\right|^2 + \left|\frac{\partial \Psi_n}{\partial y}\right|^2 \right) + \frac{\hbar^2}{2m_c s^2}|\Psi_n - \Psi_{n-1}|^2 \right] d^2\boldsymbol{r}, \tag{2.61}$$

where the sum runs over the layers and the integral is over the area of each layer. At this point we introduce the effective mass m_{ab} to describe different modes of the charge transport within each layer, and m_c to describe different modes of charge transport within each layer and between neighboring layers and discretized the derivative along the the $z-$direction. The reason to call the last term Josephson coupling becomes clear if we write $\Psi = |\Psi_n|e^{i\varphi_n}$ and assume that the amplitude of the order parameter $|\Psi_n|$ is the same in all layers. Then the term becomes

$$\frac{\hbar^2}{m_c s^2}|\Psi_n|^2[1 - \cos(\varphi_n - \varphi_{n-1})], \tag{2.62}$$

which has the same form as the Josephson energy. If we minimize variationally the LD free energy Eq.(2.61) with respect to Ψ_n^* we get the LD equation for Ψ_n

$$\alpha|\Psi|_n + \beta|\Psi_n|^2\Psi_n - \frac{\hbar^2}{2m_{ab}} \left(\frac{\partial^2}{\partial x^2} + \frac{\partial^2}{\partial y^2} \right) - \frac{\hbar^2}{2m_c s^2}(\Psi_{n+1} - 2\Psi_n + \Psi_{n-1}) = 0, \tag{2.63}$$

where in the last term we recognize the discrete second derivative. With the inclusion of magnetic field, i.e, non-zero vector potential $\boldsymbol{A}$ we have

$$\begin{aligned} \alpha|\Psi|_n + \beta|\Psi_n|^2\Psi_n - \frac{\hbar^2}{2m_{ab}} \left(\boldsymbol{\nabla} - i\frac{2e}{\hbar c}\boldsymbol{A} \right)^2 \Psi_n - \\ - \frac{\hbar^2}{2m_c s^2}(\Psi_{n+1}e^{-2ieA_z s/\hbar c} - 2\Psi_n + \Psi_{n-1}e^{2ieA_z/\hbar c}) = 0. \end{aligned} \tag{2.64}$$

where the m_{ab} term the gradient operator Δ and $\boldsymbol{A}$ are two-dimensional vectors in the xy plane.

We recover the anisotropic GL theory if the variation of Ψ along z direction is smooth enough so that we can replace $(\Psi_n - \Psi_{n+1})/s$ with $\partial\Psi/\partial z$.

$$\alpha\Psi + \beta|\Psi|^2\Psi - \frac{\hbar^2}{2} \left(\boldsymbol{\nabla} - i\frac{2e}{\hbar c}\boldsymbol{A} \right) \frac{1}{m} \left(\boldsymbol{\nabla} - i\frac{2e}{\hbar c}\boldsymbol{A} \right) \Psi = 0, \tag{2.65}$$

where $1/m$ is the reciprocal mass tensor i.e $\mathrm{diag}(1/m_{ab}, 1/m_{ab}, 1/m_c)$

2.6 BCS Theory

One had to wait until 1957 to see a microscopic model of superconductivity elaborated by J. Bardeen, L.N. Cooper and J.R. Schrieffer [42]. Even if it has been proved to fail in explaining the mechanisms of superconductivity in high-Tc and other exotic superconducting materials, it is still a widely applied formalism to interpret experimental results and a reference basis for other specific theories.

The BCS theory is based on the idea of an attractive interaction between electrons due to phonons. It is well know that the Coulomb interaction between two identical electric charges is repulsive. However, in certain circumstances and when described in momentum space, effective attraction can bind electrons due to their motion through the ionic lattice. The best intuitive way of understanding this fact is given by picture of thick and soft mattress on which heavy balls are thrown rolling: the trajectory of one ball leaves a depression in which a second ball moving on the mattress would fall as if the balls would attract each other. The microscopic picture of superconducting metals is identical: electrons slightly deform the crystal lattice by attracting ions cores, creating an area of greater positive charge density around itself; this excess of positive charge attracts in turn another electron. At a quantum level, those distortion and vibrations of the thermal excitations of the lattice which would break then up, the electrons remain paired; roughly, this explains why superconductivity requires very low temperatures. Cooper also showed that the optimal pairing is obtained by electrons with opposite spins and momenta.

2.6.1 The Cooper Problem

Cooper first introduced the concept of electron pairs-further called *Cooper pairs* by showing that the Fermi sea of conducting electrons was unstable in the presence of an attractive interaction; he demonstrated the possibility of bound states solutions, with negative energy with respect to the Fermi state, involving two electrons whose momenta belong to a thin shell above the Fermi level. At a quantum level, since the formed pairs have a bosonic character, nothing prevents then from condensing in the same quantum state: hence the attractive interaction leads to a condensation of paried electrons close to the Fermi level until an equilibrium is reached. The usual picture of BCS superconductivity is a twofold electron scattering by phonons. In its simplest realisation, which we shall also consider in the present study, it assumed that the process is dominated by exchanges which do not flip the electron spin, hence the so-called s-wave pairing channel.

Originally, Cooper considered to add a pair of electrons with momenta $\boldsymbol{k}$ and $-\boldsymbol{k}$ and their energies $E_{\boldsymbol{k}}$ slightly beyond the Fermi surface of the system. Their wave functions are

$u_{\boldsymbol{k}} = e^{i\boldsymbol{k}\cdot\boldsymbol{r}}U_{\boldsymbol{k}}$ and $u_{-\boldsymbol{k}} = e^{-i\boldsymbol{k}\cdot\boldsymbol{r}}U_{-\boldsymbol{k}}$, respectively. Adding an electron with momentum $-\boldsymbol{k}$ is equivalent to annihilating a hole with $-\boldsymbol{k}$ and wavefunction $v^*_{\boldsymbol{k}} = u_{-\boldsymbol{k}}$. Here, we write $v^*_{\boldsymbol{k}} = e^{-i\boldsymbol{k}\cdot\boldsymbol{r}}V^*_{\boldsymbol{k}}$ and we see that $V^*_{\boldsymbol{k}} = U_{-\boldsymbol{k}}$. Then, the pair state $\Psi_{\boldsymbol{k}}$ for momentum $\boldsymbol{k}$ can be expressed as

$$\Psi_{\boldsymbol{k}}(\boldsymbol{r}_1, \boldsymbol{r}_2) = u_{\boldsymbol{k}}(\boldsymbol{r}_1)u_{-\boldsymbol{k}}(\boldsymbol{r}_2) = U_{\boldsymbol{k}}V^*_{\boldsymbol{k}}e^{i\boldsymbol{k}\cdot(\boldsymbol{r}_1-\boldsymbol{r}_2)}. \tag{2.66}$$

The linear combination of different $\boldsymbol{k}$ states gives the real space wave function

$$\Psi(\boldsymbol{r}_1, \boldsymbol{r}_2) = \sum_{\boldsymbol{k}} g(\boldsymbol{k})e^{i\boldsymbol{k}\cdot(\boldsymbol{r}_1-\boldsymbol{r}_2)}, \tag{2.67}$$

where $g(\boldsymbol{k}) = U_{\boldsymbol{k}}V^*_{\boldsymbol{k}}$. Note that $g(\boldsymbol{k}) = 0$ for $|\boldsymbol{k}| < k_F$ due to the Pauli exclusion principle.

The Schrödinger equation for the paired electrons has the form

$$\left[-\frac{\hbar^2}{2m}(\nabla_1^2 + \nabla_2^2) + V(\boldsymbol{r}_1 - \boldsymbol{r}_2)\right]\Psi(\boldsymbol{r}_1, \boldsymbol{r}_2) = (E + 2E_F)\Psi(\boldsymbol{r}_1, \boldsymbol{r}_2), \tag{2.68}$$

where $V(\boldsymbol{r}_1 - \boldsymbol{r}_2)$ is the interacting potential between the paired electrons and E is the energy of the relative to the state when the two electrons are at the Fermi level. Inserting Eq.(2.67) into Eq. (2.68), we obtain the Schrödinger equation in momentum space,

$$[2(E_{\boldsymbol{k}} - E_F) - E]g(\boldsymbol{k}) = -\sum_{\boldsymbol{k}'} V_{\boldsymbol{k},\boldsymbol{k}'}g(\boldsymbol{k}') \tag{2.69}$$

with

$$E_{\boldsymbol{k}} = \frac{\hbar^2\boldsymbol{k}^2}{2m}, \tag{2.70}$$

$$V_{\boldsymbol{k},\boldsymbol{k}'} = \Omega^{-1}\int e^{i(\boldsymbol{k}-\boldsymbol{k}')\cdot\boldsymbol{r}}V(\boldsymbol{r})d\boldsymbol{r}, \tag{2.71}$$

where Ω is the volume of the system. For simplicity, he assumed that the interaction is constant near the Fermi level, within the Deybe window $\hbar\omega_D$,

$$V_{\boldsymbol{k},\boldsymbol{k}'} = \begin{cases} V/\Omega, & |E_{\boldsymbol{k}} - E_F| \quad \text{and} \quad |E_{\boldsymbol{k}'} - E_F| < \hbar\omega_D \\ 0 & \text{otherwise.} \end{cases} \tag{2.72}$$

Then, Eq. (2.69) becomes

$$g_{\boldsymbol{k}} = -\frac{VC/\Omega}{E - 2(E_{\boldsymbol{k}} - E_F)}, \tag{2.73}$$

where

$$C = \sum_{|E_{\boldsymbol{k}'} - E_F| < \hbar\omega_D} g(\boldsymbol{k}'). \tag{2.74}$$

is a constant. Eqs.(2.73) and (2.74) form a set of self-consist equations.

After using the density of states $N(E)$ to replace the summation by an integral, the solution of eigenvalue can be found:

$$E = -\frac{2\hbar\omega_D}{e^{2/VN(E_f)} - 1}, \tag{2.75}$$

where $N(E_F)$ is the density of states at the Fermi level. This is the binding energy of a Cooper pair and it is always lower than the energy of the normal state no matter the interaction V.

2.6.2 The BCS Hamiltonian

The previous section showed that the Fermi becomes unstable when attractive interactions exist between electrons. The BCS theory suggested that the attractive interaction are a consequence of electron-electron interactions mediated by electron-lattice interaction (electron-phonon). The motivation is the isotope effect $T_c \propto M^{-\alpha}$ where M is the isotope mass of the ion and $\alpha \sim 0.5$. The nature of this electron-phonon interaction is shown in Fig. **2-17** and the Hamiltonian is

$$\mathcal{H}_I = \frac{1}{2} \sum_{\boldsymbol{q},\boldsymbol{k},\boldsymbol{k}',\sigma_1,\sigma_2} V_{\boldsymbol{k}_1,\boldsymbol{q}} c^\dagger_{\boldsymbol{k}_1+\boldsymbol{q},\sigma_1} c^\dagger_{\boldsymbol{k}_2-\boldsymbol{q},\sigma_2} c_{\boldsymbol{k}_2,\sigma_2} c_{\boldsymbol{k}_1,\sigma_1}, \tag{2.76}$$

where $c^\dagger_{\boldsymbol{k},\sigma}$ and $c_{\boldsymbol{k},\sigma}$ are the creation and destruction operation of electrons with momentum $\boldsymbol{k}$ and spin σ, and $\boldsymbol{q}$ is the momentum of the phonon. The interaction potential $V_{\boldsymbol{k},\boldsymbol{q}}$ is

$$V_{\boldsymbol{k},\boldsymbol{q}} = 2|M_{\boldsymbol{q}}|^2 \frac{\hbar\omega_{\boldsymbol{q}}}{(\epsilon_{\boldsymbol{k}+\boldsymbol{q}} - \epsilon_{\boldsymbol{k}}) - (\hbar\omega_{\boldsymbol{q}})^2}, \tag{2.77}$$

where $M_{\boldsymbol{q}}$ is the ion-electron interaction, ϵ and $\hbar\omega_{\boldsymbol{q}}$ are the energy of electrons and phonon, respectively.

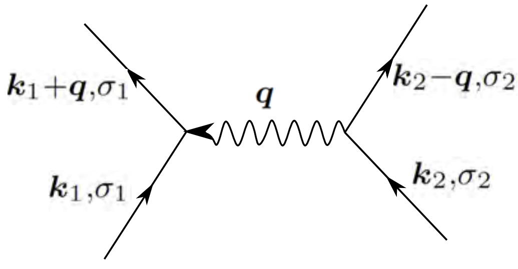

Figure 2-17 : Phonon mediated electron-electron interaction. The electron $(\boldsymbol{k}_2, \sigma_2)$ emits a phonon of momentum $\boldsymbol{q}$, absorbed by the electron $(\boldsymbol{k}_1, \sigma_1)$

Next, the BCS theory considered a reduce case. First, only electrons within the Debye energy $\hbar\omega_D$ around the Fermi energy E_F are considered, i.e $|\epsilon_{\boldsymbol{k}+\boldsymbol{q}} - \epsilon_{\boldsymbol{k}}| < \hbar\omega_D$. The interaction potential $V_{\boldsymbol{k},\boldsymbol{q}}$ is assumed to be constant V. Second, only those pairs with $\boldsymbol{k}_1 + \boldsymbol{k}_2 = 0$ are considered. As shown in Fig. **2-18**, for the pairs with total momentum $\boldsymbol{k}_1 + \boldsymbol{k}_2 = \boldsymbol{K}$, only those electrons in the dashed area can participate. When $\boldsymbol{K} = 0$, the dashed area is maximum and gives most important contribution. In addition, to insure the antisymmetry of the wavefunction, it is desirable to take pairs of opposite spin. Thus, the best choice for the ground state pairing is $(\boldsymbol{k}\uparrow, -\boldsymbol{k}\downarrow)$ and the BCS reduced Hamiltonian is written as

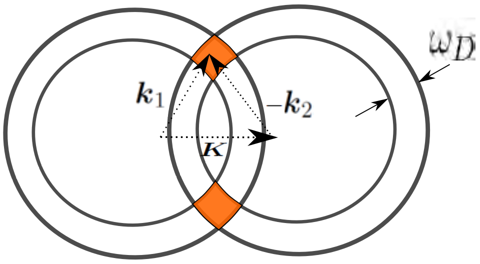

Figure 2-18 : If the Cooper pair consist of two electrons having a momentum sum $\boldsymbol{k}_1 + \boldsymbol{k}_2 = \boldsymbol{K}$, then the total number of such pairs is proportional to the dashed area.

$$\mathcal{H} = \sum_{\boldsymbol{k},\sigma} \epsilon_{\boldsymbol{k}} c^\dagger_{\boldsymbol{k},\sigma} c_{\boldsymbol{k},\sigma} - \sum_{\boldsymbol{k},\boldsymbol{k}'} V_{\boldsymbol{k},\boldsymbol{k}'} c^\dagger_{\boldsymbol{k}',\uparrow} c^\dagger_{-\boldsymbol{k}',\downarrow} c_{\boldsymbol{k},\downarrow} c_{\boldsymbol{k},\uparrow}. \tag{2.78}$$

The first term represents a sum of kinetic energies of all electrons. The second term represents the interaction among electrons. Here, $V_{\boldsymbol{k},\boldsymbol{k}'} > 0$ represents the attractive interaction.

2.6.3 The BCS Ground State

In the second quantisation formalism, we can represent the ground state of a normal metal at zero temperature by

$$\prod_{\boldsymbol{k} \leq \boldsymbol{k}_F} c^\dagger_{-k\downarrow} c^\dagger_{k\uparrow} |\text{vac}\rangle, \tag{2.79}$$

that is, for normal metals with a spherical Fermi surface, all energy states are completely filled up to the Fermi level and none are occupied above that level.

At $T = 0$K, the BCS theory proposes that all electrons near the Fermi energy E_F the form of Cooper pairs. This is the so called BCS ground state. The proposed trial wave functions for the many-body ground state $|\Psi_{BCS}\rangle$ is:

$$|\Psi_{BCS}\rangle = \prod_{\boldsymbol{k}} (u_{\boldsymbol{k}} + v_{\boldsymbol{k}} c^\dagger_{\boldsymbol{k},\uparrow} c^\dagger_{-\boldsymbol{k},\downarrow}) |\text{vac}\rangle. \tag{2.80}$$

Here $u_{\boldsymbol{k}}$ and $v_{\boldsymbol{k}}$ are the probability amplitude of the unoccupied and occupied pair state, respectively. They are variational parameters. The normalization conditions reads $|u_{u_{\boldsymbol{k}}}|^2 + |v_{u_{\boldsymbol{k}}}|^2 = 1$. As seen from Eq. (2.80), the number of particles in the system is not conserved. The BCS theory is based on the grand canonical ensemble. Therefore we have to impose a constraint on the number of electrons N:

$$\langle \Psi_{BCS}|\hat{N}|\Psi_{BCS}\rangle = \langle \Psi_{BCS}|\sum_{\boldsymbol{k}\sigma} c^{\dagger}_{\boldsymbol{k}\sigma} c_{\boldsymbol{k}\sigma}|\Psi_{BCS}\rangle = N. \tag{2.81}$$

Using a Lagrange multiplier, i.e., the Fermi energy E_F, one can minimize the ground state energy E_S with constant N:

$$\delta E_S = \langle \Psi_{BCS}|\hat{\mathcal{H}} - E_F\hat{N}|\Psi_{BCS}\rangle = 0. \tag{2.82}$$

Substituting the Hamiltonian Eq. (2.78) and wavefunction Eq. (2.80) into this equation, we obtain

$$E_S = \sum_{\boldsymbol{k}} 2\xi_{\boldsymbol{k}} v^2_{\boldsymbol{k}} + \sum_{\boldsymbol{k}\boldsymbol{k}'} V_{\boldsymbol{k}\boldsymbol{k}'} u_{\boldsymbol{k}} v_{\boldsymbol{k}} u_{\boldsymbol{k}'} v_{\boldsymbol{k}'}, \tag{2.83}$$

where $\xi_{\boldsymbol{k}} = \epsilon_{\boldsymbol{k}} - E_F$. By minimizing this energy with respect to $u_{\boldsymbol{k}}$ and $v_{\boldsymbol{k}}$ and making use of the normalization condition, one obtains:

$$|u_{\boldsymbol{k}}|^2 = \frac{1}{2}\left(1 + \frac{\xi_{\boldsymbol{k}}}{E_{\boldsymbol{k}}}\right), \tag{2.84}$$

$$|v_{\boldsymbol{k}}|^2 = \frac{1}{2}\left(1 - \frac{\xi_{\boldsymbol{k}}}{E_{\boldsymbol{k}}}\right). \tag{2.85}$$

where $E_{\boldsymbol{k}}$ is

$$E_{\boldsymbol{k}} = \sqrt{\xi^2_{\boldsymbol{k}} + \Delta^2_{\boldsymbol{k}}} \tag{2.86}$$

and $\Delta_{\boldsymbol{k}}$ satisfies the relation:

$$\Delta_{\boldsymbol{k}} = -\sum_{\boldsymbol{k}'} V_{\boldsymbol{k}\boldsymbol{k}'} u_{\boldsymbol{k}'} v^*_{\boldsymbol{k}'} = -\frac{1}{2}\sum_{\boldsymbol{k}'} V_{\boldsymbol{k}\boldsymbol{k}'} \frac{\Delta_{\boldsymbol{k}'}}{E_{\boldsymbol{k}'}}. \tag{2.87}$$

$\Delta_{\boldsymbol{k}}$ is called the *pairing potential* or *the order parameter*. Eq. (2.87), the so-called gap equation, must be solved self-consistently.

The total energy of the superconducting ground state ($V_{\boldsymbol{k}\boldsymbol{k}} \equiv V$ in the BCS theory) is given by

$$E_S = \sum_{\boldsymbol{k}} \left(\xi_{\boldsymbol{k}} - \frac{\xi^2_{\boldsymbol{k}}}{E_{\boldsymbol{k}}}\right) - \frac{\Delta}{V}. \tag{2.88}$$

The condensation energy is the energy difference between the superconducting state and the normal state:

$$E_{cond} = E_s - E_N \approx \sum_{\boldsymbol{k}} [\xi_{\boldsymbol{k}} - E_{\boldsymbol{k}}] = -\frac{1}{2}\mathcal{N}(0)|\Delta|^2, \tag{2.89}$$

where $\mathcal{N}(0)$ is the density of states at the Fermi energy. It also show that the energy of the superconducting ground state is lower than the energy of the normal state.

2.6.4 Elementary Excitations

Form the superconducting ground state, the total energy of the system will increase when the pair state ($\boldsymbol{k} \uparrow, -\boldsymbol{k} \downarrow$) is broken. Due to the Pauli exclusion principle, this can be done by adding an electron in state $\boldsymbol{k} \uparrow$ or removing an electron from state $-\boldsymbol{k} \downarrow$. The total energy change must be accounted for (1) energy for removing a pair state from the system and (2) energy for adding the single electron in the system.

According to Eq. (2.83), breaking a pair state with $\boldsymbol{k}$ increases the energy of the system by an amount

$$\delta F = -2\xi_{\boldsymbol{k}} v_{\boldsymbol{k}}^2 - 2\sum_{\boldsymbol{k}'} V_{\boldsymbol{k}\boldsymbol{k}'} u_{\boldsymbol{k}} v_{\boldsymbol{k}} u_{\boldsymbol{k}'} v_{\boldsymbol{k}'}. \tag{2.90}$$

With Eq. (2.87), it may be written as

$$\delta F = -2\xi_{\boldsymbol{k}} v_{\boldsymbol{k}}^2 + 2\Delta_{\boldsymbol{k}} u_{\boldsymbol{k}} v_{\boldsymbol{k}}. \tag{2.91}$$

After including the kinetic energy of the added electron, the total energy changes by an amount:

$$\begin{aligned} \delta E &= -2\xi_{\boldsymbol{k}}(1 - 2v_{\boldsymbol{k}}^2) + 2\Delta_{\boldsymbol{k}} u_{\boldsymbol{k}} v_{\boldsymbol{k}} \\ &= \xi_{\boldsymbol{k}}\left[1 - \left(1 - \frac{\xi_{\boldsymbol{k}}}{E_{\boldsymbol{k}}}\right)\right] + \frac{\Delta_{\boldsymbol{k}}^2}{E_{\boldsymbol{k}}} \\ &= E_{\boldsymbol{k}}. \end{aligned} \tag{2.92}$$

Thus, $E_{\boldsymbol{k}}$ is the minimum energy to break a Cooper pair and to create an create an excitation. $\Delta_{\boldsymbol{k}}$ is also called the energy gap because it is the smallest energy that can be added ($E_{\boldsymbol{k}} = \Delta_{\boldsymbol{k}}$ if $\xi_{\boldsymbol{k}} = 0$).

A single-particle excitation is a superposition of an electron and a hole. This is referred to as *quasiparticle* and $E_{\boldsymbol{k}}$ is the energy of the quasiparticle excitation. Excited states of the reduced Hamiltonian can be obtained through a (Bogoliubov-Volatin transformation), which diagonalizes the Hamiltonian. Bogoliubov interpreted E_k as the energy of quasiparticles $\gamma_k^\dagger = u_{\boldsymbol{k}} + v_{\boldsymbol{k}} c_{\boldsymbol{k},\uparrow}^\dagger c_{-\boldsymbol{k},\downarrow}^\dagger$ which create electron-like excitations above the Fermi level or correspondingly hole-like excitations below the Fermi surface [43].

The value of the gap δ at zero temperature $T = 0\text{K}$ can be shown to be

$$\Delta(0) \approx 2\hbar\omega_D e^{-1/\mathcal{N}(0)V}, \tag{2.93}$$

where ω_D is the Deybe frequency and $N(0)$ is the density of energy states at the Fermi level.

At finite temperature, excitations above the ground state must be taken into account and physical state will take the form

$$\prod_{\text{occ. states}} \gamma_k^\dagger |\Psi_{BCS}\rangle, \tag{2.94}$$

which express the fact the quasiparticles progressively fill the excited states according too the Fermi-Dirac probability distribution

$$f(E_k) = (1 + e^{\beta E_k})^{-1}, \qquad \beta = \frac{1}{kT}. \tag{2.95}$$

The BCS treatment of the electron pairing allows for the identification of the gap equation at any temperature:

$$\frac{1}{\mathcal{N}(0)} = \frac{1}{2}\int_{-\hbar\omega_D}^{\hbar\omega_D} d\epsilon \frac{\tanh(\beta E_k/2)}{E_k}. \tag{2.96}$$

In particular, the critical temperatures is defined as the temperature at which the gap is completely closed; analysis of the previous integral yields

$$kT_c \approx 1.13\hbar\omega_D e^{-1/\mathcal{N}(0)V}. \tag{2.97}$$

Finally, the temperature dependence of the gap can be obtained by analysis of (2.96) and is shown in Fig. **2-19**. Close to the critical temperature, the curve can be approximated by

$$\Delta(T) \approx 1.74\Delta(0)\left(1 - \frac{T}{T_c}\right)^{\frac{1}{2}}, \qquad \text{at} T \sim T_c. \tag{2.98}$$

Summarising the main results of the original BCS theory: it is possible to create bound states of electron pairs around the Fermi surface due to their interactions through lattice phonons. This attractive s-wave pairing gives rise to a modified energy spectrum of the conduction electrons, with a gap between the ground state and the first excited states, corresponding to the minimal excitation energy of Bogoliubov's quasiparticles, which correlate electrons with opposite momenta and spins close to the Fermi level. The energy gap has a definite temperature dependence, and the temperature at which it vanishes, restituting the original energy spectrum of non-paired electrons, gives the critical temperature for the super-

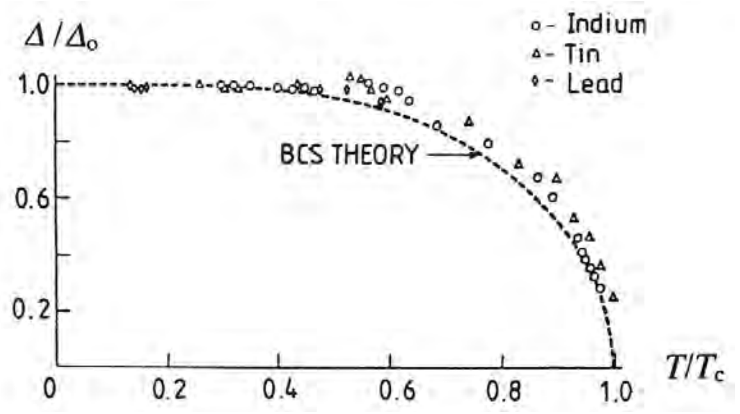

Figure 2-19 : Temperature dependence of the energy gap according to the BCS theory, compared to some experimental data for typical superconductors. Taken from [44].

conducting transition. The coherence and penetration lengths can also be recovered within this framework and they match with those of the Ginzburg-Landau formalism.

3 The Extended Ginzburg Landau Formalism (EGL)

In this chapter, we present the Extended GL formalism (EGL) derived based on Gor'kov formalism for a clean s-wave superconductor and in the absence of the magnetic field.

3.1 Introduction

By applying Landau's theory of second-order transitions to study the superconductivity, Ginzburg and Landau [13] in 1950, derived a set of two equations, one describing the spatial variation of Ψ and the other describing the magnetic field, now known as the Ginzburg-Landau (GL) equations for superconductivity.

As seen in the previous chapter, the microscopic theory of superconductivity was proposed in 1957 by Bardeen, Cooper and Schrieffer [42]. The theory explained the superconducting current as a superfluid of "Cooper pairs", pairs of electrons interaction through the exchange of phonons. In 1959, Gor'kov showed that the BCS theory reduced to the GL theory close the critical temperature.

Based on Gor'kov formalism for a clean s-wave superconductor A. Vagov and A. Shanenko *et al.* [45] develop an extended version of the single-band Ginzburg-Landau (GL) theory. They derive the extended theory in the form of the perturbation expansion of the microscopic free-energy functional and the gap equation using the proximity to the critical temperature as the small parameter. The two lowest orders of this expansion yield the standard Ginzburg-Landau theory and the higher orders are its corrections. They demonstrate that the EGL formalism is not just a mathematical extension to the theory, where the variation of the gap and thermodynamic critical field with temperature calculated within the EGL theory are found in very good agreement with the full BCS result down to low temperatures. Also, this plan has sketched for two-bands superconductors [46,47] and multiband superconductors [48].

In this chapter, we will find how the GL equation and EGL formalism for a single band superconductor can be derived from the BCS theory. Recall that the GL formalism works near Tc, therefore using the assumption that the energy gap is small and varies slowly near to the critical temperature T_c. The derivation is founded on the method proposed by Gor'kov [49] and based on the Green's function formalism at arbitrary temperatures and fields. For the calculation we consider the absence of the magnetic field. The absence of the magnetic field greatly simplifies the situation, because the electronic Green's function calculated to next-to-leading order in τ in the presence of the magnetic field is more complicated than the one in zero magnetic field.

3.2 Nambu - Gor'kov Theory

Let's consider an homogeneous system. The Hamiltonian with s-wave singlet pairing is given

$$\mathcal{H}_{BCS} = \sum_{\sigma} \int d\boldsymbol{r} \left[\psi^{\dagger}_{\sigma}(\boldsymbol{r}) \mathcal{T}_{\boldsymbol{r}} \psi_{\sigma}(\boldsymbol{r}) + \psi^{\dagger}_{\uparrow}(\boldsymbol{r}) \psi^{\dagger}_{\downarrow}(\boldsymbol{r}) \Delta(\boldsymbol{r}) + h.c \right], \tag{3.1}$$

where $\mathcal{T}_{\boldsymbol{r}}$ is the single-electron kinetic energy operator

$$\mathcal{T}_{\boldsymbol{r}} = -\frac{\hbar^2}{2m_e} \left(\boldsymbol{\nabla} - i\frac{e}{\hbar c}\boldsymbol{A} \right) - \mu, \tag{3.2}$$

and the energy gap is:

$$\Delta(\boldsymbol{r}) = -g \langle \psi_{\uparrow}(\boldsymbol{r}) \psi_{\downarrow}(\boldsymbol{r}) \rangle \tag{3.3}$$

It is not convenient to work with the usual Heisenberg picture at finite temperatures due to the factor $e^{-\beta\mathcal{H}}$. To overcome this problem the Heisenberg picture with imaginary time is usually introduced. In this case the Heisenberg operators are defined as:

$$\begin{aligned} \psi_{\sigma}(\boldsymbol{r}, \mathrm{t}) &= e^{\mathcal{H}_{BCS}\mathrm{t}/\hbar} \psi_{\sigma}(\boldsymbol{r}) e^{-\mathcal{H}_{BCS}\mathrm{t}/\hbar}, \\ \overline{\psi}_{\sigma}(\boldsymbol{r}, \mathrm{t}) &= e^{\mathcal{H}_{BCS}\mathrm{t}/\hbar} \psi^{\dagger}_{\sigma}(\boldsymbol{r}) e^{-\mathcal{H}_{BCS}\mathrm{t}/\hbar}. \end{aligned}$$

The equation of motion, in the imaginary-time Heisenberg picture is of form:

$$-\hbar\partial_{\mathrm{t}}\psi_{\uparrow}(\boldsymbol{r}, \mathrm{t}) = [\psi_{\uparrow}(\boldsymbol{r}, \mathrm{t}), \mathcal{H}_{BCS}] = \mathcal{T}_{\boldsymbol{r}}\psi_{\uparrow}(\boldsymbol{r}, \mathrm{t}) + \Delta(\boldsymbol{r})\overline{\psi}_{\downarrow}(\boldsymbol{r}, \mathrm{t}), \tag{3.4}$$

$$-\hbar\partial_{\mathrm{t}}\overline{\psi}_{\downarrow}(\boldsymbol{r}, \mathrm{t}) = [\overline{\psi}_{\downarrow}(\boldsymbol{r}, \mathrm{t}), \mathcal{H}_{BCS}] = \Delta^{*}(\boldsymbol{r})\psi_{\uparrow}(\boldsymbol{r}, \mathrm{t}) - \mathcal{T}^{*}_{\boldsymbol{r}}\overline{\psi}_{\downarrow}(\boldsymbol{r}, \mathrm{t}). \tag{3.5}$$

Let us now introduce the temperature (Matsubara) Green's Functions

$$\begin{aligned} G(\boldsymbol{r}, \mathrm{t}; \boldsymbol{r}', \mathrm{t}') &= -\frac{1}{\hbar} \langle \mathrm{T}_{\mathrm{t}} \psi_{\uparrow}(\boldsymbol{r}, \mathrm{t}) \overline{\psi}_{\uparrow}(\boldsymbol{r}', \mathrm{t}') \rangle, \\ \overline{F}(\boldsymbol{r}, \mathrm{t}; \boldsymbol{r}', \mathrm{t}') &= -\frac{1}{\hbar} \langle \mathrm{T}_{\mathrm{t}} \overline{\psi}_{\downarrow}(\boldsymbol{r}, \mathrm{t}) \overline{\psi}_{\uparrow}(\boldsymbol{r}', \mathrm{t}') \rangle, \\ \overline{G}(\boldsymbol{r}, \mathrm{t}; \boldsymbol{r}', \mathrm{t}') &= -\frac{1}{\hbar} \langle \mathrm{T}_{\mathrm{t}} \overline{\psi}_{\downarrow}(\boldsymbol{r}, \mathrm{t}) \psi_{\downarrow}(\boldsymbol{r}', \mathrm{t}') \rangle, \\ F(\boldsymbol{r}, \mathrm{t}; \boldsymbol{r}', \mathrm{t}') &= -\frac{1}{\hbar} \langle \mathrm{T}_{\mathrm{t}} \psi_{\uparrow}(\boldsymbol{r}, \mathrm{t}) \psi_{\downarrow}(\boldsymbol{r}', \mathrm{t}') \rangle, \end{aligned} \tag{3.6}$$

where $\mathrm{T_t}$ is the time-ordering operator, generalized time-ordering proceduce $\mathrm{T_t}(A(\mathrm{t})B(\mathrm{t}')) = \Theta(\mathrm{t}-\mathrm{t}')A(\mathrm{t})B(\mathrm{t}') - \Theta(\mathrm{t}'-\mathrm{t})B(\mathrm{t}')A(\mathrm{t})$.

The equations of motion for the temperature Green's function read

$$\begin{aligned}
-\hbar\partial_{\mathrm{t}} G(\boldsymbol{r},\mathrm{t};\boldsymbol{r}',\mathrm{t}') &= \delta(\mathrm{t}-\mathrm{t}')\delta(\boldsymbol{r}-\boldsymbol{r}') + \mathcal{T}_{\boldsymbol{r}} G(\boldsymbol{r},\mathrm{t};\boldsymbol{r}',\mathrm{t}') + \Delta(\boldsymbol{r})\overline{F}(\boldsymbol{r},\mathrm{t};\boldsymbol{r}',\mathrm{t}'),\\
-\hbar\partial_{\mathrm{t}} \overline{F}(\boldsymbol{r},\mathrm{t};\boldsymbol{r}',\mathrm{t}') &= \Delta^*(\boldsymbol{r})G(\boldsymbol{r},\mathrm{t};\boldsymbol{r}',\mathrm{t}') - \mathcal{T}^*_{\boldsymbol{r}}\overline{F}(\boldsymbol{r},\mathrm{t};\boldsymbol{r}',\mathrm{t}'),\\
-\hbar\partial_{\mathrm{t}} \overline{G}(\boldsymbol{r},\mathrm{t};\boldsymbol{r}',\mathrm{t}') &= \delta(\mathrm{t}-\mathrm{t}')\delta(\boldsymbol{r}-\boldsymbol{r}') + \Delta^*(\boldsymbol{r})F(\boldsymbol{r},\mathrm{t};\boldsymbol{r}',\mathrm{t}') - \mathcal{T}^*_{\boldsymbol{r}}\overline{G}(\boldsymbol{r},\mathrm{t};\boldsymbol{r}',\mathrm{t}'),\\
-\hbar\partial_{\mathrm{t}} F(\boldsymbol{r},\mathrm{t};\boldsymbol{r}',\mathrm{t}') &= \mathcal{T}_{\boldsymbol{r}} F(\boldsymbol{r},\mathrm{t};\boldsymbol{r}',\mathrm{t}') + \Delta(\boldsymbol{r})\overline{G}(\boldsymbol{r},\mathrm{t};\boldsymbol{r}',\mathrm{t}').
\end{aligned} \tag{3.7}$$

These equation are called the Gor'kov equations [49]. Note that there are no $\delta(\mathrm{t}-\mathrm{t}')\delta(\boldsymbol{r}-\boldsymbol{r}')$ functions in the equations of motion for F and $\overline{F}$, thus they are called anomalous Green functions.

In his pioneering paper Gor'kov derived and used first two equation in (3.7). Supplemented with two additional relations, the Gor'kov equations can be rewritten as:

$$\mathbb{G}(\boldsymbol{r},\mathrm{t};\boldsymbol{r}',\mathrm{t}') = \begin{pmatrix} G(\boldsymbol{r},\mathrm{t};\boldsymbol{r}',\mathrm{t}') & F(\boldsymbol{r},\mathrm{t};\boldsymbol{r}',\mathrm{t}') \\ \overline{F}(\boldsymbol{r},\mathrm{t};\boldsymbol{r}',\mathrm{t}') & \overline{G}(\boldsymbol{r},\mathrm{t};\boldsymbol{r}',\mathrm{t}') \end{pmatrix}, \tag{3.8}$$

$$\mathcal{H}_{BdG} = \begin{pmatrix} \mathcal{T}_{\boldsymbol{r}} & \Delta(\boldsymbol{r}) \\ \Delta^*(\boldsymbol{r}) & -\mathcal{T}^*_{\boldsymbol{r}} \end{pmatrix}, \tag{3.9}$$

where BdG refers to the Bogoliubov-de Gennes Hamiltonian. Now it possible rearrange Eqs.(3.7) in the following elegant form:

$$\left(\hbar\partial_{\mathrm{t}}\mathbb{1} + \mathcal{H}_{BdG}\right)\mathbb{G}(\boldsymbol{r},\mathrm{t};\boldsymbol{r}',\mathrm{t}') = \delta(\mathrm{t}-\mathrm{t}')\delta(\boldsymbol{r}-\boldsymbol{r}')\mathbb{1}. \tag{3.10}$$

Eqs. (3.10) are often called the Gor'kov-Nambu equations [50]. It is clear from the representation given by Eq. (3.10) that the 2×2 matrix $\mathcal{H}_{BdG}$ determines all the properties of the temperature Green's function. This is why it is convenient to introduce eigenvalues and eigenfunctions of such a matrix differential operator.

One of the most important things concerning the temperature Green's functions are the imaginary-time boundary conditions.

$$\begin{aligned}
&G(\boldsymbol{r},\mathrm{t};\boldsymbol{r}',\mathrm{t}') = -\frac{1}{\hbar}\langle \mathrm{T_t}\psi_\uparrow(\boldsymbol{r},\mathrm{t})\overline{\psi}_\uparrow(\boldsymbol{r}',\mathrm{t}')\rangle\\
&= \frac{(-1)}{\hbar\,\mathrm{Tr}(e^{-\beta\mathcal{H}_{BCS}})}\,\mathrm{Tr}\Big(e^{-\beta\mathcal{H}_{BCS}}\Big[\Theta(\mathrm{t}-\mathrm{t}')e^{\mathcal{H}_{BCS}\mathrm{t}/\hbar}\psi_\uparrow(\boldsymbol{r})e^{-\mathcal{H}_{BCS}\mathrm{t}/\hbar}e^{\mathcal{H}_{BCS}\mathrm{t}'/\hbar}\psi^\dagger_\uparrow(\boldsymbol{r}')e^{-\mathcal{H}_{BCS}\mathrm{t}'/\hbar}\\
&-\ \Theta(\mathrm{t}'-\mathrm{t})e^{\mathcal{H}_{BCS}\mathrm{t}'/\hbar}\psi^\dagger_\uparrow(\boldsymbol{r}')e^{-\mathcal{H}_{BCS}\mathrm{t}'/\hbar}e^{\mathcal{H}_{BCS}\mathrm{t}/\hbar}\psi_\uparrow(\boldsymbol{r})e^{-\mathcal{H}_{BCS}\mathrm{t}/\hbar}\Big]\Big)
\end{aligned}$$

$$= \frac{(-1)}{\hbar\,\mathrm{Tr}(e^{-\beta\mathcal{H}_{BCS}})}\,\mathrm{Tr}\Big(e^{-\beta\mathcal{H}_{BCS}}\,\Big[\Theta(\mathrm{t}-\mathrm{t}')e^{\mathcal{H}_{BCS}(\mathrm{t}-\mathrm{t}')/\hbar}\psi_{\uparrow}(\boldsymbol{r})e^{-\mathcal{H}_{BCS}(\mathrm{t}-\mathrm{t}')/\hbar}\psi^{\dagger}_{\uparrow}(\boldsymbol{r}')$$

$$-\ \Theta(\mathrm{t}'-\mathrm{t})e^{\mathcal{H}_{BCS}(\mathrm{t}'-\mathrm{t})/\hbar}\psi^{\dagger}_{\uparrow}(\boldsymbol{r}')e^{-\mathcal{H}_{BCS}(\mathrm{t}'-\mathrm{t})/\hbar}\psi_{\uparrow}(\boldsymbol{r})\Big]\Big)$$

$$G(\boldsymbol{r},\mathrm{t};\boldsymbol{r}',\mathrm{t}') = G(\boldsymbol{r},\boldsymbol{r}',\mathrm{t}-\mathrm{t}'); \qquad \text{where} \qquad -\hbar\beta < \mathrm{t}-\mathrm{t}' < \hbar\beta$$

that in a general form

$$\mathcal{A}(\boldsymbol{r},\boldsymbol{r}';\eta) = -\mathcal{A}(\boldsymbol{r},\boldsymbol{r}';\eta+\beta\hbar), \qquad \text{with} \qquad \eta = \mathrm{t}-\mathrm{t}' \qquad [\mathcal{A} = G,\overline{G},F,\overline{F}]. \tag{3.11}$$

Now, one can try to rewrite Eq. (3.7)(the Gor'kov equations) and Eq. (3.10)(the Gor'kov-Nambu equations), using the boundary condition (3.11) and make an expansion in terms of the Matsubara frequencies (3.12)

$$\begin{aligned} \mathcal{A}(\boldsymbol{r},\boldsymbol{r}';\eta) \equiv \frac{1}{\beta\hbar}\sum_{n=\infty}^{\infty} e^{-i\omega_n\eta}\mathcal{A}_{\omega}(\boldsymbol{r},\boldsymbol{r}'), \qquad \mathcal{A}_{\omega}(\boldsymbol{r},\boldsymbol{r}') \equiv \int_{-\hbar\beta}^{\hbar\beta} e^{i\omega\eta}\mathcal{A}(\boldsymbol{r},\mathrm{t};\boldsymbol{r}',\mathrm{t}') \\ \delta(\eta) = \frac{1}{\beta\hbar}\sum_{n} e^{-i\tilde{\omega}_n\eta}, \qquad \text{see Appendix A.} \end{aligned} \tag{3.12}$$

where, $\omega_n = \pi(2n+1)/\beta\hbar$ are the fermionic Matsubara frequencies. Using these Fourier components, the Gor'kov-Nambu equation can be written as,

$$\hbar\partial_{\mathrm{t}}\mathbb{G}(\boldsymbol{r},\mathrm{t};\boldsymbol{r}',\mathrm{t}') \Rightarrow -\frac{1}{\beta\hbar}\sum_{n=\infty}^{\infty}(i\hbar\omega_n)e^{-i\omega_n(-\mathrm{t}-\mathrm{t}')}\mathbb{G}_{\omega}(\boldsymbol{r},\boldsymbol{r}'), \tag{3.13}$$

$$\mathbb{G}_{\omega}(\boldsymbol{r},\boldsymbol{r}') = \begin{pmatrix} G_{\omega}(\boldsymbol{r},\boldsymbol{r}') & F_{\omega}(\boldsymbol{r},\boldsymbol{r}') \\ \overline{F}_{\omega}(\boldsymbol{r},\boldsymbol{r}') & \overline{G}_{\omega}(\boldsymbol{r},\boldsymbol{r}') \end{pmatrix}. \tag{3.14}$$

Since the $\mathcal{H}_{BdG}$ operator depends only on the spacial variables, the last term is simply reduced to

$$\mathcal{H}_{BdG}\mathbb{G}(\boldsymbol{r},\mathrm{t};\boldsymbol{r}',\mathrm{t}') \Rightarrow \frac{1}{\beta\hbar}\sum_{n=\infty}^{\infty} e^{-i\omega_n(-\mathrm{t}-\mathrm{t}')}\mathcal{H}_{BdG}\mathbb{G}_{\omega}(\boldsymbol{r},\boldsymbol{r}'), \tag{3.15}$$

and the term with the δ is reduced to

$$\delta(\mathrm{t}-\mathrm{t}')\delta(\boldsymbol{r}-\boldsymbol{r}') \Rightarrow \frac{1}{\beta\hbar}\sum_{n=\infty}^{\infty} e^{-i\omega_n(-\mathrm{t}-\mathrm{t}')}\delta(\boldsymbol{r}-\boldsymbol{r}'). \tag{3.16}$$

Now Eq. (3.10) for the Fourier transform of Green functions reads

$$(i\hbar\omega\mathbb{1} - \mathcal{H}_{BdG})\,\mathbb{G}_{\omega}(\boldsymbol{r},\boldsymbol{r}') = \delta(\boldsymbol{r}-\boldsymbol{r}')\mathbb{1}. \tag{3.17}$$

Introduction the 2×2 matrix operators in the Hilbert space, to try solve these equations

$$\mathbb{G}_\omega(\boldsymbol{r},\boldsymbol{r}') = \langle \boldsymbol{r}|\breve{\mathbb{G}}_\omega|\boldsymbol{r}'\rangle, \qquad \langle \boldsymbol{r}|\hat{\mathcal{H}}_{BdG}|\boldsymbol{r}'\rangle = \delta(\boldsymbol{r}-\boldsymbol{r}')\breve{\mathcal{H}}_{GdB}(\boldsymbol{r}'), \qquad \delta(\boldsymbol{r}-\boldsymbol{r}')\mathbb{1} = \langle \boldsymbol{r}|\mathbb{1}|\boldsymbol{r}'\rangle. \tag{3.18}$$

Eq. (3.17) result a matrix equation resembling the well-known Green's function equation for the operator $\breve{\mathcal{H}}_{GdB}$,

$$(i\hbar\omega\breve{\mathbb{1}} - \breve{\mathcal{H}}_{GdB})\breve{\mathbb{G}}_\omega = \breve{\mathbb{1}}, \tag{3.19}$$

also, as the $\breve{\mathcal{H}}_{GdB}$ operator can be expressed as the sum of the kinetic and interaction contributions

$$\breve{\mathcal{H}}_{GdB} = \breve{\mathcal{T}} + \breve{\Delta}, \qquad \breve{\mathcal{T}} = \begin{pmatrix} \hat{\mathcal{T}} & 0 \\ 0 & -\hat{\mathcal{T}}^* \end{pmatrix}, \qquad \breve{\Delta} = \begin{pmatrix} 0 & \hat{\Delta} \\ \hat{\Delta}^* & 0 \end{pmatrix}. \tag{3.20}$$

The Eq.(3.19) becomes:

$$(i\hbar\omega\breve{\mathbb{1}} - \breve{\mathcal{T}})\breve{\mathbb{G}}_\omega = \breve{\mathbb{1}} + \breve{\Delta}\breve{\mathbb{G}}_\omega. \tag{3.21}$$

In the normal state where $\hat{\Delta} = 0$, the normal or unperturbed Green function operator can be constructed as

$$\begin{aligned} (i\hbar\omega\breve{\mathbb{1}} - \breve{\mathcal{T}})\breve{\mathbb{G}}_\omega^{(0)} = \breve{\mathbb{1}} \Rightarrow [\breve{\mathbb{G}}_\omega^{(0)}]^{-1}\breve{\mathbb{G}}_\omega^{(0)} = \breve{\mathbb{1}}, \\ [\breve{\mathbb{G}}_\omega^{(0)}]^{-1} = (i\hbar\omega\breve{\mathbb{1}} - \breve{\mathcal{T}}). \end{aligned} \tag{3.22}$$

The Eq. (3.22 can be used to transform (3.21) into a Dyson equation (integration and summation of repeated variables is implicit):

$$\begin{aligned} [\breve{\mathbb{G}}_\omega^{(0)}]^{-1}\breve{\mathbb{G}}_\omega &= \mathbb{1} + \breve{\Delta}\breve{\mathbb{G}}_\omega \\ \breve{\mathbb{G}}_\omega &= \breve{\mathbb{G}}_\omega^{(0)} + \breve{\mathbb{G}}_\omega^{(0)}\breve{\Delta}\breve{\mathbb{G}}_\omega \end{aligned} \tag{3.23}$$

3.3 Extend Ginzburg-Landau Formalism (EGL)

The GL theory and EGL formalism can be derived from the microscopic BCS model. Near the transition line the function Δ is small, and the Dyson equation (3.23) for $\breve{\mathbb{G}}_\omega$ can be solved by iteration. Then, to construct the self-equation for the the superconducting gap, one needs to extract the equation for the anomalous Green function. In its explicit form Eq.(3.23) is given by

$$\begin{pmatrix} \hat{G}_\omega & \hat{F}_\omega \\ \hat{\bar{F}}_\omega & \hat{\bar{G}}_\omega \end{pmatrix} = \begin{pmatrix} \hat{G}_\omega^{(0)} & 0 \\ 0 & \hat{\bar{G}}_\omega^{(0)} \end{pmatrix} + \begin{pmatrix} \hat{G}_\omega^{(0)} & 0 \\ 0 & \hat{\bar{G}}_\omega^{(0)} \end{pmatrix} \begin{pmatrix} 0 & \hat{\Delta} \\ \hat{\Delta}^* & 0 \end{pmatrix} \begin{pmatrix} \hat{G}_\omega & \hat{F}_\omega \\ \hat{\bar{F}}_\omega & \hat{\bar{G}}_\omega \end{pmatrix}, \tag{3.24}$$

and one get the following relation:

$$\begin{aligned} \hat{G}_\omega &= \hat{G}^{(0)}_\omega + \hat{G}_\omega \hat{\Delta}^* \hat{\bar{F}}_\omega, \qquad & \hat{\bar{F}}_\omega &= \hat{\bar{G}}^{(0)}_\omega \hat{\Delta}^* \hat{G}_\omega, \\ \hat{\bar{G}}_\omega &= \hat{\bar{G}}^{(0)}_\omega + \hat{\bar{G}}_\omega \hat{\Delta}^* \hat{F}_\omega, \qquad & \hat{F}_\omega &= \hat{G}^{(0)}_\omega \hat{\Delta} \hat{\bar{G}}_\omega. \end{aligned} \tag{3.25}$$

Now we need to evaluated the self-consistency equation Eq.(3.25). For this we use the Eqs.3.26 iteratively to find expression for F_ω in term of $\hat{\Delta}$ and G_ω

$$\hat{F}_\omega = \hat{G}^{(0)}_\omega \hat{\Delta} \hat{\bar{G}}^{(0)}_\omega + \hat{G}^{(0)}_\omega \hat{\Delta} \hat{\bar{G}}^{(0)}_\omega \hat{\Delta}^* \hat{G}^{(0)}_\omega \hat{\Delta} \hat{\bar{G}}^{(0)}_\omega + \hat{G}^{(0)}_\omega \hat{\Delta} \hat{\bar{G}}^{(0)}_\omega \hat{\Delta}^* \hat{G}^{(0)}_\omega \hat{\Delta} \hat{\bar{G}}^{(0)}_\omega \hat{\Delta}^* \hat{G}^{(0)}_\omega \hat{\Delta} \hat{\bar{G}}^{(0)}_\omega \cdots \tag{3.26}$$

In order to obtain the GL equations, one must truncate the infinite series in Eq. (3.26) keeping only the first and third powers. To obtain the EGL formalism, it is necessary to include the fifth-power, since when $T \to T_c$, the order parameter decays as $\Delta \propto \tau^{-1/2}$. So, with terms $\tau^{1/2} \to$ we obtain the equation for T_c, $\tau^{3/2} \to$ we recover the standard GL and $\tau^{5/2} \to$ gives the Extended GL formalism. The self-consistency equation Eq.(3.3) for the order parameter $\Delta(\mathbf{r})$ and the anomalous Green functions reads

$$\begin{aligned} \Delta(\boldsymbol{r}) &= -g\hbar \lim_{\boldsymbol{r}\to\boldsymbol{r}'} \lim_{\eta\to 0} F_\omega(\boldsymbol{r}, \mathrm{t}; \boldsymbol{r}', \mathrm{t}') \\ &= -g\hbar \lim_{\boldsymbol{r}\to\boldsymbol{r}'} \lim_{\eta\to 0} \frac{1}{\beta\hbar} \sum_{w} e^{-i\omega\eta} F_\omega(\boldsymbol{r}, \boldsymbol{r}') \\ &= gT \lim_{\boldsymbol{r}\to\boldsymbol{r}'} \lim_{\eta\to 0} \sum_{\omega} e^{-i\omega\eta} F_\omega(\boldsymbol{r}, \boldsymbol{r}') \end{aligned} \tag{3.27}$$

In the absence of the magnetic field, the $G^{(0)}_\omega$ is the usual Green's function of the non-interacting electrons

$$\begin{aligned} G^{(0)}_\omega(\boldsymbol{r}, \boldsymbol{y}) &= \langle \boldsymbol{r} | (i\hbar\omega - \mathcal{T})^{-1} | \boldsymbol{y} \rangle = \\ &= \int \frac{d^3k}{(2\pi)^3} \frac{d^3k'}{(2\pi)^3} \langle \boldsymbol{r} | \boldsymbol{k} \rangle \langle \boldsymbol{k} | (i\hbar\omega - \mathcal{T})^{-1} | \boldsymbol{k}' \rangle \langle \boldsymbol{k}' | \boldsymbol{y} \rangle \\ &= \int \frac{d^3k}{(2\pi)^3} \frac{d^3k'}{(2\pi)^3} e^{i\boldsymbol{k}\cdot\boldsymbol{r}} \frac{1}{i\hbar\omega - \xi_k} (2\pi)^3 \delta(\boldsymbol{k} - \boldsymbol{k}') e^{-i\boldsymbol{k}'\cdot\boldsymbol{y}} = \\ &= \int \frac{d^3k}{(2\pi)^3} \frac{e^{i\boldsymbol{k}\cdot(\boldsymbol{r}-\boldsymbol{y})}}{i\hbar\omega - \xi_k}. \end{aligned} \tag{3.28}$$

with the single-particle energy $\xi_k = \frac{\hbar^2 k^2}{2m} - \mu$, measured from the chemical potential μ. Furthermore $G_\omega(\boldsymbol{r}, \boldsymbol{y}) = -G_{-\omega}(\boldsymbol{r}, \boldsymbol{y})$.

Using the completeness relation, by inserting identity operators $\hat{\mathbb{1}} = \int dy |\boldsymbol{y}\rangle\langle\boldsymbol{y}|$ in Eq.

(3.26), one obtain the self-consistency equation

$$\begin{aligned} F_\omega(\boldsymbol{r},\boldsymbol{y}) = &\int dy G^{(0)}_\omega(\boldsymbol{r},\boldsymbol{y})\Delta(\boldsymbol{y})\overline{G}^{(0)}_\omega(\boldsymbol{y},\boldsymbol{r})+ \\ &+\int\prod_{j=1}^{3} dy_j G^{(0)}_\omega(\boldsymbol{r},\boldsymbol{y}_1)\Delta(\boldsymbol{y}_1)\overline{G}^{(0)}_\omega(\boldsymbol{y}_1,\boldsymbol{y}_2)\Delta^*(\boldsymbol{y}_2)G^{(0)}_\omega(\boldsymbol{y}_2,\boldsymbol{y}_3)\Delta(\boldsymbol{y}_3)\overline{G}^{(0)}_\omega(\boldsymbol{y}_3,\boldsymbol{r})+ \\ &+\int\prod_{j=1}^{5} dy_j G^{(0)}_\omega(\boldsymbol{r},\boldsymbol{y}_1)\Delta(\boldsymbol{y}_1)\overline{G}^{(0)}_\omega(\boldsymbol{y}_1,\boldsymbol{y}_2)\Delta^*(\boldsymbol{y}_2)G^{(0)}_\omega(\boldsymbol{y}_2,\boldsymbol{y}_3)\Delta(\boldsymbol{y}_3)\overline{G}^{(0)}_\omega(\boldsymbol{y}_3,\boldsymbol{y}_4)\times \\ &\times\Delta^*(\boldsymbol{y}_4)G^{(0)}_\omega(\boldsymbol{y}_4,\boldsymbol{y}_5)\Delta(\boldsymbol{y}_5)\overline{G}^{(0)}_\omega(\boldsymbol{y}_5,\boldsymbol{r})+\dots. \end{aligned} \tag{3.29}$$

Inserting Eq.(3.27), we obtain the self-consistent gap equation. Then, the solution to the gap equation can be represented in the form of a perturbation series over powers of $\Delta(\boldsymbol{r})$ (which is small in the vicinity of the critical temperature T_c):

$$\begin{aligned} \Delta(\boldsymbol{r}) = &\int dy K_a(\boldsymbol{r},\boldsymbol{y})\Delta(\boldsymbol{y}) + \int\prod_{j=1}^{3} dy_j K_b(\boldsymbol{r},\{\boldsymbol{y}\}_3)\Delta(\boldsymbol{y}_1)\Delta^*(\boldsymbol{y}_2)\Delta(\boldsymbol{y}3)+ \\ &+\int\prod_{j=1}^{5} dy_j K_c(\boldsymbol{r},\{\boldsymbol{y}\}_5)\Delta(\boldsymbol{y}_1)\Delta^*(\boldsymbol{y}_2)\Delta(\boldsymbol{y}_3)\Delta^*(\boldsymbol{y}_4)\Delta(\boldsymbol{y}_5), \end{aligned} \tag{3.30}$$

where $\{\boldsymbol{y}\}_n = \{\boldsymbol{y}_1,\cdots,\boldsymbol{y}_n\}$. The integral kernel are given by:

$$K_a(\boldsymbol{r},\boldsymbol{y}) = -gk_BT\sum_\omega G^{(0)}_\omega(\boldsymbol{r},\boldsymbol{y})\overline{G}^{(0)}_\omega(\boldsymbol{y},\boldsymbol{r}), \tag{3.31}$$

$$K_b(\boldsymbol{r},\{\boldsymbol{y}\}_3) = -gk_BT\sum_\omega G^{(0)}_\omega(\boldsymbol{r},\boldsymbol{y}_1)\overline{G}^{(0)}_\omega(\boldsymbol{y}_1,\boldsymbol{y}_2)G^{(0)}_\omega(\boldsymbol{y}_2,\boldsymbol{y}_3)\overline{G}^{(0)}_\omega(\boldsymbol{y}_3,\boldsymbol{r}), \tag{3.32}$$

$$K_c(\boldsymbol{r},\{\boldsymbol{y}\}_5) = -gk_BT\sum_\omega G^{(0)}_\omega(\boldsymbol{r},\boldsymbol{y}_1)\overline{G}^{(0)}_\omega(\boldsymbol{y}_1,\boldsymbol{y}_2)G^{(0)}_\omega(\boldsymbol{y}_2,\boldsymbol{y}_3)\overline{G}^{(0)}_\omega(\boldsymbol{y}_3\boldsymbol{y}_4)G^{(0)}_\omega(\boldsymbol{r}_4,\boldsymbol{y}_5)\overline{G}^{(0)}_\omega(\boldsymbol{y}_5,\boldsymbol{r}). \tag{3.33}$$

Then, the non-linear integral form of the self-consistency equation is transformed into the differential form by introducing the gradient expansion, we define $\boldsymbol{z} = \boldsymbol{y} - \boldsymbol{r}$

$$\Delta(\boldsymbol{y}_j) = \Delta(\boldsymbol{r}+\boldsymbol{z}_j) = \sum_{n=0}^{\infty}\frac{1}{n!}(\boldsymbol{z}_j\cdot\nabla_{\boldsymbol{r}})^n\Delta(\boldsymbol{r}). \tag{3.34}$$

Fortunately from the standard single-band GL theory it turns out that as one approach T_c not only the order parameter behaves as $\Delta \propto \tau^{1/2}$, but also its spatial variations occur on the length scale $\xi \propto \tau^{-1/2}$. Then any spatial gradient is proportional to $\tau^{1/2}$, i.e., $\nabla \propto \tau^{1/2}$, therefore $\nabla\Delta \propto \tau$, meaning the τ-order of each term in the GL expansion can be found by counting one power $\tau^{1/2}$ for each occurence of the order parameter or its gradient.

The coefficients of the partial differential equation governing Δ still have to be calculated by explicitly evaluating the integrals in Eq. (3.29) to the desired precision. In particular, the GL equation obtained when keeping only the first two term, including K_a and K_b in the Eqs. (3.31-3.33) and the second-order spatial derivatives in the gradient expansion, where the terms are of the order of $\tau^{3/2}$. Now for the EGL where the terms are in an order of $\tau^{5/2}$ its necessary to incorporate all the spatial derivatives up to the fourth order in the gradient expansion inside the integral in K_a, up to second order inside the integral involving K_b and just the leading term inside the integral involving K_c. Due to the spherical symmetry of the kernels, with respect to the transformation $\boldsymbol{z} \to -\boldsymbol{z}$, some odd-order terms of these expansions can be neglected. The details of calculation can be found in Appendix B, here we quote the results.

The first tern in Eq. (3.30) evaluates to:

$$\int dy K_a(\boldsymbol{r}, \boldsymbol{y})\Delta(\boldsymbol{y}) \approx a_1\Delta + a_2\nabla\Delta + a_3\nabla(\nabla^2\Delta), \tag{3.35}$$

where

$$\begin{aligned}
&a_1 = \mathcal{A} - a[\tau + \frac{\tau}{2} + \mathcal{O}(\tau^3)], \quad \mathcal{A} = g\mathcal{N}(0)\ln\left(\frac{2e^{\Gamma}}{\pi}\frac{\hbar\omega_D}{T_c}\right), \quad a = -g\mathcal{N}(0).\\
&a_2 = \mathcal{K}[1 + 2\tau + \mathcal{O}(\tau^2)], \quad \mathcal{K} = g\mathcal{N}(0)\frac{\hbar^2 v_f^2}{6}\frac{7\zeta(3)}{8\pi^2 T_c^2}.\\
&a_3 = \mathcal{Q}[1 + \mathcal{O}(\tau)], \quad \mathcal{Q} = g\mathcal{N}(0)\frac{\hbar^4 v_f^4}{30}\frac{93\zeta(5)}{128\pi^4 T_c^4}.
\end{aligned} \tag{3.36}$$

From the second term of the Eq. (3.30) we get:

$$\begin{aligned}
&\int \prod_{j=1}^{3} dy_j K_b(\boldsymbol{r}, \{\boldsymbol{y}\}_3)\Delta(\boldsymbol{y}_1)\Delta^*(\boldsymbol{y}_2)\Delta(\boldsymbol{y}3)\\
&\approx -b1\Delta|\Delta|^2 - b_2[2\Delta|\nabla\Delta|^2 + 3\Delta^*(\nabla\Delta)^2 + \Delta^2\nabla^2\Delta^* + 4|\Delta|^2\nabla^2\Delta]
\end{aligned} \tag{3.37}$$

With

$$\begin{aligned}
&b_1 = b[1 + 2\tau + \mathcal{O}(\tau^2)], \quad b = g\mathcal{N}(0)\frac{7\zeta(3)}{8\pi^2 T_c^2},\\
&b_2 = \mathcal{L}[1 + \mathcal{O}(\tau)], \quad \mathcal{L} = g\mathcal{N}(0)\frac{\hbar^2 v_f^2}{9}\frac{93\zeta(5)}{128\pi^4 T_c^4}.
\end{aligned} \tag{3.38}$$

Finally the last term contributes in the order $\tau^{5/2}$ only as:

$$\int \prod_{j=1}^{5} dy_j K_c(\boldsymbol{r}, \{\boldsymbol{y}\}_5)\Delta(\boldsymbol{y}_1)\Delta^*(\boldsymbol{y}_2)\Delta(\boldsymbol{y}_3)\Delta^*(\boldsymbol{y}_4)\Delta(\boldsymbol{y}_5) \approx c_1|\Delta|^4\Delta, \tag{3.39}$$

with

$$c_1 = c[1 + \mathcal{O}(\tau)], \quad c = g\mathcal{N}(0)\frac{93\zeta(5)}{128\pi^4 T_c^4}, \tag{3.40}$$

where $a = -\mathcal{N}(0)$ and $\mathcal{N}(0) = mk_f/(2\pi^2\hbar^2)$ is the DOS at the Fermi energy; v_f the Fermi velocity; ω_D denotes the Debye (cutoff) frequency, $\Gamma = 0.577$ is the Euler constant, and $\zeta(...)$ is the Riemann zeta function.

In total we have:

$$\begin{aligned} \Delta =& a_1\Delta + a_2\nabla^2\Delta + a_3\nabla(\nabla^2\Delta) - b1\Delta|\Delta|^2 \\ &- b_2[2\Delta|\nabla\Delta|^2 + 3\Delta^*(\nabla\Delta)^2 + \Delta^2\nabla^2\Delta^* + 4|\Delta|^2\nabla^2\Delta] + c_1|\Delta|^4\Delta. \end{aligned} \tag{3.41}$$

A systematic expansion of the gap equation in τ can be facilitated by introducing the scaling transformation for the order parameter, the coordinates, and the spatial derivatives of the order parameter in the following form:

$$\overline{\boldsymbol{r}} = \tau^{1/2}\boldsymbol{r}, \quad \Delta = \tau^{1/2}\overline{\Delta}, \quad \overline{\boldsymbol{\nabla}} = \tau^{1/2}\boldsymbol{\nabla} \tag{3.42}$$

Where it is understood that $\Delta = \Delta(\boldsymbol{r})$, i.e., the gap is spatially dependent. The solution to the gap Eq. (3.41), must also be sought in the form of a series expansion in τ

$$\overline{\Delta} = \Delta_0 + \tau\Delta_1 + \tau^2\Delta_2 \ldots \tag{3.43}$$

By substituting Eq. (3.43) into Eq. (3.42) and collecting terms of the same order, we obtain a set of equations for each Δ_n, $(n = 0, 1, 2, \cdots)$. At $\tau^{1/2}$ we obtain

$$\tau^0 : \quad \Delta_0 = \mathcal{A}\Delta_0. \tag{3.44}$$

The solution to this equation, i.e., $\mathcal{A} = 1$, gives the ordinary BCS expression for the critical temperature, i.e.,

$$T_c = \frac{2^\Gamma}{\pi} h\omega_D \exp[-1/(g\mathcal{N}(0))]. \tag{3.45}$$

The terms of the order $\tau^{3/2}$ recovers the standard GL equation for the leading contribution to the order parameter Δ_0

$$0 = a\Delta_0 - \mathcal{K}\overline{\nabla}^2\Delta_0 + b|\Delta_0|^2\Delta_0. \tag{3.46}$$

Finally, at $\tau^{5/2}$ one gets

$$a\Delta_1 + b(2|\Delta_0|^2\Delta_1 + \Delta_0^2\Delta_1^*) - \mathcal{K}\overline{\nabla}\Delta_1 = \mathsf{F} \tag{3.47}$$

This is a linear differential inhomogeneous equations to be solved after Δ_0 is found from Eq. (3.46), where F is given by

$$\begin{aligned}\mathsf{F} = &-\frac{a}{2}\Delta_0 + 2\mathcal{K}\overline{\nabla}^2\Delta_0 + \mathcal{Q}\overline{\nabla}^2(\overline{\nabla}^2\Delta_0) - \\ &- 2b|\Delta_0|^2\Delta_0 - \mathcal{L}[2\Delta_0|\nabla\Delta_0|^2 + 3\Delta^*(\nabla\Delta_0)^2 + \Delta_0^2\overline{\nabla}^2\Delta_0^* + 4|\Delta_0|^2\overline{\nabla}^2\Delta_0^*] + c|\Delta_0|^4\Delta_0\end{aligned} \tag{3.48}$$

3.3.1 Validity Domain of the EGL Formalism

We obtain the quantitative and qualitative validity domain of the GL approach when extended to the next-to-leading order in τ.

The Uniform case (terms with $\overline{\nabla} = 0$)

$$\begin{aligned}&a\Delta_0 + b|\Delta_0|^2\Delta_0 = 0, \quad \Rightarrow |\Delta_0|^2 = -\frac{a}{b}\\ &a\Delta_1 + b(2|\Delta_0|^2\Delta_1 + \Delta_0^2\Delta_1^*) = -\frac{a}{2}\Delta_0 - 2b|\Delta_0|^2\Delta_0 + c|\Delta_0|^4\Delta_0\\ &\Delta_1(a + 3b\Delta_0^2) = (-a/2 - 2b\Delta_0^2 + c\Delta_0^4)\Delta_0\\ &\frac{\Delta_1}{\Delta_0} = -\frac{1}{2}\left(\frac{3}{2} + \frac{ca}{b^2}\right),\end{aligned}$$

where

$$\frac{ca}{b^2} = -\frac{93\zeta(5)}{98\zeta^2(3)},$$

$$\frac{\Delta_1}{\Delta_0} = -\frac{1}{2}\left(\frac{3}{2} - \frac{93\zeta(5)}{98\zeta^2(3)}\right). \tag{3.49}$$

Taking into account Eq. (3.43) and using Eq. (3.49), we obtain the order parameter in the unscaled representation up to the order τ as

$$\begin{aligned}\Delta &= \tau^{1/2}\Delta_0\left(1 - \tau\frac{\Delta_1}{\Delta_0}\right)\\ &= \tau^{1/2}\sqrt{-\frac{a}{b}}\left(1 - \frac{\tau}{2}\left(\frac{3}{2} - \frac{93\zeta(5)}{98\zeta^2(3)}\right)\right), \quad -\frac{a}{b} = \frac{g\mathcal{N}(0)}{g\mathcal{N}(0)\frac{7\zeta(3)}{8\pi^2T_c^2}},\end{aligned}$$

$$\Delta = \tau^{1/2}\pi T_c\sqrt{\frac{8}{7\zeta(3)}}\left(1-\frac{\tau}{2}\left(\frac{3}{2}-\frac{93\zeta(5)}{98\zeta^2(3)}\right)\right),$$

$$\Delta = \tau^{1/2}\pi T_c\sqrt{\frac{8}{7\zeta(3)}}(1-0.35\tau). \tag{3.50}$$

With $\Delta_{BCS}(0) = \pi/e^{\gamma}T_c$ is the zero- temperature gap calculated from the full BCS formalism [51] we obtain,

$$\boxed{\frac{\Delta(T)}{\Delta_{BCS}(0)} = \tau^{1/2}e^{\gamma}\sqrt{\frac{8}{7\zeta(3)}}(1-0.35\tau)} \tag{3.51}$$

The result from the standard and extended GL formalism compared to the full BCS solution are shown in Fig. (**3-1**)

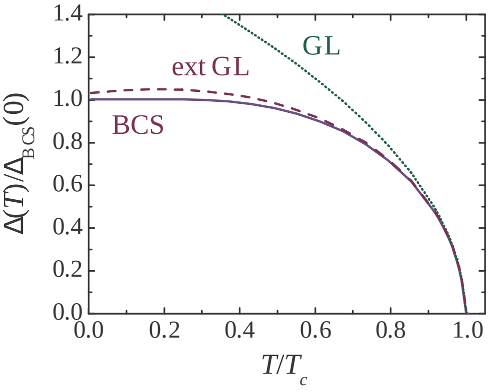

Figure 3-1 : (Color online) The temperature-dependent gap (unscaled) in units of the zero-temperature order parameter calculated within the full BCS approach $\Delta_{BCS}(0)$ versus the relative temperature T/T_c: the solid curve represents the full BCS; the dashed curve shows the result of the EGL formalism given by Eq. (3.51); the dotted curve illustrates the standard GL approach. Taken from [45].

It is seen that the EGL approach is in very good quantitative agreement with the BCS theory up to T =0.2T_c, and only below this temperature is the order parameter calculated within the extended formalism, as with the GL theory there is a noticeable difference with the BCS curve for temperature below $T = 0.7T_c$.

For details of the calculation as well as the extended GL theory for nonzero field one is referred to Refs. [45]. Some of the results of the extended GL formalism in the presence of an with the applied field can be found in Chapter 8, where we apply them to calculate vortex interaction in a superconducting thin film including stray field.

4 Numerical Methods

The range of problems in superconductivity which can be solved by analytic methods is extremely limited. More complex problems must be solved numerically. In this Chapter we will present the numerical methods used in this thesis. The time-dependent Ginzburg-Landau theory will be described, and we included a subsection concerned with how these equations can be written in a dimensionless form amenable to computation. Also we describe the popular $U - \Psi$ *method used in the most numerical computation work on superconductivity. Finally, we present the monte Carlo method used in this work.*

4.1 Time Dependent Ginzburg-Landau (TDGL)

Equations (2.17), (2.24) and (2.25) have been utilized by many groups to study equilibrium states in a superconductor. However, often one finds several meta stable states that satisfy these *time-independent* GL equations and it is not clear which of these states will occur in an experiment. An expression for the time evolution of the order parameter is needed that makes possible to study the transition between meta stables states driven by changes of external parameters such as magnetic field, voltage and temperature.

The simplest assumption is that the order parameter relaxes towards a local minimum of the free energy with a rate proportional to slope of the free energy,

$$\frac{\hbar^2}{2mD}\frac{\partial \Psi}{\partial t} = -\frac{\delta \mathcal{G}}{\delta \Psi^*}, \tag{4.1}$$

where D is a phenomenological diffusion constant that characterises the decay time of an excitation. The relaxation mechanism is due to an interaction with the lattice via exchange of quasi-particles.

$$\frac{\partial}{\partial t} \rightarrow +\frac{ie^*}{\hbar}\varphi, \tag{4.2}$$

where φ is the electrical potential. To the left hand side of equation (2.24), a normal current

$\boldsymbol{j}_n$ is added to account for non-condensed electrons which obey Ohm's law,

$$\boldsymbol{j}_n = \sigma_n \boldsymbol{E} = \sigma_n \left(-\nabla\varphi - \frac{1}{\boldsymbol{c}}\partial_t \boldsymbol{A} \right). \tag{4.3}$$

Take this considerations into account, it can be shown that the Time Dependent Ginzburg-Landau (TDGL) equations are given by,

$$\frac{\hbar^2}{2mD}\left(\partial_t + i\frac{e^*}{\hbar}\varphi\right)\Psi = \frac{1}{2m}\left(-i\hbar\nabla - \frac{e^*}{\boldsymbol{c}}\boldsymbol{A}\right)^2\Psi + |\alpha|\Psi - \beta|\Psi|^2\Psi, \tag{4.4}$$

$$\sigma_n\left(-\nabla\varphi - \frac{1}{\boldsymbol{c}}\partial_t\boldsymbol{A}\right) = \boldsymbol{j}_s - \frac{\boldsymbol{c}}{4\pi}\boldsymbol{\nabla}\times\boldsymbol{\nabla}\times\boldsymbol{A}, \tag{4.5}$$

To make the model suitable for computations and numerical methods, it must first be rescaled through non-dimensionalization. This alleviates the large difference in scale between the terms in the G-L model, making a numerical solution more precise, and the non dimensionalization process introduces more well known values as parameters, such as the characteristic lengths, in place of the more obscure parameters such as α and β for a superconducting material.

4.1.1 Dimensional Units

For convenience, to facilitate calculations we will introduce dimensionless units into the TDGL equations described by Eq. (4.4) and (4.5). We transform the variable as: $T = T/T_c$, $\boldsymbol{r}' = \boldsymbol{r}/\xi(0)$, $t' = t/\tau$, $\psi = \Psi/\Psi_0(T)$, $\boldsymbol{A}' = \boldsymbol{A}/A_0$, $\varphi' = \varphi/\varphi_0$ e $\alpha = -\alpha_0(1-T')$.

Substituting these transformations into the TDGL equations we have (we will omit the tilde to simplify the notation), we obtain:

$$-\frac{\Gamma}{\tau}(\partial_t + i\varphi)\psi = -\alpha_0(1-T)\psi + \beta\Psi_0^2|\psi|^2\psi + \frac{\hbar^2}{2m\xi(0)^2}\left(-i\boldsymbol{\nabla} - \boldsymbol{A}\right)^2\psi, \tag{4.6}$$

$$\frac{\sigma_n}{2e\tau}(\partial_t\boldsymbol{A} + \boldsymbol{\nabla}\varphi) = \frac{2e\Psi_0^2}{m}\mathcal{R}[\psi^*(-i\boldsymbol{\nabla} - \boldsymbol{A})\psi] - \frac{\boldsymbol{c}^2}{8\pi e\xi(0)^2}\boldsymbol{\nabla}\times\boldsymbol{\nabla}\times\boldsymbol{A}, \tag{4.7}$$

where $A_0 = \hbar c/2e\xi(0)$ and $\varphi_0 = \hbar/2e\tau$. Equating all the coefficients on the right side of Eq. (4.6) and using the order parameter value definition $\Psi_0 = mc^2/16\pi e^2\lambda^2(T)$ in the Eq. (4.7) we have

$$-\frac{\Gamma}{\tau}(\partial_t + i\varphi)\psi = -\alpha_0(1-T)[(-i\boldsymbol{\nabla} - \boldsymbol{A})^2\psi + (1-T)(|\psi|^2 - 1)\psi], \tag{4.8}$$

$$\frac{\sigma_n}{\tau}(\partial_t\boldsymbol{A} + \boldsymbol{\nabla}\varphi) = \frac{c^2}{2\pi\lambda^2}\mathcal{R}[\psi^*(-i\boldsymbol{\nabla} - \boldsymbol{A})\psi] - \frac{\boldsymbol{c}^2}{4\pi e\xi(0)^2}\boldsymbol{\nabla}\times\boldsymbol{\nabla}\times\boldsymbol{A}, \tag{4.9}$$

remembering that $\lambda^2(T) = \lambda_0^2/(1 - T/T_c)$, we have

$$\frac{\sigma_n}{\tau}(\partial_t \boldsymbol{A} + \boldsymbol{\nabla}\varphi) = \frac{\boldsymbol{c}^2}{2\pi\lambda^2}\left\{(1-T)\mathcal{R}[\psi^*(-i\boldsymbol{\nabla} - \boldsymbol{A})\psi] - \frac{\boldsymbol{c}^2}{4\pi e\xi(0)^2}\boldsymbol{\nabla}\times\boldsymbol{\nabla}\times\boldsymbol{A}\right\}, \tag{4.10}$$

where $\tau = 4\pi\lambda_0\sigma_n/c^2$, we obtain the TDGL equations in dimensionless units:

$$(\partial_t + i\varphi)\psi = \frac{1}{\eta}\left[(-i\boldsymbol{\nabla} - \boldsymbol{A})^2\psi + (1-T)(|\psi|^2 - 1)\psi\right], \tag{4.11}$$

$$(\partial_t \boldsymbol{A} + \boldsymbol{\nabla}\varphi) = (1-T)\mathcal{R}[\psi^*(-i\boldsymbol{\nabla} - \boldsymbol{A})\psi] - \kappa\boldsymbol{\nabla}\times\boldsymbol{\nabla}\times\boldsymbol{A}. \tag{4.12}$$

One can find in the above equation a gauge symmetry whereby the equation is unchanged under transformation of the type

$$\varphi' = \varphi - \frac{\partial\chi}{\partial t}, \qquad \psi' = \psi e^{i\chi}, \qquad \boldsymbol{A}' = \boldsymbol{A} + \boldsymbol{\nabla}\chi. \tag{4.13}$$

According to this transformation, we are free to choose the function χ. Then, let $\chi = \int_0^t \varphi dt$, this is so-called "Zero electric potential gauge" (see [52]). It gives us the new electric potential $\varphi' = 0$ and removes the term φ from the TDGL equation.

The gauge invariant transform of these equations allows the choice of the potential to scale zero. So we finally have,

$$\frac{\partial\psi}{\partial t} = \frac{1}{\eta}\left[(-i\boldsymbol{\nabla} - \boldsymbol{A})^2\psi + (1-T)(|\psi|^2 - 1)\psi\right], \tag{4.14}$$

$$\frac{\partial\boldsymbol{A}}{\partial t} = (1-T)\mathcal{R}[\psi^*(-i\boldsymbol{\nabla} - \boldsymbol{A})\psi] - \kappa\boldsymbol{\nabla}\times\boldsymbol{\nabla}\times\boldsymbol{A}. \tag{4.15}$$

Where distances are measured in units of the coherence length $\xi(0) = \sqrt{\hbar/2m\alpha_0}$, time in $\tau = 4\pi\lambda_0^2\sigma_n/c^2$, the external field in units of $H_{c2}(0) = \Phi_0/2\pi\xi^2(0) = \sqrt{2}\kappa H_c(0)$, the potential vector in units $H_{c2}\xi(0)$ and temperature in T_c units. $\eta = t_\psi/A$ is proportional to the relation existing between the characteristic times for ψ and $\boldsymbol{A}$, and was determined from the BCS theory for various limits: $\eta = 1$ clear limit, $\eta = 12$ for superconductors with magnetic impurities [53] and $\eta = 5.79$ for weakly coupled superconductors [54].

In this work, we consider that the order parameter and the potential magnetic vector have the same relaxation time, so $\eta = 1$. This assumption is acceptable since we will determine configurations.

4.2 The $U-\psi$ method

The problems that we generally want to solve in this thesis consist of a superconductor immersed in an empty space subjected to a magnetic field, as shown in the figure **4-1**. The superconductor has dimension $a\times b\times c$ and the total volume $A\times B\times C$. The geometry and the boundary conditions varies according to the problem, and the vacuum space is taken large enough in order to consider demagnetization effects and the stray magnetic field

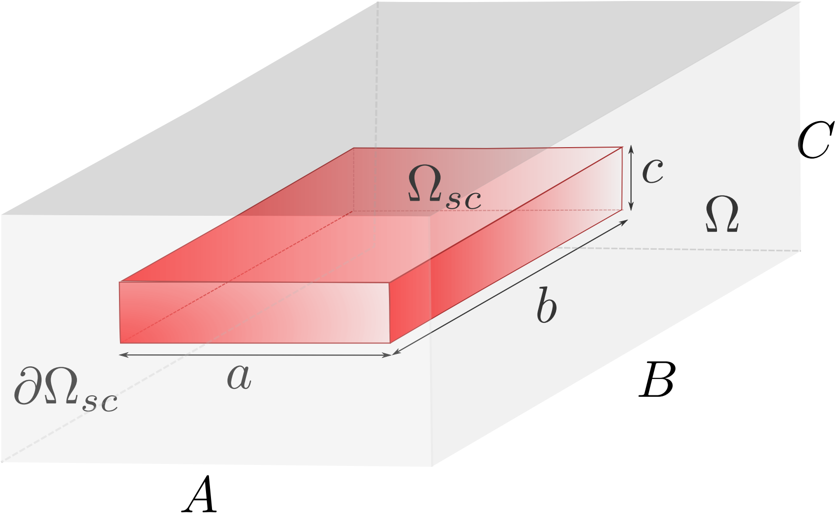

Figure 4-1 : Illustration of the cell utilized in this work, a superconductor with dimension $a\times b\times c$ immersed in an empty space $A\times B\times C$.

The widely used $U-\psi$ method is described in detail by Gropp et al. [55]. As this method forms the basis of our algorithm we briefly review the main points here. Complex link variables $\mathcal{U}^x$, $\mathcal{U}^y$ and $\mathcal{U}^z$ are introduced to preserve the gauge invariant properties of the discretized equations:

$$\begin{aligned}\mathcal{U}^x(x,y,z,t) &= \exp\left(-i\int_{x_0}^{x} A_x(\xi,y,z)d\xi\right),\\ \mathcal{U}^y(x,y,z,t) &= \exp\left(-i\int_{y_0}^{y} A_y(x,\eta,z)d\eta\right),\\ \mathcal{U}^z(x,y,z,t) &= \exp\left(-i\int_{z_0}^{z} A_z(x,y,\zeta)d\zeta\right),\end{aligned} \tag{4.16}$$

where (x_0,y_0,z_0) is an arbitrary reference point. This will allow to write the first of the TDGL equations in a form that resembles a heat diffusion equation. This procedure not only ensures gauge invariance when discretizing the TDGL equations [55,56], it is also important to ensure the stability of the explicit Euler method that will be used in temporal integration. Therefore, using the link variables, can rewritten the TDGL equations can be rewritten, as [55]:

$$\partial_\mu \mathcal{U}^\mu = -i\mathcal{U}^\mu \boldsymbol{A}, \tag{4.17}$$

such that

$$\begin{aligned}\partial_\mu[\mathcal{U}^\mu \Psi] &= \Psi \partial_\mu \mathcal{U}^\mu + \mathcal{U}^\mu \partial_\mu \Psi, \\ &= -i\Psi \mathcal{U}^\mu \boldsymbol{A}_\mu + \mathcal{U}^\mu \partial_\mu \Psi, \\ &= i\mathcal{U}^\mu(-i\partial_\mu - \boldsymbol{A}_\mu)\Psi, \end{aligned} \tag{4.18}$$

indicating that

$$(-i\partial_\mu - \boldsymbol{A}_\mu)\Psi = -i\overline{\mathcal{U}}^\mu \partial_\mu[\mathcal{U}^\mu \Psi]. \tag{4.19}$$

Now, applying the derivative to the equation above

$$\begin{aligned}\partial_\mu(-i\partial_\mu - \boldsymbol{A}_\mu)\Psi &= \partial_\mu(-i\overline{\mathcal{U}}^\mu \partial_\mu[\mathcal{U}^\mu \Psi]) \\ &= \overline{\mathcal{U}}^\mu(\boldsymbol{A}_\mu \partial_\mu[\mathcal{U}^\mu \Psi] - i\partial_\mu^2 \mathcal{U}^\mu \Psi]) \\ &= \overline{\mathcal{U}}^\mu(i\boldsymbol{A}_\mu \mathcal{U}^\mu(-i\partial_\mu - \boldsymbol{A}_\mu)\Psi - i\partial_\mu^2[\mathcal{U}^\mu \Psi]) \\ -i\partial_\mu^2\Psi - \partial_\mu \boldsymbol{A}_\mu \Psi &= i\boldsymbol{A}_\mu(-i\partial_\mu - \boldsymbol{A}_\mu)\Psi - i\overline{\mathcal{U}}^\mu \partial_\mu^2[\mathcal{U}^\mu \Psi] \\ -\partial_\mu^2\Psi + i(\partial_\mu \boldsymbol{A}_\mu + \boldsymbol{A}_\mu \partial_\mu)\Psi + \boldsymbol{A}_\mu^2 \Psi &= -\overline{\mathcal{U}}^\mu \partial_\mu^2[\mathcal{U}^\mu \Psi] \\ (-i\partial_\mu - \boldsymbol{A}_\mu)^2 &= -\overline{\mathcal{U}}^\mu \partial_\mu^2[\mathcal{U}^\mu \Psi]. \end{aligned} \tag{4.20}$$

The first TDGL equation (4.14) is rewritten as

$$\frac{\partial \psi}{\partial t} = \sum_{\mu=x,y,z} \overline{\mathcal{U}}_\mu \frac{\partial^2}{\partial \mu^2}(\mathcal{U}_\mu \psi) - (1-T)(1-|\psi|)\psi. \tag{4.21}$$

The supercurrent density $\boldsymbol{j}_s$ is given in terms of ψ and $\boldsymbol{A}$ by (4.15), or, alternatively, in terms of ψ and $\mathcal{U}$ by

$$\boldsymbol{j}_s = (1-T)\Im\left[\overline{\mathcal{U}}_\mu \overline{\psi} \frac{\partial}{\partial \mu}(\mathcal{U}_\mu \psi)\right], \qquad \mu = x, y, z. \tag{4.22}$$

where $\Im$ indicates the imaginary part of the complex variable.

4.2.1 Computational mesh

Consider that the domain Ω_{sc} covers the superconductor parallelepiped of thickness c and lateral sizes a and b. The interface between this region and vacuum is denoted by $\partial\Omega_{sc}$.

Because the demagnetization effects, we need to consider a larger domain Ω of dimensions $A \times B \times C$, such $\Omega_{sc} \subset \Omega$, the vacuum-vacuum interface is indicated by Ω. [See Fig. **4-1**].

The method used to obtain numerical solutions of TDGL equations is that of finite differences. Here, we consider a grid in the form of a parallelepiped, with $N_x \times N_y \times N_z$ unit cells, each with dimension $a_x \times a_y \times a_z$, in such a way that the $A = N_x a_x$, $B = N_y a_y$ and $C = N_z a_z$. Therefore, we have a grid of $(N_x - 1) \times (N_y - 1) \times (Nz - 1)$ points, so that the computational simulations will be developed in a box composed of unit cell given by:

$$\Omega_{i,j,k} = \{\mathbf{r} = (x, y, z) : x_i < x < x_{i+1}, y_j < y < y_{j+1}, z_k < z < z_{k+1}\}, \tag{4.23}$$

where

$$x_i = (i - 1)a_x, \qquad y_j = (j - 1)a_y, \qquad z_k = (k - 1)a_z. \tag{4.24}$$

Fig. **4-2** show a typical grid cell of the domain Ω_{sc} and the evaluation points for all physical quantities.

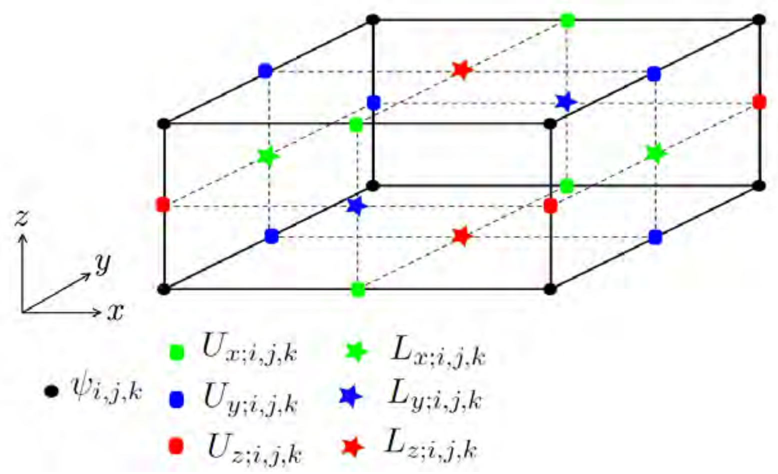

Figure 4-2 : Unit cell in a 3-dimensional mesh.

The domain Ω_{sc} is located an integer number of mesh width inside Ω, in such a way that there is always at least one layer of grid points between Ω_{sc} and Ω, that is

$$\begin{aligned}\Omega_{sc;i,j,k} =&\{\boldsymbol{r} = (x, y, z) : d_{x1} + \frac{1}{2}a_x < x < d_{x2-1} - \frac{1}{2}a_x, d_{y1} + \frac{1}{2}a_y < y < d_{y2-1} - \frac{1}{2}a_y,\\ &d_{z1} + \frac{1}{2}a_z < z < d_{z2-1} - \frac{1}{2}a_z\}.\end{aligned} \tag{4.25}$$

To solve the TDGL equations it is necessary to replace continuous variables with equivalent discrete variables. In order to assure the equivalence of the method, it is necessary to define in which grid points the physical quantities are calculated. Since such TDGL equations are differential equations that have gauge invariance, some care is needed because when we discretizing such equations, this invariance can break (symmetry breaking) and the results may not be satisfactory (non physical). The use of the so-called link variables guarantee the invariance of gauge in the discretization process [56].

We denote the discrete variables by the same symbols as their continuous counterparts. The index (i, j, k) is assigned to any quantity related to the grid cell $\Omega_{i,j,k}$. The primary variables are the order parameter and the vector of link variables; all other variables (vector potential, induced magnetic field, supercurrent) are expressed in terms of these primary variables. The primary variable are evaluated on staggered grids.

- The order parameter ψ,

$$\psi = \{\psi_{i,j,k} : i = x_1, \ldots, x_2; j = y_1, \ldots, y_2; k = z_1, \ldots, z_2\}, \tag{4.26}$$

  where

$$\psi_{i,j,k} = \psi(x_i, y_j, z_k). \tag{4.27}$$

- The vector of link variables $\boldsymbol{U} = (U_x, U_y, U_z)$,

$$U_x = \{U_{x;i,j,k} : i, j, k\}, \qquad U_y = \{U_{y;i,j,k} : i, j, k\}, \qquad U_z = \{U_{z;i,j,k} : i, j, k\}. \tag{4.28}$$

To derive the discrete equations it is useful to notice that,from the definition of the link variables,discrete analogs of $\mathcal{U}_x$, $\mathcal{U}_y$ and $\mathcal{U}_z$ from (4.16) can be defined at the nodes as

$$\mathcal{U}^x_{i,j,k} = \prod_{l=1}^{i-1} U^x_{l,j,k}, \qquad \mathcal{U}^y_{i,j,k} = \prod_{l=1}^{j-1} U^y_{i,l,k}, \qquad \mathcal{U}^z_{i,j,k} = \prod_{l=1}^{k-1} U^z_{i,j,l}, \tag{4.29}$$

which leads to

$$U^x_{i,j,k} = \mathcal{U}^x(x_{i+1}, y_j, z_k)\overline{\mathcal{U}}^x(x_i, y_j, z_k) = \exp\left(-i\int_{x_i}^{x_{i+1}} A_x(\xi, y_j, z_k)d\xi\right), \tag{4.30}$$

$$U^y_{i,j,k} = \mathcal{U}^y(x_i, y_{j+1}, z_k)\overline{\mathcal{U}}^y(x_i, y_j, z_k) = \exp\left(-i\int_{y_j}^{y_{j+1}} A_x(x_i, \eta, z_k)d\eta\right), \tag{4.31}$$

$$U^z_{i,j,k} = \mathcal{U}^z(x_i, y_j, z_{k+1})\overline{\mathcal{U}}^z(x_i, y_j, z_k) = \exp\left(-i\int_{z_k}^{z_{k+1}} A_x(x_i, y_j, \zeta)d\zeta\right). \tag{4.32}$$

Using the midpoint method for simple integration (for example $\int_{x_i}^{x_{i+1}} A_x(\xi, y_j, z_k)d\xi =$

$A_{x_i,y_j,z_k}a_x + \mathcal{O}(a_x^2))$, we can also write in general form:

$$U^{\mu}_{i,j,k} = \exp(-iA_{\mu;i,j,k}a_\mu), \qquad \mu = x, y, z, \tag{4.33}$$

where $A_{x;i,j,k} = A_x(x_i{+}a_x/2, y_j, z_k)$, $A_{y;i,j,k} = A_x(x_i, y_j{+}a_y/2, z_k)$ and $A_{z;i,j,k} = A_z(x_i, y_j, z_k{+}a_z/2)$

Calculation of the path integral of the vector potential in a unit cell of the mesh results in the magnetic flux. Let $\mathcal{D}$ be any two-dimensional domain that is orthogonal to the z direction. so, take $\mathcal{D} = \boldsymbol{r} = (x, y, z) \in \Omega : x_i < x < x_{i+1}, y_j < y < y_{j+1}, z = z_k$, exactly one unit cell: let $\partial\mathcal{D}$ denote the boundary of $\mathcal{D}$. According to Stokes's identity then we have:

$$\begin{aligned}\exp\left(-i\int_{\mathcal{D}} B_z dxdy\right) &= \exp\left(-i\oint_{\partial\mathcal{D}} \boldsymbol{A}\cdot d\boldsymbol{r}\right) && (4.34)\\ &= U_{x;i,j,k}U_{y;i+1,j,k}\overline{U}_{x;i,j+1,k}\overline{U}_{y;i,j,k}\\ &= L_{z;i,j,k}. && (4.35)\end{aligned}$$

If we approximate the area integral in (4.34) by the midpoint rule and the resulting exponential by the first two terms of its Taylor expansion

$$\begin{aligned}\exp\left(-i\int_{\mathcal{D}} B_z dxdy\right) &= \exp(-iB_{z;i,j,k}a_x a_y)\\ &= 1 - iB_{z;i,j,k}a_x a_y, && (4.36)\end{aligned}$$

where $B_{z;i,j,k} = B_z(x_i + \frac{a_x}{2}, y_j + \frac{a_y}{2}, z_k)$, we get:

$$B_{z;i,j,k} = -\frac{1}{a_x a_y}\Im(L_{z;i,j,k}). \tag{4.37}$$

In general, we have

$$B_{\mu;i,j,k} = -\frac{a_\mu}{a_x a_y a_z}\Im(L_{\mu;i,j,k}), \qquad \mu = x, y, z, \tag{4.38}$$

where we have introduced the abbreviations

$$L_{x;i,j,k} \equiv U_{y;i,j,k}U_{z;i,j+1,k}\overline{U}_{y;i,j,k+1}\overline{U}_{z;i,j,k} \tag{4.39}$$

$$L_{y;i,j,k} \equiv U_{z;i,j,k}U_{y;i,j,k+1}\overline{U}_{z;i+1,j,k}\overline{U}_{x;i,j,k} \tag{4.40}$$

$$L_{z;i,j,k} \equiv U_{x;i,j,k}U_{y;i+1,j,k}\overline{U}_{x;i,j+1,k}\overline{U}_{y;i,j,k} \tag{4.41}$$

4.2.2 Discretization of the Equations

In the following, discrete approximations for each term of (4.14)-(4.15) are derived, maintaining second order accuracy in space. Thus using that

$$\begin{aligned} (\partial_x f)_{i,j,k} &\approx \frac{f_{i+1,j,k} - f_{i,j,k}}{a_x}, \\ (\partial_x^2 f)_{i,j,k} &\approx \frac{f_{i+1,j,k} - 2f_{i,j,k} + f_{i-1,j,k}}{a_x^2}, \end{aligned}$$

we can write:

$$\overline{\mathcal{U}}_x \frac{\partial^2}{\partial x^2}(\mathcal{U}_x\psi)\bigg|_{x_i,y_j,z_k} = \frac{U_{x;i,j,k}\psi_{i+1,j,k} - 2\psi_{i,j,k} + \overline{U}_{x;i-1,j,k}\psi_{i-1,j,k}}{a_x^2}, \tag{4.42}$$

$$\overline{\mathcal{U}}_y \frac{\partial^2}{\partial y^2}(\mathcal{U}_x\psi)\bigg|_{x_i,y_j,z_k} = \frac{U_{y;i,j,k}\psi_{i,j+1,k} - 2\psi_{i,j,k} + \overline{U}_{y;i,j-1,k}\psi_{i,j-1,k}}{a_y^2}, \tag{4.43}$$

$$\overline{\mathcal{U}}_z \frac{\partial^2}{\partial z^2}(\mathcal{U}_z\psi)\bigg|_{x_i,y_j,z_k} = \frac{U_{z;i,j,k}\psi_{i,j,k+1} - 2\psi_{i,j,k} + \overline{U}_{z;i,j,k-1}\psi_{i,j,k-1}}{a_z^2}. \tag{4.44}$$

Now $(1 - |\psi|^2)\psi$, is readily approximated by

$$(1 - \overline{\psi}_{i,j,k}\psi_{i,j,k})\psi_{i,j,k}. \tag{4.45}$$

Collecting the previous results, the TDGL equation for order parameter reads:

$$\begin{aligned} \frac{\partial \psi_{i,j,k}}{\partial t} =& \frac{U_{x;i,j,k}\psi_{i+1,j,k} - 2\psi_{i,j,k} + \overline{U}_{x;i-1,j,k}\psi_{i-1,j,k}}{a_x^2} \\ &+ \frac{U_{y;i,j,k}\psi_{i,j+1,k} - 2\psi_{i,j,k} + \overline{U}_{y;i,j-1,k}\psi_{i,j-1,k}}{a_y^2} \\ &+ \frac{U_{z;i,j,k}\psi_{i,j,k+1} - 2\psi_{i,j,k} + \overline{U}_{z;i,j,k-1}\psi_{i,j,k-1}}{a_z^2} + (1-T)(1 - \overline{\psi}_{i,j,k}\psi_{i,j,k})\psi_{i,j,k} \end{aligned} \tag{4.46}$$

We now turn to the process of discretization of the second TDGL equation (4.15), we can rewrite the equation (4.22) as:

$$\begin{aligned} j_{sx;i,j,k} = j_{sx}\left(x_i + \frac{a_x}{2}, y_j, z_k\right) &= (1-T)\Im\left[\overline{\mathcal{U}}_x\overline{\psi}\frac{\partial}{\partial x}(\mathcal{U}_x\psi)\right]\bigg|_{x_i+\frac{a_x}{2},y_j,z_k} \\ &= \frac{(1-T)}{a_x}\Im[\overline{\psi}_{i,j,k}U_{x;i,j,k}\psi_{i+1,j,k}], \end{aligned} \tag{4.47}$$

$$\begin{aligned} j_{sy;i,j,k} &= j_{sy}\left(x_i, y_j + \frac{a_y}{2}, z_k\right) = (1-T)\Im\left[\overline{\mathcal{U}}_y\overline{\psi}\frac{\partial}{\partial y}(\mathcal{U}_y\psi)\right]\Bigg|_{x_i, y_j + \frac{a_y}{2}, z_k} \\ &= \frac{(1-T)}{a_y}\Im[\overline{\psi}_{i,j,k}U_{y;i,j,k}\psi_{i,j+1,k}], \end{aligned} \tag{4.48}$$

$$\begin{aligned} j_{sz;i,j,k} &= j_{sz}\left(z_i, y_j, z_k + \frac{a_z}{2}\right) = (1-T)\Im\left[\overline{\mathcal{U}}_z\overline{\psi}\frac{\partial}{\partial z}(\mathcal{U}_y\psi)\right]\Bigg|_{x_i, y_j, z_k + \frac{a_z}{2}} \\ &= \frac{(1-T)}{a_z}\Im[\overline{\psi}_{i,j,k}U_{z;i,j,k}\psi_{i,j,k+1}]. \end{aligned} \tag{4.49}$$

For the term $\boldsymbol{\nabla} \times \boldsymbol{\nabla} \times \boldsymbol{A} = \boldsymbol{\nabla} \times \boldsymbol{B}$, using the definition

$$\boldsymbol{\nabla} \times \boldsymbol{B} = \hat{x}\left(\frac{\partial B_z}{\partial y} - \frac{\partial B_y}{\partial z}\right) + \hat{y}\left(\frac{\partial B_x}{\partial z} - \frac{\partial B_z}{\partial x}\right) + \hat{z}\left(\frac{\partial B_y}{\partial x} - \frac{\partial B_x}{\partial y}\right), \tag{4.50}$$

we can use the approximations

$$\begin{aligned} L_{z;i,j,k}\overline{L}_{z;i,j-1,k} &= \exp[-ia_x a_y(B_{z;i,j,k} - B_{z;i,j-1,k})] \\ &\approx 1 - ia_x a_y(B_{z;i,j,k} - B_{z;i,j-1,k}) \\ &\approx 1 - ia_x a_y \partial_y B_z, \\ \Rightarrow \partial_y B_z &\approx \frac{i}{a_x a_y^2}(L_{z;i,j,k}\overline{L}_{z;i,j-1,k} - 1), \end{aligned} \tag{4.51}$$

then,

$$\partial_y B_z(x_i + \frac{a_x}{2}, y_j, z_k) \approx \frac{i}{a_x a_y^2}(L_{z;i,j,k}\overline{L}_{z;i,j-1,k} - 1), \tag{4.52}$$

$$-\partial_x B_z(x_i, y_j + \frac{a_y}{2}, z_k) \approx \frac{i}{a_x^2 a_y}(L_{z;i-1,j,k}\overline{L}_{z;i,j,k} - 1). \tag{4.53}$$

Proceeding analogously it is done for the other derivatives, the term $\partial_t \boldsymbol{A}$, is written as:

$$\begin{aligned} \partial_t[\overline{\mathcal{U}}^x(x,y,z,t)\mathcal{U}^x(x+a_x,y,z,t)] &= \partial_t U^x \\ &= -i\overline{\mathcal{U}}^x(x,y,z,t)\mathcal{U}^x(x,y,z,t)\int_x^{x+a_x}\partial_t A^x(\xi,y,z,t)d\xi, \\ &= -ia_x\overline{\mathcal{U}}^x(x,y,z,t)\mathcal{U}^x(x,y,z,t)\partial_t A^x(x + \frac{a_x}{2}, y, z, t) + \mathcal{O}(a_x^2) \end{aligned} \tag{4.54}$$

thus it follows that

$$\partial_t A^x(x_i, y_j, z_k, t) = \frac{i}{a_x}\overline{U}_{x;i,j,k}\partial_t U_{x;i,j,k}. \tag{4.55}$$

So, the equation of motion for U_μ is

$$\begin{aligned}\frac{\partial U_{x;i,j,k}}{\partial t} =& -i(1-T)\partial_t U_{x;i,j,k}\Im[\overline{\psi}_{i,j,k}U_{x;i,j,k}\psi_{i+1,j,k}] - \frac{\kappa^2}{a_y^2}(L_{z;i,j,k}\overline{L}_{z;i,j-1,k}-1)+\\ &+\frac{\kappa^2}{a_z^2}(L_{y;i,j,k}\overline{L}_{y;i,j,k-1}-1).\end{aligned} \tag{4.56}$$

The equation for U_y and U_z are obtained by cycling permutation.

Finally, a simple forward-Euler scheme is adopted to discretize the time variable with step Δt,namely

$$\psi_{i,j,k}(t+\Delta t) = \psi_{i,j,k}(t) + \Delta t\partial_t\psi_{i,j,k}(t). \tag{4.57}$$

$$U\mu, i, j, k(t+\Delta t) = U_{\mu,i,j,k}(t) + \Delta t\partial_t U_{\mu,i,j,k}(t), \qquad \mu = x, y, z. \tag{4.58}$$

The magnetization $4\pi M = B - H$, where B is the induction (the spatial average of the local magnetic field), is

$$-4\pi M_n = \frac{1}{N_xN_yN_z}\sum_{i=1}^{N_x}\sum_{j=1}^{N_y}\sum_{k=1}^{N_z} h^n_{z;i,j,k} - H \tag{4.59}$$

4.2.3 Boundary Condition

Equations (4.57)-(4.58) are not defined for boundary nodes or links. Generally, in superconducting systems, are considered problems with Dirichlet or Neumann boundary conditions representing the superconducting/metal interface or the superconducting/insulating interface or vacuum, respectively. The boundary condition implies that no superconducting current can transpose the limit of the superconducting sample. For the superconductor/insulator interface it is described by equation (2.26) with $b \to \infty$ that is

$$(-i\nabla - \mathbf{A})\psi \cdot \hat{n}|_{\partial\Omega} = 0. \tag{4.60}$$

For example, if the boundary is aligned with y-axis, the zero-current condition implies $(-i\partial_x - A_x)\psi = 0$ or, equivalently, $-i\overline{\mathcal{U}_x}\partial_x(\mathcal{U}_x\psi) = 0$. For the order parameter at $i = d_{x1+\frac{a_x}{2}}$ (west boundary) is implemented as

$$\begin{aligned}\partial_x(\mathcal{U}_x\psi)\Big|_{d_{x1+\frac{a_x}{2}},j,k} &= 0\\ \Rightarrow \frac{\mathcal{U}_{x,2,j,k}\psi_{2,j,k} - \mathcal{U}_{x,1,j,k}\psi_{1,j,k}}{a_x} &= 0\\ \mathcal{U}_{x,1,j,k}\psi_{1,j,k} &= \mathcal{U}_{x,2,j,k}\psi_{2,j,k}\\ \psi_{1,j,k} &= U_{x,1,j,k}\psi_{2,j,k}.\end{aligned}$$

It also occurs for the other faces. Therefore, the boundary conditions applied to the faces of the superconductor are:

$$\psi_{d_{x1},j,k} = U_{x;d_{x1},j,k}\psi_{d_{x1}+1,j,k}, \qquad \text{West boundary} \tag{4.61}$$

$$\psi_{d_{x2},j,k} = \overline{U}_{x;d_{x2}-1,j,k}\psi_{d_{x2}-1,j,k}, \qquad \text{East boundary} \tag{4.62}$$

where, $d_{y1}+1 \leq j \leq d_{y2}-1$ and $d_{z1}+1 \leq k \leq d_{z2}-1$,

$$\psi_{i,d_{y1},k} = U_{y;i,d_{y1},k}\psi_{i,d_{y1}+1,k}, \qquad \text{Behind boundary} \tag{4.63}$$

$$\psi_{i,d_{y2},k} = \overline{U}_{y;i,d_{y2}-1,k}\psi_{i,d_{y2},k}, \qquad \text{East boundary} \tag{4.64}$$

where, $d_{x1}+1 \leq i \leq d_{x2}-1$ and $d_{z1}+1 \leq z \leq d_{z2}-1$,

$$\psi_{i,j,d_{z1}} = U_{z;i,j,k}\psi_{i,j,d_{z1}+1}, \qquad \text{Botton boundary} \tag{4.65}$$

$$\psi_{i,j,d_{z2}} = \overline{U}_{z;i,j,d_{z2}-1}\psi_{i,j,d_{z2}-1}, \qquad \text{Top boundary} \tag{4.66}$$

where, $d_{x1}+1 \leq i \leq d_{x2}-1$ and $d_{y1}+1 \leq j \leq d_{y2}-1$.

Note that we now have all the values of $\psi_{i,j,k}$ inside the sample and on the surface $\partial\Omega_{sc}$. For the edges of the superconducting sample we make an approximation by calculating the arithmetic averages of the two nearest points adjacent in the faces. Likewise, we make an approximation for the vertices of the sample, taking, however, the three closest points on the faces.

After updating $\psi_{i,j,k}$, it is possible to update the values of the variable $U_{\mu,i,j,k}$. The magnetic field is updated through equations (4.30)-(4.32). The local magnetic field is equated to the applied magnetic field, maintaining the continuity of the field. In our simulations, we used the field applied only in the z direction, so that, $B_{z,i,j,k} = H$, where H is the applied magnetic field.

$$\begin{aligned}
&U_{y;1,j,k} = U_{x;1,j,k}U_{y;2,j,k}\overline{U}_{x;1,j+1,k}e^{ia_xa_yH}; \qquad U_{y;N_x+1,j,k} = U_{x;N_x,j+1,k}U_{y;N_x,j,k}\overline{U}_{x;N_x,j,k}e^{-ia_xa_yH},\\
&U_{x;i,1,k} = \overline{U}_{y;i+1,1,k}U_{x;i,2,k}U_{y;i,1,k}e^{-ia_xa_yH}; \qquad U_{x;i,N_x+1,k} = \overline{U}_{y;i,N_y,k}U_{x;i,Nx,k}U_{y;i+1,N_y,k}e^{ia_xa_yH},\\
&U_{z;i,j,i} = e^{ia_xa_yH}; \qquad U_{z;i,j,N_z+1} = e^{ia_xa_yH};
\end{aligned} \tag{4.67}$$

In some simulations we consider periodic boundary conditions on one of the axes. In this way, we only require that the lower and upper faces in the direction to be periodic have the same value. Periodic boundary conditions $\psi_{i,j,k}$ and $U_{\mu;i,j,k}$ for example in the edge x are:

$$\psi_{i,1,k} = \psi_{i,N_y,k}, \qquad \psi_{i,N_y+1,k} = \psi_{i,2,k}, \tag{4.68}$$

$$U_{x;i,1,k} = U_{x;i,N_y,k}, \qquad U_{x;i,Ny+1,k} = U_{x;i,2,k}, \tag{4.69}$$

Periodic boundary condition

Sometimes it is not necessary to take into account the influence of the boundary on the physical properties that we are interested in studying. Numerically, the most economical way to achieve this is to study the problem in a periodical region, where the observable physical magnitudes are invariant before a spatial translation with period given by the size of the analyzed region. In the case of superconductor we must also request that the magnetic flux Φ is quantized within the periodic region that we will assume of size $L_x \times L_y$.

Therefore, one of the necessary conditions to be able to apply periodic boundary condition is that the vector potential is also periodic in such a way that, in the boundary of the simulation cell, the values of the potential vector coincide with the boundary of the neighboring cell. To satisfy the gauge invariance of the problem, the periodic conditions for a translation of the potential vector and the order parameter in a lattice have the form

$$\begin{aligned} \mathbf{A}(x + a_\mu) &= \mathbf{A}(x) + \nabla\chi_\mu(x), \\ \psi(x + a_\mu) &= \psi(x)\exp\left[i\frac{2e}{\hbar c}\chi_\mu(x)\right], \end{aligned} \tag{4.70}$$

These transformations follow those used in the development of the TDGL equations, and depend on the mesh structure, which is characterized by the translation vectors a_μ and the gauge potential $\chi_\mu(x)$ associated with each vector a_μ. The conditions (4.70) establish that a translation by a lattice vector maintains the gauge invariance, that is, the transformation in ψ and $\mathbf{A}$ ensure the invariance of the equations, and hence of the physical measurable quantities, such $\mathbf{B}$ and the density of Cooper pairs $|\psi|^2$.

The potential vector for a uniform magnetic field applied in the direction z can be expressed as follows, $\mathbf{A} = xH_z\hat{y}$, where, H_z is a applied magnetic field. Thus, one chooses for the transformation (4.70) a gauge potential directly related to this form of the vector potential. For a rectangular sample with area $L_x \times L_y$ subject to the external field H, we have:

$$\chi_\mu = HL_xy = y\frac{\Phi}{L_y}, \qquad \chi_y = 0, \tag{4.71}$$

where $\Phi = HL_xL_y$. With the choice of this potential the conditions of invariance Eq. (4.70) for translation in the x-direction can be written as:

$$\begin{aligned} A_x(x+b_x,y) &= A_x(x) + \partial_x\left(y\frac{\Phi}{L_y}\right) = A_x(x), \\ A_y(x+b_x,y) &= A_y(x) + \partial_y\left(y\frac{\Phi}{L_y}\right) = A_y(x) + \frac{\Phi}{L_y}, \end{aligned} \tag{4.72}$$

and for translations in the y direction:

$$A_x(x,y+b_y) = A_x(x), \qquad A_y(x,y+b_y) = A_y(x). \tag{4.73}$$

For the order parameter using the gauge potential given by Eq. (4.71), we obtain the following boundary condition for translation in the $x-$direction:

$$\begin{aligned} \psi(x+b_x,y) &= \psi(x)\exp\left(i2\pi\frac{y}{L_y}\frac{\Phi}{\Phi_0}\right), \\ \psi(x,y+b_y) &= \psi(x). \end{aligned} \tag{4.74}$$

Using the translation invariance condition given by equation 4.72-4.74 the periodic boundary condition can be obtained for each axis. Proceeding in this way for the cell simulation of size $L_x \times L_y$, we have in the x and y direction [57]:

$$\begin{aligned} A_x(L_x,y) &= A_x(0,y), & A_x(x,L_y) &= A_x(x,0), \\ A_y(L_x,y) &= A_y(0,y) + \frac{\Psi}{L_y}, & A_x(x,L_y) &= A_y(x,0), \\ \psi(L_x,y) &= \psi(0,y)\exp\left(i2\pi\frac{y}{L_y}n\right), & \psi(x,L_y) &= \psi(x,0). \end{aligned} \tag{4.75}$$

where n is the total number of flow quanta present in the system, given by $\Phi = n\Phi_0$. The discrete form of the boundary condition for the vector potential components are contained in the discrete form of the link variables. Therefore, in the grid simulation size $N_x \times N_y$ we have:

$$\begin{aligned} U_{x;N_x+1,j,k} &= U_{x;1,j,k}, & U_{x;i,N_y+1,k} &= U_{x;i,1,k}, \\ U_{y;N_x+1,j,k} &= U_{y;1,i,k}\exp\left(i2\pi\frac{n}{N_y}\right) & U_{y;i,N_y+1,k} &= U_{y;i,1,k}, \\ \psi_{N_x+1,j,k} &= \psi_{1,j,k}\exp\left(i2\pi\frac{y}{L_y}n\right), & \psi_{i,N_y+1,k} &= \psi_{i,1,k}. \end{aligned} \tag{4.76}$$

Those are the boundary conditions that make the order parameter and the magnetic field.

4.2.4 Algorithm to solve TDGL

In this work we perform two types of simulations to solve the TDGL equations. In the first, which correspond to field cooled (FC) process the magnetic field is assumed constant and the temperature is varied. On the second the temperature is keepted fixed we set one the magnetic field is varied.

In the first case, we start at $T = T_c$ and with $\psi_0(i,j,k) = 0$ in every grid point, in the FC . Since the magnteic field is constant it is converted to link-variable arrays, $U_x^0(i,j,k)$, $U_y^0(i,j,k)$ and $U_z^0(i,j,k)$ and, upon using the TDGL and the boundary condition, the new order parameter and the link-variables are determined. This process is repeated until a equilibrium state is achieved. The temperatura is decreased by a small temperature interval ΔT and the process is repeated, using as a starting point the equilibrium state obtained previously to obtain the new equilibrium state. That is the time evolution of the equilibrium configurations, at each temperature is obtained.

In the second case, for the fixed temperature, the magnetic field H is ramped up in small intervals of ΔH. The stationary state found for fixed value of H is then used as the initial condition for $H + \Delta H$. For the first value of H the system is initialized at the Meissner state where $\psi_0(i,j,k) = 1$ and $U_x(i,j,k) = U_y(i,j,k) = U_z(i,j,k) = 1$. At each fixed applied field we follow the time evolution of the local magnetic field an the superconducting order parameter until we obtain a steady state solution. Thus, as the applied magnetic field increases and the time changes, we preserve the magnetic history of the system. That is, we study the time evolution of the system at each fixed applied magnetic field.

The stationary state is accepted when the absolute values of the order parameter does not change a certain precision $||\psi_{i,j,k}^{n+1}| - |\psi_{i,j,k}^{n}||$, in some calculation also obtain the precision with the variation of local magnetic field.

In all simulation we choose equally spaced points ($a_x = a_y = a_z$) in space and time Δt. A finite-difference representation of the order parameter is chosen to be $0.25\xi_0$. On average, the step in Δt is approximately 10^{-3}, depending on the grid used, as well as on a specific distribution of the order parameter. This value is aimed at minimization of the number of steps in Δt and, at the same time, keeps the procedure stable. A practical rule for selection of Δt is is given by [58]:

$$\Delta t \leq \min\left\{\frac{\delta^2}{4}, \frac{\beta\delta^2}{4\kappa^2}\right\}, \qquad \text{where} \qquad \delta = \frac{2}{\frac{1}{a_x^2} + \frac{1}{a_y^2} + \frac{1}{a_z^2}}. \tag{4.77}$$

Algorithm used to solve the TDGL Equation

1. `main`

```
2. Initial condition to $\psi^0(i,j,k)$, $U^0_\mu(i,j,k)$

3. for $(H \pm \Delta H)$ or $T - \Delta T$

4. for $t_n + \Delta t$

5. - $\psi(t+\Delta t) = \psi(t) + \Delta t \psi(t)$
   - $j_{sc,\mu}$, $\mu = x, y, z$.
   - $U\mu(t+\Delta t) = U_\mu(t) + \Delta t U_\mu(t)$


6. Calculate the Boundary condition

7. Convergence criterion (Conv)
   $|\psi^{n+1}_{i,j,k}| - |\psi^n_{i,j,k}|$ or $|B^{n+1}_{z:i,j,k}| - |B^n_{z;i,j,k}|$
   if (Conv) is Ok the program continues
   If not return to 5.
   end for $t_n$

8. Calculation The magnetization $-4\pi M$,
   Calculation of induction magnetic field $\boldsymbol{B}$,
   Calculation of $|\psi|^2$

9. end for H or T
```

4.3 The Monte Carlo Method

The Monte Carlo method is, as the name might suggests, a method using probability arguments and random numbers to perform calculations and provide estimates of averages. The whole idea is built around the fact that we can use random numbers to calculate physical properties of systems. More precisely we can calculate physical observables, such as the internal energy and magnetization, using a probabilistic approach. In this thesis, it will be used the so-called classical Metropolis Monte Carlo. The Metropolis Monte Carlo algorithm generates configurations according to the desired statistical mechanics distribution. It allows to study the equilibrium properties of the system. In this method it is not possible to study the time evolution of the system.

Statistical physics provides us tools to calculate physical quantities in terms of average values of the physical observables of interest. A ensemble average of quantity $A(\boldsymbol{r}, \boldsymbol{p})$ can be calculated for a given distribution function $\rho(\boldsymbol{r}, \boldsymbol{p})$ as,

$$\rho(\boldsymbol{r}^N, \boldsymbol{p}^N) = \frac{1}{Z} \exp\left(-\frac{\mathcal{E}(\boldsymbol{r}^N, \boldsymbol{p}^N)}{kT}\right) \tag{4.78}$$

$$\langle A(\boldsymbol{r}^N, \boldsymbol{p}^N)\rangle = \frac{1}{Z} \int A(\boldsymbol{r}^N, \boldsymbol{p}^N) \exp\left(-\frac{\mathcal{E}(\boldsymbol{r}^N, \boldsymbol{p}^N)}{kT}\right) d\boldsymbol{r}^N d\boldsymbol{p}^N \tag{4.79}$$

Energy can always be expressed as a sum of kinetic and potential contributions. The contribution of the kinetic part is trivial and we can consider integral in only configurational 3N dimensional space, where Z is a configurational integral.

$$\langle A(\boldsymbol{r}^N)\rangle = \frac{1}{Z} \int A(\boldsymbol{r}^N) \exp\left(-\frac{U(\boldsymbol{r}^N)}{kT}\right) d\boldsymbol{r}^N, \qquad Z = \int \exp\left(-\frac{U(\boldsymbol{r}^N)}{kT}\right) d\boldsymbol{r}^N \tag{4.80}$$

Statistical-mechanics integrals typically have significant contributions only from very small fractions of the 3N space. For example for hard spheres contributions are coming from the areas of the configurational space where there are no spheres that overlap, see Fig. **??**.

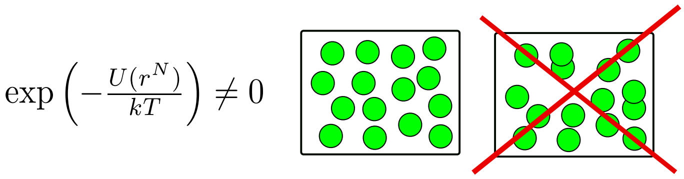

Figure 4-3 : Example of the random sampling of the configuration space.

We have to restrict the sampling to the areas of space contributing to the intergral "**concept of importance sampling**".

4.3.1 Importance sampling: Metropolis Monte Carlo

We can use importance sampling concept and the Monte Carlo method to calculate the ensemble average of a quantity A: Average over measurements of A for configurations generated according to distribution $P(\boldsymbol{r}^N)$ is given by:

$$\langle A(\boldsymbol{r}^N)\rangle = \int A(\boldsymbol{r}^N) \underbrace{\frac{\exp\left(-\frac{U(\boldsymbol{r}^N)}{kT}\right)}{Z}}_{P(\boldsymbol{r}^N)} d\boldsymbol{r}^N, \qquad Z = \int \exp\left(-\frac{U(\boldsymbol{r}^N)}{kT}\right) d\boldsymbol{r}^N. \tag{4.81}$$

To generate configurations according to the desired distribution $P(\boldsymbol{r}^N)$ we can create a random walk process in the phase space, sampling it with the ensemble distribution. This can be realized in different ways. The approach that is used in famous Metropolis Monte Carlo algorithm uses random walk in the phase space with transition probability to go from state m to state n equal to 1 if the move is downhill in energy ($\Delta U_{nm} < 0$). If the move is uphill in energy ($U_{nm} > 0$) than the move is accepted with a probability defined by the ratio of probabilities of initial and final states:

$$\frac{\rho_n}{\rho_m} = \frac{\frac{1}{Z}\exp\left(-\frac{U_n}{kT}\right)}{\frac{1}{Z}\exp\left(-\frac{U_m}{kT}\right)} = \exp\left(-\frac{U_n - U_m}{kT}\right) = \frac{1}{Z}\exp\left(-\frac{U_{nm})}{kT}\right) \tag{4.82}$$

Let us set up a random walk through the configurational space (so-called Markov chain of configurations) by the introduction of a fictitious kinetics. The “time” t is a computer time (reflecting the number of iterations of the procedure), it is not the real time - our statistical system is considered to be in equilibrium, and thus time is irrelevant.

Take $P(m,t)$ as being the probability of finding the system in configuration m at time t, $P(n,t)$ the probability of being in configuration n at time t, and $W(m \to n, t)$ the probability of going from state m to state n per unit time (transition probability). Then we have

$$P(m, t+1) = P(m,t) + \sum_n [W(n \to m)P(n,t) - W(m \to n)P(m,t)]. \tag{4.83}$$

At large t, once the arbitrary initial configuration is “forgotten”, we want $P(m,t)$ to be $P(m)$. Clearly a sufficient (but not necessary) condition for an equilibrium (time independent) probability distribution is the so-called detailed balance condition:

$$W(n \to m)P(n,t) = W(m \to n)P(m,t). \tag{4.84}$$

This can be applied to any probability distribution, but if we choose the Boltzmann distribution we have

$$\frac{W(n \to m)}{W(m \to n)} = \frac{P(n)}{P(m)} = \frac{\frac{1}{Z}\exp\left(\frac{-U_n}{kT}\right)}{\frac{1}{Z}\exp\left(\frac{-U_m}{kT}\right)} = \exp\left(-\frac{U_{nm}}{kT}\right), \qquad U_{mn} = U_n - U_m. \tag{4.85}$$

Z does not appear in this expression. It only involves quantities that we know, T, or can easily calculate, U.

There are many possible choices of the W which will satisfy detailed balance. Each choice would provide a dynamic method of generating an arbitrary probability distribution. Let us make sure that Metropolis algorithm satisfies the detailed balance condition.

$$W(m \to n) = \exp\left(-\frac{U_{mn}}{kT}\right) \qquad U_{nm} > 0, \tag{4.86}$$

$$W(m \to n) = 1 \qquad U_{nm} \leq 0. \tag{4.87}$$

$$\text{if} \qquad U(n) > U(m) \qquad \frac{W(m \to n)}{W(n \to m)} = \frac{\exp\left(-\frac{U_{nm}}{kT}\right)}{1} = \exp\left(-\frac{U_{nm}}{kT}\right) \tag{4.88}$$

$$\text{if} \qquad U(n) < U(m) \qquad \frac{W(m \to n)}{W(n \to m)} = \frac{1}{\exp\left(-\frac{U_{nm}}{kT}\right)} = \exp\left(-\frac{U_{nm}}{kT}\right) \tag{4.89}$$

Thus, the Metropolis Monte Carlo algorithm generates a new configuration n from a previous configuration m so that the transition probability $W(m \to n)$ satisfies the detailed balance condition.

4.3.2 Metropolis Monte Carlo algorithm

1. Choose the initial configuration, calculate energy
2. Make a "move" (e.g., pick a random displacement). Calculate the energy for new "trail" configuration.
3. Decide whether to accept the move:

   If $U_{nm} = U_n - U_m < 0$ then accept the new configuration,

   If $U_{nm} = U_n - U_m > 0$, then calculate $W(m \to n) = \exp\left(-\frac{U_{nm}}{kT}\right)$

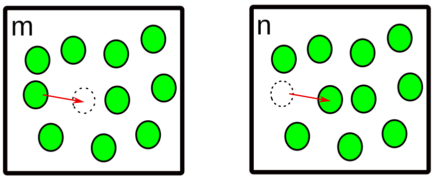

4. Draw a random number R from 0 to 1. If $W(m \to n) > R$ then accept the new configuration, otherwise, stay at the same place.
5. Repeat from step 2, accumulating sums for averages (if particle is retained at its old position, the old configuration is recounted as a new state in the random walk).

5 Between types I and II: Intertype superconductivity-exotic flux states in thin superconductors[a]

This charter presents results of our numerical simulations for thin superconducting films that, in full agreement with the picture of breaking the Bogomolnyi degeneracy, demonstrate the intertype domain with a rich internal structure based on variety of non-standard flux/condensate configurations. In particular, our calculations reveal various lattices of superconducting islands separated by vortex chains, complex patterns of vortex stripes and worms, and mixtures of giant vortices and vortex clusters.

5.1 Introduction

Late discoveries of novel superconducting materials with high critical temperatures (see, e.g., [59, 60]) prompted revisiting many old-standing problems in the field. One of them is the classification of a superconductor taking into account it magnetic properties. As is well-known [31, 61, 62], the Ginzburg-Landau (GL) theory distinguishes superconductors of ideally diamagnetic type I and of type II, where the field penetrates the condensate as a regular lattice of Abrikosov single-quantum vortices. Which of the types is realized depends on the GL parameter $\kappa = \lambda/\xi$, with λ and ξ being, respectively, the magnetic penetration depth and the GL coherence length. The types interchange abruptly when κ crosses the critical value $\kappa_0 = 1/\sqrt{2}$.

As was shown already in one 1970's, the reality is more complex than what follows from the GL theory (see [39, 63–67] and references therein): the picture of the superconductivity types separated by the single point $\kappa_0 = 1/\sqrt{2}$ applies only in the limit $T \to T_c$. Below T_c the intertype regime occupies a finite interval of κ's, forming the intertype domain between types I and II in the (κ, T)-plain [39]. This domain exhibits a non-conventional field dependence of the magnetization, in particular, the first order phase transition between the Meissner and the mixed state [39, 63]. Subsequent works revealed that the physics of the inter-type domain is closely related to the Bogomolnyi self-duality [19, 20] that results in an infinite degeneracy

---

[a] Contains material published in the paper [91].

of the superconducting state at the Bogomolnyi point (κ_0, T_c), see, e.g., [68]. This degeneracy follows from the symmetry of the GL equations at κ_0 and implies that the mixed state has an infinite number of possible spatial configurations of the magnetic flux, including very exotic ones (here referred to as "exotic flux states"). When the degeneracy is lifted, for example, by lowering the temperature, it is possible to expect that the exotic flux states break out of the Bogomolnyi-point "prison" and spread over the finite IT domain in the phase diagram, shaping the domain internal structure.

A comprehensive investigation of possible flux/condensate configurations in the IT domain has not been presented so far. The related theoretical study for bulk materials requires an approach beyond the GL theory that is technically very demanding, see, e.g., [65, 69]. The corresponding experimental study is also rather nontrivial because one should change κ by an appropriate doping in order to cross the intertype domain in the (κ, T)-plane [39, 63]. To date, only the appearance of a long-range attraction between Abrikosov vortices has been investigated in detail, see, e.g., [67]. Such an attraction is often regarded as the main characteristic of the intertype regime which is then referred to as type II/1 [39], as opposed to the standard type-II with repulsive Abrikosov vortices. Few interesting theoretical works [69–71] considered giant (multi-quantum) vortices in single- and multi-band superconductors with $\kappa \sim 1$ but decisive conclusions on their stability cannot be made based on the current theoretical evidence.

The intertype domain can also be found in superconducting films. Here the Bogomolnyi-point degeneracy is removed due to non-local interactions via stray magnetic fields outside superconducting samples. It has long been known [4–6] that very thin superconductors made of a type-I material demonstrate type-II properties in the presence of a perpendicular magnetic field. This behavior can be explained by recalling that the vortex-vortex interaction has two contributions of opposite signs: one of them is due to the magnetic field and the other comes from the condensate [61]. In bulk type-I materials the condensate contribution is dominant and the resulting vortex interaction is attractive. However, as the film thickness w decreases, the contribution due to stray magnetic fields grows, and finally the interaction becomes repulsive. The thickness is, therefore, a parameter that can be used to gradually drive the system from type-I to type-II by passing through the intertype domain in the (w, T)-plane. However, contrary to the (κ, T)-plane, here the intertype domain does not collapse into a single point at $T \to T_c$. Indeed, unlike bulk materials, the intertype regime for thin films can be at least qualitatively described by the GL theory amended with the equations for the stray fields. The reason is that here the degeneracy is removed mainly by the stray field contribution and thus the non-local condensate interactions beyond the realm of the GL theory (responsible for lifting the Bogomolnyi-point degeneracy in bulk) can be safely neglected if the temperature is not so low.

We note that solving the GL formalism for thin films is much more technically demanding than in bulk: the appearance of stray fields makes the problem three-dimensional. Experiments with thin films are also challenging because results are often invalidated by structural imperfections. [Superconducting films with an atomically uniform thickness have been produced only recently, see the review in Ref. [72].] Thought the appearance of the intertype domain was demonstrated by solving the linearized GL equations [73], subsequent studies of the full GL formalism [74, 75] did not confirm the predictions of the linearized theory about a honeycomb lattice of multi-quantum vortices. In particular, the authors of [74] found that the double-fluxoid lattices never preempt the single-fluxoid lattice in thin films. Calculations in [75] suggested that a mixture of different multi-quantum vortices (two-quantum, three-quantum etc.) can be stable but does not exhibit any well-defined periodic lattice. There are experimental signatures of multi-quantum vortices reported for thin films previously [76, 77] but these results are questionable due to structural imperfections of the samples unavoidable at that time. Thus, until now the existence of the intertype plethora of non-standard flux configurations has been unambiguously confirmed (theoretically and experimentally) neither in bulk superconductors nor in thin superconducting films.

5.2 Formalism

Our calculations are done for a superconducting film (slab) of a type-I material, placed parallel to the (x, y)-plane so that the material fills interval $z \in [-w/2, w/2]$. The superconducting order parameter Ψ and the vector potential $\boldsymbol{A}$ are governed by the GL equations, which in the standard dimensionless units (see, e.g., [78]) writes as

$$(-i\boldsymbol{\nabla} - \boldsymbol{A})^2\,\Psi - (1-T)(1-|\Psi|^2)\Psi = 0, \tag{5.1}$$

$$\kappa^2\boldsymbol{\nabla}\times\boldsymbol{\nabla}\times\boldsymbol{A} = (1-T)\Re\left[\Psi^*\left(-i\boldsymbol{\nabla} - \boldsymbol{A}\right)\Psi\right], \tag{5.2}$$

where $\boldsymbol{\nabla}$ is the gradient operator and the order parameter is assumed to be zero outside the slab. We use the standard boundary conditions demanding zero current through the slab boundary, which implies

$$\hat{\boldsymbol{z}}\cdot\left(i\boldsymbol{\nabla} + \boldsymbol{A}\right)\Psi\Big|_{z=\pm w/2} = 0, \tag{5.3}$$

with $\hat{\boldsymbol{z}}$ being the unit vector of the z-axis. In addition, the magnetic field satisfies the standard field-continuity conditions on the superconductor surface. We assume that the field becomes uniform at infinity, i.e.,

$$\boldsymbol{\nabla}\times\boldsymbol{A}\Big|_{z\to\pm\infty} = \mathbf{H}, \tag{5.4}$$

with $\mathbf{H} = (0, 0, H)$ (H is constant) being parallel to the z-axis. The model defined by Eqs. (5.1) - (5.4) depends on four parameters κ, T, w and H. In practical calculations the condition in Eq. (5.4) is defined at $z = \pm L_z$, and the problem is solved inside a square unit cell $0 \leq x, y \leq L$ with the in-plane periodic boundary conditions [79]. The values of L_z and L are chosen sufficiently large not to affect the results.

The solution to the model equations is obtained using the standard method of the auxiliary time dependence, in which the GL equations become time-dependent by adding the first-order time derivative term to simulate the decaying time evolution that converges to the solution of the original stationary GL theory. The modified equations are then solved by the link-variable approach [80]. The complete numerical procedure also utilizes the so-called "field cooling" algorithm, where one starts from the normal state at $T = T_c$ and then gradually decreases the temperature while keeping the magnetic field fixed; the equilibrium configuration obtained for the previous temperature step is used as the initial condition for the next step.

5.3 Intertype Exotic States

The obtained results are qualitatively similar for all values of κ as long as they correspond to a type-I material (we considered $\kappa = 0.4$ - 0.6). Spatial configurations of the absolute value of the order parameter shown in Figs. **5-1** and **5-2** are calculated for $\kappa = 0.55$, $L = 50\xi_0$ and $L_z = w/2 + 5\xi_0$, where ξ_0 is the GL coherence length at zero temperature. Our grid cell size is $0.25\xi_0$. For the obtained results we do not use any extrapolation or averaging. The external magnetic field is set as $H = 90\Phi_0/L^2$, with Φ_0 being the flux quantum. Another choice, namely, $H = 60\Phi_0/L^2$, yielded the same structure of the inter-type domain.

The results given in the upper and lower sets of panels in Fig. **5-1** are obtained for relatively thick, $w/\xi_0 = 20$, and thin, $w/\xi_0 = 2$, samples, respectively, and calculated for the central plane $z = 0$. The upper panels demonstrate intermediate states (the laminar structure) typical of type-I superconductors, where the Meissner superconducting S-phase (red) coexists with, but is spatially separated from, the normal N-phase (blue). Notice, that the geometry of the system bans the uniform Meissner S-phase since the total magnetic flux is non-zero. The obtained configurations tend to have a minimal $S - N$ interface area reflecting positive surface energy of the interface. Such type-I configurations in relatively thick films are dictated by a type-I material of the film.

The type-II configurations, shown in the lower panels of Fig. **5-1**, appear in very thin films where the repulsive interaction due to the stray fields overweighs the vortex-vortex attraction of the type-I material [4–6]). The surface energy of $S - N$ interfaces becomes negative, favoring a configuration with the maximal interface area, i.e., a triangular lattice of Abrikosov

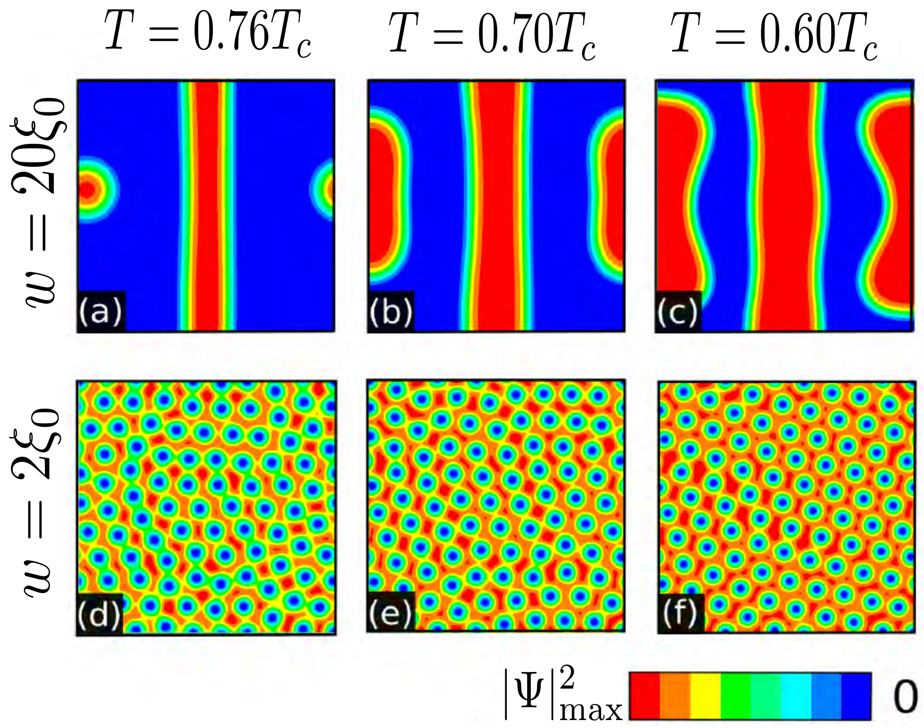

Figure 5-1 : The local density of Cooper pairs $|\Psi|^2$ in films with thicknesses $w/\xi_0 = 20$ [panels (a), (b) and (c)] and $w/\xi_0 = 2$ [panels (d), (e) and (f)], calculated at temperatures $T/T_c = 0.76, 0.7, 0.6$. Other parameters are given in the text.

vortices [31, 61, 62]. This lattice is clearly seen in panel (f) of Fig. **5-1** that corresponds to $T/T_c = 0.6$. A visible lattice distortion at larger temperatures is a consequence of a slow convergence of the numerical procedure when the superconducting state approaches the point of the normal-superconducting transition. In this regime the minimum of the energy functional is very flat and the convergence time of the "field cooling" algorithm increases significantly (it diverges at the transition point). Notice that at $T/T_c = 0.76$ and $w/\xi_0 = 2$ the chosen external magnetic field $H = 90\Phi_0/L^2$ is close to the upper critical field as the superconducting solution decays at $T/T_c > 0.77$. For clear comparison of our results for different thicknesses, all the data in Figs. **5-1** and **5-2** are also shown below $T/T_c = 0.76$.

Contrary to Fig. **5-1**, Fig. **5-2** demonstrates quite exotic flux configurations. In particular, one can see a rich variety of exotic flux states that appear in the mixed state of films with

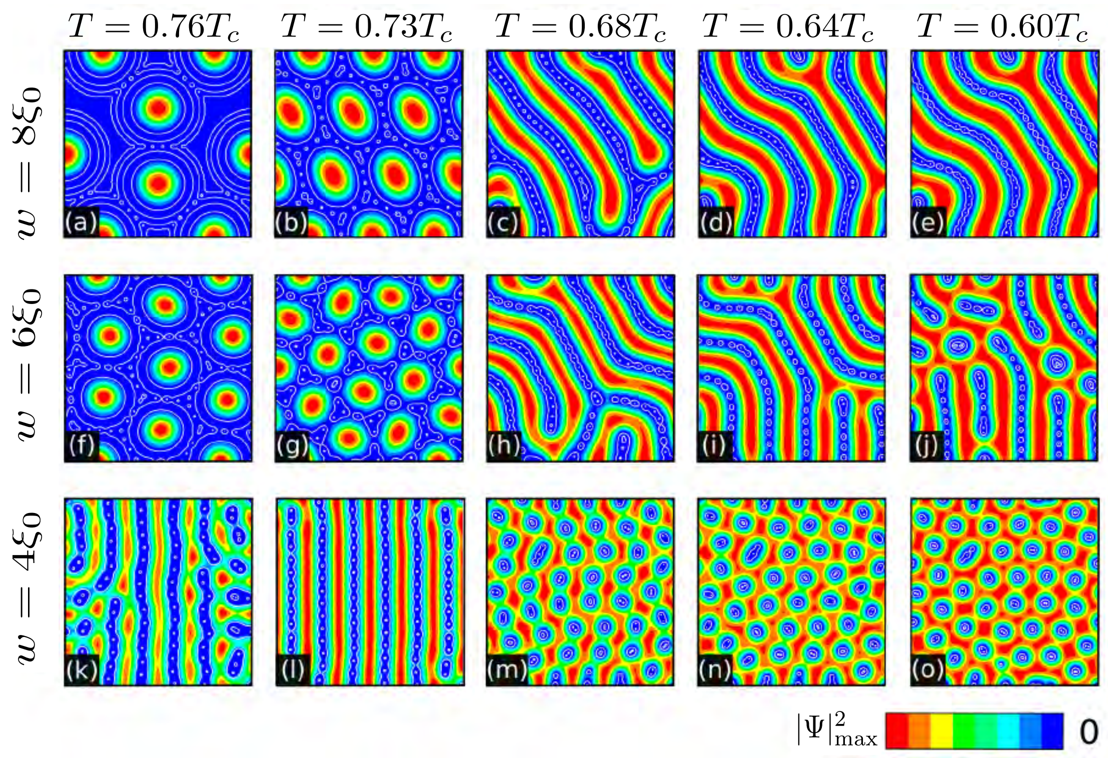

Figure 5-2 : The local density of Cooper pairs $|\Psi|^2$ for film thicknesses $w/\xi_0 = 8$ [panels (a) - (e)], $w/\xi_0 = 6$ [panels (f) - (j)], and $w/\xi_0 = 4$ [panels (k) - (o)], calculated at temperatures $T/T_c = 0.76, 0.73, 0.68, 0.64, 0.6$. Other parameters are the same as in Fig. **5-1**.

thicknesses in the interval $4 \lesssim w/\xi_0 \lesssim 8$. [Again the results for the central plane $z = 0$ are given.] For films with $w/\xi_0 = 6$ and 8, at higher temperatures, one can see superconducting islands arranged in a periodic triangular lattice and separated by chains of single-quantum vortices [panels (a), (b), (f) and (g) in Fig. **5-2**].

Vortices are represented by white small empty circles in the blue background. Their identification is supported by checking the phase twist of the order parameter. For example, in Fig. **5-3**-(a) one can see two panels: the left one represents the phase of the superconducting order parameter while the right panel gives its amplitude for one of the island patterns. In the left panel one can see the blue and red stripes: when crossing the blue or red stripes, the phase of the order parameter changes by $\pi/2$. As seen from the figure, each vortex is a junction of four such stripes, i.e., the phase twist around the vortex center is 2π. Vortices can be observed in Figs. **5-2**-(b),(f),(g)(and also in the right panel of Fig. **5-3**-(a)) as small white (black in Fig. **5-3**-(a)) circles in the blue background. Though the order parameter is suppressed there it is not exactly equal to zero. However, in Fig. **5-2**-(a) vortices can be seen between superconducting islands only when the islands are in a close proximity to each other (otherwise the order parameter becomes negligible). This explanations concerning the vortex structure around the superconducting islands are indeed necessary and the same is related to the stripe/worm patterns.

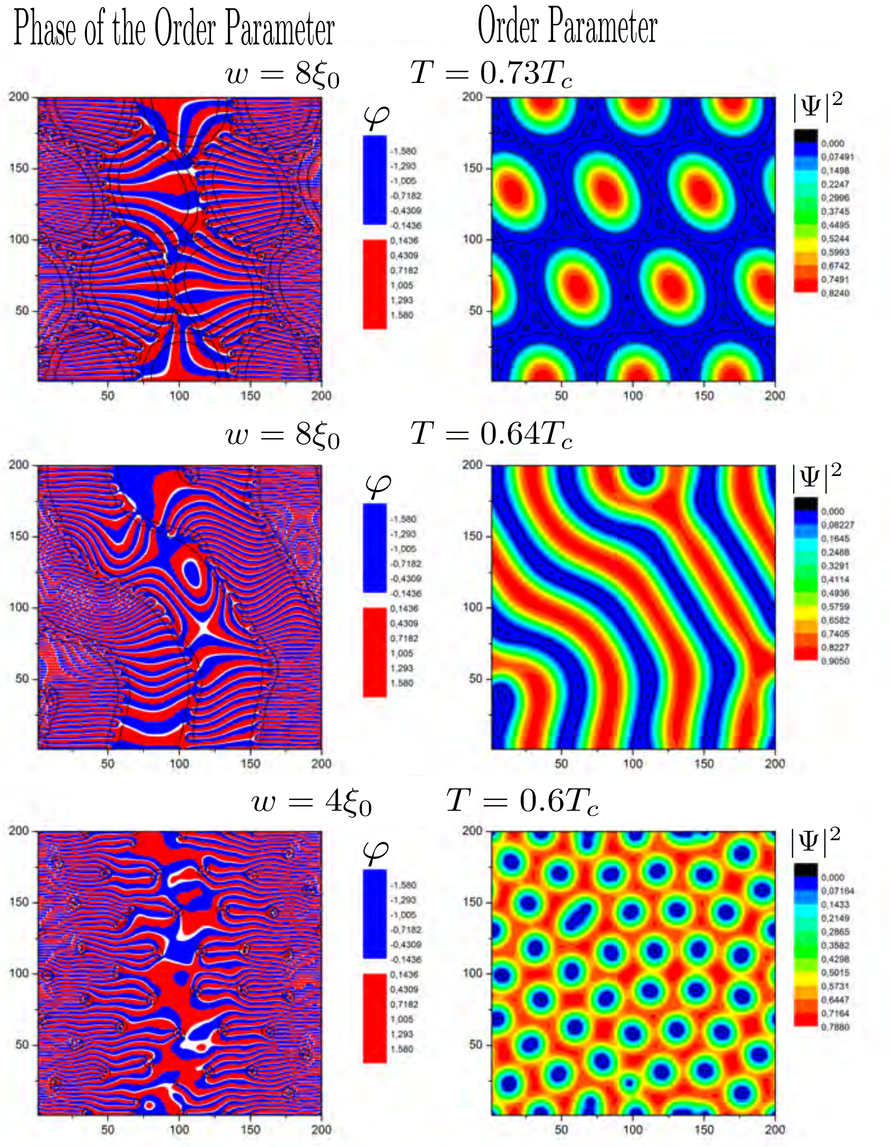

Figure 5-3 : The spatially-dependent phase and amplitude of the order parameter for island, stripes and multi-quantum vortices patterns.

The shape and size of the islands change visibly with the temperature. For example, in panels (a) and (f) of Fig. **5-2** the islands are almost perfectly circular while in panels (b) and (g) they tend to become elliptic. One can also see that the distance between islands decreases at lower temperatures, which makes the separating chains of vortices more visible. At $T/T_c \sim 0.7$ the island pattern abruptly disappears: the superconducting islands merge in the condensate stripes while the vortex honey-comb chain changes to stripes/worms of vortices. Whether such an island-stripe transformation is a phase transition is unclear at this stage.

When the temperature is lowered further, stripes of single-quantum vortices break into vortex clusters and then the cluster constituents merge into multi-quantum vortices (as supported by the analysis of the order-parameter phase portraits (see Fig. **5-3**-(b),(c))). The temperature of this crossover depends on the film thickness: for $w/\xi_0 = 6$, it occurs at $T/T_c \sim 0.6$, while for $w/\xi_0 = 4$ it takes place at $T/T_c \sim 0.7$. We note that for $w/\xi_0 = 8$ a similar crossover happens at $T/T_c = 0.5$. However, the corresponding panel is not shown in Fig. **5-2** for the reason that the validity of the GL theory is typically restricted to temperatures $T/T_c \gtrsim 0.6$ - 0.7, although in some cases its qualitative predictions still hold down to lower temperatures. As is seen, mixtures of different giant vortices and vortex clusters in Fig. **5-2** do not form well-defined periodic lattices, which agrees with the results calculated for low magnetic fields (as compared to the upper critical field) in [75]. Notice that we reach the low-field regime when decreasing the temperature (as the upper critical field grows).

Comparing results for different T and w in Fig. **5-2**, one notices a general trend: for thinner films the qualitative transformations of the intertype patterns are shifted to larger temperatures. For example, for $w/\xi_0 = 8$ and 6 the stripe/worm configurations are stable below $T/T_c \sim 0.7$ [see panels (c), (d), (e) and (h), (i), (j)] while for $w = 4\xi_0$ the stripe/worm configuration appears already at $T/T_c = 0.76$ [panels (k) and (l)]. Similarly, for $w = 6\xi_0$ the stripes/worms start to break into vortex clusters and giant vortices at $T/T_c \sim 0.6$ while for $w = 4\xi_0$ it happens at $T/T_c \sim 0.7$, compare panels (j) and (m). Finally, we note that vortex clusters and multi-quantum vortices becomes smaller in thinner films, tending to form a periodic triangular lattice (thus approaching type-II).

As already mentioned above, our calculations for other values of the system parameters yield the same qualitative results: similar patterns of islands, stripes and multi-quantum vortices/vortex clusters as well as their temperature transformations are observed if one takes other κ and H. The results can be summarized in the form of the schematic phase diagram in the (w, T)-plane shown in Fig. **5-4**. Types-I and type-II exist, respectively, at large $w > w_I$ and small $w < w_{II}$ film thicknesses (for simplicity the temperature dependencies of the boundaries w_I and w_{II} are neglected). The intertype regime takes place for $w_{II} < w < w_I$, where one finds the non-conventional flux/condensate configurations discussed above, i.e., superconducting islands surrounded by vortex chains; stripes/worms of vortices separating condensate stripes; and mixtures of giant vortices and vortex clusters. When the system approaches the lower boundary of the inter-type domain, multi-quantum vortices and vortex clusters get smaller, their spatial distribution becomes more regular, until finally single-quantum (Abrikosov) vortices arranged in Abrikosov lattices appear. Close to the upper boundary of the inter-type domain vortices gradually disappear and we arrive at lamellas of type-I.

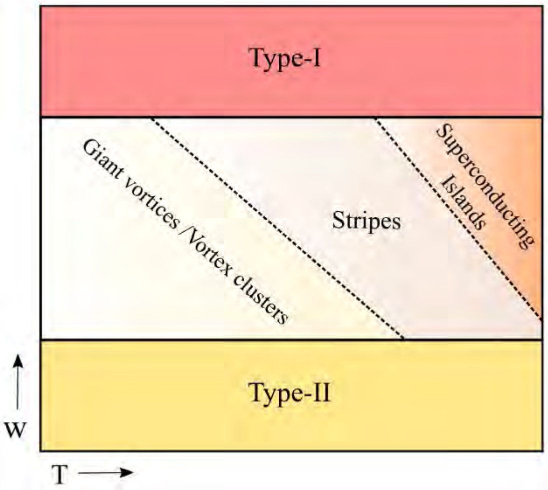

Figure 5-4 : A schematic phase diagram of thin film superconductors: a qualitative summary of the results of Figs. (**5-1**) and (**5-2**). Type I and II are found at $w > w_I$ and $w > w_{II}$ (T-dependence of boundaries w_I, w_{II} is neglected for the sake of simplicity). The inter-type domain $w_{II} < w < w_I$ is divided into subdomains with distinguished non-standard flux patterns: superconducting islands separated by vortex chains; vortex stripes/worms that separate condensate stripes; and mixtures of giant vortices and vortex clusters.

After having raised the phase diagram discussed above, we decided to properly build this and show the different phases present and already discussed, and also build the phase diagram when $H = 60\Phi_0/L^2$. These diagrams are presented in the Fig. **5-5** [$H = 90\Phi_0/L^2$] and Fig. **5-6** [$H = 60\Phi_0/L^2$]. It can be observed that for the lower field and for $w \leqslant 8\xi_0$ the giant vortex and cluster phases are favored. Also there is a growth of the superconducting island and laminar phases. On the other hand the laminar structure phase is not found for $w \leqslant 20\xi_0$ to find a type-I behavior it is necessary to go beyond this thickness.

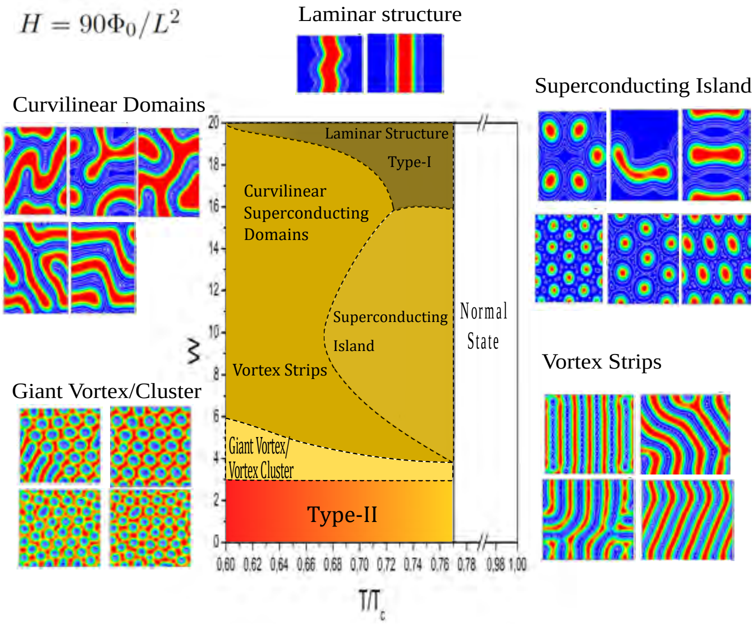

Figure 5-5 : Phase diagram of thin film superconductors in the $(w - T)$-plane, for external magnetic field $H = 90\Phi_0/L^2$ and representative patterns corresponding to each phase

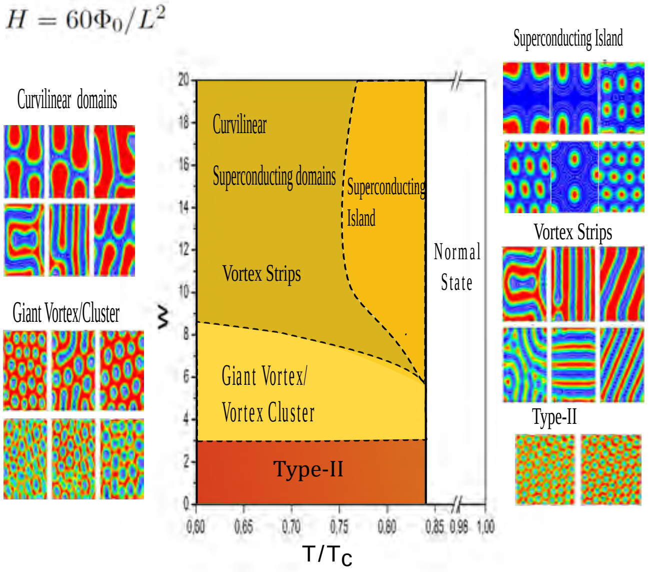

Figure 5-6 : Phase diagram of thin film superconductors in the $(w - T)$-plane, for external magnetic field $H = 60\Phi_0/L^2$ and representative patterns corresponding to each phase.

5.4 Intertype in a Rectangular Sample

In order to to study the effect of the sample geommetry we decide to study the intertype domain in a retangular parallelepiped, as shown in Fig. **5-7**, where the superconducting sample is a rectangular parallelepiped with thickness w and lateral sizes $a = 50\xi_0$ and $b = 75\xi_0$. The interface between the sample and the vacuum is large enough to consider the effects of demagnetization and stray field, ($\Delta L = 10\xi_0$). Also in this calculations we assume the superconductor material has $\kappa = 0.55$ (type-I in bulk superconductor). The superconductor is submitted to an uniform perpendicular magnetic field $\boldsymbol{H} = (0, 0, H)$. Since presence of the superconductor will modify the profile of the local magnetic field near the edges. ΔL is taken sufficiently large such that the local magnetic field equals the external applied magnetic field $\boldsymbol{H}$ at $w + \Delta L$.

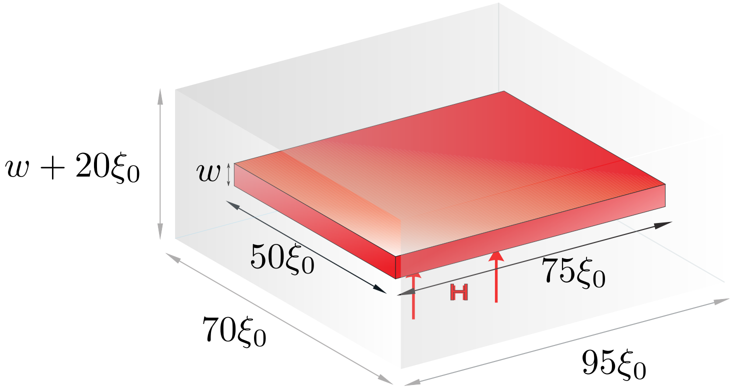

Figure 5-7 : Layout of the studied sample: thin film superconducting rectangle submitted to a perpendicular a magnetic field.

The TDGL equations (5.1) and (5.2) are solved, with the boundary condition

$$\hat{\boldsymbol{n}} \cdot (i\boldsymbol{\nabla} + \boldsymbol{A})\,\Psi\Big|_{\partial\Omega_{sc}} = 0, \tag{5.5}$$

$$\boldsymbol{\nabla} \times \boldsymbol{A} = \mathbf{H}. \tag{5.6}$$

It is also imposed that the current density does not flow out of the superconductor into the vacuum. This means that the perpendicular component of $\boldsymbol{j}_s$ vanishes at the surface. Let us denote by $\hat{n}$ the unit vector outward normal to the superconductor-vacuum interface.

The superconducting film thickness was taken as $w = 6\xi_0$ and a field cooling process was done for each H value. Figures **5-8**(a)-(h) show the flux patterns obtained when the temperature $T = 0.7T_c$. At low fields, the sample is in the Meissner state with no flux observed Fig. **5-8**(a). By increasing the magnetic field(H =0.032$H_c(0)$), the magnetic flux begins to penetrate into the sample in form of single vortex Fig. **5-8**(b). A further increase of the field, some of vortex merge into giant vortex, there is a coexistence of single vortex and giant vortex Fig. **5-8**(c) typical of the intertype superconductivity. At $H = 0.093H_c(0)$ vortex cluster are formed Fig. **5-8**(d). When the magnetic field reaches $H = 0.14H_c(0)$ clusters start to merge and form normal domain stripes, resulting in a configuration with the coexistence of cluster and stripes Fig. **5-8**(e). For higher field, as show in Fig. **5-8**(g)-(h), once it become favorable

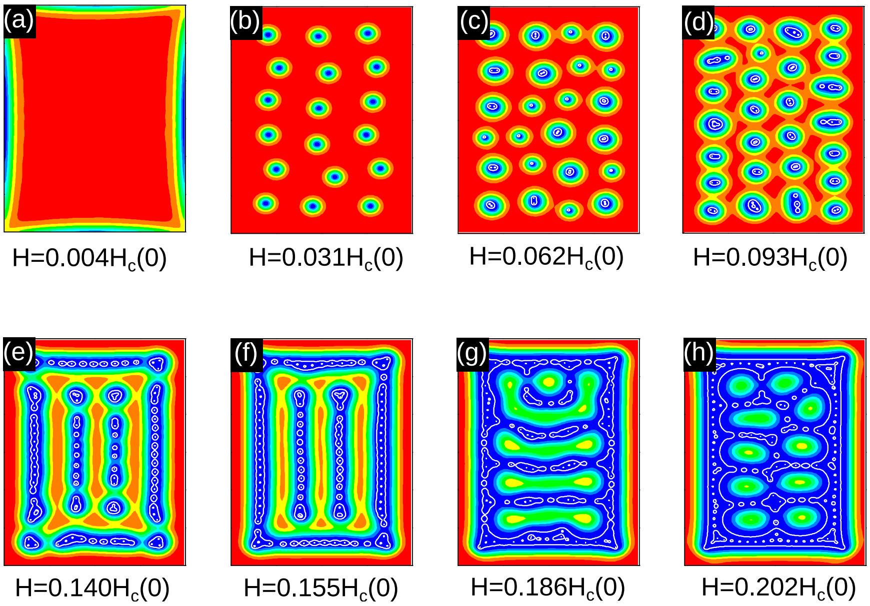

$H=0.004H_c(0)$ $H=0.031H_c(0)$ $H=0.062H_c(0)$ $H=0.093H_c(0)$

$H=0.140H_c(0)$ $H=0.155H_c(0)$ $H=0.186H_c(0)$ $H=0.202H_c(0)$

Figure 5-8 : Flux patters for rectangular parallelepiped superconductor with thickness $w = 6\xi_0$, calculated for differents $\boldsymbol{H}$ at $T = 0.7T_c$

for the system to form superconducting island (small regions where only superconductivity prevails), they thrive as the magnetic field increases, resulting in the formation of small domains of superconductivity, which eventuality merge to form wider normal domains that cover almost all the superconductor until only having surface superconductivity which is formed before the system transits to the normal state.

Notice that the ground state flux structures in thin films type-I superconductors do not depend only on the applied magnetic field, but also on the confinement due of the finite size of the sample. In a superconducting sample, with rectangular symmetry, in the intertype superconductor regime, the flux structures are not preserved [81] as in the case of samples with squared symmetry [82], as a consequence of confinement.

6 Quasi-One-Dimensional Vortex Matter in Superconducting Nanowires[a]

It is well-known that superconducting films made of a type-I material can demonstrate a type-II magnetic response, developing stable vortex configurations in a perpendicular magnetic field. In this chapter we show that the superconducting state of a type-I nanowire undergoes more complex transformations, depending on the nanowire thickness. Sufficiently thin nanowires deviate from type-I and develop multi-quantum vortices and vortex clusters similar to intertype (IT) vortex states in bulk superconductors between conventional superconductivity types I and II. When the nanowire thickness decreases further, the quasi-one dimensional vortex matter evolves towards type II so that the IT vortex configurations gradually disappear in favour of the standard Abrikosov lattice (chain) of single-quantum vortices. However, type II is not reached. Instead, an ultrathin nanowire re-enters abruptly the type-I regime while vortices tend to be suppressed by the boundaries, eventually becoming one-dimensional phase-slip centers.

6.1 Introduction

Low dimensional superconductors attract significant interest due to a tantalising possibility to manipulate their properties by varying the sample geometry. A prospective example is recently fabricated arrays of superconducting nanowires (see, for instance, Refs. [83–89]) produced, e.g., by electrochemical deposition of a metal in a nanoporous insulating matrix or by the focused ion beams (FIB) lithography. Dimensional parameters of such a composite superconducting material are controlled with high precision. As a result, one can tune the superconducting magnetic response that is a cornerstone characteristic of superconductors for their applications.

In particular, when a superconducting film made of a type-I material becomes sufficiently thin it can develop stable vortex configurations in a perpendicular magnetic field [4–6], becoming a type-II superconductor. This type interchange takes place due to a stray magnetic field

---

[a] Contains material from the manuscript: Quasi-One-Dimensional Vortex Matter in Superconducting Nanowires

that introduces repulsion between initially attractive (and thus unstable) vortices. Extrapolating results for superconducting films to the case of a nanowire made of a type-I material in a perpendicular magnetic field, one expects that it can also become a type-II superconductor. Recent experiments [86] have indeed demonstrated that the magnetisation of an array of superconducting nanowires changes notably when the wire thickness decreases. However, interpreting these changes is not straightforward. Indeed, extrapolating results for films must be taken with care. Nanowires are quasi-1D objects, where the condensate and its possible vortex-matter state are inevitably affected by the confining potential of the boundaries. If the boundary effects overcome the stray field influence, one can expect that a nanowire made of a type-I material remains a type-I superconductor irrespective of its thickness. Which of these factors actually dominates and whether a superconductivity type interchange can be observed in thin superconducting wires has not been investigated to date.

The present work fills this gap by studying the magnetic response of a single superconducting nanowire made of a type-I material. Our study demonstrates that sufficiently thin nanowires develop the mixed state in a perpendicular magnetic field. However, the related quasi-1D vortex matter is shown to exhibit vortex clusters and multi-quantum vortices that are found in neither type-II nor in type-I but similar to IT vortex configurations in bulk superconductors [69, 90, 91]. When the nanowire thickness decreases further, vortices tend to arrange themselves in a regular chain (1D Abrikosov lattice) so that the system evolves towards type-II. However, due to the 1D character of the sample, the type-II magnetic response is not reached. Instead, ultrathin nanowires re-enter the type-I regime: vortices become 1D phase-slip centres typical for 1D weak superconducting links [92] and are then expelled from the wire. We stress that our work differs fundamentally from earlier studies of the geometry related effects in small superconducting samples where vortices are confined in all dimensions and the geometry forces them to merge into clusters or multi-quantum vortices. In contrast here the nanowire is assumed infinite (very long), vortices are not confined along it and thus the appearance of nonstandard IT configurations such as vortex clusters is not simply induced by the interaction with the boundaries.

6.2 Method and model

Our analysis is done on the basis of the GL theory. Although this approach cannot explain a finite IT domain in bulk superconductors [69], it is sufficient for systems where the Bogomolnyi degeneracy is lifted due to geometry-related factors, as in the case of thin films, see Ref. [91] for a detailed discussion.

In the calculations we assume that a nanowire is in the form of a slab of the length L (in the

z direction) and with the square cross section $d \times d$ (in the x and y directions), see Fig **6-1**. The boundary condition for the order parameter Ψ on the wire surface is $[\mathbf{n} \cdot (-i\hbar\nabla - 2e\mathbf{A}/c)]\Psi = 0$, where $\mathbf{A}$ is the vector potential whose curl is the magnetic field $\mathbf{B} = \boldsymbol{\nabla} \times \mathbf{A}$, and $\mathbf{n}$ is the unit vector perpendicular to the surface. We consider that $L \gg d$ and use the periodic boundary conditions with period L in the z direction for both Ψ and $\mathbf{B}$. The nanowire is placed in the perpendicular external homogeneous magnetic field $\mathbf{H} = (H, 0, 0)$, which implies an asymptotic condition $\mathbf{B} \to \mathbf{H}$ at infinity. In the calculations this condition is fulfilled on a surface of a larger embedding slab, also with the square cross section, with the surface located at distance $\Delta L = 10$ from the wire (hereafter all distances are given in the units of the bulk Cooper pair size ξ_0).

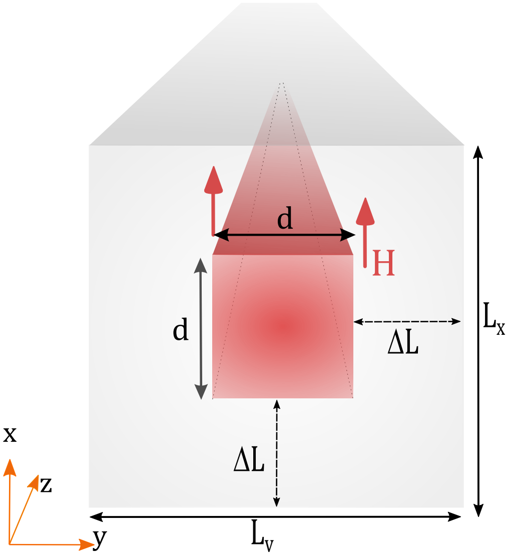

Figure 6-1 : Layout of the studied sample: nanowire is in the form of a slab of the length L and with the square cross section $d \times d$ (in the x and y directions). The nanowire is placed in the perpendicular external homogeneous magneic field

The GL equations for Ψ and $\mathbf{A}$ are solved using a standard method of auxiliary time dependence, where the time dependence is introduced by adding the first-order time derivatives of Ψ and $\mathbf{A}$ in the equations, such that the solution converges to the stationary point at sufficiently large times. The resulting time-dependent equations are solved by using the link variable method [80, 91].

The dimensionless GL equations for a nanowire depend on just two parameters: the GL parameter of the material $\kappa = \lambda/\xi$ (the ratio between the bulk GL coherence and magnetic lengths) and the nanowire thickness d. We choose $\kappa = 0.55$ which corresponds to a type-I material. This particular choice of κ is not essential as the results are qualitatively similar for any type-I material with $\kappa < 1/\sqrt{2}$. For this value of κ the main changes in the magnetic response take place when $d < 50$ and so we focus on this thickness interval. For clean superconductors with large bulk ξ_0 the length $d = 50$ can go far beyond the nanoscale. However, in practice the electronic mean free path, which is $\sim d$ [93], significantly reduces ξ_0 so that changes of the magnetic response are expected for the nanosize wires [86]. The external field is varied in the interval $0 < H < 0.5H_c(0)$, where $H_c(0)$ is the bulk thermodynamic critical field at zero temperature. To investigate the hysteresis in the magnetisation, the calculations are done for the ascending and descending magnetic field. Finally, we assume $T = 0.7T_c$, where the GL theory is still applicable.

6.3 Results

A summary of the results is shown in Figs. **6-2**, **6-3**and **6-4**. Magnetisation curves (the volume averaged value of $-4\pi M$ as a function of H), shown in panels (i) to (vi), correspond to the wire thicknesses $d = 50$, 20, 15, 10, 8 and 5, respectively correspondingly. The upper magnetisation curve (red circles) illustrates the ascending field case, the lower curve (blue circles) is the magnetisation for descending field. The color density plots below each panel show the spatial distribution of $|\Psi|^2$ in the center cross section plane of the slab perpendicular to the applied magnetic field, calculated for different representative points shown on the magnetisation curve.

Figure **6-2**(i) demonstrates results for a relatively thick wire with $d = 50$. Considering the ascending field magnetisation curve together with the corresponding profiles of $|\Psi|^2$, one notes that the field does not enter the wire until the magnetisation starts to decrease. This is a clear signature of the Meissner state. A decrease in $-4\pi M(H)$ indicates that the field penetrates the sample, where it forms the well-known intermediate state of type-I superconductors [18,31,94] with coexisting stratified normal and superconducting phases [see “b”,“c”, “d”, and “e” in Fig. **6-2**(i)]. The field occupies first the vicinity of the boundaries [see “b” in Fig. **6-2**(i)], and then creates bubbles of the normal phase inside the superconducting condensate [see “c” in Fig. **6-2**(i)]. The bubbles grow in size with increasing the field and then merge into a stripe, producing alternating normal and superconducting lamellas, see “d” in Fig. **6-2**(i). Finally, the normal phase occupies almost the entire volume of the wire and superconductivity survives only near the boundaries [the surface superconductivity, see “e” and “f” in Fig. **6-2**(i)]. Here lamellas are observed due to finite dimensions of the system. As the result, the magnetisation does not drop to zero abruptly, as expected for type I in bulk but decreases gradually like in type-II materials.

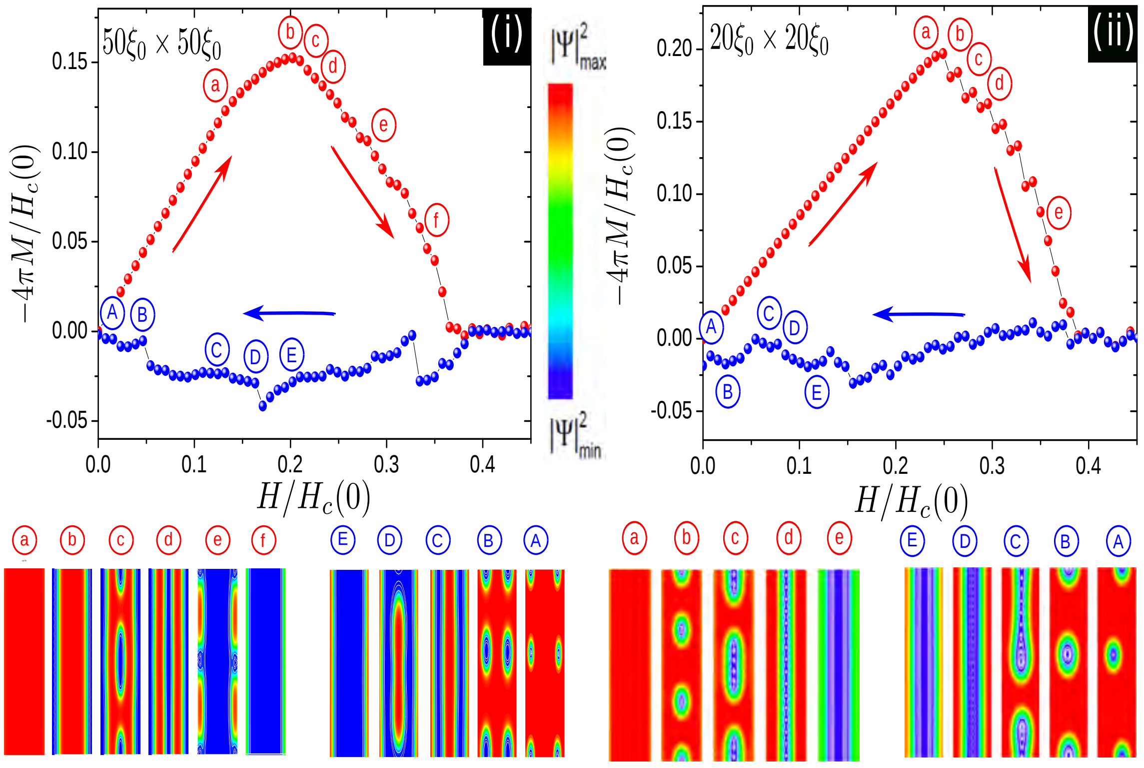

Figure 6-2 : Magnetization M as a function of applied magnetic field H is plotted for increasing (red points) and decreasing (blue points) field is calculated for wires of different crossection with $L_{x,y} = 50\xi_0$, $20\xi_0$. The field H as well as M are expressed in the units of the thermodynamic bulk critical field $H_c(0)$ at zero temperature. Density colour plots below magnetization panels illustrate the order parameter profiles, that correspond to points in the magnetization curve. Points denoted by small red letters $a, b, c\dots$ are found on the ascending field curve and points denoted by capital letters $A, B, C, \dots$ are on the descending field curve. All calculations are done at temperature $T = 0.7T_c$.

The descending-field magnetisation [blue curve in Fig. **6-2**(i)] has a different sign (i.e., a paramagnetic response) and a much smaller absolute value. This is a hysteretic behaviour, which takes place due to trapping of the magnetic flux inside the nanowire. For the descending field the intermediate state undergoes a similar sequence of patterns, however, in the reverse order as compared to the ascending field case [cf. “a” - “f” and “A” - “E” in Fig. **6-2**(i)]. We note that for $d = 50$ the spatial field/condensate configurations has an effectively 2D character: the nanowire can accommodate more than one normal state bubble or stripe in its perpendicular direction [see “c”, “d”, “A” and “B” in Fig. **6-2**(i)]. It is also worth noting that when the field decreases, bubbles of the normal phase survive even in the limit $H \to 0$ due to the flux trapping, i.e., the system remains in a paramagnetic state at zero external field.

A wire with $d = 20$ is no longer a type-I superconductor, as seen from Fig. **6-2** (ii). Here, similarly to Fig. **6-2**(i), the interval on the ascending field curve (red) with increasing $-4\pi M$ corresponds to the Meissner state. However, the magnetisation decrease is no longer smooth: it follows a sequence of saw-like drops. This is explained by looking at the density plots below, which demonstrates that unlike the case of $d = 50$ [cf. "b" in Fig. **6-2**(i)], here the magnetic field penetrates the sample in the form of vortices. A drop in the magnetisation occurs each time when additional vortices enter the wire, rearranging the vortex configuration [see "a" - "e" in Fig. **6-2**(ii)].

However, Fig. **6-2**(ii) does not exhibit standard type-II superconductivity either. An important difference is that at relatively small ascending fields (just after the Meissner state), the mixed state develops giant (multi-quantum) vortices which are unstable in a type-II material [see "b" in Fig. **6-2**(ii)]. Giant vortices are arranged in a 1D lattice (chain), and the magnetic flux carried by one vortex increases with the field (the vortices grow). When the external field exceeds a certain threshold, the multi-quantum vortices are replaced by a chain of elongated clusters of single-quantum (Abrikosov) vortices [see "c" in Fig. **6-2**(ii)]. While the field increases further, these clusters merge into a 1D lattice of single-quantum vortices located in the wire center [see "d" in Fig. **6-2**(ii)]. Finally, at larger fields only surface superconductivity survives [see "e" in Fig. **6-2**(ii)], before the superconducting state eventually disappears.

The field patterns seen in Fig. **6-2**(ii) appear to be similar to those attributed earlier to the IT regime in bulk superconductors. This regime is found between conventional types-I and -II in the phase diagram for both single- and multiband superconductors [69, 90]. Such non-standard vortex configurations are related to a special vortex-vortex interaction that combines repulsion and attraction at different ranges and has a significant many-body (many-vortex) contribution favouring the formation of clusters [90] and giant vortices [69]. We expect that despite a strong boundary influence these IT features of the interaction between vortices are also present in nanowires. We note that this mechanism for the formation of giant vortices and vortex clusters is totally different from what is observed in small (mesoscopic) superconductors, where vortices are squeezed by the boundaries in all dimensions, see, e.g., [95–97]. A nanowire is an extended quasi-1D object where vortices can move freely along its length and their longitudinal arrangement is determined by the nontrivial interaction between them, rather than with boundaries. The infinite length implies that a system is in the thermodynamic limit so that one can still use the concept of superconductivity types.

For the descending field the plots of $|\Psi|^2$ in Fig. **6-2**(ii) are similar to those of the ascending field case, though the sequence of patterns is reversed [cf. "a" - "e" with "A" - "E" in Fig. **6-2**(ii)]. The descending-field magnetisation is still negative, similarly to that in Fig. **6-2**(i), but its amplitude becomes smaller, which indicates a weaker magnetic flux trapping. However, this is not the case in the limit $H \to 0$: the zero-field paramagnetic response (i.e., the paramagnetic Meissner effect) in Fig. **6-2**(ii) is more pronounced then in Fig. **6-2**(i). It should also be noted that a giant paramagnetic Meissner effect has previously been reported for bulk IT two-band superconductors. [98].

The field-condensate patterns in Fig. **6-2**(ii) are essentially of the 1D character (with the exception of "A"), in contrast with the 2D character of the density plots shown in Fig. **6-2**(i). This can be viewed as the dimensional crossover in the mixed-state configuration. Surprisingly, the crossover occurs for values of d that are an order of magnitude larger than ξ_0.

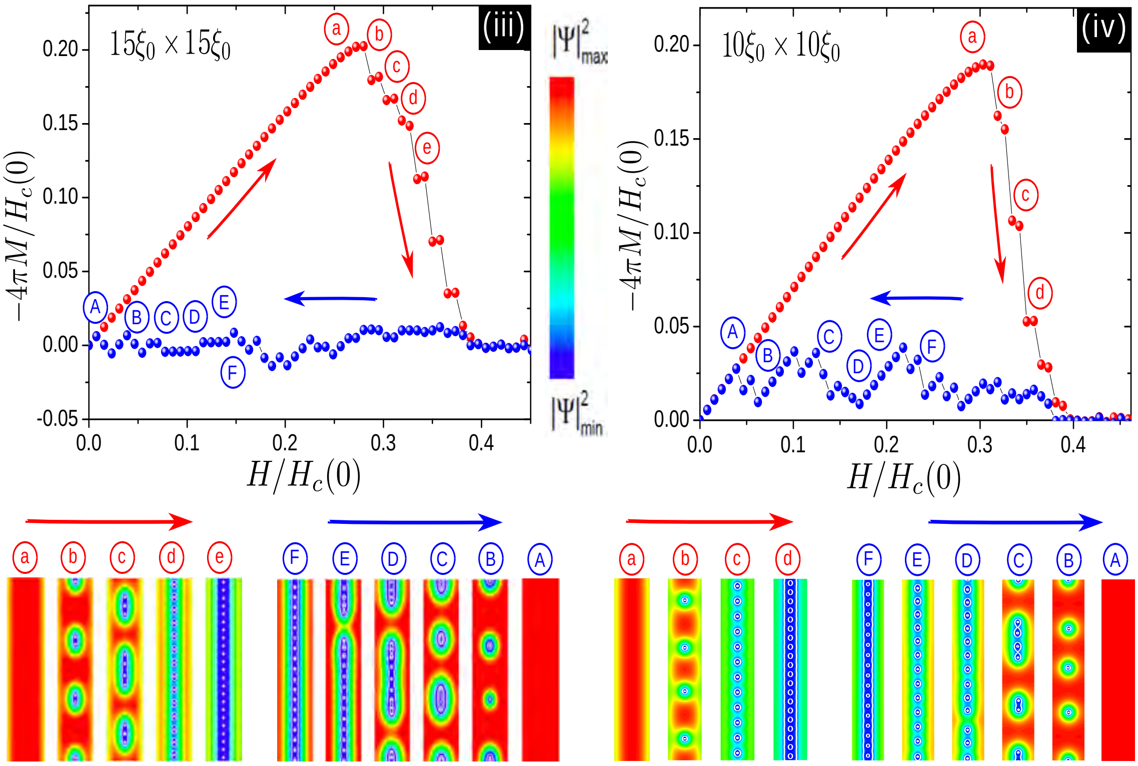

Figure 6-3 : Magnetization M as a function of applied magnetic field H is plotted for increasing (red points) and decreasing (blue points) field is calculated for wires of different crossection with $L_{x,y} = 15\xi_0$, $10\xi_0$. The field H as well as M are expressed in the units of the thermodynamic bulk critical field $H_c(0)$ at zero temperature. Density colour plots below magnetization panels illustrate the order parameter profiles, that correspond to points in the magnetization curve. Points denoted by small red letters $a, b, c\ldots$ are found on the ascending field curve and points denoted by capital letters $A, B, C, \ldots$ are on the descending field curve. All calculations are done at temperature $T = 0.7T_c$.

For $d = 15$ [see Fig. **6-3**(iii)] the magnetisation is qualitatively similar to that of Fig. **6-2**(ii). However, multi-quantum vortices here play a minor role: they are absent for the ascending field case and visible only at point "B" on the descending field curve. However, clusters of single-quantum vortices observed at lower fields [see, e.g., "b" in Fig. **6-3**(iii)] are still a clear signature of the IT superconductivity.

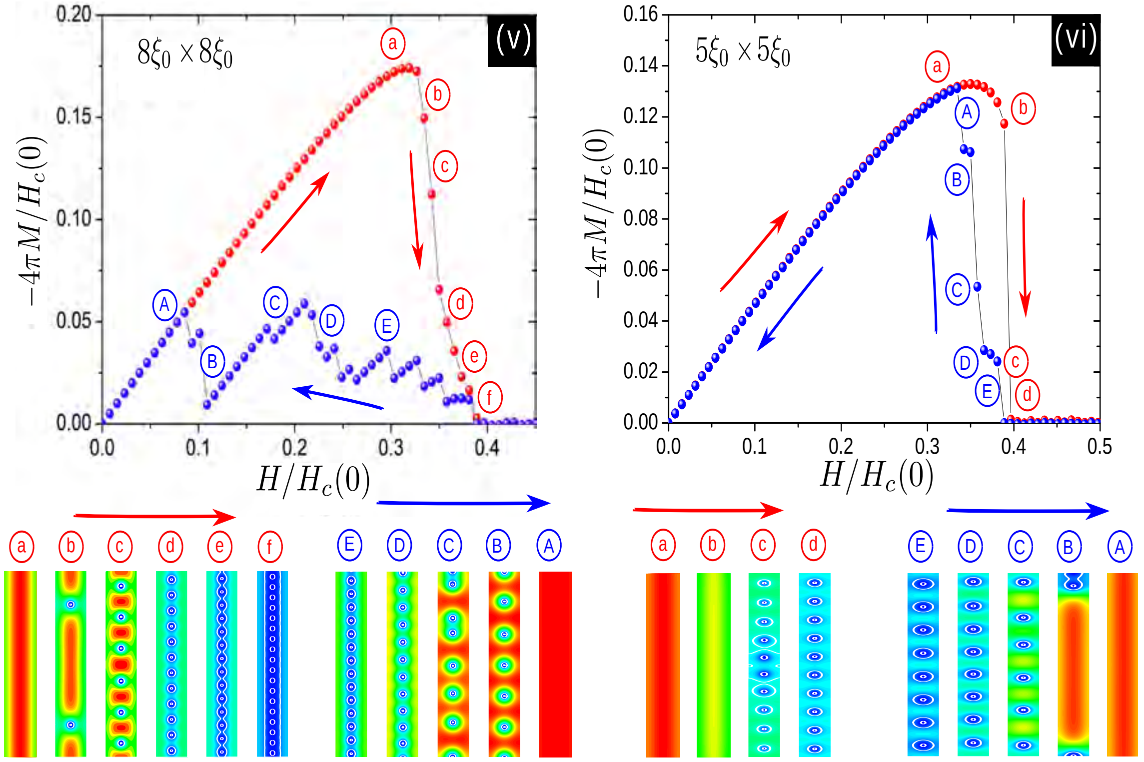

Figure 6-4 : Magnetization M as a function of applied magnetic field H is plotted for increasing (red points) and decreasing (blue points) field is calculated for wires of different crossection with $L_{x,y} = 8\xi_0$ and $5\xi_0$. The field H as well as M are expressed in the units of the thermodynamic bulk critical field $H_c(0)$ at zero temperature. Density colour plots below magnetization panels illustrate the order parameter profiles, that correspond to points in the magnetization curve. Points denoted by small red letters $a, b, c\ldots$ are found on the ascending field curve and points denoted by capital letters $A, B, C, \ldots$ are on the descending field curve. All calculations are done at temperature $T = 0.7T_c$.

Panels **6-3** (iv) and **6-4** (v), calculated, respectively, for $d = 10$ and $d = 8$, demonstrate that the nanowire is still in the IT regime, although in both ascending and descending cases giant vortices disappear. Vortex clusters are not seen at the ascending field but they are still present at the descending field [see "C" in Figs. **6-3** (iv) and **6-4**(v)]. One also sees that the descending and ascending magnetisation curves become closer one to another. This can be explained by the decrease of the Bean-Livingston barrier [99], which makes it easier for vortices to escape the wire. The magnetisation patterns in Figs. **6-3**(iv) and **6-4**(v) are apparently in agreement with the type II/1 concept of the IT superconductivity: the Abrikosov lattice at large fields is stable because of the short-range repulsion between single-quantum vortices whereas clusters of vortices at smaller fields are explained by the long-range vortex attraction [39, 100–105] [see also the discussion of type-II/1 configurations in the IT regime in Ref. [69]].

Finally, type II is almost approached at $d = 5$ [see Fig. **6-4**(vi)]. Here the mixed state contains only single-quantum vortices arranged in a 1D Abrikosov lattice while the ascending and descending magnetisation curves are very close one to another. However, in sharp contrast to type-II superconductors, the magnetisation in Fig. **6-4**(vi) almost instantly drops to zero when the field starts to penetrate the nanowire, so that the mixed state is restricted to a very narrow interval of the external field values. When decreasing the nanowire thickness further, vortices become energetically unfavourable and, finally, the system demonstrates a magnetic response of a type-I material. Surprisingly, the corresponding magnetisation as a function of the applied magnetic field is close to that observed in bulk type-I superconductors, without any lamellas and bubbles of the normal state usually observed in finite samples. It is also worth noting that vortices in Fig. **6-4**(vi) become elongated in the direction perpendicular to the nanowire. This is an onset of the formation of phase slip centers typical for 1D weak superconducting links [92].

The identification of such vortex states can easily be done with the help of Fig. **6-5** which shows the phase portraits of the order parameter for different cross section area of the wires at chosen normalized magnetic field.

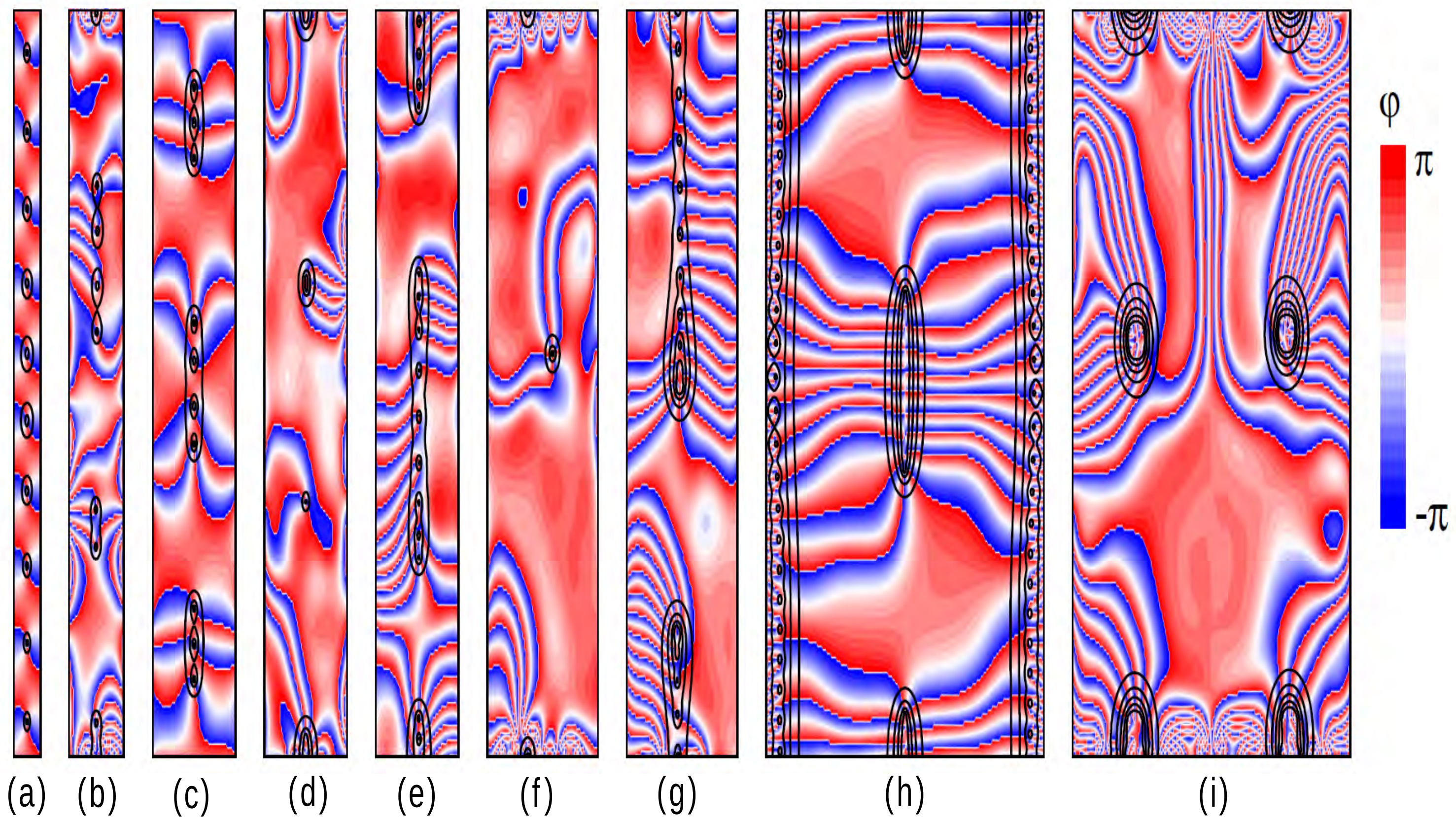

Figure 6-5 : Phase portraits of the order parameter as for different wire's cross section area at chosen normalized magnetic field ($h = H/Hc(0)$). (a) Single vortex chain for $d = 5\xi_0$ wire and, $h = 0.396$-up; (b) two vortex cluster for $d = 10\xi_0$ wire and, $h = 0.319$-down; (c) tri and four vortex cluster for $d = 15\xi_0$, $h = 0.311$-up;(d) single and giant vortices for $d = 15\xi_0$ wire and, $h = 0.046$-down;(e) double head worm for $d = 15\xi_0$ wire and, $h = 0.109$-down; (f) giant vortex for $d = 20\xi_0$ wire and, $h = 0.0077$-down;(g) double head snake for $d = 20\xi_0$ wire and, h = 0.07-down (h) and(i) lamelas for $d = 50\xi_0$ wire and, $h = 0.225$-up and $h = 0.046$-down

7 Superconductor Bilayer[a]

In this chapter we studyd a mechanism for superconducting bilayer. The superconducting bilayer is formed by two layers, where the top type-II superconducting layer by the top type-I superconducting layer. In the results we show that the complexity of the patterns obtained in the penetration of the magnetic field comes from the changes in the interaction of short and medium range between the vortices (non-monotonic interaction), where these patterns implicitly depends on parameters such as the coupling between layers and temperature.

7.1 Introduction

According to the Ginzburg-Landau (GL) theory, a conventional superconductor near T_c is described by a parameter κ, the GL parameter. This parameter determines the response of a superconductor immersed in an external magnetic field, H, sorting them into two categories as follows: type-I when $\kappa < 1/\sqrt{2}$ and type-II when $\kappa > 1/\sqrt{2}$ [106]. Type-I superconductors expel weak magnetic fields, while strong fields give rise to formation of macroscopic normal magnetic flux domains [35,107,108] whereas type-II superconductors behaves differently; when H is below the critical H_{c1}, it is expelled from the superconducting sample. When H is above this value a vortex lattice appears in the superconductor until other critical field, H_{c2}, is reached. At such critical field the superconductivity is destroyed.

These different responses are usually viewed as consequences of the interaction between vortices in these systems. In type-II superconductor the energy cost of a boundary between the normal and the superconductor state is negative, leading to a repulsive vortex-vortex interaction [106]. This favors the formation of stable vortex lattices. In type-I superconductors the situation is opposite to that, the normal-superconducting interface has positive energy favoring an attractive vortex-vortex interaction. Thus a vortex lattice is not stable because the vortices collapse to form larg magnetic flux bundles. At exactly $\kappa = 1/\sqrt{2}$, also called Bogomolnyi point, the vortices do not interact with each other [19, 20].

---

[a] Contains material from the manuscript: Superconducting type-II/N/type-I bilayer (in preparation)

Recently there has been increased interest in superconductors with several superconducting components. The main situations where multiple superconducting components arise are, multiband superconductor [109–114] and artificially fabricated superconducting layers [115, 116]. It was discussed recently that in multicomponent systems the magnetic response is much complex than that in ordinary systems, and that the type-I or type-II behavior is not sufficient to classify such superconductors. Rather, in a wide range of parameters, as a consequence of the existence of three fundamental length scales, there is a separate superconducting regime where vortices have long-range attractive combined to a short-range repulsive interaction which induces the formation of vortex cluster immersed in superconducting domains [98, 117]. Experimental works [118, 119] have suggested that this state is realized in the two-band material MgB_2.

Several works have recently discussed the type of superconductors comprising multiple coherence lengths, some of which are larger and some smaller than the magnetic field penetration length. These multiple coherence lengths arise in superconducting states that break multiple symmetries and also in materials with multiple superconducting bands.

Several materials have been suggested in experiments to belong to this type of superconductors [118, 120], where vortices can display multi-scale attractive and repulsive inter-vortex interactions [117, 118, 121, 122]. Multiple attractive length scales come from core-core inter-vortex interactions. Multiple repulsive length scales can be obtained instead in (i) artificially fabricated superconducting bilayers, where the different layers give rise to two coherence lengths, or rather generally in (ii) thin films of type-I materials due to stray fields.

An ultrathin superconductor bi-layer can be considered as an artificial multicomponent superconductor [123]. The emergence of controlled fractional vortices has been studied in Ref. [115] and [124]. Multiband superconductors can develop vortex states that are qualitatively different from those in single-band materials. A trivial configuration is a composite vortex that comprises two vortices from the different band condensates, that are centered at the same point, and have equal winding numbers. Stationary equilibrium states in two-band bulk superconductors are formed by the composite vortices. However, a nonequilibrium system can develop a state in which the band vortices are shifted spatially, the so-called noncomposite vortices. Those vortices are associated with a nonquantized magnetic flux: each of the partial vortices in the band condensates carry a fraction of the total (quantized) flux, and are often called fractional vortices. As an example, the aluminum bi-layer was originally considered to mimic a multi-band superconductor [112, 123] and presents evidences of the flux fractionalization. The ability to produce this type of condensate using a conventional superconductor or a multi-band superconductor creates a brand-new platform on which new topological electronics can be constructed. This would require us to establish fractional quantization in a superconducting bi-layer and multi-band superconductors to confirm whether such an elegant approach toward realizing multi-component quantum condensates really exists. With this idea, Tanaka *at al* have shown in Ref. [125] the experimental formation of a fractional vortex generated by using a thin superconducting bi-layerformed by two niobium single layers.

Other theoretical works investigated a bilayer structure [126–129], made of two different single-gap superconductors [116, 130], for which they show a phenomenology very similar that found for two-gap superconductors, however much more easily tunable. The theoretical description used is a variant of the famous Lawrence-Doniach model for high-temperature cuprates emphasizing the layered aspect of the structure. It has been found that there is indeed a mid-range intervortex attraction present in combination with the long-range $1/\boldsymbol{r}$ repulsion stemming from the interaction of stray magnetic fields from the vortices. This aspect of the vortex-vortex interaction leads to myriads of possible vortex structures forming soft-matter-like gels, glasses, chain-like structures and other intriguing patterns [38, 107, 119, 120, 131].

Besides these pioneering works, searching appearance of fractional vortices under other setups is challenging and important since it gives new viewpoints of the problem an also new possibility for experimental discovery. In this section, we studied a mechanism for superconducting bilayer which can mimic two-band superconductors. We consider the system under an applied perpendicular magnetic field and discuss how the variation of the coupling between layers with the variation of external variables (temperature, external magnetic field and inclusion of stray field) can lead to a behavior similar to two-band superconductors (no-monotonic interaction and vortex dissociate).

7.2 Theoretical model

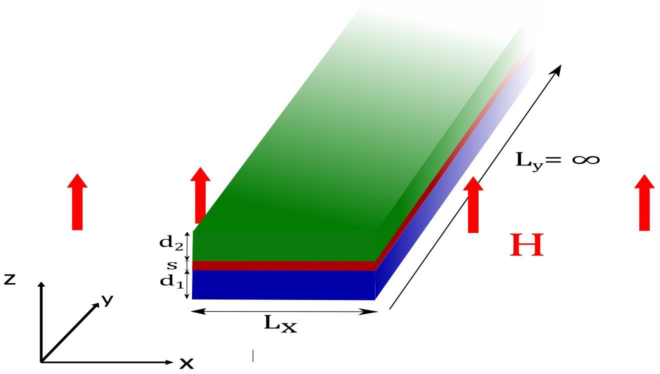

Figure 7-1 : The studied system: two superconducting layers with thicknesses d_1 and d_2, respectively, separated by an insulating material with thickness s in the presence of a magnetic field H perpendicular to the layers.

We consider superconducting bilayer formed by two layers, where the bottom type-II superconducting layer (layer-1) with thickness d_1 and the top type-I superconducting layer (layer-2) with thickness d_2 are separated by a thin insulator with thickness s. The layers are coupled by both Josephson and magnetic couplings and are immersed in a magnetic field applied perpendicular to them, [see Fig. **7-1**].

This system can then be described by the Lawrence-Doniach (LD) model [116, 132–134], which is based on the Ginzburg-Landau (GL) theory. In this model, the free energy is composed of the individual contributions of each layer, the LD coupling and the magnetic field energy.

$$\mathcal{F} = \mathcal{F}_N + \sum_{n=1,2} d_n \int_S \left[\alpha_n |\Psi_n(\boldsymbol{r})|^2 + \frac{1}{2}\beta_n |\Psi_n(\boldsymbol{r})|^4 + \frac{1}{2m_n} \left| \left(\frac{\hbar}{i}\boldsymbol{\nabla} - \frac{2e}{\boldsymbol{c}}\boldsymbol{A}(\boldsymbol{r}) \right) \Psi_n(\boldsymbol{r}) \right|^2 \right] d^2\boldsymbol{r} + \tag{7.1}$$

$$+ s \int_S \eta |e^{(-i\frac{2e}{\hbar \boldsymbol{c}}\int_0^s A_z dz)} \Psi_2(\boldsymbol{r}) - \Psi_1(\boldsymbol{r})|^2 d^2\boldsymbol{r} + \frac{1}{8\pi}\int_V (\boldsymbol{h} - \boldsymbol{H})^2 d^3\boldsymbol{r},$$

where Ψ_n represent the order parameter of each superconducting layer, the coefficients $\alpha_n = -\alpha_{0n}(1 - T/T_{cn})$ and β_n are the GL coefficients, and the phenomenological constant η is proportional to the Josephson coupling between adjacent layers, $[\eta = \hbar^2/(2m_\perp s^2)]$, which inversely proportional to the effective Cooper pair mass for the tunnelling between the layers $m_\perp$ and the thickness of the insulating layer s. The last integral in (7.1) is taken over the entire space, whereas the first two are assumed uniform over the superconducting layer thickness and spacer layer, and the integral over surface projection of the layers.

The equations for the order parameter for each layer are given by Eqs. (7.2) and (7.3) with $e^{-i\frac{2e}{\hbar \boldsymbol{c}}} = 1$. These equations are identical as the GL equations, plus a coupling term

$$\frac{1}{2m_1}\left(-i\hbar\boldsymbol{\nabla}_{2D} - \frac{2e}{\boldsymbol{c}}\boldsymbol{A}\right)^2 \Psi_1 + \alpha\Psi_1 + \beta|\Psi_1|^2\Psi_1 + \frac{s\eta}{d_1}(\Psi_1 - \Psi_2) = 0, \tag{7.2}$$

$$\frac{1}{2m_2}\left(-i\hbar\boldsymbol{\nabla}_{2D} - \frac{2e}{\boldsymbol{c}}\boldsymbol{A}\right)^2 \Psi_2 + \alpha\Psi_2 + \beta|\Psi_2|^2\Psi_2 + \frac{s\eta}{d_2}(\Psi_2 - \Psi_1) = 0, \tag{7.3}$$

and the equation for the current is given as

$$-\nabla^2 \boldsymbol{A}_{3D} = \frac{4\pi}{\boldsymbol{c}}\boldsymbol{j}_{2D}. \tag{7.4}$$

The equations for Ψ_1 and Ψ_2 are solved in 2D and in the middle of each layer. For the vector potential, we consider $A_z = 0$ in Eq. (7.4), which implies that the phase factor is the coupling term is equal to one. The other implication is that $j_z = 0$, therefore the j_z component of the current in each layers can be neglected and the supercurrent will flow only within of the respective layers, and can be spatially separated:

$$\boldsymbol{j}_n = -\frac{e}{m_n}\Re\left[\Psi_n^*\left(-i\hbar\boldsymbol{\nabla} - \frac{2e}{\boldsymbol{c}}\boldsymbol{A}\right)\Psi_n\right]. \tag{7.5}$$

If we consider that s is much smaller than ξ ($s \ll \xi$), we can assume that the superconducting currents of each of the layers can be added algebrically in the plane corresponding to half of the sample, $s/2$. Then we write the current equation as,

$$-\left.\nabla^2\boldsymbol{A}\right|_{s/2} = \frac{4\pi}{\boldsymbol{c}}(\boldsymbol{j}_1 + \boldsymbol{j}_2). \tag{7.6}$$

Here we assume that the bilayer is infinity in y direction (periodic boundary conditions were set in this direction). Its width is L_x in the x direction and L_z represents the thickness of the bilayer ($L_z = d_1 + s + d_2$), as shown in Fig. **7-1**. The super-currents $\boldsymbol{j}_n$ in Eq. (7.5) are also calculated in 2D. However, the Eq. (7.4) is solved in 3D. We solve the Eqs. (7.2)-(7.3) and (7.4) self-consistently, with the boundary condition corresponding to the sides of the sample as given by the Eq. (7.7) below. This imposes that no supercurent can pass through the sample boundary,

$$\left.\left(-i\hbar\nabla - \frac{2e}{c}\mathbf{A}\right)\Psi_n\right|_{\perp,\text{boundary}} = 0, \qquad \boldsymbol{j}_s = 0. \tag{7.7}$$

The bilayer is placed in a perpendicular homogeneous field $\boldsymbol{H}$ along the z axis, what leads to the boundary condition for the field as $\boldsymbol{B} = \boldsymbol{H}$ at infinity.

To present the above equation in dimensionless form we express the length in units of $\xi_{10}(\xi_{n0} = \hbar/\sqrt{2m_n|\alpha_{n0}|})$, the vector potential in $A_0 = \hbar c/2e\xi_{10}$, the order parameter $\Psi_{n0} = \Psi_{n0}(T = 0, \eta = 0, H_a = 0) = \sqrt{-\alpha_{n0}/\beta_n}$ and the temperature in T_{c1}, the magnetic field in $\mathrm{H}_{c2,1}$, additionally we use a new variable $\alpha = \xi_{10}^2/\xi_{20}^2$.

This system of non-linear coupled differential equations are then solved by the link-variable approach seen in chapter 3. In the first part of this chapter we used the so-called “field cooling” algorithm, where one starts from the normal state at $T = T_{c1}$ and then gradually decreases the temperature while keeping the magnetic field fixed; the equilibrium configuration obtained for the previous temperature step is used as the initial condition for the next step and the second part we make a magnetic history for different coupling values and fixed temperatures.

We chose the Nb and Sn superconductors for the first and the second layers. The Nb is a type II superconductor with κ_1=1.03 and T_{c1}=9.2K and the Sn is a type I superconductor with κ_2=0.15 and T_{c2}=3.7K.

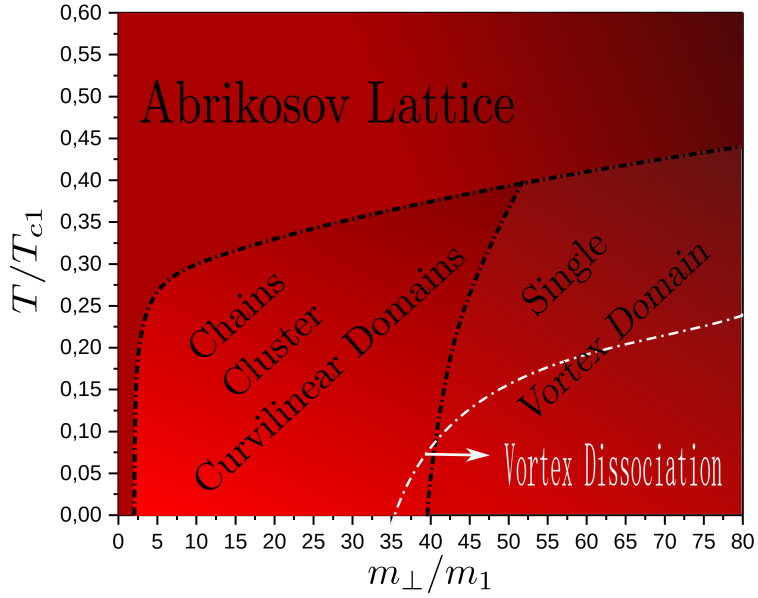

Figure 7-2 : Phase diagram ($T \times m_\perp/m_1$) for $H = 0.1H_{c2,1}$ The regions with different colors identify the phases of vortex when temperature decreasse to each value of coupling. The dotted line show when the vortex dissociates

7.3 Results

7.3.1 Magnetic response dependence on the Josephson coupling between the superconducting layers

In this section we will see how the variation of electronic coupling between the layers affects the behavior of vortices. To do this aim we considered the sample dimensions $L_x = 45\xi_{10}$, $L_y = 60\xi_{10}$ and $L_z = d_1 + d_2 + s$, where $d_1 = 5\xi_{10}$, $d_2 = 5\xi_{10}$ and s =0.05ξ_{10}, with a variation of the term $m_\perp$ in a range $m_1 \leq m_\perp \leq 200m_1$. We simulated a Field Cooling process with a range of temperatures $T_{c1} < T < 0.1T_{c1}$ for the fixed value of the applied magnetic field, H =0.1$H_{c2,1}$ (that corresponds to 39 vortices inside of sample) and $\zeta = 0.2$.

The phase diagram presented on Fig. **7-2** show how the configuration of vortices vary as a function of coupling $m_\perp/m_1$ and T/T_{c1}. Each point in the diagram corresponds to a stable configuration of vortices, for each value of T/T_{c1}. We note that some configurations are formed by vortices of both layers that share the same axis, *i. e.* composite vortices as show in the Fig. **7-3**. It is seen that the density of cooper pairs in layer-1 (a) as well in layer-2 (b) are the same, but this structure of composited vortices only prevail up to a value of coupling ($m_\perp/m_1 \approx 35$). Beyond this value we have dissociation of vortices, observed for certain two-component systems [124, 135–138]. This transition, is shown by the dotted line in the phase diagram and it is going to be studied later.

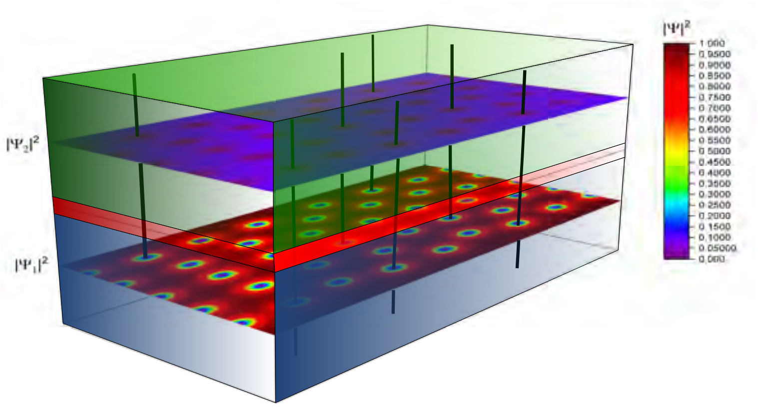

Figure 7-3 : Composite vortex, $m_\perp/m_1 = 2$ at $T = 0.1T_{c1}$. Vortices are centered at the same point and have equal flux number.

Notice that for $T > Tc2$, the vortices arrange them selves in a Abrikosov Lattice. This was expected, since the influence of type-I superconductor on the bilayer is only reflected when the temperature reaches its critical temperature. In Fig. **7-4** we present vortex configuration for $m_\perp/m_1$ =2 and 4. For this case, we observed that for whatever temperature, an almost homogeneous distribution of vortex is present, indicating a type-II behavior. That can be explained by the fact that stronger couplings between layers mean stronger influence of the type-II layer.

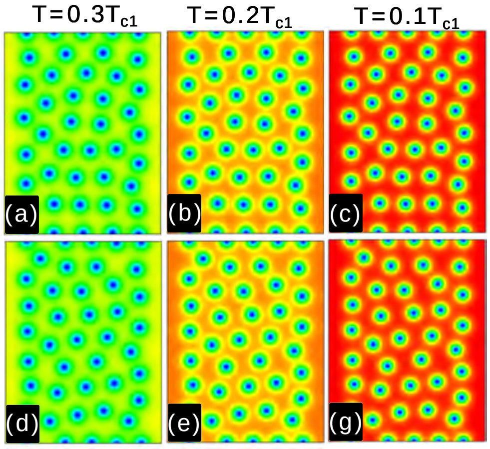

Figure 7-4 : Abrikosov Lattice $m_\perp/m_1$ =2 [(a),(b)and (c)] and 4[(e),(f) and (g)], profile in the type-II layer.

When coupling is increasing for low temperatures new effects on the vortex lattice appear. At $m_\perp/m_1$ =6 and T =0.1T_{c1} different types of cluster show up (dimers, three vortex cluster and short individual chains [see Fig. **7-5**(e)]. The transition to from the cristaline (Abrikosov) lattice to the vortex cluster phase is distinguished by the vortex interaction, where by effects of temperature a slight attraction between vortices is present and leads to the formation of this kind of state. This interaction is a typical non-monotonic interaction, where the interaction between vortices is short-range repulsive and long-range attractive.

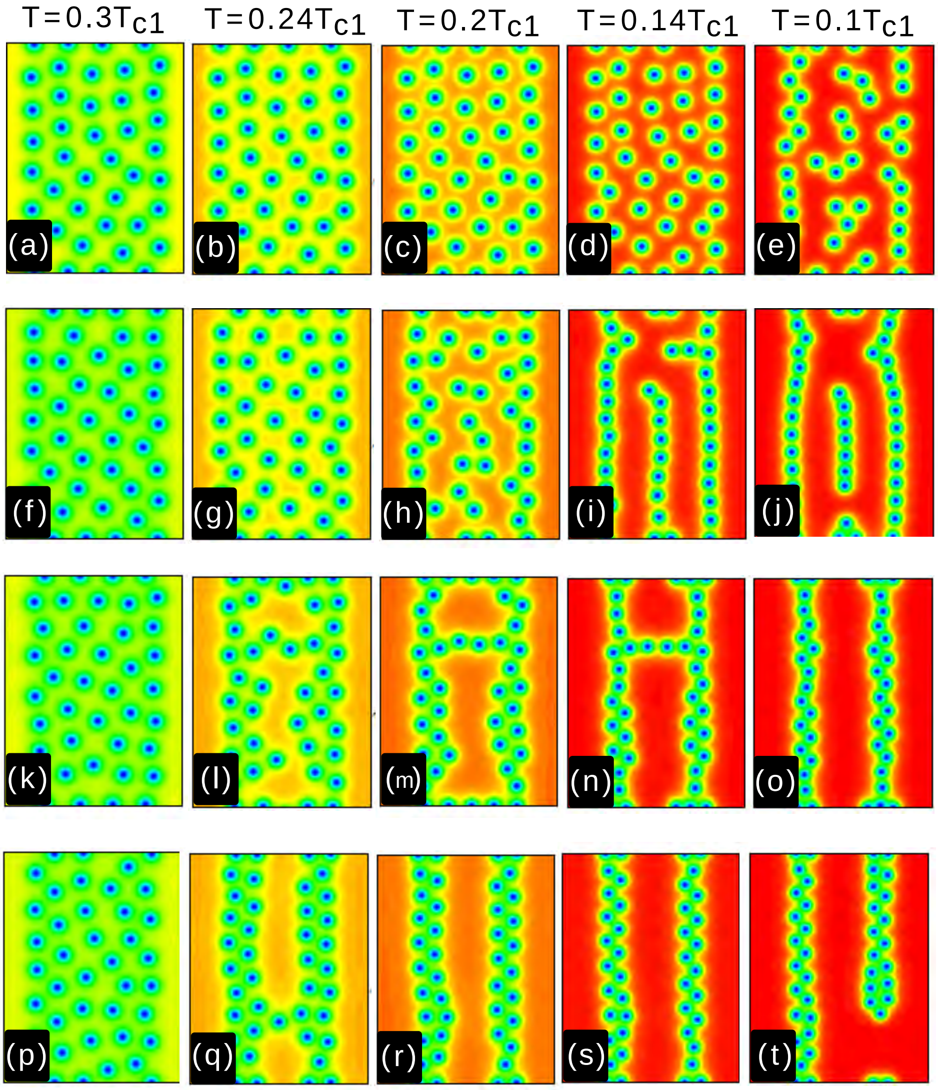

Figure 7-5 : The evolution the vortex structure with temperature, shown order parameter profile in the type-II layer consider very strongly coupled layers, $m_{\perp}/m_1$ =6 (a-e) (Abrikosov Lattice → Clusters),$m_{\perp}/m_1$ =10 (f-j) (Abrikosov Lattice → Clusters, chains), $m_{\perp}/m_1$ =20 (k-o) (Abrikosov Lattice → Domains Vortex-Chains) and $m_{\perp}/m_1$ =30 (p-t) (Abrikosov Lattice → Domains Vortex-Chains)

Figures. **7-5**(f)-(j), show the vortex configuration for the coupling between layers $m_{\perp}/m_1 =$

10. The long-range vortex attractive is set at higher temperatures that that found for $m_\perp/m_1 = 6$, in the panel (h) small vortex cluster of two and four vortices are already. For lower temperatures, the panels (i)-(j) show that chains are established and follow the sample geometry. For $m_\perp/m_1 = 20$, attractive part of the interaction becomes stronger, because the formation of small vortex cluster is suppressed in favor of large vortex agglomeration as depicted in panels (i)-(n). At $T = 0.1T_{c1}$ these agglomeration becomes and form two rows of vortex aligned to the sample borders (m)-(o). The same behavior is observed for $m_\perp/m_1 = 30$, but here on of row is broken (t), due to the strong interaction between vortex and the layer of superconductor type-I become more apparented.

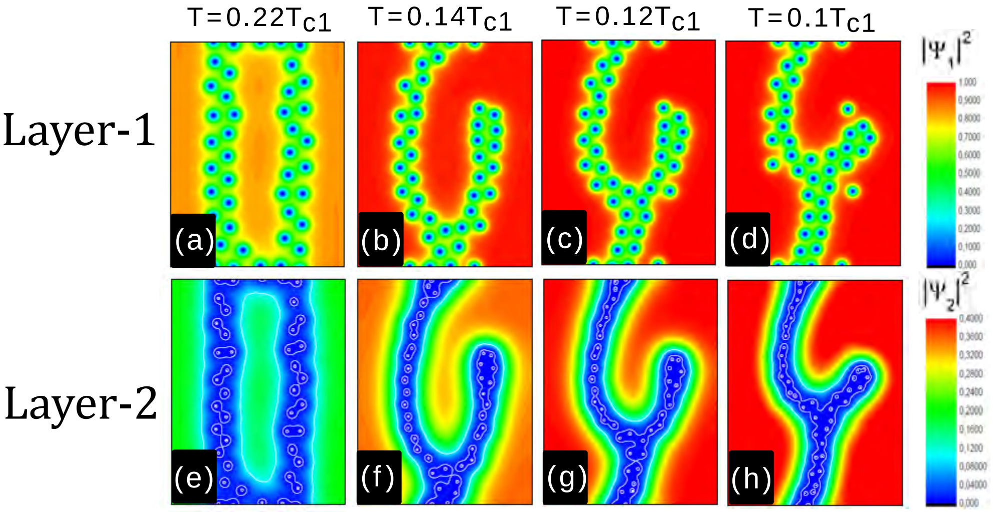

Figure 7-6 : The evolution of the vortex structure with decreasing temperature, with electronic coupling $m_\perp/m_1 = 35$. Transition agglomeration → curvilinear domains, and vortex dissociation.

When the coupling between the superconductor layer is further reduced $m_\perp/m_1 = 35$, we observe Another interesting feature for such low couplings is the phenomenon of vortex dissociation between layers. Notice in Figs. **7-6**(d),(h) that many vortices in the first layer do not share the same axis with the corresponding vortices in the second layer.

These effect is still more stronger for smaller coupling as $m_\perp/m_1$ =40, 100 and 200 Fig. **7-7**. It is clear that low couplings favor the distinct superconducting behavior inside each layer, type-2 behavior in the first layer and type-1 behavior in the second layer. Thus, in the layer 2 there is a trend to form a single vortex domain in the center of the sample. On the other hand, the layer 1 vortices are forced to follow the the layer 2 vortex domain by influence of the magnetic coupling, but, at the same time, they experience a strong intra-layer repulsion. That produces the vortex dissociation mentioned above.

Fig. **7-8** shows the profiles of the magnetic field induction crossing the superconducting

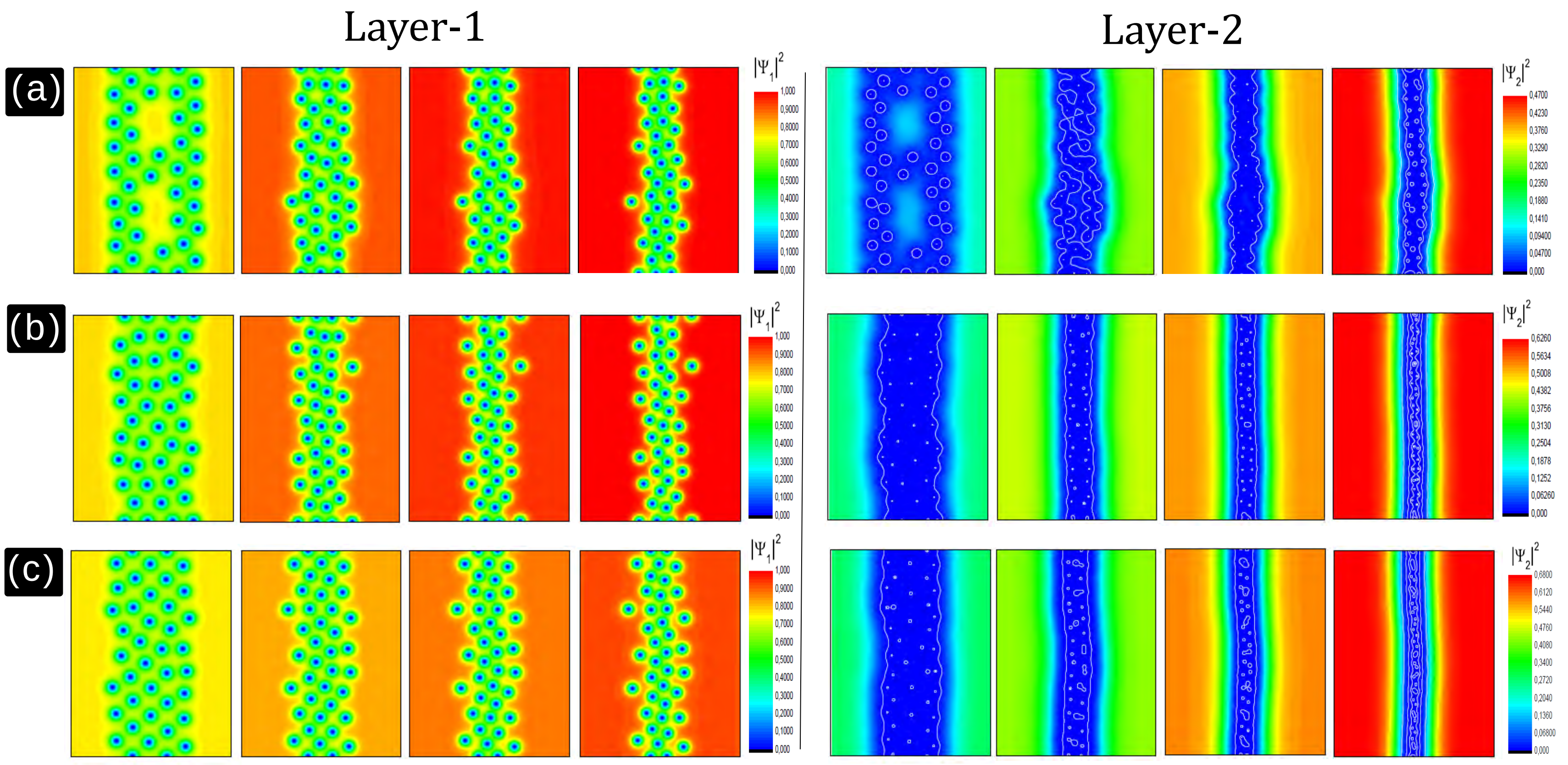

Figure 7-7 : Evolution of the vortex states with decreasing coupling $m_{\perp}/m_1$ =40(a), 100(b) and 200(c), and decreasing temperature the spatial profile of $|\Psi_1|^2$ (left) and $|\Psi_2|^2$ (right) is shown.

and insulator layers. It can be observed how the field on the z-direction is curved due to the attraction exerted by vortices in the layer-2. The schematic picture of this shown the effect of the field is show Fig. **7-8**(c).

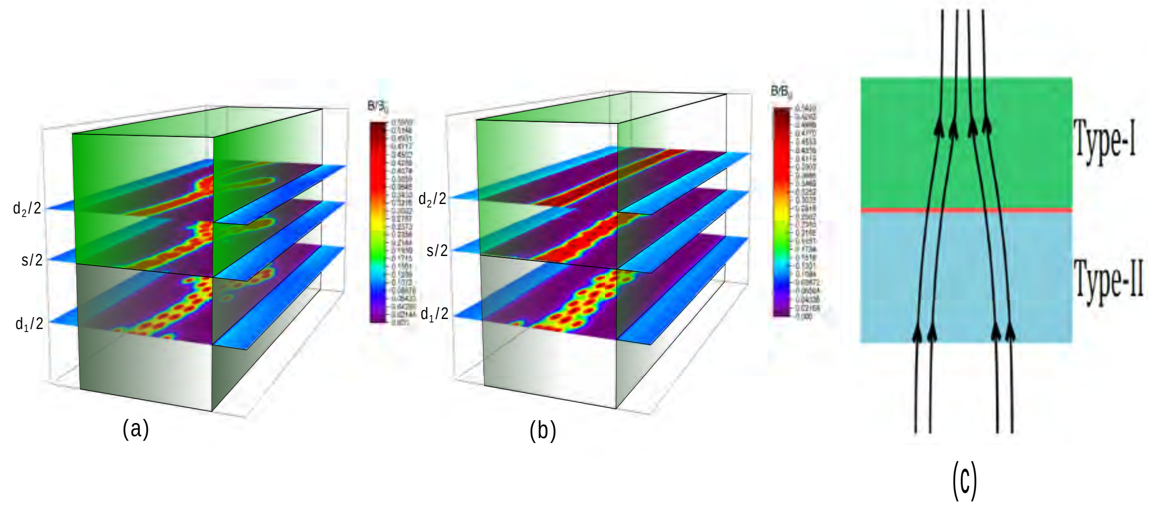

Figure 7-8 : Profile of the magnetic induction at three planes $d_1/2$, $s/2$ and $d_2/2$ for two couplings $m_\perp/m_1 = 35$(a) and 60(b) to $T = 0.1T_{c1}$ showing how it is curved in the sample.c) Schematic picture of this effect. Different localization of magnetic field in each layer gives multi-scale interaction for configuration of vortex.

Fig. **7-9** represents a situation in which there is vortex dissociation between layers. In this Fig. we depict the phase difference between layers calculated by $\Im(\Psi_1^*\Psi_2)$, that shows the process of vortex splitting. The phase difference is marked in the graph as the color variation from red to blue indicating where vortex has dissociated. To make a better identification we superimposed the phase difference plot over the vortex distribution in each layer. The latter is illustrate by the contour lines of the condensate density $|\Psi|^2$. Vortices in the layer-1 are represented by the red lines, while the vortices in layer-2 are given by blue lines. The panels (a) and (b) were calculated for $m_\perp/m_1$ =100 and 200 at T =0.1T_{c1}.

One can clearly distinguish the dissociated vortex pairs because they leave traces in the plots. These traces show what vortex have been dissociated.

Fig. **7-10** shows the sample magnetization as function of the reduced temperature T/T_{c1}, i.e. the phase diagram (Mc, $M \times T/T_{c1}$), for several values of the coupling parameter $m_\perp/m_1$. The magnetization M as function of temperature, $M(T) = (\langle h\rangle - H)/4\pi$, where $\langle h\rangle$ is the local magnetic field average over sample was calculated in each layer separately and then averaged $M_{\text{total}} = (M_{\text{layer-I}} + M_{\text{layer-II}})/2$.

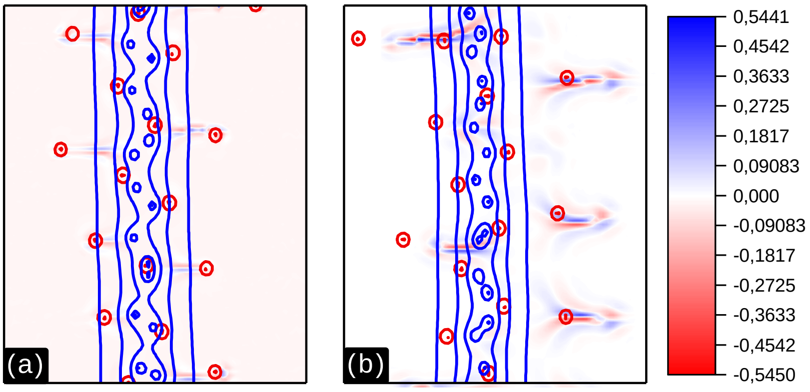

Figure 7-9 : Phase difference between layers, showing dissociation of vortices in layer-I (red) and layer-II(blue) for coupling (a)$m_\perp/m_1$=100 and (b)$m_\perp/m_1$=200 both at $T = 0.1T_{c1}$

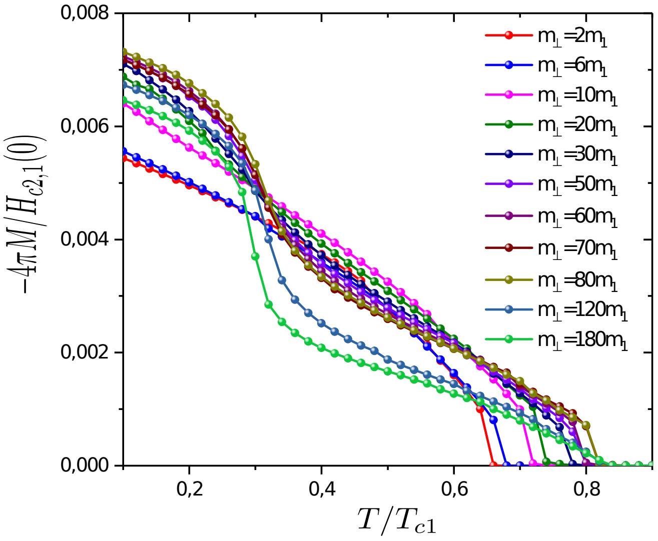

Figure 7-10 : Phase diagram $M \times T$ for sevral values of the coupling $m_\perp/m_1$.

For small values of $m_\perp$ ($m_\perp \leq 10$) one sees a monotonic groth of the magnetization with decreasing temperature. This is a expected behavior since for low values of $m_\perp$ we have the formation of the Abrikosov lattice, showing the prevalence of the repulsive interaction between vortices. In contrast for values above $m_\perp \geq 10$ and low temperatures, the magnetization presents a jump and this jump is associated with the vortex structure. It happens near $0.3T_c$, approximately where the transition for non-monotonic vortex-vortex interaction induced configurations takes place. It is reasonable to assume that the $M(T)$ signature can be useful to classify layers according to the strength of the Josephson coupling between them.

7.3.2 Magnetization behavior

Fig. **7-11** presents the increasing brunch of the magnetization loops ($M \times H$) of the bilayer for different values of the Josephson coupling strength and temperature. We chose temperatures close to T_{c2}, $T = 0.3T_{c1}$ and $T = 0.1T_{c1}$. Figs. **7-12** to **7-15** present the order parameter profiles, corresponding to the specified point in the magnetization curve (Fig. **7-11** (i)-(iv),for coupling between layer $m_\perp/m_1 = 2$; 35; 100 and 500, respectively at T =0.3T_{c1} and T =0.1T_{c1}.

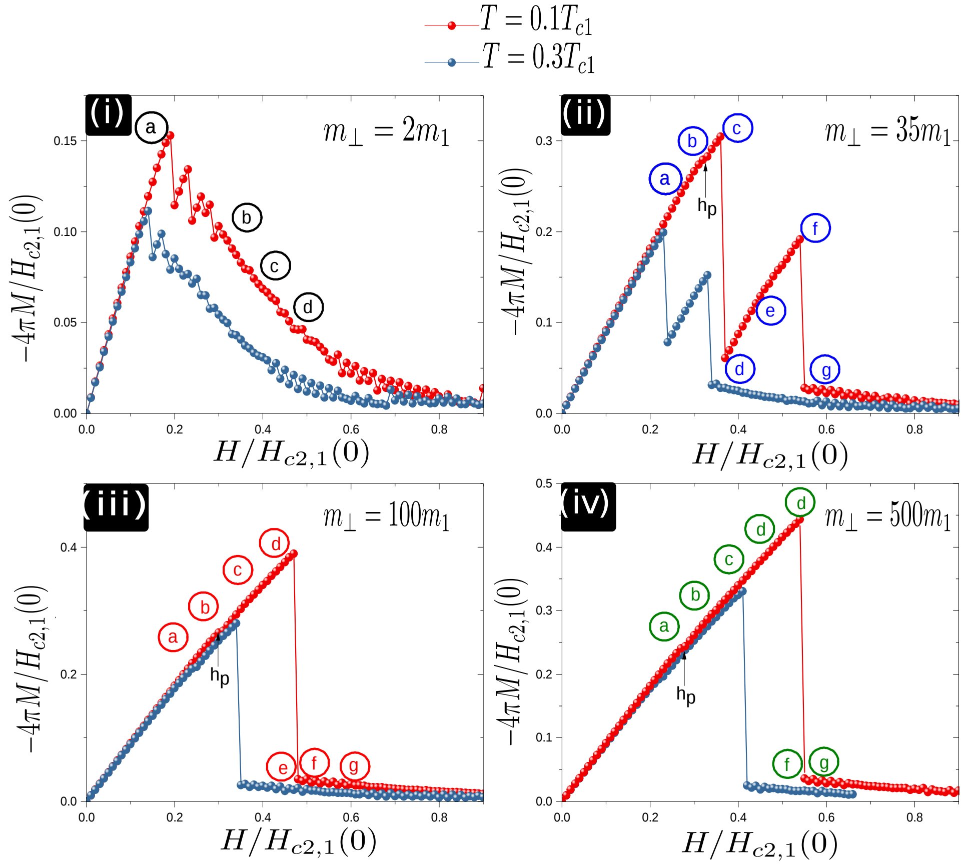

Figure 7-11 : Increasing brunch of the magnetization $M(H)$ loop at T =0.3T_{c1} and 0.1T_{c1}, for sequentially increased the coupling of the bilayer $m_\perp/m_1$

Considering $m_\perp/m_1 = 2$ [see Fig. **7-11**(i)], the shape of the M(H)-loop suggests that the whole system still behaves like a type-II superconductor, This is confirmed by the order parameter profiles show in Fig. **7-12**(a)-(d).

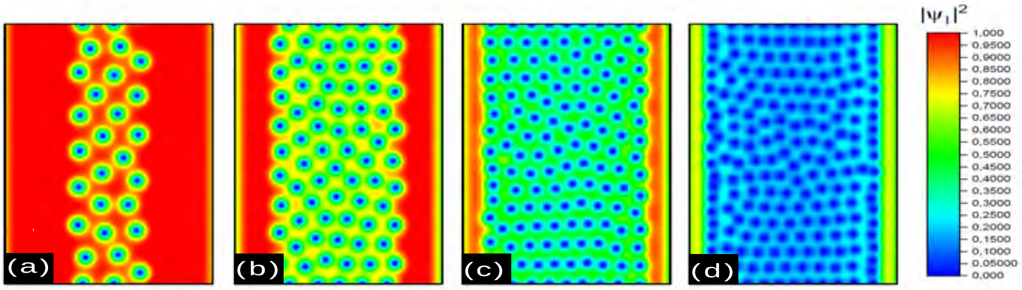

Figure 7-12 : Order parameter profiles for the bilayer system, that correspond to point in the magnetization curve for coupling between layer $m_\perp/m_1 = 2$ at T=$0.1T_{c1}$ (see Fig. **7-11**(i)).

However, for $m_\perp/m_1 = 35$, we find that in the Meissner state is a small concavity at h_p. This field marks the entry of vortices in layer-1, while layer-2 is kept in the Meissner state [see Fig. **7-11**(ii) and Fig. **7-13**(b)-(c)] until the first jump [see Fig. **7-11**(ii) and Fig. **7-13**(d)] occurs, precisely when the field manages to penetrate layer-2. This behavior of magnetization versus external magnetic is neither type-I or type-II like. This state is characterized by a strong drop of the magnetization at a transition field Fig. **7-11**(ii)(f). Beyond the transition field, the flux continues to enter the sample gradually, exhibiting a mixed state that leads to the overall behavior of magnetization as a superposition of type-I (steep drop) and type-II (gradual decrease) behavior.

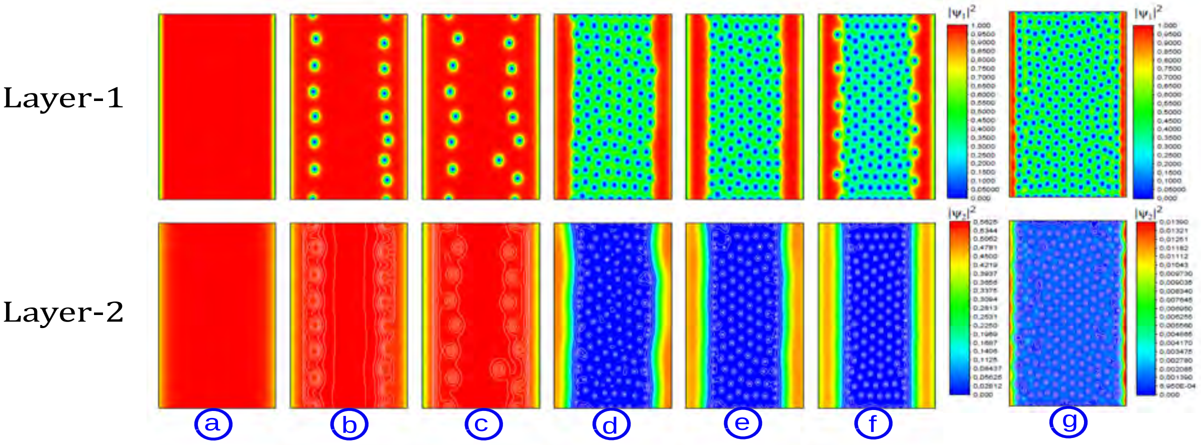

Figure 7-13 : Order parameter profiles for the bilayer system, that correspond to point in the magnetization curve for coupling between layer $m_\perp/m_1 = 35$ at T=$0.1T_{c1}$ (see Fig. **7-11**(ii))

For $m_\perp/m_1$ =100 and 500 the magnetization presents the same behavior for the Meissner state, where the magnetic field first penetrates the layer-1 in h_p [see Fig. **7-11**(iii) and Fig. **7-14**(b)-(d)) and [see Fig. **7-11**(iv) and Fig. **7-15**(b)-(e)] and a pronounced jump from the

Meissner state to mixed state. This behavior does not have a type-I behavior since the influence of type-II allows the entry of vortices and generates one mixed state for layer-1 and a completely dissociate state for layer-2 [see Fig. **7-14**(e)-(g) and Fig. **7-15**(f)-(g)].

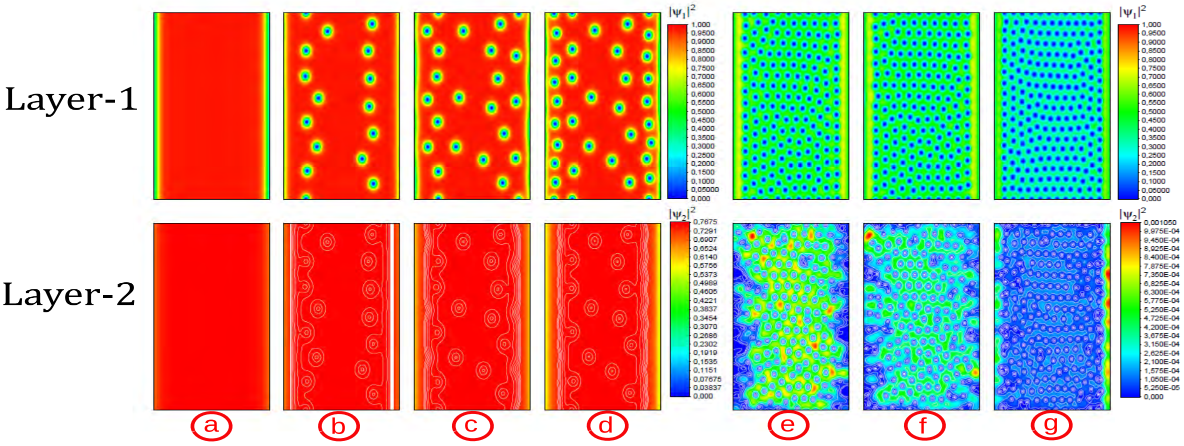

Figure 7-14 : Order parameter profiles for the bilayer system, that correspond to point in the magnetization curve for coupling between layer $m_\perp/m_1 = 100$ at T=0.1T_{c1} (see Fig. **7-11**(iii))

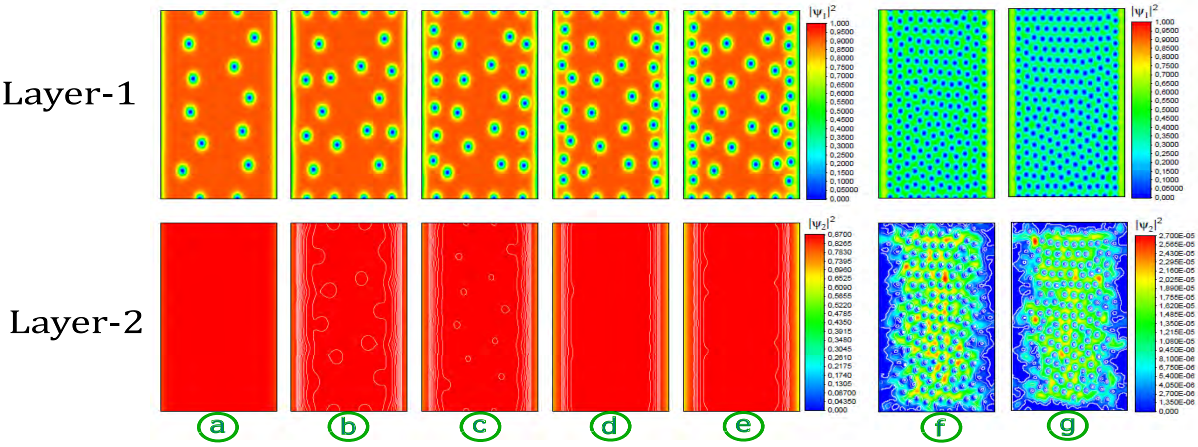

Figure 7-15 : Order parameter profiles for the bilayer system, that correspond to point in the magnetization curve for coupling between layer $m_\perp/m_1 = 500$ at T=0.1T_{c1} (see Fig. **7-11**(iv))

8 Stray Field Contribution to Vortex Interaction in Thin Films: Extended Ginzburg-Landau Analysis[a]

In this chapter we presents the results on the vortex-vortex interaction dependence on the sample thickness, and the influence of stray field on different vortex cluster configuration, in the intertype (IT) domain. The results reveal that the IT domain interaction has a considerable many-body (many-vortex)contribution. Such many-body interactions play a crucial role in the formation of the vortex matter in the mixed state stabilizing multi-vortex clusters. Properties of the vortex-vortex interactions depend strongly on the number of vortices in a cluster.

8.1 Introduction

Several theoretical and experimental works showed that for $\kappa = 1/\sqrt{2} = \kappa_0$, and $T \to T_c$, there exist a intertype domain between the type-I and type-II superconductor in the (κ, T) plain [39, 63–67], see Fig. **8-1**. This domain exhibits a non-conventional field dependence of the magnetization and reveals a first-order transitions between Meissner and the mixed state [39, 63].

The physics of the intertype domain results from the infinite degeneracy of the mixed state at the Bogomolnyi point (κ_0, T_c) [68] which is closely related to the Bogomolnyi self-duality [19,20]. This degeneracy implies that at (κ_0, T_c) the mixed state has an infinity number of possible configurations for the magnetic flux. By lifting this degeneracy, for example by doping or by decreasing the temperature, one is able to exhibit new flux configurations, different from those on either type-I or type-II domains, thus forming the inter-type domain.

The intertype domain does not exist only in the bulk samples, it can be found also in thin superconducting films, where the Bogomolnyi degeneracy can be lifted by the magnectic stray fields outside the sample. Indeed, there are experimental reports on the existence of nonconventional flux configuration, as multiquantum vortices, in thin films [76, 77]. Also, it has been known since 1960's [4, 6] that, in the presence of a perpendicular magnetic field, an originally type I superconductor thick film must present type II properties as the film

---

[a] Contains material from the manuscript: Stray Field Contribution to Vortex Interaction in superconducting Thin Films: Extended Ginzburg-Landau Analysis (in preparation)

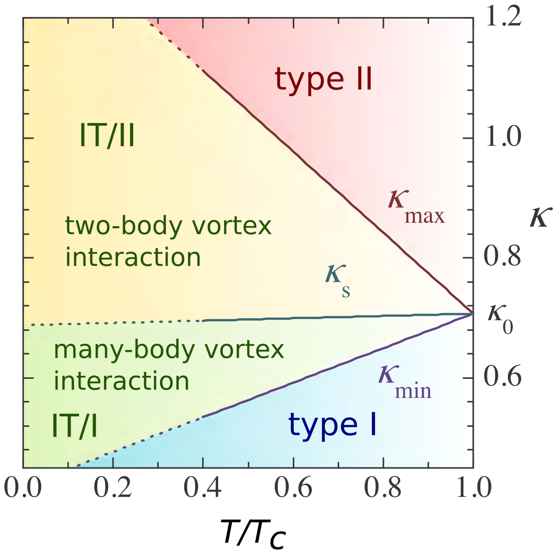

Figure 8-1 : Phase diagram of the superconductivity types in the $(\kappa, T\ )$plane. (see [90, 139])

thickness decreases sufficiently. We have shown in Chapter 4 and [91], that this transition from type-I to type-II domain occurs via the intertype domain. Our results have revealed various non-standard patterns such as lattices of superconducting islands separated by vortex chains; complex vortex stripes and worms, and mixtures of giant vortices and vortex clusters. All this configurations are qualitatively different from the standard flux/condensate patterns observed in traditional types-I and type-II superconductors. They can be explained by recalling that the vortex-vortex interaction has two contributions of opposite signs: one of them is due to the magnetic field and the other comes from the condensate. In bulk type-I materials the condensate contribution is dominant and the resulting vortex interaction is attractive. However, as the film thickness d decreases, the contribution due to stray magnetic fields grows, and finally the interaction becomes repulsive. The thickness is, therefore, a parameter that can be used to gradually drive the system from type-I to type-II by passing through the intertype domain in the (d, T)-plane. However, contrary to what is seen in the (κ, T)-plane, here the intertype domain does not collapse into a single point as $T \to T_c$. Indeed, unlike bulk materials, the intertype regime for thin films can be at least qualitatively described by the Ginzburg-Landau theory amended with the equations for the stray fields. The reason is that here the degeneracy is removed mainly by the stray field contribution and thus the non-local condensate interactions beyond the realm of the Ginzburg-Landau theory (responsible for lifting the Bogomolnyi-point degeneracy in bulk) can be safely neglected if the temperature is not so low.

Recently theoretical studies using the Extended Ginzburg Landau (EGL) formalism [45–47] have show that the intertype regime can be found in both single and multiband superconducting bulk samples [90,139]. Moreover, by analyzing the character of the vortices interaction in IT domain in superconductors, the authors of ref [90], have shown that the IT domain is composed of two subdomains, IT/I and IT/II, each of them with diferent characteristics. Whereas in the IT/II the vortex interaction potential has a two-body character and a non-monotonic spacial interaction (long-range attraction and short-range repulsion), in the IT/I subdomain the vortex interaction is dominated by many body interaction wich stabilize large clusters and can develop very peculiar vortex matter.

With this in mind, we calculate the vortex-vortex interaction for different clusters [see Fig. **8-3**] for a superconducting film in the presence of a perpendicular external magnetic field. Our objective is to understand how the vortex-vortex interaction change with thickness and what is the influence of stray fields on it. These calculation will be done using the EGL formalism.

8.2 Formalism

We work with the Gibbs free energy, that contained both contribution, the Gibbs energy of the superconducting sample with thickness d and the Gibbs free energy of the stray fields outside the superconductor, as shown in Fig. **8-2**.

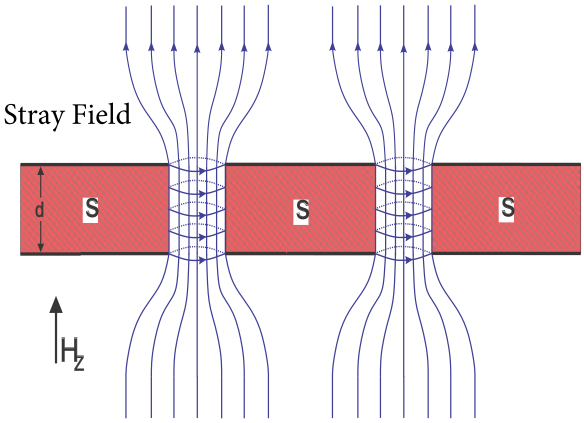

Figure 8-2 : Schematic representation of a thin film showing the curvature of the field (stray fields)

$$\mathcal{G} = \mathcal{G}_{\text{Sup.sample}} + \mathcal{G}_{\text{Stray field}}. \tag{8.1}$$

8.2.1 Gibbs free energy of the superconductive sample

We consider that the free energy does not change over the thickness of the sample (d), therefore,the Gibbs free energy of the superconductor is written as

$$\mathcal{G}_{Sup.sample} = \int g d^3\boldsymbol{r} = d \int g d^2\boldsymbol{r}, \qquad g = f_s + \frac{\boldsymbol{B}^2}{8\pi} - \frac{\boldsymbol{BH}}{4\pi}, \tag{8.2}$$

where $\boldsymbol{B}$ is the magnetic field (induction), $\boldsymbol{H}$ is external (uniform) field, both directed along the z direction and f_s is the energy of the condensate. We subtract the Gibbs energy density g_M of the uniform Meissner state at $H = H_c$, where the Gibbs free energy difference is analysed.

$$\begin{aligned} \mathfrak{g} &= g - g_M = f_s + \frac{\boldsymbol{B}^2}{4\pi} - \frac{\boldsymbol{B}H_c}{4\pi} - \frac{H_c^2}{8\pi} + \frac{H_c^2}{4\pi} \\ \mathfrak{g} &= f_s + \frac{(B - H_c)^2}{8\pi} \end{aligned} \tag{8.3}$$

Now, the total flux of the field B coincides with the flux of the external field $H = H_c + \delta H$, where the energy density takes a new version

$$\begin{aligned} &g = f_s + \frac{\boldsymbol{B}^2}{8\pi} - \frac{\boldsymbol{BH}}{4\pi} = f_s + \frac{\boldsymbol{B}^2}{8\pi} - \frac{\boldsymbol{B}H_c}{4\pi} - \frac{\boldsymbol{B}\delta H}{4\pi} \\ &g = g + g_{H_c} - g_{H_c} = f_s + \frac{\boldsymbol{B}^2}{8\pi} - \frac{\boldsymbol{B}H_c}{4\pi} - \frac{\boldsymbol{B}\delta H}{4\pi} + \frac{H_c^2}{8\pi} - \frac{H_c^2}{8\pi} = f_s + \frac{(B - H_c)^2}{8\pi} - \frac{\boldsymbol{B}\delta H}{4\pi} - \frac{H_c^2}{8\pi} \\ &g = \mathfrak{g} - \frac{B\delta H}{4\pi} - \frac{H_c^2}{8\pi}, \end{aligned} \tag{8.4}$$

obtained by expanding all pertinent physical quantities. The spatial coordinates are scaled as $\tau^{1/2}\boldsymbol{r}$, which introduces the corresponding scaling into the spatial derivatives. The gap function Δ and the magnetic field $\boldsymbol{B}$ (or the vector potential $\boldsymbol{A}$) are represented in the form

$$\begin{aligned} \Delta &= \tau^{1/2}(\Psi + \tau\psi + \cdots) \\ \boldsymbol{B} &= \tau(\mathfrak{B} + \tau\mathfrak{b} + \cdots) \\ \boldsymbol{A} &= \tau^{1/2}(\mathfrak{A} + \tau\mathfrak{a} + \cdots) \end{aligned} \tag{8.5}$$

The density of the Gibbs free energy difference is given by the expansion

$$\mathfrak{g} = \tau^2(\mathfrak{g}^{(0)} + \tau\mathfrak{g}^{(1)} + \cdots), \tag{8.6}$$

the free energy density of the condensate as [69],

$$f = \tau^2(f^{(0)} + \tau f^{(1)} + \cdots), \tag{8.7}$$

the leading-order correlation to GL free energy are split into two parts

$$f^{(1)} = f_1^{(1)} + f_2^{(1)}, \tag{8.8}$$

then

$$\mathfrak{g}^{(0)} = \frac{(\mathfrak{B} - H_c^{(0)})^2}{8\pi} + f^{(0)} \tag{8.9}$$

$$\mathfrak{g}^{(1)} = \frac{(\mathfrak{B} - H_c^{(0)})(\mathfrak{b} - H_c^{(1)})}{8\pi} + f^{(1)} \tag{8.10}$$

where

$$f^{(0)} = a|\Psi|^2 + \frac{b}{2}|\Psi|^4 + \mathcal{K}|\mathfrak{D}\Psi|^2, \tag{8.11}$$

with $\mathfrak{D} = \boldsymbol{\nabla} - i\frac{2e\mathfrak{A}}{\hbar\boldsymbol{c}}$ the gauss invariant derivative with the leading order contribution of the vector potential and $\mathfrak{i} = i\frac{2e}{\hbar\boldsymbol{c}}(\Psi\mathfrak{D}^*\Psi^* - \Psi^*\mathfrak{D}\Psi)$

$$\begin{aligned} f_1^{(1)} &= \frac{a}{2}|\Psi|^2 + 2\mathcal{K}|\mathfrak{D}\Psi|^2 + b|\Psi|^4 + \frac{b}{36}\frac{e^2\hbar^2}{m^2\boldsymbol{c}}\mathfrak{B}^2|\Psi|^2 \\ &- \mathcal{Q}\left\{|\mathfrak{D}^2\Psi|^2 + \frac{1}{3}(\mathrm{rot}\mathfrak{B}\cdot\mathfrak{i}) + \frac{4e^2}{\hbar^2\boldsymbol{c}^2}\mathfrak{B}^2|\Psi|^2\right\} \\ &- \frac{\mathcal{L}}{2}\left\{8|\Psi|^2|\mathfrak{D}\Psi|^2 + [\Psi^2(\mathfrak{D}^*\Psi^*)^2 + c.c]\right\} - \frac{c}{3}|\Psi|^6 \end{aligned} \tag{8.12}$$

and includes only the lowest-order contribution Ψ and $\mathfrak{B}(\mathfrak{A})$ to the gap field, respectively, while the second part writes

$$f_2^{(1)} = (a + b|\Psi|^2)(\Psi^*\psi + \Psi\psi^*) + \mathcal{K}[(\mathfrak{D}\Psi\cdot\mathfrak{D}^*\psi^* + c.c.) - \mathfrak{a}\cdot\mathfrak{i}] \tag{8.13}$$

The coefficients in Eqs. (8.11)-(8.13) are obtained using a chosen microscopic model of the charge-carrier states. In particular, for a spherical Fermi surface in the clean limit one gets

$$\begin{aligned} a &= -\mathcal{N}(0), & \mathcal{K} &= \frac{b}{6}\hbar^2 v_F^2, \\ b &= \mathcal{N}(0)\frac{7\zeta(3)}{8\pi^2 T_c^2}, & \mathcal{Q} &= \frac{c}{30}\hbar^4 v_F^4, \\ c &= \mathcal{N}(0)\frac{93\zeta(5)}{128\pi^4 T_c^4}, & \mathcal{L} &= \frac{c}{9}\hbar^2 v_F^2 \end{aligned} \tag{8.14}$$

where $\mathcal{N}(0) = \frac{mk_F}{(2\pi^2\hbar^2)}$ is the carrier density of states (DOS) at the Fermi surface with the Fermi momentum k_F and Fermi velocity $v_F = \hbar k_F/m$. To proceed further, it is convenient to introduce the following dimensionless quantities:

$$\begin{aligned}
&\widetilde{\boldsymbol{r}} = \frac{\boldsymbol{r}}{\sqrt{2}\lambda}, \quad \widetilde{\mathfrak{A}} = \kappa\frac{\mathfrak{A}}{H_c^{(0)}\lambda}, \quad \widetilde{\mathfrak{B}} = \kappa\sqrt{2}\frac{\mathfrak{B}}{H_c^{(0)}}, \quad \widetilde{\Psi} = \sqrt{-\frac{b}{a}}\Psi \\
&\widetilde{\mathfrak{D}} = \sqrt{2}\lambda\mathfrak{D}, \qquad \widetilde{\mathfrak{i}} = 4\pi\frac{\mathcal{K}\lambda}{H_c^{(0)}}, \quad \mathfrak{g} = \frac{(H_c^{(0)})^2}{4\pi}\widetilde{\mathfrak{g}} \quad \mathcal{G} = \frac{(H_c^{(0)})^2(\sqrt{2}\lambda)^3}{4\pi}\widetilde{G}
\end{aligned} \tag{8.15}$$

where $\lambda = \hbar^2\boldsymbol{c}b/32\pi e^2\mathcal{K}|a|$ and $\kappa = \lambda/\xi = \lambda\sqrt{|a|/\mathcal{K}}$.

$$\mathcal{G}_{\text{Sup.sample}} = \frac{(H_c^{(0)})^2}{4\pi}(\sqrt{2}\lambda)^3\tilde{d}\left[\int_s \widetilde{\mathfrak{g}}d^2\widetilde{r} - \int_s \widetilde{\mathfrak{B}}\delta\widetilde{H}d^2r - \int_s \frac{1}{2}d^2r\right] \tag{8.16}$$

the Gibbs energy difference becomes (see Appendix C)

$$\mathfrak{g}^{(0)} = \frac{1}{2}\left(\frac{\mathfrak{B}}{\kappa\sqrt{2}} - 1\right) - |\widetilde{\Psi}|^2 + \frac{1}{2}|\widetilde{\Psi}|^4 + \frac{1}{2\kappa^2}|\widetilde{\mathfrak{D}}\widetilde{\Psi}|^2 \tag{8.17}$$

$$\begin{aligned}
\mathfrak{g}^{(1)} = &\left(\frac{\widetilde{\mathfrak{B}}}{\kappa\sqrt{2}} - 1\right)\left(\frac{1}{2} + \frac{ac}{3b^2}\right) - \frac{1}{2}|\widetilde{\Psi}|^2 + |\widetilde{\Psi}|^4 + \frac{ca}{3b^2}|\widetilde{\Psi}|^6 + \frac{1}{\kappa^2}|\widetilde{\mathfrak{D}}\widetilde{\Delta}|^2 \\
&+ \frac{\mathcal{Q}a}{\mathcal{K}^2}\frac{1}{4\kappa^4}\left(|\widetilde{\mathfrak{D}}^2\widetilde{\Psi}|^2 + \frac{1}{3}\text{rot}\widetilde{\mathfrak{B}} \cdot \widetilde{\mathfrak{i}} + \widetilde{\mathfrak{B}}|\widetilde{\Psi}|^2\right) \\
&+ \frac{\mathcal{L}a}{\mathcal{K}b}\frac{1}{4\kappa^2}\left(8|\widetilde{\Psi}|^2|\widetilde{\mathfrak{D}}\widetilde{\Psi}|^2 + \widetilde{\Psi}^{*2}(\widetilde{\mathfrak{D}}\widetilde{\Psi})^2 + \widetilde{\Psi}^2(\widetilde{\mathfrak{D}}^*\widetilde{\Psi}^*)^2\right)
\end{aligned} \tag{8.18}$$

The physical quantities are scaled in function τ, also the Gibbs free energy scaled in τ is equal to:

$$\widetilde{\mathcal{G}}_{\text{Sup.sample}} = \tau^{1/2}(\tilde{d}\sqrt{\tau})\left[\int_s \widetilde{\mathfrak{g}}d^2\widetilde{r} - \int_s \widetilde{\mathfrak{B}}\delta\widetilde{H}d^2r - \int_s \frac{1}{2}d^2r\right] \tag{8.19}$$

Since we are interested in the solution near the Bogomolnyi point, it is also useful to introduce the expansion over $\delta\kappa = \kappa - \kappa_0$, where $\kappa_0 = 1/\sqrt{2}$, and employ the perturbation expansion. With respect to $\delta\kappa$, with this aim we need to expand $\widetilde{\mathfrak{g}}^{(0)}$ in $\delta\kappa$

$$\begin{aligned}
\widetilde{\mathfrak{g}}^{(0)} &= \widetilde{\mathfrak{g}}^{(0)}\Big|_{\kappa=\frac{1}{\sqrt{2}}} + \delta\kappa\left\{\frac{\partial\widetilde{\mathfrak{g}}^{(0)}}{\partial\kappa}\Big|_{\kappa=\frac{1}{\sqrt{2}}} + \int dr\left(\underbrace{\frac{\delta\widetilde{\mathfrak{g}}^{(0)}}{\delta\Psi}\frac{d\Psi}{d\kappa}}_{=0} + \underbrace{\frac{\delta\widetilde{\mathfrak{g}}^{(0)}}{\delta\Psi^*}\frac{d\Psi^*}{d\kappa}}_{=0} + \underbrace{\frac{\delta\widetilde{\mathfrak{g}}^{(0)}}{\delta\mathfrak{A}}\frac{d\mathfrak{A}}{d\kappa}}_{=0}\right)\right\} + \widetilde{\mathfrak{g}}^{(1)}\Big|_{\kappa=\frac{1}{\sqrt{2}}}\tau \\
\widetilde{\mathfrak{g}}^{(0)} &= \widetilde{\mathfrak{g}}^{(0)}\Big|_{\kappa=\frac{1}{\sqrt{2}}} + \frac{\partial\widetilde{\mathfrak{g}}^{(0)}}{\partial\kappa}\Big|_{\kappa=\frac{1}{\sqrt{2}}}\delta\kappa + \widetilde{\mathfrak{g}}^{(1)}\Big|_{\kappa=\frac{1}{\sqrt{2}}}\tau.
\end{aligned} \tag{8.20}$$

Then, the free energy can be written as,

$$\begin{aligned}\widetilde{\mathcal{G}}_{\text{Sup.sample}} =&\tau^{1/2}(\tilde{d}\sqrt{\tau})\left[\int_s d^2\widetilde{r}\left(\widetilde{\mathfrak{g}}^{(0)}\Big|_{\kappa=\frac{1}{\sqrt{2}}} + \frac{\partial\widetilde{\mathfrak{g}}^{(0)}}{\partial\kappa}\Big|_{\kappa=\frac{1}{\sqrt{2}}}\delta\kappa + \widetilde{\mathfrak{g}}^{(1)}\Big|_{\kappa=\frac{1}{\sqrt{2}}}\tau\right) -\right.\\ &\left. -\int_s \widetilde{\mathfrak{B}}\delta\widetilde{H}d^2r - \int_s \frac{1}{2}d^2r\right].\end{aligned} \tag{8.21}$$

Note, that the implicit contributions are zero because they are proportional to $\delta\widetilde{\mathfrak{g}}^{(0)}/\delta\Psi^*$ and $\delta\widetilde{\mathfrak{g}}^{(0)}/\delta\mathfrak{A}$, which are zero in the equilibrium. At $\kappa = \kappa_0 = 1/\sqrt{2}$, a solution to the GL equation can be obtained by using Bogomolnyi self-duality equations (see Appendix D)

$$\mathfrak{B} = 1 - |\Psi|^2, \qquad (\partial_y + i\partial_x)\Psi = (\mathfrak{A}_x - i\mathfrak{A}_y)\Psi \tag{8.22}$$

Using a solution to Bogomonlyi equation one can represent $\mathcal{G}_{\text{Sup.sample}}$ in terms of Ψ

$$\begin{aligned}\widetilde{\mathfrak{g}}^{(0)}|_{\kappa=\frac{1}{\sqrt{2}}} &= \frac{1}{2}(1-\widetilde{\mathfrak{G}})^2 - |\widetilde{\Psi}|^2 + \frac{1}{2}|\widetilde{\Psi}|^4 + |\widetilde{\mathfrak{D}}\widetilde{\Psi}|^2\\ &= \frac{1}{2}(1-1+|\widetilde{\Psi}|^2)^2 - |\widetilde{\Psi}|^2 + \frac{1}{2}|\widetilde{\Psi}|^4 + \widetilde{\Psi}^*(-\widetilde{\mathfrak{g}}^2\widetilde{\Psi})\\ &= \frac{1}{2}|\widetilde{\Psi}|^4 - |\widetilde{\Psi}|^2 + \frac{1}{2}|\widetilde{\Psi}|^4 + \widetilde{\Psi}^*(\widetilde{\Psi}(1-|\widetilde{\Psi}|^2))\\ &= 0.\end{aligned} \tag{8.23}$$

The contribution $\widetilde{\mathfrak{g}}^{(0)}|_{\kappa=\frac{1}{\sqrt{2}}}$ corresponds to the GL contribution and at $\kappa = \kappa_0$ is equal to zero due to the Bogomonlnyi degeneracy. The other contributions

$$\begin{aligned}\frac{\partial\widetilde{\mathfrak{g}}^{(0)}}{\partial\kappa}|_{\kappa=\frac{1}{\sqrt{2}}} &= \frac{2}{2}\left(1-\frac{\widetilde{\mathfrak{B}}}{\kappa\sqrt{2}}\right)\left(-\frac{\widetilde{\mathfrak{B}}}{\sqrt{2}}\right)\left(-\frac{1}{\kappa}\right) - \frac{1}{\kappa^3}|\widetilde{\mathfrak{D}}\widetilde{\Psi}|\Bigg|_{\kappa=\frac{1}{\sqrt{2}}}\\ &= (1-\widetilde{\mathfrak{B}})\widetilde{\mathfrak{B}}\frac{1}{\kappa} + \frac{1}{\kappa^3}\widetilde{\Psi}^*\widetilde{\mathfrak{D}}^2\widetilde{\Psi}\Bigg|_{\kappa=\frac{1}{\sqrt{2}}}\\ &= -\sqrt{2}|\widetilde{\Psi}|^2(1-|\widetilde{\Psi}|^2).\end{aligned} \tag{8.24}$$

the terms that correspond to $\mathfrak{g}^{(1)}$ can be writen as function of Ψ

$$|\widetilde{\mathfrak{D}}\widetilde{\Psi}|^2 \rightarrow |\widetilde{\Psi}|^2(1-|\widetilde{\Psi}|^2), \tag{8.25}$$

$$|\widetilde{\mathfrak{B}}^2\widetilde{\Psi}|^2 \rightarrow |\widetilde{\Psi}|^2(1-|\widetilde{\Psi}|^2) - |\widetilde{\Psi}|^4(1-|\widetilde{\Psi}|^2), \tag{8.26}$$

$$\text{rot}\widetilde{\mathfrak{B}}\cdot\widetilde{\mathfrak{i}} = \mathfrak{i}^2 = \widetilde{2}|\widetilde{\Psi}|^2|\widetilde{\mathfrak{D}}\widetilde{\Psi}|^2, \qquad |\widetilde{\Psi}|^2|\widetilde{\mathfrak{D}}\widetilde{\Psi}|^2 = \frac{1}{2}|\widetilde{\Psi}|^2(1-|\widetilde{\Psi}|^2). \tag{8.27}$$

Now we can represent $\mathcal{G}$ in terms of $\mathcal{I}$ and $\mathcal{J}$ which are integrals that depend exclusively as a function of order parameter Ψ

$$\mathcal{I} = \int d^2\mathbf{r}|\Psi|^2(1-|\Psi|^2), \quad \mathcal{J} = \int d^2\mathbf{r}|\Psi|^4(1-|\Psi|^2), \tag{8.28}$$

$$\mathcal{G}_{\text{Sup.sample}} = \tau^{1/2} d\sqrt{\tau}\left\{-\sqrt{2}\mathcal{I}\delta\kappa + \tau\left[(1-\widetilde{c}+2\widetilde{\mathcal{Q}})\mathcal{I} + \left(2\widetilde{\mathcal{L}}-\widetilde{c}-\frac{5}{3}\widetilde{\mathcal{Q}}\right)\mathcal{J}\right] - \int_s \mathfrak{B}\delta H d^2r - \int_s \frac{H_c^2}{2}d^2r\right\}. \tag{8.29}$$

with the dimensionless coefficients

$$\widetilde{c} = \frac{ca}{3b^2} = -0.227, \qquad \widetilde{\mathcal{Q}} = \frac{\mathcal{Q}a^2}{\mathcal{K}} = -0.454, \qquad \widetilde{\mathcal{L}} = \frac{\mathcal{L}a}{b\mathcal{K}} = -0.817. \tag{8.30}$$

these constants are material independent for the chosen model [69].

8.2.2 Stray Field Gibbs Energy Outside the Superconductor

The Gibbs free energy of the stray field is given by,

$$\mathcal{G}_{\text{Stray field}} = \int d^3r \frac{\boldsymbol{B}(\boldsymbol{r})^2}{8\pi}. \tag{8.31}$$

We consider that the field inside the superconductor has component z and outside the superconductor there is no current. Thus from Ampère's law we have $\boldsymbol{\nabla}\times\boldsymbol{B} = 4\pi\boldsymbol{J} = 0; \quad \nabla\cdot\boldsymbol{B} = 0$, which results $\boldsymbol{\nabla}\times\boldsymbol{B} = 0 \Rightarrow \boldsymbol{\nabla}\times\boldsymbol{\nabla}\varphi = 0$ which implies that $\boldsymbol{B}$ can be written in terms of a magnetic scalar potential $\boldsymbol{B} = -\boldsymbol{\nabla}\varphi$

$$\boldsymbol{\nabla}\cdot\boldsymbol{B} = 0 \Rightarrow \nabla^2\varphi = 0 \tag{8.32}$$

The boundary condition is $\nabla_z\varphi = -B_z(x,y) \Rightarrow \nabla_\perp\varphi = f(x,y)$. If $\boldsymbol{B}$ has only the normal component, than φ is constant on the plane $\nabla_{\|}\varphi = 0 \rightarrow \varphi = \text{Constant}$. Therefore, our work is reduced to in solving the Laplace equation for φ.

The solution of Laplace's equation for the scalar pottential can be found by direct integration of the Green's function.

$$\varphi(\boldsymbol{r}) = \frac{1}{4\pi}\oint_s\left(\frac{1}{\boldsymbol{R}}\frac{\partial\varphi(\boldsymbol{r})}{\partial\hat{n}} + \varphi(\boldsymbol{r})\frac{\partial}{\partial\hat{n}}\frac{1}{\boldsymbol{R}}\right)d^2\boldsymbol{r}, \qquad \boldsymbol{R} = |\boldsymbol{r}-\boldsymbol{r}'|. \tag{8.33}$$

With the boundary condition φ reduce to

$$\varphi(\boldsymbol{r}) = \frac{1}{4\pi}\oint_s \frac{1}{|\boldsymbol{r}-\boldsymbol{r}'|}\frac{\partial\varphi(\boldsymbol{r}')}{\partial\hat{n}}d^2\boldsymbol{r} = -\frac{1}{4\pi}\oint_s \frac{B_z(\boldsymbol{r}')}{|\boldsymbol{r}-\boldsymbol{r}'|}d^2\boldsymbol{r}', \tag{8.34}$$

therefore,

$$\boldsymbol{B}(\boldsymbol{r}) = -\boldsymbol{\nabla}\varphi(\boldsymbol{r}) = \frac{1}{4\pi}\oint_s d^2\boldsymbol{r}'\boldsymbol{\nabla}\frac{B_z(\boldsymbol{r}')}{|\boldsymbol{r}-\boldsymbol{r}'|}. \tag{8.35}$$

Since the magnetic flux is independent on the distance form boundary of the superconductor, we can write,

$$\begin{aligned}\mathit{\Phi} = \frac{\int_S \boldsymbol{B}d^2\boldsymbol{r}}{\int_S d^2\boldsymbol{r}} &= \frac{1}{4\pi S}\int_S\oint_s \boldsymbol{\nabla}\frac{B_z(\boldsymbol{r}')}{|\boldsymbol{r}-\boldsymbol{r}'|}d^2\boldsymbol{r}'d^2\boldsymbol{r} = \frac{1}{4\pi S}\int_V\oint_s \nabla^2\frac{B_z(\boldsymbol{r}')}{|\boldsymbol{r}-\boldsymbol{r}'|}d^2\boldsymbol{r}'d^3\boldsymbol{r}\\ &= \frac{1}{4\pi S}\oint_s B_z(\boldsymbol{r}')d^2\boldsymbol{r}'\int_V \underbrace{\nabla^2\frac{1}{|\boldsymbol{r}-\boldsymbol{r}'|}}_{-4\pi\delta(\boldsymbol{r}-\boldsymbol{r}')}d^3\boldsymbol{r} = \frac{1}{S}\oint_s B_z(\boldsymbol{r}')d^2\boldsymbol{r}'.\end{aligned} \tag{8.36}$$

Then, the stray field energy is given by,

$$\begin{aligned}\mathcal{G}_{\text{Stray field}} &= \frac{1}{8\pi}\int \boldsymbol{B}^2(\boldsymbol{r})d^3\boldsymbol{r} = \frac{1}{8\pi}\frac{1}{4\pi}\frac{1}{4\pi}\int_V\int_s\int_s \boldsymbol{\nabla}\frac{B_z(\boldsymbol{r}')}{|\boldsymbol{r}-\boldsymbol{r}'|}\boldsymbol{\nabla}\frac{B_z(\boldsymbol{r}'')}{|\boldsymbol{r}-\boldsymbol{r}''|}d^2\boldsymbol{r}'d^2\boldsymbol{r}''d^3\boldsymbol{r}\\ &= \frac{1}{8\pi}\frac{1}{4\pi}\frac{1}{4\pi}\int_s\int_s\left(\int_V \boldsymbol{\nabla}\frac{1}{|\boldsymbol{r}-\boldsymbol{r}'|}\boldsymbol{\nabla}\frac{1}{|\boldsymbol{r}-\boldsymbol{r}''|}d^3\boldsymbol{r}\right)B_z[\boldsymbol{r}']B_z[\boldsymbol{r}'']d^2\boldsymbol{r}'d^2\boldsymbol{r}''.\end{aligned} \tag{8.37}$$

Using the relation $\boldsymbol{\nabla}(\boldsymbol{a}(\boldsymbol{r})\boldsymbol{\nabla}\boldsymbol{b}(\boldsymbol{r})) = \boldsymbol{\nabla}\boldsymbol{a}(\boldsymbol{r})\boldsymbol{\nabla}\boldsymbol{b}(\boldsymbol{r}) + \boldsymbol{a}(\boldsymbol{r})\nabla^2\boldsymbol{b}(\boldsymbol{r})$, we can write,

$$\frac{1}{4\pi}\frac{1}{4\pi}\int_V \boldsymbol{\nabla}\frac{1}{|\boldsymbol{r}-\boldsymbol{r}'|}\boldsymbol{\nabla}\frac{1}{|\boldsymbol{r}-\boldsymbol{r}''|}d^3\boldsymbol{r} = \frac{1}{4\pi}\frac{1}{4\pi}\int_s \frac{1}{|\boldsymbol{r}-\boldsymbol{r}'|}\boldsymbol{\nabla}\frac{1}{|\boldsymbol{r}-\boldsymbol{r}''|}d^2\boldsymbol{r} + \frac{1}{4\pi}\frac{1}{|\boldsymbol{r}''-\boldsymbol{r}'|}. \tag{8.38}$$

Since that field is calculated on both sides of the superconducting sample, and since it is antisymmetric.

$$\int_s \frac{1}{|\boldsymbol{r}-\boldsymbol{r}'|}\boldsymbol{\nabla}\frac{1}{|\boldsymbol{r}-\boldsymbol{r}''|}d^2\boldsymbol{r} = \int_{s_1} d^2\boldsymbol{r}_1 + \int_{s_2} d^2\boldsymbol{r}_2\left(\frac{1}{|\boldsymbol{r}-\boldsymbol{r}'|}\boldsymbol{\nabla}\frac{1}{|\boldsymbol{r}-\boldsymbol{r}''|}\right) = 0, \tag{8.39}$$

due to the symetry $d^2\boldsymbol{r}_1 = -d^2\boldsymbol{r}_2$, and to the fact that the integral is now extended on the entire space

$$\mathcal{G}_{\text{Stray field}} = \frac{1}{8\pi}\frac{1}{4\pi}\int_S\int_s \frac{B_z(\boldsymbol{r}')B_z[\boldsymbol{r}'']}{|\boldsymbol{r}''-\boldsymbol{r}'|}d^2\boldsymbol{r}'d^2\boldsymbol{r}'' \tag{8.40}$$

scaling the expression for the energy with the dimensional units defined in (8.14) and τ (8.5)

$$\widetilde{\mathcal{G}}_{\text{Stray field}} = \frac{\tau^{1/2}}{8\pi}\int_S\int_s \frac{\mathfrak{B}(\boldsymbol{r}')\mathfrak{B}(\boldsymbol{r}'')}{|\boldsymbol{r}''-\boldsymbol{r}'|}d^2\boldsymbol{r}'d^2\boldsymbol{r}''. \tag{8.41}$$

It is important to notice that the $\mathcal{G}_{\text{Sup.sample}}$ defined by Eqs. (8.28), (8.29) and (8.41) depends only on the solution of Eq. (8.22), demonstrating that the properties of the vortex matter in the IT domain are fully determined by the Bogomolyi self-duality.

8.2.3 Multi-vortex Configurations

We consider now the case of multi-vortex configuration. We start by rewriting the Bogomolnyi equations in order to simplify the work for obtaining a solution for any arbitrary configuration of vortices (both single- and multi-quantum). To solve the Bogomolnyi equations it is conveniently to recall that the vector potential is generally written as $\boldsymbol{A} = (A_x, A_y, 0)$, when the magnetic field has only z component $\boldsymbol{B} = (0, 0, B_z)$.

Adopting the Coulomb gauge $\nabla \cdot \mathbf{A} = \partial_x A_x + \partial_y A_y = 0$, we can introduce the scalar potential ϕ so that

$$A_x = -\partial_y \phi, \quad A_y = \partial_x \phi. \tag{8.42}$$

In this case for the magnetic field we have

$$\boldsymbol{B} = \mathrm{rot}\boldsymbol{A} = \nabla^2 \phi = (\partial_x^2 + \partial_y^2)\phi. \tag{8.43}$$

Using the substitution $\Psi = e^{-\phi}\Phi$, Substituting this ansatz into Bogomolnyi self equation, we obtain

$$\begin{aligned}
\mathfrak{D}_-\Psi = (\mathfrak{D}_x - i\mathfrak{D}_y)\Psi = [(\partial_x + iA_x) - i(\partial_y + iA_y)]e^{-\phi}\Phi &= 0 \\
(\partial_x - i\partial_y\phi)e^{-\phi}\Phi - i(\partial_y + i\partial_x\phi)e^{-\phi}\Phi &= 0 \\
{}^{-\phi}\partial_x\Phi - ie^{-\phi}\partial_y\Phi = (\partial_y + i\partial_x)\Phi &= 0.
\end{aligned} \tag{8.44}$$

This is the standard condition that Φ is an analytical function of the complex variable $Z = x + iy$. The other equation is,

$$\mathfrak{B} = 1 - |\Psi|^2 \quad \Longrightarrow \quad \nabla^2\phi = 1 - |e^{-\phi}\Phi|^2 = 1 - e^{-2\phi}|\Phi|^2, \tag{8.45}$$

Φ can easily be chosen to represent a mixed state with an arbitrary vortex spatial configuration. Indeed, the positions of vortices are defined by the zeros of Φ that fully define any analytic properties of a complex function. For example, a single vortex positioned at $\boldsymbol{a}$ is obviously described by $\Phi = Z - \boldsymbol{a}$, where $\boldsymbol{a} = a_x + a_y$. Two vortices located at a_1 and a_2 correspond to $\Phi = (Z - a_1)(Z - a_2)$, with $a_i = a_{i,x} + a_{i,y}$. Similarly one can construct Φ that corresponds to any spatial configuration of multiple single-quantum vortices at positions

$\mathbf{a}_i$'s, i.e., $\Psi = \prod_i (Z - a_i)$, see [69]. In turn, an isolated N-quantum vortex located at $\mathbf{a}$ yields $\Psi = (Z - a)^N$, etc.

Then, the solution that describes N vortex with the centers at $\boldsymbol{r}_i$ is obtained as follows. First find $\Psi_1(\boldsymbol{r})$ that describes an isolated Abrikosov vortex with the center at $\boldsymbol{r} = 0$. Then we represent the N-vortex solution in the form

$$\Psi(\boldsymbol{r}) = e^{-\delta\phi} \prod_{i=1}^{N} \Psi_i, \quad \Psi_i = \Psi_1(\boldsymbol{r} - \boldsymbol{r}_i). \tag{8.46}$$

Here Ψ represents the solution for an isolated N_i-quantum vortex located at $\boldsymbol{r}_i$. As already mentioned in the previous paragraph, Ψ_i is given by

$$\Psi_i = (Z - a_i)^{N_i} e^{-\phi_i}, \tag{8.47}$$

where ϕ_i satisfies

$$(\partial_x^2 + \partial_y^2)\phi_i = 1 - |\Psi_i|^2, \tag{8.48}$$

so that

$$\phi = \delta\phi + \sum_i \phi_i. \tag{8.49}$$

Substituting this into the last equation, we obtains,

$$(\partial_x^2 + \partial_y^2)\delta\phi = 1 + \sum_i (|\Psi_i|^2 - 1) - e^{-2\delta\phi} \prod_i |\Psi_i|^2 \tag{8.50}$$

Solving this equation and substituting the obtained Ψ, we find the Gibbs free energy difference G for the N-vortex and then extract the corresponding interaction energy (interaction potential) by subtracting the energies of N isolated vortices

$$\mathcal{G}_{int} = \mathcal{G}/N - \mathcal{G}_1, \tag{8.51}$$

where the $\mathcal{G}_1$ the free energy by the single vortex solution.

To simulate structure formations of a system of interacting vortex, we use the Metropolis Monte Carlo method as discussed in Chapter 4 section 4.3.

We consider a thin superconducting define a square region with dimensions $L \times L$, where vortices are treated as interacting elementary particles in two dimensions with position (x, y), free to move in any direction in the plane. To reduce surface effects we impose periodic boundary conditions. The simulations will be performed at a constant number of particles N (vortices), constant system area $L \times L$, and constant temperature T, in this case, we choose

$\tau = 1$ (exactly in the Bogomonlyi point).

Applied for a system of vortices, the Metropolis Monte Carlo algorithm is as follows:

1. Generate a starting configuration and calculate the energy $\mathcal{G}_0$.
2. Randomly pick one vortex and change position in a random direction by a length of $\chi \cdot d$, where χ is a random number between 0 and 1 and d is the maximal step length.
3. Calculate the new energy $\mathcal{G}$ of the system.
4. If the net change of energy $\Delta\mathcal{G} = \mathcal{G} - \mathcal{G}_0$ is positive, keep the new vortex state. If $\Delta\mathcal{G}$ is negative, draw a random number η between 0 and 1, and keep the new vortex position if $\exp(-\beta\Delta\mathcal{G}) > \eta$, otherwise, the old state is the new state.
5. Set $\mathcal{G}_0 = \mathcal{G}$ and repeat from step 1 for a desired number of iterations.

To calculate the Gibbs energy, we calculate Ψ using Eqs. (8.50) and (8.46), after calculate integrals $\mathcal{I}$, $\mathcal{J}$ Eqs. (8.28) and $\mathfrak{B} = 1 - |\Psi|^2$, finally calculate the Gibs free energy $\mathcal{G}$. In order to solve numerically (8.50) and (8.41), one can use either fast Fourier transform (FFT) algorithm [140].

8.3 Results

The vortex interaction in superconductors depends on control parameters, some of these parameters can be: Type of superconductor, which in the case depends on the value of GL-parameter κ and the thickness of the superconducting sample where effects produced by stray fields take an important role [91].

Under these conditions, we will analyse how the vortices interaction behaves with the variation of the thickness of the superconductor sample. We will consider superconductors with different thicknesses that can represent volumetric superconductors until the thinner one which will be of the order of λ, for different values of $\delta\kappa$.

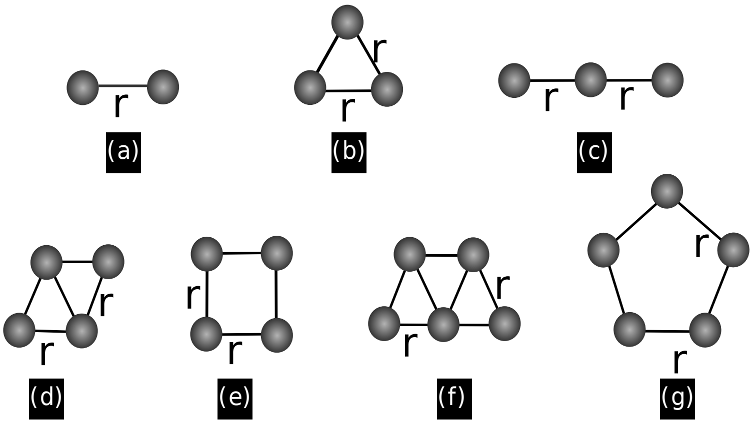

Figure 8-3 : Vortex cluster configuration (a) two vortex (b)-three vortex -T (c) three vortex -L (d) four vortex -T (e) four vortex -S (f) five vortex -T (g) five vortex -P

For this analysis we choose different configurations of vortex cluster. Fig. **8-3** shows each one of the vortex-cluster configurations which we consider: The configuration for two vortex cluster is shown in the Fig. **8-3**(a); for three-vortex cluster we consider two different configurations, the equilateral triangle-T **8-3**(b) and linear-L array of vortices **8-3**(c); for four-vortex cluster we limited for two possible configuration, one rhombic or hexagonal-T **8-3**(d) and the square-S **8-3**(e); finally for five-vortex cluster we also choose two different configurations, the hexagonal-T **8-3**(f) and the pentagonal-P **8-3**(g).

In all cases, we only consider one degree of freedom which represents the case that all distances $\boldsymbol{r}$ between vortices are varied in the same way.

The vortex interaction potential can be extracted from the free energy with the chosen positions of the vortex centers, from which the energy of isolated vortices is subtracted, the interaction energy was then calculated for all different vortex cluster configurations in function of r(in units of $\lambda/\sqrt{2}$ with λ the magnetic penetration depth) and for different thickness d (in units of $\lambda/\sqrt{2}$).

The values of thickness that we consider are d =(100, 10, 5, 3 ,1)$\lambda/\sqrt{2}$ and $\delta\kappa = 1$, 0.2, 0.1, 0, -0.05, -0.08, -0.11, -0.5, where $\delta\kappa = 1$ and -0.5 represents values for type-II and type-I superconductor and the other values are values close to the point of Bogomonlyi $\kappa = 1/\sqrt{2}$, especially IT states.

The first result to be presented are for $d = 100$, that corresponds to our volumetric system limit. The results of vortex interaction are shown in the Fig. **8-4**. In this figure, we show how the interaction potential varies with the variation of the GL parameter for the vortices cluster previously mentioned [2-vortex panel (A), 3 vortex panel (B) and 4-vortex panel (C)].

We consider the different values of $\delta\kappa$.

When $\delta\kappa = 1$ the interaction potential is purely repulsive (type II superconductor), below this value (δ =0.2 and δ =0.1) the vortex are repulsive at short and attractive al large inter-vortex distances - this agrees with the early results the type II/1,2 picture. For the case of small $\delta\kappa$(=0, -0.05, -0.08, -0.11) values near the boundary between the IT/I and IT/II subdomains and IT-domain and near the Bogomolnyi point. In a more general view of the behavior between the vortex interaction, we found an attraction a large distance while the short-range interaction remains repulsive, then, vortex interaction becomes more attractive.

For small distances between vortex we have the following scenario: in the case of two vortices, it becomes more attractive at smaller $\delta\kappa$, where the minimum becomes local and disappear for increasing $\delta\kappa$,[see Fig. **8-4** (A.1) → (A.2) → (A.3) → (A.4)]. For the clusters with three and four vortex, we see that when $\delta\kappa = 0$ we are in the vicinity of the IT/I - IT/II boundary, and the vortex interaction potential is similar to the 2-vortex case. For δ =0.1 and 0.2, that correspond to the IT/II and type II regimes, the results are similar for all the three cases. In the IT/II subdomain, we do not see a qualitative change in the total vortex interaction due to many body contribution. Nevertheless, for the IT/I case, we observe substantial changes in the interaction profiles for two vortices cluster. For example, when $\delta\kappa$ = -0.08 we find a minimum for 3- and 4-vortices clusters [see Fig. **8-4**(B.3)-(C.3)], whereas for the 2-vortex cluster this minimum disappears [see Fig. **8-4**(A.3)]. This means that the interaction is already for the 2-vortices cluster, attractive and for 3- and 4-vortex cluster the non-monotonic type interaction is maintained, indicating an increased role of the many-body interaction. At $\delta\kappa$ =-0.11 the 3- and 4-vortex cluster potential become qualitative different: the interaction is fully repulsive for the 3-vortex cluster [see Fig. **8-4**(B.4)] while the potential for the 4-vortex case still non-monotonic [see Fig. **8-4**(C-4)]. Finally, for $\delta\kappa = -0.5$ we see the vortex interaction becomes attractive for all cases and corresponds typically to the type-I behavior superconductor.

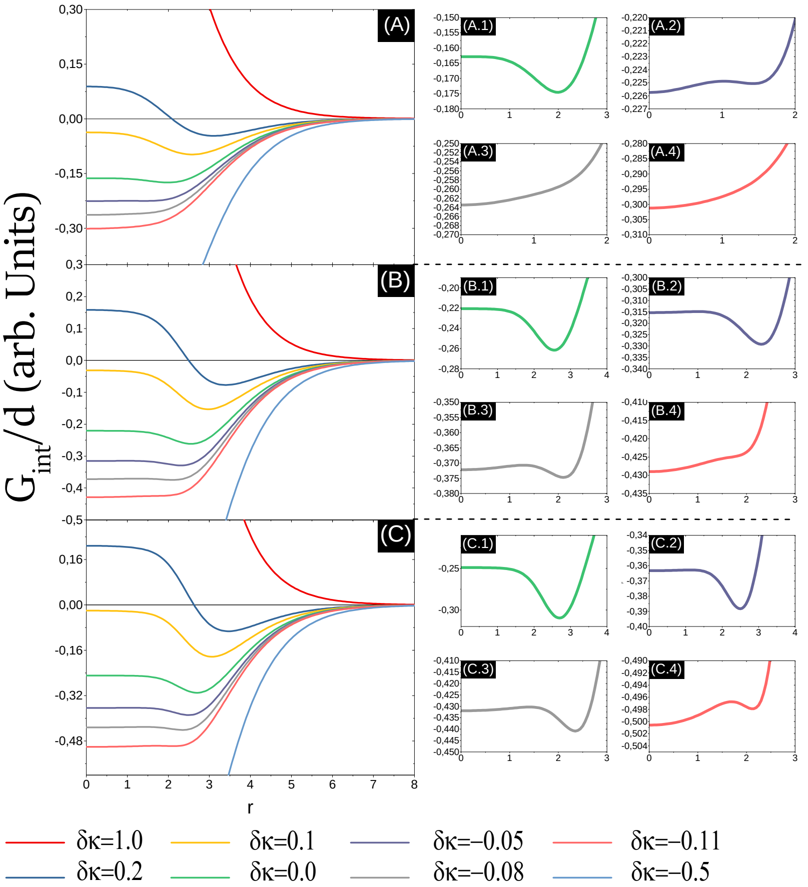

Figure 8-4 : Vortex interaction potential for N-vortex cluster (panel (A) 2-vortex, panel (B) 3-vortex and panel (C) 4-vortex) at different parameter $\delta\kappa$ in a film with thickness $d = 100\lambda\sqrt{2}$. Panels on th right are amplifications of the left panels for $\delta\kappa$ =0, -0.05, -0.08 and -0.11

In this second part of the results, we will discuss the effect of the sample tickness and the stray field on the behavior of the interaction potential. We will consider the same $\delta\kappa$ values and the configurations for 2-,3- and 4-vortex cluster previously studied. The film tickness we choose are $d = (10, 5, 3, 1)\lambda/\sqrt{2}$.

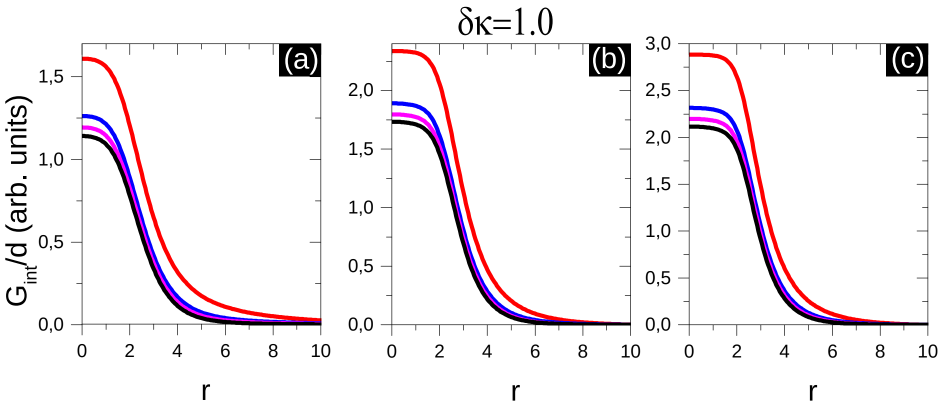

Figure 8-5 : Interaction potential (per vortex and per thickness of samples) as function of the vortex separation for the vortex clusters studied(panel (a) 2-vortex, panel (b) 3-vortex and panel (c) 4-vortex) for $\delta\kappa = 1$. Each color line represents a different thickness (d=$1\lambda\sqrt{2}$ red, d=$3\lambda\sqrt{2}$ blue, d=$5\lambda\sqrt{2}$ magenta and d=$10\lambda\sqrt{2}$ black)

As shown in Fig. **8-5** for $\delta\kappa = 1.0$, the interaction potential, per vortice and per film thickness, decreases monotonically with the distance for all configuration and film tickness. The vortex-vortex interaction is repulsive in all cases. Also the amplitude of the interaction potential increases with decreasing film tickness, i.e. the vortex - vortex repulsion increases with increasing stray field contribution.

For $\delta\kappa = 0.2$, it is seen in Fig. **8-6**[panels (a.I), (b.I), and (c.I)] that, for all clusters configurations, and, decreasing the film thickness, the interaction potential is increasingly repulsive. The IT/II behavior dominates for small $d(d < 5)$, and disapear for lager $d(d > 5)$.

For $\delta\kappa = 0$, Fig. **8-6**[panels (a.II), (b.II), (c.III)], and $d > 1$ we see a non-monotonic behavior, where the potential preserves a stability minimum. By decreasing d the minimum moves to bigger r. At long distances a repulsive interaction dominates, as seen in the two vortices cluster where the potential has a maximum in $r \approx 5$ (a.II). For all clusters configurations and for d =1, we see a drastic change in the potential, showing monotonically decreasing behavior favoring the repulsion between the vortices at long distances. For 3-, 4-vortex cluster (b.II, c.II), at small distances $r < 2$, the potential has a minimum that can correspond to metastable states, where the vortices prefer to remain as an agglomerate.

For the case $\delta\kappa$ = -0.05 and -0.11, which corresponds to the IT/I case, we observe a similar behavior to the previous case where for d =10, 5 and 3 the non-monotonic interaction prevails and for $d = 1$ the change in the potential is also observed, but with a peculiarity, that the potential does not decay monotonically, since, some minimum of instability are observed mainly when $r \approx r_{min}$.

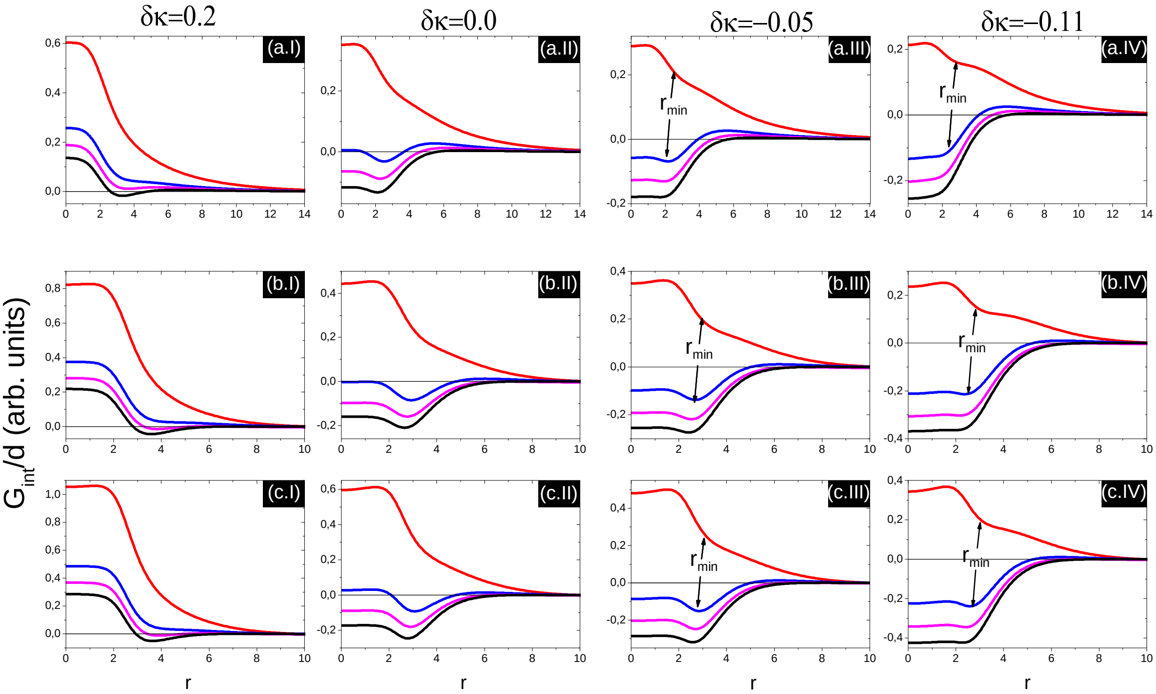

Figure 8-6 : Interaction potential (per vortex and per thickness of samples) as function of the vortex separation for the vortex clusters studied (panels (a.i) 2-vortex, panels (b.i) 3-vortex and panels (c.i) 4-vortex) for $\delta\kappa = 0.2$, $\delta\kappa = 0$, $\delta\kappa = -0.08$ and $\delta\kappa = -0.11$. Each color line represents a different thickness (d=$1\lambda\sqrt{2}$ red, d=$3\lambda\sqrt{2}$ blue, d=$5\lambda\sqrt{2}$ magenta and d=$10\lambda\sqrt{2}$ black)

Now we analyze the case in which when $\delta\kappa$ can be considered as type I, here we take $\delta\kappa = -0.5$ and the same 2-, 3- and 4-vortex cluster. For $d = 10$, 5 and 3, and for all vortex clusters we find vortex attraction that is typically type-I behavior [see Fig. **8-7**]. For $d = 1$ and $\delta\kappa = -0.5$ cases [see red line Fig. **8-7**-(a), (b), (c)] we find an repulsion at large distance while the short-range interaction remain attractive, also, this indicates that for this thickness and $\delta\kappa$ we have an IT behavior.

8.3.1 Stability of different vortex cluster symmetry in bulk samples (d=100), with $\delta\kappa$ close to Bogomolnyi point

In this section we will compare the behavior of the interaction potential of different vortex cluster symmetry, with the same number of vortices, in bulk samples ($d = 100$), and for $\delta\kappa$ close to the Bolgomolnyi point. In figure **8-8** we present the interaction energy(per vortex and

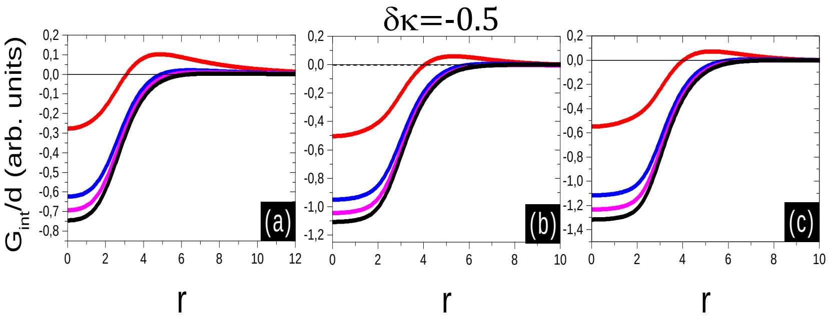

Figure 8-7 : Interaction potential (per vortex and per thickness of samples) as function of the vortex separation for the vortex clusters studied (panel (a) 2-vortex, panel (b) 3-vortex and panel (c) 4-vortex) for $\delta\kappa = -0.5$ and $\delta\kappa = -1$, where each line of color represents a different thickness (d=$1\lambda\sqrt{2}$ red, d=$3\lambda\sqrt{2}$ blue, d=$5\lambda\sqrt{2}$ magenta and d=$10\lambda\sqrt{2}$ black)

per thickness of samples) profile as function of the vortex separation, for n-vortex clusters, n = 3, 4 and 5 [panels (a), (b) and (c) respectively], and different symmetries in the bulk limit ($d =$ 100). For the 3-vortex clusters configuration [see Fig. **8-8**(a)] it is seen that the triangular (T) symmetry is much more stable than the linear one (L), for $\delta\kappa < -0.11$. For $\delta\kappa = -0.11$ the interaction potential of both symmetries, present a attractive potential with minimum energy at $r = 0$. Neverless, while interaction energy for the 3-vortex cluster configuration with L symmetry presents a monotonic dependence on r, the one with T symmetry presents a non-monotonic dependence.

For 4-vortex cluster configuration [Fig. **8-8**(b)] the potential profiles presented in figure **8-8** show that for $\delta\kappa$ = - 0.2, 0 and -0.05, both simmetries, S and T are stable for finite r, but the S symmetry presents a greater potential depth. This indicates that the system favors having S symmetry when consider IT/I. For $\delta\kappa$ =-0.11 the situation is significantly different, for the T symmetry the absolute minimum of the potential is found at $r = 0$. On the other hand, the 4-vortex cluster with S symmetry presents an stable configuration for vortices sitting at a finite distance, $r_{min} = 2.1$, between them.

For 5-vortex cluster configuration, the interaction potential profiles are similar to those observed in the 4-vortex cluster configuration, for all values of $\delta\kappa$ studied [see Fig. **8-8**(c)]. In this case, IT/I regime, the system favors the configuration with P symmetry.

In summary, these results show that, in the IT/II regime, vortices clusters can form closed configurations with L, T, S or P symmetry. On the other hand, in the IT/I regime, vortex clusters prefer configurations with symmetry other than triangular one. To investigate this further we obtained the configuration of 49 vortices with different $\delta\kappa$'s [see Fig. **8-9**(a)]. When $\delta\kappa = 1$ the vortices forms an the Abrikosov lattice [see Fig. **8-9**(a)]. For $\delta\kappa$ =0.2 and 0.1, the

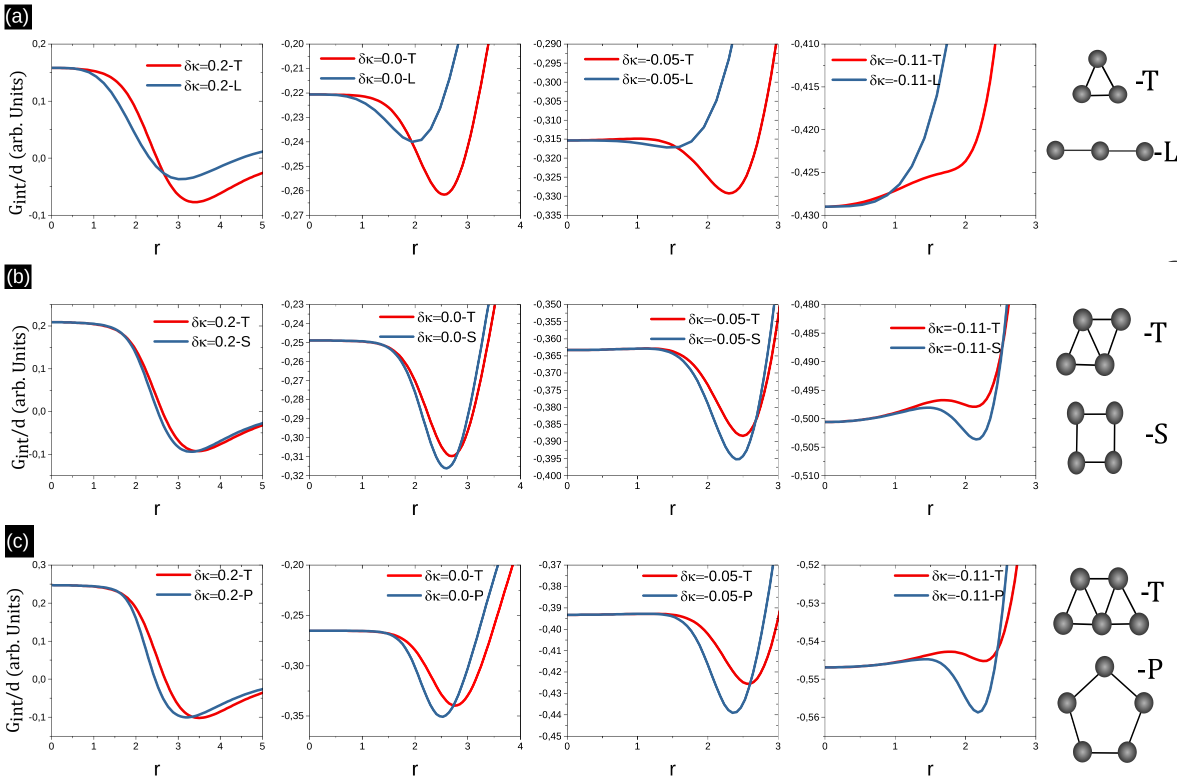

Figure 8-8 : Interaction potential of different vortex cluster symmetry, with the same number of vortices, in bulk samples (d = 100)

vortices are attracted forming domains of vortices - where the triangular vortex configuration is kept inside-with superconducting regions within these domains [see Fig. **8-9**(b),(c)]. When $\delta = 0$ a vortex agglomerate is formed with superconducting regions within this agglomerate, the vortices here do not form a triangular lattice but prefer to follow the agglomerate geometry [see Fig. **8-9**(d)]. For $\delta\kappa =$ - 0.05 and - 0.1 the vortices form an agglomerate with curvilinear domains, where the vortices also prefer to follow the agglomerate contour [see Fig. **8-9**(e)-(f)]. Finally, for $\delta\kappa =$ -0.15 and -0.2 a single agglomerate appears where some vortices sitting at the agglomerate contour the rest forming dimers, cluster, chains and giant vortices inside the agglomerate [see Fig. **8-9**(g)-(h)].

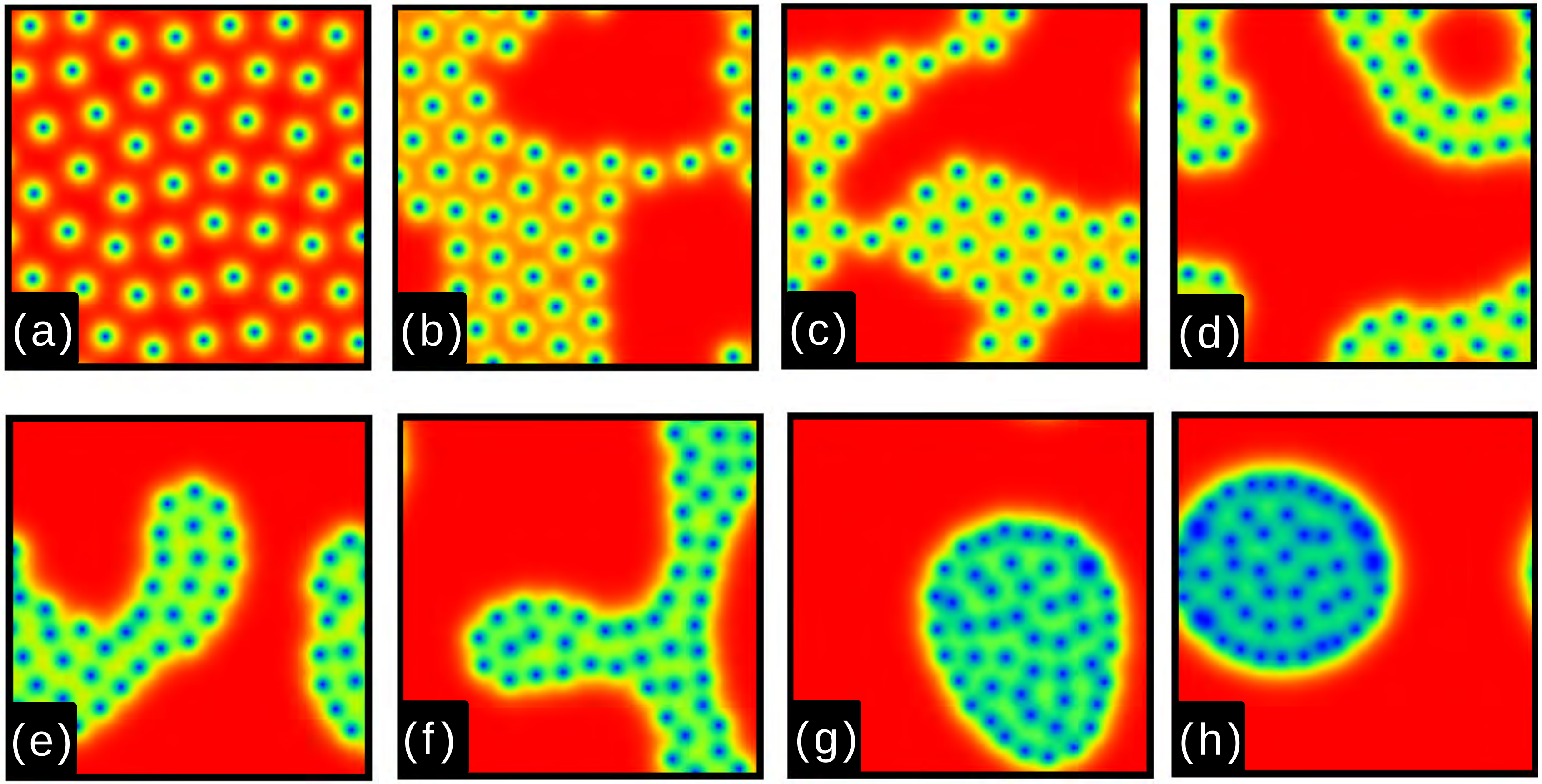

Figure 8-9 : Vortex patterns for the case of a bulk type superconductor, (d = 100) with 49 vortices for $\delta\kappa = 1$(a), 0.2(b), 0.1(c), 0(d), -0.05(e), -0.1(f), -0.15(g) and -0.2(h)

9 Summary and Future works

9.1 Summary

In the introductory chapters of this thesis, I first reviewed the phenomenology of conventional superconductors and the theoretical approaches used to describe them (London theory, Ginzburg-Landau theory, Lawrence-Doniach model and BCS theory). Subsequently I reviewed the recently developed Extended Ginzburg-Landau (EGL) theory.

The numerical simulations done in this thesis were based on the Time-Dependent Ginzburg-Landau theory and Monte Carlo method, which are explained in details in Chapter 4. We have introduced the equations of the TDGL model using both phenomenological and microscopic approaches. Then, the TDGL equations were written in their dimensionless form, making them easier for analysis and computation. The numerical method for solving TDGL equations have been also discussed and implemented in this work. We have introduced the method to discretize the TDGL equations with the help of the link variable. This method was also used to study the problem of superconducting bilayer using the Lawrence-Doniach model as theoretical support. The complete numerical procedure was done using the so-called "field cooling" process and magnetic response with respect to temperature and magnetic field. In the case of EGL formalism, we used the Monte Carlo method with the standard Metropolis algorithm to calculated the vortex-vortex interaction for different configurations and $\delta\kappa$.

Using the theoretical and computational formalisms discussed above we studied the properties of the intertype superconductivity differents superconducting systems.

In **Chapter 5**, we presented the analysis of the mixed states configurations in thin superconducting films. Our consideration was focused on the problem of the change from traditional type-I to type-II superconductivity when, starting with a type-I superconducting material, its thickness is decreased. Here the infinite topological degeneracy of the Bogomolnyi point is removed due to the stray magnetic fields and the intertype domain appears in the thickness-temperature phase diagram. It was found that, between the type-I and type-II regimes there exist an intertype domain which presents a rich internal structure presenting a variety of non-standard flux patterns in the mixed state. Our investigation identified three distinguished exotic magnetic flux configurations, i.e., lattices of superconducting islands separated by vortex chains, stripes/worms of vortices, and mixtures of giant vortices and vortex clusters. The observed flux distributions cannot be considered as any simple combination of the standard configurations observed on type-I and type-II superconductor. Thus, our results demonstrate that the magnetic response of thin superconductors cannot be described via the standard dichotomy of types-I and type-II, questioning the completeness of the textbook classification of the superconductivity types, breaks the grounds of understanding the superconductor magnetic response, and opens important prospects in further studies of the intertype regime in superconducting materials.

In **Chapter 6**, we have investigated the formation of quasi-1D vortex matter in a single nanowire made of a type-I material in a perpendicular magnetic field. It has been demonstrated that the magnetic response of the nanowire notably changes when its thickness decreases. Sufficiently thin nanowires deviate from type-I in favor of the IT regime with multi-quantum vortices and vortex clusters in the mixed state. In this case a regular chain of Abrikosov vortices is observed in the mixed state only when the field is close to its upper critical value. When decreasing the nanowire thickness further, signatures of the IT regime gradually disappear. However, the regime of type-II superconductivity is not reached. Instead, ultrathin nanowires re-enter the type-I regime because the confinement due to boundaries suppress the vortex matter. Although the calculations have been done for a single nanowire, our results are relevant for arrays of nanowires when they are sufficiently far from each another in an insulating template. This study opens prospects of creating composite superconducting materials with widely tuneable magnetic properties.

In **Chapter 7**, we concentrated our attention on vortex matter on a type-II/type-I superconducting bilayer. In the first part of our results, we studied in detail the phase transition between the Abrikosov lattice to the vortex clusters by decreasing the decreasing the temperature and changing the magnetic coupling between the layers. We found that the vortex matter in a bilayer has proven to be an exciting study object, presenting structures as rich as: Abrikosov Lattice, different kind of clusters, chains, or phases where type-I flux domains in one layer trap the type-II vortices in the other leading to vortex dissociation between layers. These configurations reflects the potential interaction between vortices that can be repulsive, attractive or non-monotonic. In the second part of this chapter, we showed that the superconducting bilayer depending on the stregth of the magnetic coupling between them. For strong couplings, the layer type II has a domain in the bilayer. For weak couplings, we found different profiles, especially an abnormal behavior in the Meissner state where one of the layer (layer-2) remains in Meissner state whereas the magnetic field has already penetrated the other one, therefore, the profiles of magnetization are neither type-I or type-II like.

In **Chapter 8** using the extended Gizburg Landau (EGL) formalism we investigate vortex-

vortex interaction in thin superconducting films, between standard type-I and type-II superconductors as a function of $\delta\kappa$. The developed approach takes into account the stray magnetic fields outside the sample. Using this approach we demonstrated that the vortex-vortex interaction has two contributions of opposite signs: one is due to the magnetic field and the other one induced by the condensate. In bulk samples the latter is dominant and the resulting vortex interaction is attractive in type-I superconductors and repulsive in type-II. However, as the film thickness decreases the contribution due to stray field increases, and the interaction demonstrate a different behaivor. We show that for the thickness of the order of λ, the interaction between vortices is completely repulsive for $\delta\kappa$'s close to κ_0 whereas for smaller thickness the behaviour is typical of the IT domain being a non-monotonic function. Analysis of the vortex interactions in the IT domain reveals that they have a considerable many-body (many-vortex) component. Such many-body interactions play a crucial role in the formation of the vortex matter. Properties of the vortex-vortex interactions depend strongly on the number and symmetry of vortices in a cluster.

9.2 Future works

- Recent advances in nanotechnology-enabled the fabrication of nanoscale superconductors with artificial structuring, e.g., designed interfaces, impurities, edge steps and other more complex boundary profiles. These factors directly alter the electronic states of the material and result in different superconducting properties, the tuning of which could be purposefully made useful when engineering electronic. In order to extend the study of the vortex states in a clean thin film and in nanowires type-I superconductors (see Chapter 5 and Chapter 6), we will investigate the effect of non-magnetic impurities and edge steps on the electrical and magnetic properties of the these low-dimensional system.
- A promising superconducting device is an array of superconducting nanowires embedded in an insulating matrix. It can be readily produced by, e.g., the process of electrochemical deposition in nanoporous materials, where related dimensional parameters can be controlled with high precision [83, 84, 86]. Theoretical analysis of superconductivity in such structures is a nontrivial problem because geometrical factors give rise to qualitative effects and cannot be assumed small. For example, extrapolating the known results for superconducting films (see,e.g., Refs. [5,6,14]), one can expect that a nanowire made of a type-I material in a perpendicular magnetic field becomes a type-II superconductor due to additional repulsion between vortices induced by stray magnetic fields. Recent experiments [86] have indeed demonstrated that the magnetization of an array of su-

perconducting wires changes notably, when the wire thickness decreases. Our plan is to apply the results obtained for a single nanowire and to design new superconducting devices with novel and unconventional properties. In particular one of the focuses is to investigate the magnetic response of arrays superconducting nanowires made of a type-I material, that are arranged in matrices with different geometries, e.g. separation between wires. *This work is already in progress.* Some preliminary results are shown in Figs. **9-1** and **9-2**, where we consider an array with four type-I nanowires with the dimensions $a = c = 6\xi_0$ and $b = 50\xi_0$. The results demonstrate that this system has a hysteresis-like dependence on the magnetic field.

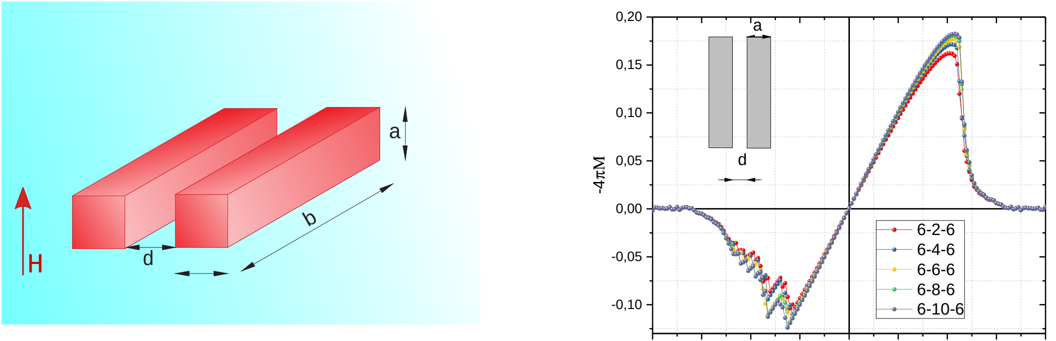

Array of two superconducting nanowires in a perpendicular magnetic field $\boldsymbol{H} = (0, 0, H)$, ($a = c = 6\xi_0$ and $b = 50\xi_0$ and variation d)

Magnetization $-4\pi M$ as a function of the applied perpendicular magnetic field H for two nanowires.

Figure 9-1 : Preliminary results for the magnetic field dependece for a two superconducting nanowire array in a perpendicular magnetic field.

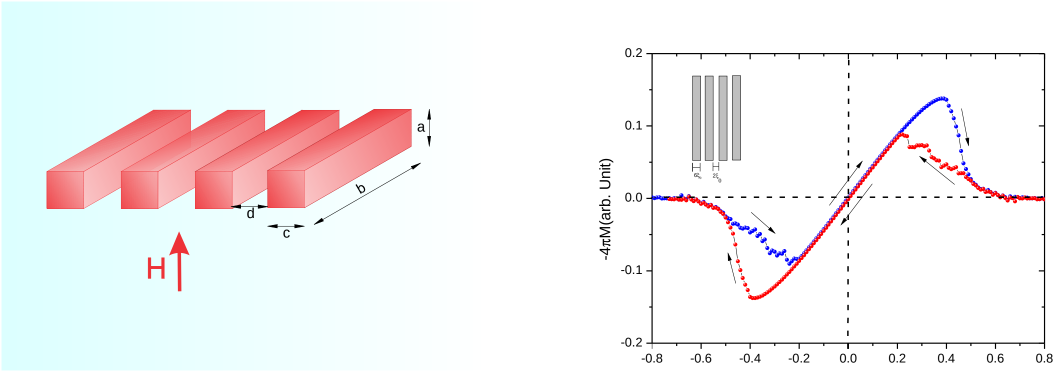

Array 4 Nano-wire System inside perpendicular magnetic field $\boldsymbol{H} = (0, 0, H)$, $(a = c = 6\xi_0$, $b = 50\xi_0$ and $d = 2\xi_0)$

Magnetization $-4\pi M$ as a function of the applied perpendicular magnetic field H for four nanowires.

Figure 9-2 : Preliminary resuls for results for the magnetic field dependece for a fuor superconducting nanowire array in a perpendicular magnetic field.

- On other possible work, would be to extend the study done with of superconducting bilayers including mixtures of different superconductors in each layer and arrays of pinning centers or deffect in one layer, in order to study their magnetic properties [125, 141, 142].

References

[1] G. N. Gol'tsman, O. Okunev, G. Chulkova, A. Lipatov, A. Semenov, K. Smirnov, B. Voronov, A. Dzardanov, C. Williams, and Roman Sobolewski. Picosecond superconducting single-photon optical detector. *Applied Physics Letters*, 79:705–707, 2001.

[2] John M. Blatt and Colin J. Thompson. Shape resonances in superconducting thin films. *Phys. Rev. Lett.*, 10:332–334, 1963.

[3] C. C. de Souza Silva, Leonardo R. E. Cabral, and J. Albino Aguiar. Flux penetration, matching effect, and hysteresis in homogeneous superconducting films. *Phys. Rev. B*, 63:134526, 2001.

[4] M. Tinkham. Effect of fluxoid quantization on transitions of superconducting films. *Phys. Rev.*, 129:2413–2422, 1963.

[5] J. Pearl. Current distribution in superconducting films carrying quantized fluxoids. *Applied Physics Letters*, 5:65–66, 1964.

[6] Kazumi Maki. Fluxoid structure in superconducting films. *Annals of Physics*, 34:363 – 376, 1965.

[7] H. Kamerlingh Onnes. Further experiments with liquid helium. d. on the change of electric resistance of pure metals at very low temperatures, etc. v. the disappearance of the resistance of mercury. *Commun. Phys. Lab. Unv. Leiden*, 122b, December 1911.

[8] H. Kamerlingh Onnes. Further experiments with liquid helium. c. on the change of electric resistance of pure metals at very low temperatures, etc. iv. the resistance of pure mercury at helium temperatures. *Commun. Phys. Lab. Unv. Leiden*, 120b, April 1911.

[9] H. Kamerlingh Onnes. Further experiments with liquid helium. d. on the change of electric resistance of pure metals at very low temperatures, etc. v. the disappearance of the resistance of mercury. *Commun. Phys. Lab. Unv. Leiden*, 122b, May 1911.

[10] W. Meissner and R. Ochsenfeld. Ein neuer Effekt bei Eintritt der Supraleitfähigkeit. *Die Naturwissenschaften*, 21:787–788, 1933.

[11] B.D. Josephson. Possible new effects in superconductive tunnelling. *Physics Letters*, 1:251 – 253, 1962.

[12] F. London and H. London. *Proc. Roy. Soc.*, A149:71, 1935.

[13] V.L. Ginzburg and L.D. Landau. Toward the superconductivity theory. *Zh. Eksp. Teor. Fiz.*, 20:1064–1082, 1950.

[14] M. Tinkham. *Introduction to Superconductivity.* McGraw-Hill, New York, 1996.

[15] D. Saint-James, G. Sarma, and E. J. Thomas. *Type II superconductivity.* Pergamon Press, Oxford, 1969.

[16] L.D. Landau and E.M Lifsgitz. *statistical, 3rd ed., part 1.* Pergamon Press, Oxford, 1980.

[17] L.P. Gor'kov. Microscopic derivation of the ginzburg-landau equations in the theory of superconductivity. *Sov. Phys. JETP*, 123:1364, 1959.

[18] P. D. Gennes. *Superconductivity of metals and alloys.* Advanced Book Program, Perseus Books, Reading, Mass, 1999.

[19] E. B. Bogomolnyi and A. I. Vainstein. Stability of strings in gauge abelian theory. *Sov. J. Nucl. Phys.*, 23:588–591, 1976.

[20] E. B. Bogomolnyi. The stability of classical solution. *Sov. J. Nucl. Phys.*, 24:449, 1976.

[21] W. H. Kleiner, L. M. Roth, and S. H. Autler. Bulk solution of ginzburg-landau equations for type ii superconductors: Upper critical field region. *Phys. Rev.*, 133:A1226–A1227, 1964.

[22] I. A. Parinov. *Microstructure and properties of high-temperature superconductors.* Springer, Berlin -New York, 2007.

[23] U. Essmann and H. Tr auble. The direct observation of individual flux lines in type ii superconductors. *Physics Letters A*, 24:526 – 527, 1967.

[24] P. L. Gammel, D. J. Bishop, G. J. Dolan, J. R. Kwo, C. A. Murray, L. F. Schneemeyer, and J. V. Waszczak. Observation of hexagonally correlated flux quanta in yba$_2$cu$_3$o$_7$. *Phys. Rev. Lett.*, 59:2592–2595, 1987.

[25] H. F. Hess, R. B. Robinson, R. C. Dynes, J. M. Valles, and J. V. Waszczak. Scanning-tunneling-microscope observation of the abrikosov flux lattice and the density of states near and inside a fluxoid. *Phys. Rev. Lett.*, 62:214–216, 1989.

[26] C. A. Bolle, P. L. Gammel, D. G. Grier, C. A. Murray, D. J. Bishop, D. B. Mitzi, and A. Kapitulnik. Observation of a commensurate array of flux chains in tilted flux lattices in bi-sr-ca-cu-o single crystals. *Phys. Rev. Lett.*, 66:112–115, 1991.

[27] K. Harada, T. Matsuda, J. Bonevich, M. Igarashi, S. Kondo, G. Pozzi, U. Kawabe, and A. Tonomura. Real-time observation of vortex lattices in a superconductor by electron microscopy. *Nature*, 360:51–53, 1992.

[28] J. R. Kirtley, C. C. Tsuei, Martin Rupp, J. Z. Sun, Lock See Yu-Jahnes, A. Gupta, M. B. Ketchen, K. A. Moler, and M. Bhushan. Direct imaging of integer and half-integer josephson vortices in high- T_c grain boundaries. *Phys. Rev. Lett.*, 76:1336–1339, 1996.

[29] Alexander Grigorenko, Simon Bending, Tsuyoshi Tamegai, Shuuichi Ooi, and Mohamed Henini. A one-dimensional chain state of vortex matter. *Nature*, 414:728–731, 2001.

[30] Pal Erik Goa, Harald Hauglin, Michael Baziljevich, Eugene Il'yashenko, Peter L Gammel, and Tom H Johansen. Real-time magneto-optical imaging of vortices in superconducting nbse 2. *Superconductor Science and Technology*, 14:729, 2001.

[31] J. B. Ketterson and S. N. Song. *Superconductivity.* Univ. Press, Cambridge, 1999.

[32] Lorenz Kramer. Thermodynamic behavior of type-ii superconductors with small κ near the lower critical field. *Phys. Rev. B*, 3:3821–3825, 1971.

[33] U. Krägeloh. Flux line lattices in the intermediate state of superconductors with Ginzburg Landau parameters near 12. *Physics Letters A*, 28, 1969.

[34] U. Essmann. Observation of the mixed state. *Physica*, 55:83–93, 1971.

[35] Huebener. *Magnetic Flux Structures in Superconductors.* Springer-Verlag Berlin Heidelberg GmbH-New York, 1979.

[36] Victor V Moshchalkov and Joachim Fritzsche. *Nanostructured Superconductors.* World Scientific Publishing Co. Pte. Ltd., 2011.

[37] J. D. Livingston and W. DeSorbo. *Superconductivity.* Marcel Dekker, New York, 1969.

[38] Ruslan Prozorov. Equilibrium Topology of the Intermediate State in Type-I Superconductors of Different Shapes. *Physical Review Letters*, 98:257001, 2007.

[39] J. Auer and H. Ullmaier. Magnetic Behavior of Type-II Superconductors with Small Ginzburg-Landau Parameters. *Physical Review B*, 7:136–145, 1973.

[40] J. Q. You and Franco Nori. Atomic physics and quantum optics using superconducting circuits. *Nature*, 474:589–597, 2011.

[41] Lawrence W. and S. Doniach. *In: Proceedings of the twelfth International Conference on Low Temperature Physics.* Academic Press of Japan, Kyoto, 1971.

[42] J. Bardeen, L. N. Cooper, and J. R. Schrieffer. Theory of superconductivity. *Phys. Rev.*, 108:1175–1204, 1957.

[43] N N Bogoliubov. A new method in the theory of superconductivity. *J. Exptl. Theoret. Phys. (U.S.S.R.)*, 34:58–65, 1958.

[44] J.R. Waldram. *Superconductivity of Metals and Cuprates.* IOP Publishing, Bristol, 1996.

[45] A. V. Vagov, A. A. Shanenko, M. V. Milošević, V. M. Axt, and F. M. Peeters. Extended ginzburg-landau formalism: Systematic expansion in small deviation from the critical temperature. *Phys. Rev. B*, 85:014502, 2012.

[46] A. A. Shanenko, M. V. Milošević, F. M. Peeters, and A. V. Vagov. Extended ginzburg-landau formalism for two-band superconductors. *Phys. Rev. Lett.*, 106:047005, 2011.

[47] A. Vagov, A. A. Shanenko, M. V. Milošević, V. M. Axt, and F. M. Peeters. Two-band superconductors: Extended ginzburg-landau formalism by a systematic expansion in small deviation from the critical temperature. *Phys. Rev. B*, 86:144514, 2012.

[48] N. V. Orlova, A. A. Shanenko, M. V. Milošević, F. M. Peeters, A. V. Vagov, and V. M. Axt. Ginzburg-landau theory for multiband superconductors: Microscopic derivation. *Phys. Rev. B*, 87:134510, 2013.

[49] L P Gor 'kov. On the energy spectrum of superconductors. *J. Exptl. Theoret. Phys. (U.S.S.R.)*, 34:735–739, 1958.

[50] Yoichiro Nambu. Quasi-particles and gauge invariance in the theory of superconductivity. *Phys. Rev.*, 117:648–663, 1960.

[51] Alexander L. Fetter and John Dirk Walecka. *Quantum Theory of Many-Particle Systems.* Dover Books on Physics, New York, 2003.

[52] Q. Du. Discrete gauge invariant approximations of a time dependent ginzburg-landau model of superconductivity. *Mathematics of Computation*, 67:965 – 986, 1998.

[53] L. P. Gor'kov and G. M. Eliashber. Discrete gauge invariant approximations of a time dependent ginzburg-landau model of superconductivity. *Soviet Physics. Journal of Experimental and Theoretical Physics,*, 27:328, 1968.

[54] L. Kramer and R. J. Watts-Tobin. Theory of dissipative current-carrying states in superconducting filaments. *Physical Review Letters*, 40:1041, 1978.

[55] William D. Gropp, Hans G. Kaper, Gary K. Leaf, David M. Levine, Mario Palumbo, and Valerii M. Vinokur. Numerical simulation of vortex dynamics in type-ii superconductors. *Journal of Computational Physics*, 123:254 – 266, 1996.

[56] T. Winiecki and C.S. Adams. A fast semi-implicit finite-difference method for the tdgl equations. *Journal of Computational Physics*, 179:127 – 139, 2002.

[57] M. M. Doria, J. E. Gubernatis, and D. Rainer. Solving the ginzburg-landau equations by simulated annealing. *Phys. Rev. B*, 41:6335–6340, 1990.

[58] G. C. Buscaglia, C. Bolech, and A. López. On the numerical solution of the time dependent ginzburg landau equations in multiply connected domains. *Connectivity and Superconductivity*, m62:200–214, 2000.

[59] Jian-Feng Ge, Zhi-Long Liu, Canhua Liu, Chun-Lei Gao, Dong Qian, Qi-Kun Xue, Ying Liu, and Jin-Feng Jia. Superconductivity above 100 K in single-layer FeSe films on doped SrTiO 3. *Nature Materials*, 14:285–289, 2015.

[60] Ivan Bozovic and Charles Ahn. A new frontier for superconductivity. *Nature Physics*, 10:892–895, 2014.

[61] P. G. de Gennes. *Superconductivity of Metals and Alloys.* Benjamin, New York, 1966.

[62] E. M. Lifshitz and L. P. Pitaevskii. *Statistical Physics, Part 2, Landau and Lifshitz Course of Theoretical Physics*, volume 9. Oxford, Pergamon, 1980.

[63] H.W. Weber, E. Seidl, M. Botlo, C. Laa, E. Mayerhofer, F.M. Sauerzopf, R.M. Schalk, H.P. Wiesinger, and J. Rammer. Magnetization of low-Î° superconductors i the phase transition at hc1. *Physica C: Superconductivity*, 161:272 – 286, 1989.

[64] A. E. Jacobs. First-order transitions at hc1 and hc2 in type ii superconductors. *Physical Review Letters*, 26:629–631, 1971.

[65] A. E. Jacobs. Theory of inhomogeneous superconductors near $t = T_c$. *Phys. Rev. B*, 4:3016–3021, 1971.

[66] A. E. Jacobs. Theory of inhomogeneous superconductors near $t = T_c$. *Phys. Rev. B*, 4:3016–3021, 1971.

[67] A. E. Jacobs. Interaction of vortices in type-ii superconductors near $t = T_c$. *Phys. Rev. B*, 4:3029–3034, 1971.

[68] Erick J. Weinberg. Multivortex solutions of the ginzburg-landau equations. *Phys. Rev. D*, 19:3008–3012, 1979.

[69] A. Vagov, A. A. Shanenko, M. V. Milošević, V. M. Axt, V. M. Vinokur, J. Albino Aguiar, and F. M. Peeters. Superconductivity between standard types: Multiband versus single-band materials. *Phys. Rev. B*, 93:174503, 2016.

[70] Yu. N. Ovchinnikov. Generalized ginzburg-landau equation and the properties of superconductors with ginzburg-landau parameter κ close to 1. *Journal of Experimental and Theoretical Physics*, 88:398–405, 1999.

[71] I. Luk'yanchuk. Theory of superconductors with κ close to $1/\sqrt{2}$. *Phys. Rev. B*, 63:174504, 2001.

[72] A A Shanenko, J Albino Aguiar, A Vagov, M D Croitoru, and M V Milošević. Atomically flat superconducting nanofilms: multiband properties and mean-field theory. *Superconductor Science and Technology*, 28:054001, 2015.

[73] Gordon Lasher. Mixed state of type-i superconducting films in a perpendicular magnetic field. *Phys. Rev.*, 154:345–348, 1967.

[74] Mark C. Sweeney and Martin P. Gelfand. Simple vortex states in films of type-i ginzburg-landau superconductor. *Phys. Rev. B*, 82:214508, 2010.

[75] H Palonen, J Jäykkä, and P Paturi. Giant vortex states in type i superconductors simulated by ginzburg landau equations. *Journal of Physics: Condensed Matter*, 25:385702, 2013.

[76] G. J. Dolan and J. Silcox. Critical thicknesses in superconducting thin films. *Phys. Rev. Lett.*, 30:603–606, 1973.

[77] Shuji Hasegawa, Tsuyoshi Matsuda, Junji Endo, Nobuyuki Osakabe, Masukazu Igarashi, Toshio Kobayashi, Masayoshi Naito, Akira Tonomura, and Ryozo Aoki. Magnetic-flux quanta in superconducting thin films observed by electron holography and digital phase analysis. *Phys. Rev. B*, 43:7631–7650, 1991.

[78] J. Barba-Ortega, Ariel Becerra, and J. Albino Aguiar. Two dimensional vortex structures in a superconductor slab at low temperatures. *Physica C: Superconductivity*, 470:225 – 230, 2010.

[79] M. M. Doria, J. E. Gubernatis, and D. Rainer. Virial theorem for ginzburg-landau theories with potential applications to numerical studies of type-ii superconductors. *Phys. Rev. B*, 39:9573–9575, 1989.

[80] Ryuzo Kato, Yoshihisa Enomoto, and Sadamichi Maekawa. Effects of the surface boundary on the magnetization process in type-ii superconductors. *Phys. Rev. B*, 47:8016–8024, 1993.

[81] Alexander D. Hernández and Daniel Domínguez. Magnetic properties of the intermediate state in small type-i superconductors. *Phys. Rev. B*, 72:020505, 2005.

[82] G. R. Berdiyorov, A. D. Hernandez, and F. M. Peeters. Confinement effects on intermediate-state flux patterns in mesoscopic type-i superconductors. *Phys. Rev. Lett.*, 103:267002, 2009.

[83] James S. Kurtz, Robert R. Johnson, Mingliang Tian, Nitesh Kumar, Zhigang Ma, Shengyong Xu, and Moses H. W. Chan. Specific heat of superconducting zn nanowires. *Phys. Rev. Lett.*, 98:247001, 2007.

[84] T. G. Sorop and L. J. de Jongh. Size-dependent anisotropic diamagnetic screening in superconducting sn nanowires. *Phys. Rev. B*, 75:014510, 2007.

[85] Ying Zhang, Chi Ho Wong, Junying Shen, Sin Ting Sze, Bing Zhang, Haijing Zhang, Yan Dong, Hui Xu, Zifeng Yan, Yingying Li, Xijun Hu, and Rolf Lortz. Dramatic enhancement of superconductivity in single-crystalline nanowire arrays of sn. *Scientific Reports*, 6, 2016.

[86] K. O. Moura, K. R. Pirota, F. Béron, C. B. R. Jesus, P. F. S. Rosa, D. Tobia, P. G. Pagliuso, and O. F. de Lima. *Scientific Reports*, 7:15306, 2017.

[87] R Córdoba, T I Baturina, J Sesé, A Yu Mironov, J M De Teresa, M R Ibarra, D A Nasimov, A K Gutakovskii, A V Latyshev, I Guillamón, H Suderow, S Vieira, M R Baklanov, J J Palacios, and V M Vinokur. ARTICLE Magnetic field-induced dissipation-free state in superconducting nanostructures. *Nature Communications*, 4:1437, 2013.

[88] Tyler Morgan-Wall, Benjamin Leith, Nikolaus Hartman, Atikur Rahman, and Nina Marković. Measurement of critical currents of superconducting aluminum nanowires in

external magnetic fields: Evidence for a weber blockade. *Phys. Rev. Lett.*, 114:077002, 2015.

[89] Rosa Córdoba, Alfonso Ibarra, Dominique Mailly, and José Ma De Teresa. Vertical growth of superconducting crystalline hollow nanowires by he+ focused ion beam induced deposition. *Nano Letters*, 18:1379–1386, 2018.

[90] S. Wolf, A. Vagov, A. A. Shanenko, V. M. Axt, and J. Albino Aguiar. Vortex matter stabilized by many-body interactions. *Phys. Rev. B*, 96:144515, 2017.

[91] W. Y. Córdoba-Camacho, R. M. da Silva, A. Vagov, A. A. Shanenko, and J. Albino Aguiar. Between types i and ii: Intertype flux exotic states in thin superconductors. *Phys. Rev. B*, 94:054511, 2016.

[92] K. K. Likharev. Superconducting weak links. *Rev. Mod. Phys.*, 51:101–159, 1979.

[93] M. Zgirski, K.-P. Riikonen, V. Touboltsev, and K. Yu. Arutyunov. Quantum fluctuations in ultranarrow superconducting aluminum nanowires. *Phys. Rev. B*, 77:054508, 2008.

[94] L. D. Landau. On the theory of superconductivity. *Sov. Phys. JETP*, 7:371, 1937.

[95] V. A. Schweigert, F. M. Peeters, and P. Singha Deo. Vortex phase diagram for mesoscopic superconducting disks. *Phys. Rev. Lett.*, 81:2783–2786, 1998.

[96] L. R. E. Cabral and J. Albino Aguiar. Vortex configurations in thin superconducting equilateral triangles. *Phys. Rev. B*, 80:214533, 2009.

[97] J. Barba-Ortega, Edson Sardella, J. Albino Aguiar, and E.H. Brandt. Vortex state in a mesoscopic flat disk with rough surface. *Physica C: Superconductivity*, 479:49 – 52, 2012.

[98] R. M. da Silva, M. V. Milošević, A. A. Shanenko, F. M. Peeters, and J. Albino Aguiar. Giant paramagnetic Meissner effect in multiband superconductors. *Scientific Reports*, 5:12695, 2015.

[99] C. P. Bean and J. D. Livingston. Surface barrier in type-ii superconductors. *Phys. Rev. Lett.*, 12:14–16, 1964.

[100] M. Laver, E. M. Forgan, S. P. Brown, D. Charalambous, D. Fort, C. Bowell, S. Ramos, R. J. Lycett, D. K. Christen, J. Kohlbrecher, C. D. Dewhurst, and R. Cubitt. Spontaneous symmetry-breaking vortex lattice transitions in pure niobium. *Phys. Rev. Lett.*, 96:167002, 2006.

[101] M. Laver, C. J. Bowell, E. M. Forgan, A. B. Abrahamsen, D. Fort, C. D. Dewhurst, S. Mühlbauer, D. K. Christen, J. Kohlbrecher, R. Cubitt, and S. Ramos. Structure and degeneracy of vortex lattice domains in pure superconducting niobium: A small-angle neutron scattering study. *Phys. Rev. B*, 79:014518, 2009.

[102] S. Mühlbauer, C. Pfleiderer, P. Böni, M. Laver, E. M. Forgan, D. Fort, U. Keiderling, and G. Behr. Morphology of the superconducting vortex lattice in ultrapure niobium. *Phys. Rev. Lett.*, 102:136408, 2009.

[103] Ernst Helmut Brandt and Mukunda P. Das. Attractive vortex interaction and the intermediate-mixed state of superconductors. *Journal of Superconductivity and Novel Magnetism*, 24:57–67, 2011.

[104] A Pautrat and A BrÃ»let. Temperature dependence of clusters with attracting vortices in superconducting niobium studied by neutron scattering. *Journal of Physics: Condensed Matter*, 26:232201, 2014.

[105] T. Reimann, S. Mühlbauer, M. Schulz, B. Betz, A. Kaestner, V. Pipich, P. Böni, and C. Grünzweig. Visualizing the morphology of vortex lattice domains in a bulk type-ii superconductor. *Nature Communications*, 6:8813, 2015.

[106] A.A. Abrikosov. On the magnetic properties of superconductors of the second group. *Phys. JETP*, 5:1174, 1957.

[107] Ruslan Prozorov, Andrew F. Fidler, Jacob R. Hoberg, and Paul C. Canfield. Suprafroth in type-I superconductors. *Nature Physics*, 4:327–332, 2008.

[108] L. LANDAU. The Intermediate State of Supraconductors. *Nature*, 141:688–688, 1938.

[109] H. Suhl, B. T. Matthias, and L. R. Walker. Bardeen-cooper-schrieffer theory of superconductivity in the case of overlapping bands. *Phys. Rev. Lett.*, 3:552–554, Dec 1959.

[110] Amy Y. Liu, I. I. Mazin, and Jens Kortus. Beyond eliashberg superconductivity in mgb$_2$: Anharmonicity, two-phonon scattering, and multiple gaps. *Phys. Rev. Lett.*, 87:087005, 2001.

[111] Mazin I. I., Andersen O. K., Jepsen O., Dolgov O. V., Kortus J., Golubov A. A., Kuz'menko A. B., and van der Marel D. Superconductivity in mgb$_2$: Clean or dirty? *Phys. Rev. Lett.*, 89:107002, 2002.

[112] A. Gurevich. Enhancement of the upper critical field by nonmagnetic impurities in dirty two-gap superconductors. *Phys. Rev. B*, 67:184515, 2003.

[113] A. Gurevich. Limits of the upper critical field in dirty two-gap superconductors. *Physica C: Superconductivity*, 456:160 – 169, 2007. Recent Advances in MgB2 Research.

[114] Zhitomirsky M. E. and Dao V.-H. Ginzburg-landau theory of vortices in a multigap superconductor. *Phys. Rev. B*, 69:054508, 2004.

[115] Y. Tanaka. Soliton in two-band superconductor. *Phys. Rev. Lett.*, 88:017002, 2001.

[116] L. Komendová, M. V. Milošević, and F. M. Peeters. Soft vortex matter in a type-i/type-ii superconducting bilayer. *Phys. Rev. B*, 88:094515, 2013.

[117] Egor Babaev and Martin Speight. Semi-meissner state and neither type-i nor type-ii superconductivity in multicomponent superconductors. *Phys. Rev. B*, 72:180502, 2005.

[118] Moshchalkov Victor, Menghini Mariela, Nishio T., Chen Q. H., Silhanek A. V., Dao V. H., Chibotaru L. F., Zhigadlo N. D., and Karpinski J. Type-1.5 superconductivity. *Phys. Rev. Lett.*, 102:117001, 2009.

[119] Nishio Taichiro, Dao Vu Hung, Chen Qinghua, Chibotaru Liviu F., Kadowaki Kazuo, and Moshchalkov Victor V. Scanning squid microscopy of vortex clusters in multiband superconductors. *Phys. Rev. B*, 81:020506, 2010.

[120] J. Gutierrez, B. Raes, A. V. Silhanek, L. J. Li, N. D. Zhigadlo, J. Karpinski, J. Tempere, and V. V. Moshchalkov. Scanning hall probe microscopy of unconventional vortex patterns in the two-gap mgb$_2$ superconductor. *Phys. Rev. B*, 85:094511, 2012.

[121] Egor Babaev, Johan Carlström, and Martin Speight. Type-1.5 superconducting state from an intrinsic proximity effect in two-band superconductors. *Phys. Rev. Lett.*, 105:067003, 2010.

[122] Mihail Silaev and Egor Babaev. Microscopic theory of type-1.5 superconductivity in multiband systems. *Phys. Rev. B*, 84:094515, 2011.

[123] Hendrik Bluhm, Nicholas C. Koshnick, Martin E. Huber, and Kathryn A. Moler. Magnetic response of mesoscopic superconducting rings with two order parameters. *Phys. Rev. Lett.*, 97:237002, 2006.

[124] Y Tanaka. Multicomponent superconductivity based on multiband superconductors. *Superconductor Science and Technology*, 28:034002, 2015.

[125] Tanaka Y., Yamamori H., Yanagisawa T., Nishio T., and Arisawa S. Experimental formation of a fractional vortex in a superconducting bi-layer. *Physica C: Superconductivity and its Applications*, 548:44–49, 2018.

[126] Chao-Yu Liu, G. R. Berdiyorov, and M. V. Milošević. Vortex states in layered mesoscopic superconductors. *Phys. Rev. B*, 83:104524, 2011.

[127] G. R. Berdiyorov, M. V. Milošević, F. Kusmartsev, F. M. Peeters, and S. Savel'ev. Josephson vortex loops in nanostructured Josephson junctions. *Scientific Reports*, 8:2733, 2018.

[128] G R Berdiyorov, S E Savel'ev, F V Kusmartsev, and F M Peeters. In-phase motion of josephson vortices in stacked sns josephson junctions: effect of ordered pinning. *Superconductor Science and Technology*, 26:125010, 2013.

[129] G. R. Berdiyorov, S. E. Savel'ev, M. V. Milošević, F. V. Kusmartsev, and F. M. Peeters. Synchronized dynamics of josephson vortices in artificial stacks of sns josephson junctions under both dc and ac bias currents. *Phys. Rev. B*, 87:184510, 2013.

[130] R. Geurts, M. V. Milošević, J. Albino Aguiar, and F. M. Peeters. Enhanced stability of vortex-antivortex states in two-component mesoscopic superconductors. *Phys. Rev. B*, 87:024501, 2013.

[131] H J Zhao, V R Misko, and F M Peeters. Analysis of pattern formation in systems with competing range interactions. *New Journal of Physics*, 14:063032, 2012.

[132] Lawrence W. and Doniach S. in proceedings of the twelfth international conference on low temperature physics. *edited by Eizo Kanda (Academic Press of Japan, Kyoto, 1971)*, pages pp. 361–362.

[133] R. A. Klemm, A. Luther, and M. R. Beasley. Theory of the upper critical field in layered superconductors. *Phys. Rev. B*, 12:877–891, 1975.

[134] L. N. Bulaevskii and I. D. Vagner. Magnetic critical fields of y-ba-cu-o superconductors in the lawrence-doniach model with inequivalent layers. *Phys. Rev. B*, 43:8694–8697, 1991.

[135] Egor Babaev. Vortices with fractional flux in two-gap superconductors and in extended faddeev model. *Phys. Rev. Lett.*, 89:067001, 2002.

[136] R. Geurts, M. V. Milošević, and F. M. Peeters. Vortex matter in mesoscopic two-gap superconducting disks: Influence of josephson and magnetic coupling. *Phys. Rev. B*, 81:214514, 2010.

[137] L. F. Chibotaru, V. H. Dao, and A. Ceulemans. Thermodynamically stable noncomposite vortices in mesoscopic two-gap superconductors. *EPL (Europhysics Letters)*, 78:47001, 2007.

[138] L. F. Chibotaru and V. H. Dao. Stable fractional flux vortices in mesoscopic superconductors. *Phys. Rev. B*, 81:020502, 2010.

[139] A. Vagov, A. A. Shanenko, M. V. Milošević, V. M. Axt, V. M. Vinokur, J. Albino Aguiar, and F. M. Peeters. Superconductivity between standard types: Multiband versus single-band materials. *Phys. Rev. B*, 93:174503, 2016.

[140] Matteo Frigo and Steven G. Johnson. The design and implementation of FFTW3. *Proceedings of the IEEE*, 93:216–231, 2005. Special issue on "Program Generation, Optimization, and Platform Adaptation".

[141] Y. Tanaka, H. Yamamori, T. Yanagisawa, T. Nishio, and S. Arisawa. Abnormal meissner state in a superconducting bilayer. *Physica C: Superconductivity and its Applications*, 551:41 – 47, 2018.

[142] Y. Tanaka, H. Yamamori, T. Yanagisawa, T. Nishio, and S. Arisawa. An unconventional vortex state in a superconducting bilayer where one layer has a hole. *Solid State Communications*, 277:39 – 44, 2018.

APPENDIX A - Time-dependent Delta Function

The matter is that delta function $\delta(\mathsf{t}-\mathsf{t}')$ (Eq. (3-12)) does not satisfy the anti-periodic boundary condition. So, what about the expansion in terms of the Matsubara frequencies.

$$\delta(\mathsf{t}-\mathsf{t}') = \frac{1}{\beta\hbar}\sum_n e^{-i\omega(\mathsf{t}-\mathsf{t}')} \tag{A.1}$$

For the periodic function varying with periodic $2\beta\hbar$ we have

$$\mathcal{F}(\mathsf{t}-\mathsf{t}') = \frac{1}{2\beta\hbar}\sum_n e^{-i\omega(\mathsf{t}-\mathsf{t}')}\mathsf{F}(\tilde{w}_n), \qquad \tilde{\omega}_n = \frac{2\pi n}{2\hbar\beta} = \frac{\pi n}{\beta\hbar}, \tag{A.2}$$

where

$$\mathsf{F}(\tilde{\omega}_n) = \int_{-\hbar\beta}^{\hbar\beta} d(\mathsf{t}-\mathsf{t}')e^{i\omega(\mathsf{t}-\mathsf{t}')}\mathcal{F}(\mathsf{t}-\mathsf{t}'). \tag{A.3}$$

Why do we need such a periodic function? We can construct a function being periodic with period $2\beta\hbar$ and obeying Eq. (3.11) for $-\beta\hbar < \mathsf{t}-\mathsf{t}' < \beta\hbar$, so, antiperiodic with period $\beta\hbar$, in this case we can write

$$\mathcal{F}(\mathsf{t}-\mathsf{t}') = \frac{1}{\beta\hbar}\sum_n e^{-i\tilde{\omega}_n(\mathsf{t}-\mathsf{t}')}\mathcal{F}(\tilde{w}_n), \qquad \mathcal{F}(\tilde{w}_n) = \frac{1}{2}\mathsf{F}(\tilde{\omega}_n), \tag{A.4}$$

with

$$\mathcal{F}(\tilde{w}_n) = \begin{cases} \dfrac{1}{2}\displaystyle\int_{-\hbar\beta}^{\hbar\beta} d(\mathsf{t}-\mathsf{t}')e^{i\tilde{\omega}_n(\mathsf{t}-\mathsf{t}')}\mathcal{F}(\mathsf{t}-\mathsf{t}') = 0, & \text{n is even} \\ \dfrac{1}{2}\displaystyle\int_{-\hbar\beta}^{\hbar\beta} d(\mathsf{t}-\mathsf{t}')e^{i\tilde{\omega}_n(\mathsf{t}-\mathsf{t}')}\mathcal{F}(\mathsf{t}-\mathsf{t}') \neq 0, & \text{n is odd} \end{cases} \qquad \Leftarrow \qquad \mathcal{F}(\mathsf{t}-\mathsf{t}'+\beta\hbar) = -\mathcal{F}(\mathsf{t}-\mathsf{t}') \tag{A.5}$$

Then, we cant get

$$\mathcal{F}(\mathsf{t}-\mathsf{t}') = \frac{1}{\beta\hbar}\sum_{n,odd} e^{-i\tilde{\omega}_n(\mathsf{t}-\mathsf{t}')}\mathcal{F}(\tilde{w}_n) = \frac{1}{\beta\hbar}\sum_n e^{-i\omega_n(\mathsf{t}-\mathsf{t}')}\mathcal{F}(w_n), \tag{A.6}$$

which is a justification of Eq. (3.12). Inserting the time delta-function, one can find $\mathcal{F}(\omega) = 1/2$. However, this is not valid because of the violation of boundary condition $\delta(\mathfrak{t}-\mathfrak{t}'+\beta\hbar) \neq -\delta(\mathfrak{t}-\mathfrak{t}')$!!!. The correct procedure is based on a little mathematical trick. First, we should make a substitution

$$\delta(\mathfrak{t}-\mathfrak{t}') \to \delta(\mathfrak{t}-\mathfrak{t}') - \delta(\mathfrak{t}+\beta\hbar) - \delta(\mathfrak{t}-\beta\hbar), \tag{A.7}$$

which replaces the delta-function by delta-function-based antiperiodic function. Whit this substitution one gets $\mathcal{F}(\omega_n) = 1$. How this substitution can distort a solution of the Gor'kov and Gor'kov-Nambu equations? The temperature Green's functions are defined only for $-\beta\hbar < \mathfrak{t}-\mathfrak{t}' < \beta\hbar$. Hence, appearance of two extra delta function exactly at the edges of this region can in no way influence solution of the time-dependent differential equations. Thus, we array at

$$\delta(\mathfrak{t}-\mathfrak{t}') = \frac{1}{\beta\hbar}\sum_n e^{-i\tilde{\omega}_n(\mathfrak{t}-\mathfrak{t}')}, \qquad -\beta\hbar < \mathfrak{t}-\mathfrak{t}' < \beta\hbar. \tag{A.8}$$

B APPENDIX B - Main Integrals of the EGL Formalism

APPENDIX B.1 - Coefficients Related to the Integral Kernel $K_a(\boldsymbol{x},\boldsymbol{y})$

We start our derivation from the terms coming from the integral involving the kernel $K_a(\boldsymbol{x},\boldsymbol{y}) = K_a(\boldsymbol{x},\boldsymbol{x}+\boldsymbol{z})$ (with $\boldsymbol{y} = \boldsymbol{x}+\boldsymbol{z}$), i.e.,

$$I_a = \int d^3\boldsymbol{y} K_a(\boldsymbol{x},\boldsymbol{y})\Delta(\boldsymbol{y}) = \int d^3\boldsymbol{z} K_a(\boldsymbol{x},\boldsymbol{x}+\boldsymbol{z})\Delta(\boldsymbol{x}+\boldsymbol{z}). \tag{B.1}$$

Following the usual practice, this integral is expanded in terms of the spatial derivatives of the order parameter $\Delta(\boldsymbol{x})$, i.e., Eq. (3.30). We conclude that working to the order $\tau^{5/2}$, it is necessary to incorporate all the spatial derivatives up to the fourth order in the gradient expansion (3.30). Due to the symmetry of the kernel $K_a(\boldsymbol{x},\boldsymbol{x}+\boldsymbol{z})$ with respect to the transformation $\boldsymbol{z} \to -\boldsymbol{z}$, the first- and third-order derivatives do not contribute.

$$\begin{aligned}
I_a &= \int d\boldsymbol{z} K_a(\boldsymbol{x},\boldsymbol{x}+\boldsymbol{z})\Delta(\boldsymbol{x}+\boldsymbol{z})\\
&= \int d\boldsymbol{z} K_a(\boldsymbol{x},\boldsymbol{x}+\boldsymbol{z})\left(\Delta(\boldsymbol{x}) + \frac{(\boldsymbol{z}\cdot\boldsymbol{\nabla})^2}{2!}\Delta(\boldsymbol{x}) + \frac{(\boldsymbol{z}\cdot\boldsymbol{\nabla})^4}{4!}\Delta(\boldsymbol{x}) + \cdots\right)
\end{aligned}$$

So, as $\Delta \propto \tau^{-1/2}$ and $\nabla\Delta \propto \tau$, or the short-hand notation $\nabla \propto \tau^{1/2}$, we obtain only the three relevant terms:

$$I_{a1} = \int d^3\boldsymbol{z} K_a(\boldsymbol{x},\boldsymbol{x}+\boldsymbol{z})\Delta(\boldsymbol{x}), \tag{B.2}$$

$$I_{a2} = \int d^3\boldsymbol{z} K_a(\boldsymbol{x},\boldsymbol{x}+\boldsymbol{z})\frac{(\boldsymbol{z}\cdot\boldsymbol{\nabla})^2}{2!}\Delta(\boldsymbol{x}), \tag{B.3}$$

$$I_{a2} = \int d^3\boldsymbol{z} K_a(\boldsymbol{x},\boldsymbol{x}+\boldsymbol{z})\frac{(\boldsymbol{z}\cdot\boldsymbol{\nabla})^4}{4!}\Delta(\boldsymbol{x}). \tag{B.4}$$

The first integral

$$I_{a1} = \int d^3\boldsymbol{z} K_a(\boldsymbol{x},\boldsymbol{x}+\boldsymbol{z})\Delta(\boldsymbol{x}) = \int d^3\boldsymbol{z}(-gT)\lim_{\eta\to 0^+}\sum_{\omega} e^{-i\omega\eta} G^{(0)}_{\omega}(\boldsymbol{z})\overline{G}^{(0)}_{\omega}(-\boldsymbol{z})\Delta(\boldsymbol{x})$$

$$G^{(0)}_{\omega}(\boldsymbol{z}) = \int \frac{d^3\boldsymbol{k}}{(2\pi)^3}\frac{e^{i\boldsymbol{k}\cdot\boldsymbol{z}}}{i\hbar\omega - \xi_k},$$

$$= -gT \lim_{\eta\to 0^+} \sum_\omega \int e^{-i\omega\eta} d^3\boldsymbol{z} \int \frac{d^3\boldsymbol{k}}{(2\pi)^3} \frac{d^3\boldsymbol{k'}}{(2\pi)^3} \frac{e^{i\boldsymbol{k}\cdot\boldsymbol{z}}}{i\hbar\omega - \xi_k} \frac{e^{-i\boldsymbol{k'}\cdot\boldsymbol{z}}}{i\hbar\omega + \xi_k} \Delta(\boldsymbol{x})$$
$$= -gT \lim_{\eta\to 0^+} \sum_\omega \int \frac{d^3\boldsymbol{k}}{(2\pi)^3} \frac{e^{-i\omega\eta}}{2\xi_k} \left(\frac{1}{i\hbar\omega - \xi_k} - \frac{1}{i\hbar\omega + \xi_k} \right) \Delta(\boldsymbol{x}).$$

Let evaluate

$$\lim_{\eta\to 0^+} \sum_\omega e^{-i\omega\eta} \frac{1}{i\hbar\omega - \xi_k},$$

this can be done with a contour integrating, $\omega \to \omega_n$, $\hbar\omega_n = \pi T(2n+1)$

$$\lim_{\eta\to 0^+} \sum_\omega \frac{e^{-i\omega\eta}}{i\hbar\omega - \xi_k} = -\frac{\beta}{2i\pi} \oint_{\mathcal{C}} \frac{dz}{e^{\beta z}+1} \frac{e^{iz\eta/\hbar}}{z+\xi_k},$$

such that the contour integral along the paths

$$\frac{1}{2i\pi} \oint_{\mathcal{C}} \frac{dz}{e^{\beta z}+1} \frac{e^{iz\eta/\hbar}}{z+\xi_k} = -\frac{e^{-i\xi_k\eta/\hbar}}{e^{-\beta\xi_k}+1}.$$

Therefore,

$$\lim_{\eta\to 0^+} \sum_\omega \frac{e^{-i\omega\eta}}{i\hbar\omega - \xi_k} = \frac{\beta}{e^{-\beta\xi_k}+1}.$$
$$\lim_{\eta\to 0^+} \sum_\omega \frac{e^{-i\omega\eta}}{i\hbar\omega + \xi_k} = \frac{\beta}{e^{\beta\xi_k}+1}.$$

the integral reduces to,

$$\begin{aligned} I_{a1} &= -gT \int \frac{d^3\boldsymbol{k}}{(2\pi)^3} \frac{1}{2\xi_k} \left(-\frac{\beta}{e^{-\beta\xi_k}+1} + \frac{\beta}{e^{\beta\xi_k}+1} \right) \Delta(\boldsymbol{x}) \\ &= -g \int \frac{d^3\boldsymbol{k}}{(2\pi)^3} \frac{1}{2\xi_k} \frac{1-e^{\beta\xi_k}}{1+e^{\beta\xi_k}} \Delta(\boldsymbol{x}) \\ &= g \int \frac{d^3\boldsymbol{k}}{(2\pi)^3} \frac{1}{2\xi_k} \tanh(\frac{\beta\xi_k}{2}) \Delta(\boldsymbol{x}) \qquad \text{making the change of variable} \qquad \frac{d^3\boldsymbol{k}}{(2\pi)^2} \to \mathcal{N}(\xi) d\xi \\ &= g\mathcal{N}(0) \int_{-\hbar\omega_D}^{\hbar\omega_D} d\xi \frac{1}{2\xi} \tanh\left(\frac{\beta\xi}{2}\right) \Delta(\boldsymbol{x}), \end{aligned}$$

where integral which corresponded to tanh is solved the following form

$$\begin{aligned} \int_{-\hbar\omega_D}^{\hbar\omega_D} d\xi \frac{1}{2\xi} \tanh\left(\frac{\beta\xi}{2}\right) &= \int_0^{\frac{\beta}{2}\hbar\omega_D} d\left(\xi\frac{\beta}{2}\right) \frac{1}{\xi\frac{\beta}{2}} \tanh\left(\frac{\beta\xi}{2}\right); \quad x = \frac{\beta\xi}{2} \\ &= \int_0^{\frac{\beta}{2}\hbar\omega_D} \frac{dx}{x} \tanh(x) = \int_0^{\frac{\beta_c}{2}\hbar\omega_D} d(\ln(x)) \tanh(x) \end{aligned}$$

$$
\begin{aligned}
&= \ln(x)\tanh(x)|_0^{\frac{\beta_c}{2}\hbar\omega_D} - \int_0^{\frac{\beta}{2}\hbar\omega_D} \ln(x)d(\tanh(x)) \\
&= \ln(x)\tanh(x)|_0^{\frac{\beta}{2}\hbar\omega_D} - \underbrace{\int_0^{\frac{\beta}{2}\hbar\omega_D} \frac{\ln(x)}{\cosh^2(x)}}_{-\ln(\frac{4e^\gamma}{\pi})}; \qquad \frac{\beta\hbar\omega_D}{2} \to +\infty \\
&= \ln\left(\frac{\beta_c\hbar\omega_D}{2}\right) + \ln\left(\frac{4e^\gamma}{\pi}\right) = \ln\left(\frac{2e^\gamma\hbar\omega_D}{\pi T_c}\right).
\end{aligned}
$$

Finally the integral I_{a1} is equal

$$
\boxed{I_{a1} = g\mathcal{N}(0)\ln\left(\frac{2e^\gamma\hbar\omega_D}{\pi T_c}\right)\Delta(\boldsymbol{x})} \tag{B.5}
$$

In this expression ω_D denotes the cut-off frequency an $\gamma = 0,577$ is the Euler constant, and $\mathcal{N}(0)$, is the density of states (DOS) at the Fermi energy.

The second integral

$$
\begin{aligned}
I_{a_2} &= \int d^3\boldsymbol{z}K_a(\boldsymbol{x},\boldsymbol{x}+\boldsymbol{z})\frac{(\boldsymbol{z}\cdot\boldsymbol{\nabla})^2}{2!}\Delta(\boldsymbol{x}) = \int d^3\boldsymbol{z}K_a(\boldsymbol{x},\boldsymbol{x}+\boldsymbol{z})\sum_{i,j}\frac{z_iz_j\nabla_i\nabla_j}{2!}\Delta(\boldsymbol{x}) \\
&= -\frac{1}{2}gT\sum_\omega\int d^3\boldsymbol{z}G_\omega^{(0)}(\boldsymbol{z})\overline{G}_\omega^{(0)}(-\boldsymbol{z})\sum_{i,j}z_iz_j\nabla_i\nabla_j\Delta(\boldsymbol{x})
\end{aligned}
$$

By using a property of Fourier's transforms, the components of the vector $\underline{o}ldsymbolz$ in the integral can be expressed as derivatives in the Fourier space

$$
\begin{aligned}
\int d^3\boldsymbol{z}e^{-i\boldsymbol{k}\cdot\boldsymbol{z}}G_\omega^{(0)}(\boldsymbol{z})z_j &= \int d^3\boldsymbol{z}(i\partial_{kj})e^{-i\boldsymbol{k}\cdot\boldsymbol{z}}G_\omega^{(0)}(\boldsymbol{z}) = i\partial_{kj}G_\omega^{(0)}(\boldsymbol{k}) \\
\int d^3\boldsymbol{z}e^{-i\boldsymbol{k}\cdot\boldsymbol{z}}\overline{G}_\omega^{(0)}(-\boldsymbol{z})z_j &= \int d^3\boldsymbol{z}(i\partial_{k_j})e^{-i\boldsymbol{k}\cdot\boldsymbol{z}}\overline{G}_\omega^{(0)}(-\boldsymbol{z}) = i\partial_{k_j}\overline{G}_\omega^{(0)}(\boldsymbol{k})
\end{aligned}
$$

The integral above can be rewritten in terms of the Fourier's transformation

$$
\begin{aligned}
\int d^3\boldsymbol{z}K_a(\boldsymbol{x},\boldsymbol{x}+\boldsymbol{z})z_iz_j &= \frac{1}{2}gT\sum_\omega\int\frac{d^3\boldsymbol{k}}{(2\pi)^3}\left(\partial_{k_i}\frac{1}{(i\hbar\omega-\xi_\kappa)^2}\right)\left(\partial_{k_j}\frac{1}{(i\hbar\omega+\xi_\kappa)^2}\right) \\
&= \frac{1}{2}gT\sum_\omega\int\frac{d^3\boldsymbol{k}}{(2\pi)^3}\frac{-\frac{\hbar^2k_i}{m}}{(i\hbar\omega-\xi_\kappa)^2}\frac{\frac{\hbar^2k_i}{m}}{(i\hbar\omega+\xi_\kappa)^2}
\end{aligned}
$$

In the case of spherical Fermi surfaces the integral are non-zero, clearly, only when $i = j$ and also k_i^2 can be substituted by $k^2/3$, then

$$
\int d^3\boldsymbol{z}K_a(\boldsymbol{x},\boldsymbol{x}+\boldsymbol{z})z_iz_j = \frac{gT}{3}\frac{\hbar^2}{m}\mathcal{N}(0)T\sum_\omega\int_{-\hbar\omega_D}^{\hbar\omega_D}d\xi\frac{\xi+\mu}{(\hbar^2\omega^2+\xi^2)^2}
$$

$$
\begin{aligned}
&= \frac{gT}{3}\frac{\hbar^2}{m}\mathcal{N}(0)\mu\sum_\omega \frac{1}{|\hbar\omega|^3}\underbrace{\int_{-\infty}^{\infty} dx \frac{1}{(1+x^2)^2}}_{\pi/2}, \qquad x=\frac{\xi}{\hbar\omega}\\
&= \frac{gT}{3}\frac{\hbar^2}{m}\mathcal{N}(0)\mu\frac{\pi}{2}\sum_\omega \frac{1}{|\hbar\omega|^3} = \frac{gT}{3}\frac{\hbar^2}{m}\mathcal{N}(0)\mu\frac{\pi}{2}\frac{2}{(2\pi T)^3}\underbrace{\sum_\omega \frac{1}{(n+1/2)^3}}_{(2^3-1)\zeta(3)}\\
&= g\mathcal{N}(0)\frac{7\zeta(3)}{8\pi^2T^2}\frac{1}{6}\hbar^2 v_F^2
\end{aligned}
$$

In the above expression using $\sum_{n=0}^{\infty}\frac{1}{(n+1/2)^z} = (2^z-1)\zeta(z)$, where $\zeta(z)$ is the Riemann zeta function. Hence, I_{a2} is equal

$$
\boxed{I_{a2} = g\mathcal{N}(0)\frac{7\zeta(3)}{8\pi^2T^2}\frac{1}{6}\hbar^2 v_F^2\nabla^2\Delta.} \tag{B.6}
$$

Finally for I_a3

$$
\begin{aligned}
I_{a3} &= \int d^3\boldsymbol{z}K_a(\boldsymbol{x},\boldsymbol{x}+\boldsymbol{z})\frac{(\boldsymbol{z}\cdot\boldsymbol{\nabla})^4}{4!}\Delta(\boldsymbol{x})\\
&= \int d^3\boldsymbol{z}K_a(\boldsymbol{x},\boldsymbol{x}+\boldsymbol{z})\sum_{i,j,k,l}\frac{z_iz_jz_kz_l\nabla_i\nabla_j\nabla_k\nabla_l}{4!}\Delta(\boldsymbol{x}), \quad \text{It is convenient to rearrange}\\
&= \int d^3\boldsymbol{z}K_a(\boldsymbol{x},\boldsymbol{x}+\boldsymbol{z})\left[\frac{1}{4!}\sum_n z_n^4\nabla_n^4 + \frac{1}{8}\sum_{n\neq m} z_n^2z_m^2\nabla_n^2\nabla_m^2\right]\Delta(\boldsymbol{x})\\
&= \left(\sum_n\int d^3\boldsymbol{z}K_a(\boldsymbol{x},\boldsymbol{x}+\boldsymbol{z})\frac{z_n^4}{4!}\right)\nabla_n^4 + \left(\sum_{n\neq m}\int d^3\boldsymbol{z}K_a(\boldsymbol{x},\boldsymbol{x}+\boldsymbol{z})\frac{z_n^2z_m^2}{8}\right)\nabla_n^2\nabla_m^2
\end{aligned}
$$

so that the integral

$$
\begin{aligned}
\int d^3\boldsymbol{z}K_a(\boldsymbol{x},\boldsymbol{x}+\boldsymbol{z})\frac{z_n^2z_m^2}{8} &= -\frac{gT}{8}\sum_\omega\int\frac{d^3\boldsymbol{k}}{(2\pi)^3}\left(-\partial_{k_n}\partial_{k_m}\frac{1}{i\hbar\omega-\xi_k}\right)\left(-\partial_{k_n}\partial_{k_m}\frac{1}{i\hbar\omega+\xi_k}\right)\\
&= -\frac{gT}{8}\sum_\omega\int\frac{d^3\boldsymbol{k}}{(2\pi)^3}\frac{2}{(i\hbar\omega-\xi_k)^3}\frac{\hbar^2k_n}{m}\frac{\hbar^2k_m}{m}\frac{2}{(i\hbar\omega+\xi_k)^3}\frac{\hbar^2k_n}{m}\frac{\hbar^2k_m}{m}\\
&= \frac{gT}{2}\sum_\omega\left(\frac{\hbar^2}{m}\right)^4\int\frac{d^3\boldsymbol{k}}{(2\pi)^3}\frac{k_n^2k_m^2}{(\hbar^2\omega^2+\xi_k^2)^3},
\end{aligned}
$$

In the following, assume spherical symmetry. In this case, the above integrals do not depend on indices n and m. For example $n = 1$, $n = 2$, so that $k_1 = k\sin\theta\cos\varphi$ and $k_2 = k\sin\theta\sin\varphi$.

$$
\begin{aligned}
\int d^3\boldsymbol{z}K_a(\boldsymbol{x},\boldsymbol{x}+\boldsymbol{z})\frac{z_n^2 z_m^2}{8} &= \frac{gT}{2}\left(\frac{\hbar^2}{m}\right)^4\sum_\omega\int\frac{d^3\boldsymbol{k}}{(2\pi)^3}\frac{k^4\sin^2\theta\cos^2\varphi\sin^2\theta\sin^2\varphi}{(\hbar^2\omega^2+\xi_k^2)^3} \\
&= \frac{gT}{2}\left(\frac{\hbar^2}{m}\right)^4\sum_\omega\int\frac{dk}{(2\pi)^3}\frac{k^6}{(\hbar^2\omega^2+\xi_k^2)^3}\underbrace{\int_0^{2\pi}\cos^2\varphi\sin^2\varphi d\varphi}_{\pi/4}\underbrace{\int_0^{\pi}\sin^4\theta\sin\theta d\theta}_{16/15} \\
&= \frac{gT}{2}\left(\frac{\hbar^2}{m}\right)^4\frac{4\pi}{15}\sum_\omega\int\frac{dk}{(2\pi)^3}\frac{k^6}{(\hbar^2\omega^2+\xi_k^2)^3}
\end{aligned}
$$

change of variable $\xi = \frac{\hbar^2k^2}{2m} \Rightarrow d\xi = \frac{\hbar^2kdk}{m}$, and $k = \sqrt{\frac{2m}{\hbar}(\xi+\mu)}$

$$
\int d^3\boldsymbol{z}K_a(\boldsymbol{x},\boldsymbol{x}+\boldsymbol{z})\frac{z_n^2 z_m^2}{8} = \frac{gT}{2}\frac{4\pi}{15}\frac{m}{\hbar^2}\left(\frac{\hbar^2}{m}\right)^4\left(\frac{2m}{\hbar^2}\right)^{5/2}\frac{1}{(2\pi)^3}\sum_\omega\int_{-\hbar\omega_D}^{\hbar\omega_D}d\xi\frac{(\xi+\mu)^{5/2}}{(\hbar^2\omega^2+\xi_k^2)^3} \tag{B.7}
$$

The same is related to the terms proportional to ω_D due to the summation over the positive and negative Matsubara frequencies. So, Eq. (B.7) is further reduced to

$$
\begin{aligned}
\int d^3\boldsymbol{z}K_a(\boldsymbol{x},\boldsymbol{x}+\boldsymbol{z})\frac{z_n^2 z_m^2}{8} &= \frac{gT}{2}\frac{m}{\hbar^2}\frac{4\pi}{15}\left(\frac{2m}{\hbar^2}\right)^{5/2}\frac{1}{(2\pi)^3}\left(\frac{\hbar^2}{m}\right)^4\mu^{5/2}\sum_\omega\int_{-\infty}^{\infty}d\xi\frac{1}{(1+\left(\frac{\xi}{\hbar\omega}\right)^2)^3} \\
x = \frac{\xi}{\hbar\omega} \\
&= \frac{gT}{2}\frac{4\pi}{15}\frac{m}{\hbar^2}\left(\frac{2m}{\hbar^2}\right)^{5/2}\frac{1}{(2\pi)^3}\left(\frac{\hbar^2}{m}\right)^4\mu^{5/2}\sum_\omega\frac{1}{|\hbar\omega|^5}\underbrace{\int_{-\infty}^{\infty}dx\frac{1}{(1+x^2)^3}}_{3\pi/8} \\
&= \frac{gT}{2}\frac{4\pi}{15}\frac{m}{\hbar^2}\left(\frac{2m}{\hbar^2}\right)^{5/2}\frac{1}{(2\pi)^3}\left(\frac{\hbar^2}{m}\right)^4\frac{3\pi\mu^{5/2}}{8}\frac{2}{(2\pi T)^5}\underbrace{\sum_{n=0}^{\infty}\frac{1}{\left(n+\frac{1}{2}\right)^5}}_{(2^n-1)\zeta(5)}
\end{aligned}
$$

as $\mu = \frac{\hbar^2k_f^2}{2m}$, $\mathcal{N}(0) = \frac{mk_f}{2\pi^2\hbar^2}$

$$
\int d^3\boldsymbol{z}K_a(\boldsymbol{x},\boldsymbol{x}+\boldsymbol{z})\frac{z_n^2 z_m^2}{8} = g\mathcal{N}(0)\frac{\hbar^4v_f^4}{30}\frac{93\zeta(5)}{128\pi^4T_c^4} \tag{B.8}
$$

The other integral

$$
\frac{1}{4!}\int d^3\boldsymbol{z}K_a(\boldsymbol{x},\boldsymbol{x}+\boldsymbol{z})z_n^4 = -\frac{gT}{4!}\sum_\omega\int d^3\boldsymbol{z}G_\omega^{(0)}(\boldsymbol{z})z_n^2\bar{G}^{(}0)_\omega(-\boldsymbol{z})(-z_n)^2
$$

$$
\begin{aligned}
&= -\frac{gT}{4!}\sum_{\omega}\int\frac{d^3\boldsymbol{k}}{(2\pi)^3}\left(\frac{2}{(i\hbar\omega-\xi_k)^3}\left(\frac{\hbar^2}{m}\right)^2 k_n^2+\frac{1}{(i\hbar\omega-\xi_k)^2}\frac{\hbar^2}{m}\right)\times\\
&\times\left(\frac{2}{(i\hbar\omega+\xi_k)^3}\left(\frac{\hbar^2}{m}\right)^2 k_n^2-\frac{1}{(i\hbar\omega+\xi_k)^2}\frac{\hbar^2}{m}\right)\\
&= -\frac{gT}{4!}\sum_{\omega}\int\frac{d^3\boldsymbol{k}}{(2\pi)^3}\left[\frac{-4}{(\hbar^2\omega^2+\xi_k^2)^3}\left(\frac{\hbar^2}{m}\right)^4 k_n^4+\right.\\
&\left.+\frac{2\xi_k}{(\hbar^2\omega^2+\xi_k^2)^3}\left(\frac{\hbar^2}{m}\right)^3 k_n^2-\frac{(1)}{(\hbar^2\omega^2+\xi_k^2)^2}\left(\frac{\hbar}{m}\right)^2\right]
\end{aligned}
$$

this integral is reduced for

$$
\frac{1}{4!}\int d^3\boldsymbol{z}K_a(\boldsymbol{x},\boldsymbol{x}+\boldsymbol{z})z_n^4=\mathcal{N}(0)\frac{g\hbar^4v_f^4}{30}\frac{93\zeta(5)}{128\pi^4T_c^4} \tag{B.9}
$$

so that:

$$
\begin{aligned}
I_{a3} &= \left[\sum_n\mathcal{N}(0)\frac{g\hbar^4v_f}{30}\frac{93\zeta(6)}{128\pi^4T_c^4}\nabla_n^4+\sum_{n,m}\mathcal{N}(0)\frac{g\hbar^4v_f^4}{30}\frac{93\zeta(5)}{128\pi^4T_c^4}\nabla_n^2\nabla_m^2\right]\Delta(\boldsymbol{x})\\
&= \mathcal{N}(0)\frac{g\hbar^4v_f^4}{30}\frac{93\zeta(5)}{128\pi^4T_c^4}\underbrace{\left[\sum_n\nabla_n^4+\sum_{n,m}\nabla_n^2\nabla_m^2\right]}_{\boldsymbol{\nabla}^4}\Delta(\boldsymbol{x})
\end{aligned}
$$

The final expression become

$$
I_{a3}=\boxed{\mathcal{N}(0)\frac{g\hbar^4v_f^4}{30}\frac{93\zeta(5)}{128\pi^4T_c^4}\nabla^2(\nabla^2\Delta(\boldsymbol{x}))} \tag{B.10}
$$

APPENDIX B.2 - Coefficients Related to the Integral Kernel $K_b(\boldsymbol{x},\{\boldsymbol{y}\}_3)$

Our next step is to calculate the coefficients that are related to the second integral kernel, i.e., $K_b(\boldsymbol{x},\{\boldsymbol{y}\}_3)$.

$$
\begin{aligned}
I_b &= \int\prod_{j=1}^{3}d^3\boldsymbol{y}_jK_b(\boldsymbol{x},\{\boldsymbol{y}\}_3)\Delta\boldsymbol{y}_1\Delta^*(\boldsymbol{y}_2)\Delta(\boldsymbol{y}_3)\\
&= -gT\sum_{\omega}\int\prod_{j=1}^{3}d^3\boldsymbol{y}_jG_{\omega}^{(0)}(\boldsymbol{x},\boldsymbol{y}_1)\bar{G}_{\omega}^{(0)}(\boldsymbol{y}_1,\boldsymbol{y}_2)G_{\omega}^{(0)}(\boldsymbol{y}_2,\boldsymbol{y}_3)\bar{G}_{\omega}^{(0)}(\boldsymbol{y}_3,\boldsymbol{x})\Delta(\boldsymbol{y}_1)\Delta^*(\boldsymbol{y}_2)\Delta(\boldsymbol{y}_3),\\
&= -gT\sum_{\omega}\int\prod_{j=1}^{3}d^3\boldsymbol{z}_jG_{\omega}^{(0)}(-\boldsymbol{z}_1)\bar{G}_{\omega}^{(0)}(\boldsymbol{z}_1-\boldsymbol{z}_2)G_{\omega}^{(0)}(\boldsymbol{z}_2-\boldsymbol{z}_3)\bar{G}_{\omega}^{(0)}(\boldsymbol{z}_3)\Delta(\boldsymbol{x}+\boldsymbol{z}_1)\Delta^*(\boldsymbol{x}+\boldsymbol{z}_2)\Delta(\boldsymbol{x}+\boldsymbol{z}_3),
\end{aligned}
$$

$$= - gT \sum_{\omega} \int \prod_{j=1}^{3} d^3\boldsymbol{z}_j K_b(\{\boldsymbol{z}\}_3) \Delta(\boldsymbol{x}+\boldsymbol{z}_1)\Delta^*(\boldsymbol{x}+\boldsymbol{z}_2)\Delta(\boldsymbol{x}+\boldsymbol{z}_3) \tag{B.11}$$

The integral in Eq. (B.11) is expanded in terms of the spatial derivatives of $\Delta(\boldsymbol{x})$ and $\Delta^*(\boldsymbol{x})$

$$I_b = -gT \sum_{\omega} \int \prod_{j=1}^{3} d^3 z_j K_b(\{\boldsymbol{z}\}_3) \times \left(\Delta(\boldsymbol{x}) + \frac{(\boldsymbol{z}_1 \cdot \boldsymbol{\nabla})}{1!}\Delta(\boldsymbol{x}) + \frac{(\boldsymbol{z}_1 \cdot \boldsymbol{\nabla})^2}{2!}\Delta(\boldsymbol{x})\right) \times$$
$$\times \left(\Delta^*(\boldsymbol{x}) + \frac{(\boldsymbol{z}_2 \cdot \boldsymbol{\nabla})}{1!}\Delta^*(\boldsymbol{x}) + \frac{(\boldsymbol{z}_2 \cdot \boldsymbol{\nabla})^2}{2!}\Delta^*(\boldsymbol{x})\right) \times \left(\Delta(\boldsymbol{x}) + \frac{(\boldsymbol{z}_3 \cdot \boldsymbol{\nabla})}{1!}\Delta(\boldsymbol{x}) + \frac{(\boldsymbol{z}_3 \cdot \boldsymbol{\nabla})^2}{2!}\Delta(\boldsymbol{x})\right).$$

The terms that contribute to the relevant orders $\tau^{3/2}$ and $\tau^{5/2}$ are the following:

$$I_{1b} = -gT \sum_{\omega} \int \prod_{j=1}^{3} d^3 z_j K_b(\{\boldsymbol{z}\}_3)(\boldsymbol{z}_1 \cdot \boldsymbol{\nabla})\Delta(\boldsymbol{x})(\boldsymbol{z}_2 \cdot \boldsymbol{\nabla})\Delta^*(\boldsymbol{x})\Delta(\boldsymbol{x}), \tag{B.12}$$

$$I_{2b} = -gT \sum_{\omega} \int \prod_{j=1}^{3} d^3 z_j K_b(\{\boldsymbol{z}\}_3)\Delta(\boldsymbol{x})(\boldsymbol{z}_2 \cdot \boldsymbol{\nabla})\Delta^*(\boldsymbol{x})(\boldsymbol{z}_3 \cdot \boldsymbol{\nabla})\Delta(\boldsymbol{x}), \tag{B.13}$$

$$I_{3b} = -gT \sum_{\omega} \int \prod_{j=1}^{3} d^3 z_j K_b(\{\boldsymbol{z}\}_3)(\boldsymbol{z}_1 \cdot \boldsymbol{\nabla})\Delta(\boldsymbol{x})\Delta^*(\boldsymbol{x})(\boldsymbol{z}_3 \cdot \boldsymbol{\nabla})\Delta(\boldsymbol{x}), \tag{B.14}$$

$$I_{4b} = -gT \sum_{\omega} \int \prod_{j=1}^{3} d^3 z_j K_b(\{\boldsymbol{z}\}_3)\frac{(\boldsymbol{z}_1 \cdot \boldsymbol{\nabla})^2}{2!}\Delta^*(\boldsymbol{x})\Delta(\boldsymbol{x})\Delta(\boldsymbol{x}) \tag{B.15}$$

$$I_{5b} = -gT \sum_{\omega} \int \prod_{j=1}^{3} d^3 z_j K_b(\{\boldsymbol{z}\}_3)\Delta(\boldsymbol{x})\Delta^*(\boldsymbol{x})\frac{(\boldsymbol{z}_3 \cdot \boldsymbol{\nabla})^2}{2!} \tag{B.16}$$

$$I_{6b} = -gT \sum_{\omega} \int \prod_{j=1}^{3} d^3 z_j K_b(\{\boldsymbol{z}\}_3)\Delta(\boldsymbol{x})\frac{(\boldsymbol{z}_2 \cdot \boldsymbol{\nabla})^2}{2!}\Delta^*(\boldsymbol{x})\Delta(\boldsymbol{x}) \tag{B.17}$$

The integral in Eqs. (B.12-B.17) is reduced by invoking the Fourier transform and applying the well-known convolution theorem provided that we rearrange the polynomial in the relevant integrand as.

$$\boldsymbol{z}_2 = \boldsymbol{z}_2 - \boldsymbol{z}_1 + \boldsymbol{z}_1$$

$$\text{for example,}\quad z_{1n}z_{2m} = z_{1n}(z_{2m} - z_{1m} + z_{1m}) = (z_{1n}(z_{2m} - z_{1m}) + z_{1n}z_{1m})$$

The integral (B.12):

$$I_{1b} = -gT \sum_{\omega} \int \prod_{j=1}^{3} d\boldsymbol{z}_j K_b(\{\boldsymbol{z}\}_3) \sum_{n} z_{1n}\nabla_n\Delta(\boldsymbol{x}) \sum_{m} z_{2m}\nabla_m\Delta^*(\boldsymbol{x})\Delta(\boldsymbol{x}),$$

$$= -gT \sum_{n,m} \sum_{\omega} \int \prod_{j=1}^{3} d\boldsymbol{z}_j z_{1n} G^{(0)}_{\omega}(-\boldsymbol{z}_1) z_{2m} \bar{G}^{(0)}_{\omega}(\boldsymbol{z}_1 - \boldsymbol{z}_2) G^{(0)}_{\omega}(\boldsymbol{z}_2 - \boldsymbol{z}_3) \bar{G}^{(0)}_{\omega}(\boldsymbol{z}_3) \nabla_n \Delta(\boldsymbol{x}) \nabla_m \Delta^*(\boldsymbol{x}) \Delta(\boldsymbol{x}),$$

$$= -gT \left(\sum_{n,m} \cdots \right) \sum_{\omega} \int \prod_{j=1}^{3} d\boldsymbol{z}_j (z_{1n}) G^{(0)}_{\omega}(-\boldsymbol{z}_1)(z_{2m} - z_{1m} + z_{1m}) \bar{G}^{(0)}_{\omega}(\boldsymbol{z}_1 - \boldsymbol{z}_2) G^{(0)}_{\omega}(\boldsymbol{z}_2 - \boldsymbol{z}_3) \bar{G}^{(0)}_{\omega}(\boldsymbol{z}_3),$$

$$= -gT \left(\sum_{n,m} \cdots \right) \sum_{\omega} \left[\int \prod_{j=1}^{3} d\boldsymbol{z}_j (-z_{1n}) G^{(0)}_{\omega}(-\boldsymbol{z}_1)(-(z_{1m} - z_{2m})) \bar{G}^{(0)}_{\omega}(\boldsymbol{z}_1 - \boldsymbol{z}_2) G^{(0)}_{\omega}(\boldsymbol{z}_2 - \boldsymbol{z}_3) \bar{G}^{(0)}_{\omega}(\boldsymbol{z}_3) + \right.$$

$$\left. + \int \prod_{j=1}^{3} d\boldsymbol{z}_j (-z_{1n} z_{1m}) G^{(0)}_{\omega}(-\boldsymbol{z}_1) \bar{G}^{(0)}_{\omega}(\boldsymbol{z}_1 - \boldsymbol{z}_2) G^{(0)}_{\omega}(\boldsymbol{z}_2 - \boldsymbol{z}_3) \bar{G}^{(0)}_{\omega}(\boldsymbol{z}_3) \right].$$

$$= \sum_{n,m} (I^{(a)}_{1b} + I^{(b)}_{1b}) \nabla_n \Delta(\boldsymbol{x}) \nabla_m \Delta^*(\boldsymbol{x}) \Delta(\boldsymbol{x}).$$

$$I^{(b)}_{1b} = -gT \sum_{\omega} \int \frac{d^3\boldsymbol{k}}{(2\pi)^3} (-\partial_{k_n} \partial_{k_m}) \frac{1}{i\hbar\omega - \xi_k} \frac{1}{i\hbar\omega + \xi_k} \frac{1}{i\hbar\omega - \xi_k} \frac{1}{i\hbar\omega + \xi_k}$$

integral to converge, $n = m$.

$$= -gT \sum_{\omega} \int \frac{d^3\boldsymbol{k}}{(2\pi)^3} \left(-\partial_n^2 \frac{1}{i\hbar\omega - \xi_k} \right) \frac{1}{(i\hbar\omega + \xi_k)^2 (i\hbar\omega - \xi_k)}$$

$$= gT \sum_{\omega} \int \frac{d^3\boldsymbol{k}}{(2\pi)^3} \left[\frac{2 \frac{\hbar^4 k_n^2}{m^2}}{(i\hbar\omega - \xi_k)^4 (i\hbar\omega + \xi_k)^2} + \frac{\frac{\hbar^2}{m}}{(i\hbar\omega - \xi_k)^3 (i\hbar\omega + \xi_k)^2} \right]$$

with $\boldsymbol{k} = \{k_1, k_2, k_3\}$. Due to the spherical symmetry of the term in the parentheses, the integral does not depend on n so that k_n^2 can be replaced by $k^2/3$, and $\xi_k = \frac{\hbar^2 k^2}{2m} - \mu$. Then, by making use of the standard approximation ($\xi = \xi_k$), $\int \frac{d^3\boldsymbol{k}}{(2\pi)^3} \approx \mathcal{N}(0) \int_{-\infty}^{+\infty} d\xi$. One gets

$$I^{(b)}_{1b} = gT \sum_{\omega} \mathcal{N}(0) \left[\frac{2\hbar^2}{3m} \int d\xi \frac{(\xi + \mu)(i\hbar\omega + \xi)^2}{(i\hbar\omega - \xi)^4 (i\hbar\omega + \xi)^4} + \frac{\hbar^2}{m} \int d\xi \frac{(i\hbar\omega + \xi)^2}{(i\hbar\omega - \xi)^3 (i\hbar\omega + \xi)^3} \right]$$

So, the integral is reduced to

$$I^{(b)}_{1b} = gT \frac{2\hbar^2}{3m} \mu \mathcal{N}(0) \sum_{\omega} \int_{-\infty}^{+\infty} d\xi \frac{(-\hbar^2\omega^2 + \xi^2)}{(\hbar^2\omega^2 + \xi^2)^4}, \quad x = \xi/\hbar\omega$$

$$= gT \frac{2\hbar^2}{3m} \mu \mathcal{N}(0) \underbrace{\sum_{\omega} \frac{1}{|\hbar\omega|}}_{\frac{2}{(2\pi T)^5}(2^5-1)\zeta(5)} \underbrace{\int_{-\infty}^{+\infty} d\xi \frac{(x^2 - 1)}{(x^2 + 1)^4}}_{-\pi/4} = -g\mathcal{N}(0) \frac{\hbar^2 v_f^2}{6} \frac{31\zeta(5)}{128\pi^4 T^4}$$

Now the first integral

$$I^{(a)}_{1b} = gT \sum_{\omega} \int \frac{d^3\boldsymbol{k}}{(2\pi)^3} (-\partial_{k_n}) \frac{1}{i\hbar\omega - \xi_k} \partial_{k_m} \frac{1}{i\hbar\omega + \xi_k} \frac{1}{i\hbar\omega - \xi_k} \frac{1}{i\hbar\omega + \xi_k}$$

$$= -gT\sum_{n,m}\sum_{\omega}\int\frac{d^3\boldsymbol{k}}{(2\pi)^3}\frac{\hbar^2 k_n}{m}\frac{1}{(i\hbar\omega-\xi_k)^2}\left(-\frac{\hbar^2 k_m}{m}\right)\frac{1}{(i\hbar\omega+\xi_k)^2}\frac{1}{(i\hbar\omega-\xi_k)}\frac{1}{(i\hbar\omega+\xi_k)}$$

integral to converge, $n = m$.

$$= gT\sum_{\omega}\int\frac{d^3\boldsymbol{k}}{(2\pi)^3}\frac{2\hbar^2(\xi_k+\mu)}{3m}\frac{1}{(i\hbar\omega-\xi_k)^3}\frac{1}{(i\hbar\omega+\xi_k)^3}$$

$$= gT\frac{2\hbar^2}{3m}\mu\mathcal{N}(0)\sum_{\omega}\int_{-\infty}^{\infty}d\xi\frac{(-1)}{(\hbar^2\omega^2+\xi^2)^3},\quad x=\xi/\hbar\omega$$

$$= gT\frac{2\hbar^2}{3m}\mu\mathcal{N}(0)(-1)\ \underbrace{\sum_{\omega}\frac{1}{|\hbar\omega|}}_{\frac{2}{(2\pi T)^5}31\zeta(5)}\ \underbrace{\int_{-\infty}^{\infty}dx\frac{1}{(x^2+1)^3}}_{3\pi/8},$$

$$I_{1b}^{(b)} = -g\mathcal{N}(0)\frac{\hbar^2 v_f^2}{4}\frac{31\zeta(5)}{128\pi^4T^4}$$

Thus, the first integral is equal

$$\boxed{I_{1b} = I_{1b}^{(a)} + I_{1b}^{(b)} = -\frac{g\mathcal{N}(0)}{9}\hbar^2 v_f^2\frac{93\zeta(5)}{128\pi^4T_c^4}\Delta(\boldsymbol{x})\boldsymbol{\nabla}\Delta(\boldsymbol{x})\cdot\boldsymbol{\nabla}\Delta^*(\boldsymbol{x})} \tag{B.18}$$

The integral (B.13) is:

$$I_{2b} = -gT\sum_{\omega}\int\prod_{j=1}^{3}d^3z_jK_b(\{\boldsymbol{z}\}_3)\Delta(\boldsymbol{x})(\boldsymbol{z}_2\cdot\boldsymbol{\nabla})\Delta^*(\boldsymbol{x})(\boldsymbol{z}_3\cdot\boldsymbol{\nabla})\Delta(\boldsymbol{x}),$$

$$= -gT\sum_{n,m}\sum_{\omega}\int\prod_{j=1}^{3}d^3z_jK_b(\{\boldsymbol{z}\}_3)\Delta(\boldsymbol{x})\underbrace{z_{2n}}_{Z_{2n}-Z_{3n}+Z_{3n}}\nabla_n\Delta^*(\boldsymbol{x})z_{3m}\nabla_m\Delta(\boldsymbol{x}),$$

$$= -gT\sum_{n,m}\sum_{\omega}\left[\int\prod_{j=1}^{3}d^3z_jG_{\omega}^{(0)}(-\boldsymbol{z}_1)\bar{G}_{\omega}^{(0)}(\boldsymbol{z}_1-\boldsymbol{z}_2)(z_{2n}-z_{3n})G_{\omega}^{(0)}(\boldsymbol{z}_2-\boldsymbol{z}_3)z_{3m}\bar{G}_{\omega}^{(0)}(\boldsymbol{z}_3)+\right.$$

$$\left.+\int\prod_{j=1}^{3}d^3z_jG_{\omega}^{(0)}(-\boldsymbol{z}_1)\bar{G}_{\omega}^{(0)}(\boldsymbol{z}_1-\boldsymbol{z}_2)G_{\omega}^{(0)}(\boldsymbol{z}_2-\boldsymbol{z}_3)z_{3n}z_{3m}\bar{G}_{\omega}^{(0)}(\boldsymbol{z}_3)\right]\Delta(\boldsymbol{x})\nabla_n\Delta^*(\boldsymbol{x})\nabla_m\Delta(\boldsymbol{x})$$

$$I_{2b} = -gT\sum_{n,m}\sum_{\omega}\int\frac{d^3\boldsymbol{k}}{(2\pi)^3}\left[\frac{1}{i\hbar\omega-\xi_k}\frac{1}{i\hbar\omega+\xi_k}\left(\partial_{k_n}\frac{1}{i\hbar\omega-\xi_k}\right)\left(\partial_{k_m}\frac{1}{i\hbar\omega+\xi_k}\right)\right.$$
$$\left.+\frac{1}{(i\hbar\omega-\xi_k)^2}\frac{1}{i\hbar\omega+\xi_k}\left(-\partial_{k_n}\partial_{k_m}\frac{1}{i\hbar\omega+\xi_k}\right)\right]\Delta(\boldsymbol{x})\nabla_n\Delta^*(\boldsymbol{x})\nabla_m\Delta(\boldsymbol{x})$$

note that these integrals are equal to those previously calculated

$$\boxed{I_{2b} = -\frac{g\mathcal{N}(0)}{9}\hbar^2 v_f^2\frac{93\zeta(5)}{128\pi^4T_c^4}\Delta(\boldsymbol{x})\boldsymbol{\nabla}\Delta^*(\boldsymbol{x})\cdot\boldsymbol{\nabla}\Delta(\boldsymbol{x})} \tag{B.19}$$

Calculate the integral (B.14).

$$
\begin{aligned}
I_{3b} &= -gT\sum_{\omega}\int\prod_{j=1}^{3} d^3z_jK_b(\{\boldsymbol{z}\}_3)(\boldsymbol{z}_1\cdot\boldsymbol{\nabla})\Delta(\boldsymbol{x})\Delta^*(\boldsymbol{x})(\boldsymbol{z}_3\cdot\boldsymbol{\nabla})\Delta(\boldsymbol{x}).\\
&= -gT\sum_{n}\sum_{\omega}\int\prod_{j=1}^{3} d^3z_jK_b(\{\boldsymbol{z}\}_3)z_{1n}\nabla_n\Delta(\boldsymbol{x})\Delta^*(\boldsymbol{x})z_{3n}\nabla_n\Delta(\boldsymbol{x}).\\
&= -gT\sum_{n}\Delta^*(\boldsymbol{x})\nabla_n\Delta(\boldsymbol{x})\nabla_n\Delta(\boldsymbol{x})\sum_{\omega}\int\prod_{j=1}^{3} d^3z_jz_{1n}G^{(0)}_{\omega}(-\boldsymbol{z}_1)\bar{G}^{(0)}_{\omega}(\boldsymbol{z}_1-\boldsymbol{z}_2)G^{(0)}_{\omega}(\boldsymbol{z}_2-\boldsymbol{z}_3)z_{3n}\bar{G}^{(0)}_{\omega}(\boldsymbol{z}_3)\\
&= -gT\sum_{n}\Delta^*(\boldsymbol{x})\nabla_n\Delta(\boldsymbol{x})\nabla_n\Delta(\boldsymbol{x})\sum_{\omega}\int\frac{d^3\boldsymbol{k}}{(2\pi)^3}\left(-\frac{1}{i}\partial_{k_n}\frac{1}{i\hbar\omega-\xi_k}\right)\frac{1}{i\hbar\omega+\xi_k}\frac{1}{i\hbar\omega-\xi_k}\left(-\frac{1}{i}\partial_{k_n}\frac{1}{i\hbar\omega+\xi_k}\right)\\
&= -gT\sum_{n}\Delta^*(\boldsymbol{x})\nabla_n\Delta(\boldsymbol{x})\nabla_n\Delta(\boldsymbol{x})\sum_{\omega}\int\frac{d^3\boldsymbol{k}}{(2\pi)^3}\frac{\frac{\hbar^2k_n}{m}}{i\hbar\omega-\xi_k}\frac{1}{i\hbar\omega+\xi_k}\frac{1}{i\hbar\omega-\xi_k}\frac{\frac{(-1)\hbar^2k_n}{m}}{i\hbar\omega+\xi_k}\\
&= gT\Delta^*(\boldsymbol{x})\boldsymbol{\nabla}\Delta(\boldsymbol{x})\cdot\boldsymbol{\nabla}\Delta(\boldsymbol{x})\sum_{\omega}\frac{1}{3}\int\frac{d^3\boldsymbol{k}}{(2\pi)^3}\frac{\frac{\hbar^4k^2}{m^2}}{(i\hbar\omega-\xi_k)^3(i\hbar\omega+\xi_k)^3}\\
&= gT\Delta^*(\boldsymbol{x})\boldsymbol{\nabla}\Delta(\boldsymbol{x})\cdot\boldsymbol{\nabla}\Delta(\boldsymbol{x})\sum_{\omega}\frac{2}{3}\frac{\hbar^2}{m}\int\frac{d^3\boldsymbol{k}}{(2\pi)^3}\frac{\xi_k+\mu}{(i\hbar\omega-\xi_k)^3(i\hbar\omega+\xi_k)^3}\\
&= -gT\Delta^*(\boldsymbol{x})\boldsymbol{\nabla}\Delta(\boldsymbol{x})\cdot\boldsymbol{\nabla}\Delta(\boldsymbol{x})\frac{2}{3}\frac{\hbar^2}{m}\mu\mathcal{N}(0)\sum_{\omega}\int_{-\infty}^{\infty}d\xi\frac{1}{(\hbar^2\omega^2+\xi^2)^3}\\
&= -gT\Delta^*(\boldsymbol{x})\boldsymbol{\nabla}\Delta(\boldsymbol{x})\cdot\boldsymbol{\nabla}\Delta(\boldsymbol{x})\frac{2}{3}\frac{\hbar^2}{m}\mu\mathcal{N}(0)\sum_{\omega}\frac{1}{|\hbar\omega|^5}\underbrace{\int_{-\infty}^{\infty}dx\frac{1}{(x^2+1)^3}}_{3\pi/8}
\end{aligned}
$$

$$\boxed{I_{3b} = -\frac{g\mathcal{N}(0)}{3}\hbar^2v_f^2\frac{93\zeta(5)}{128\pi^4T_c^4}\Delta^*(\boldsymbol{x})\boldsymbol{\nabla}\Delta(\boldsymbol{x})\cdot\boldsymbol{\nabla}\Delta(\boldsymbol{x})} \tag{B.20}$$

Calculate the integral (B.15).

$$
\begin{aligned}
I_{4b} &= -gT\sum_{\omega}\int\prod_{j=1}^{3} d^3z_jK_b(\{\boldsymbol{z}\}_3)\frac{(\boldsymbol{z}_1\cdot\boldsymbol{\nabla})^2}{2!}\Delta(\boldsymbol{x})\Delta^*(\boldsymbol{x})\Delta(\boldsymbol{x})\\
&= -gT\sum_{n}\frac{|\Delta\boldsymbol{x}|^2}{2}\nabla_n^2\Delta(\boldsymbol{x})\sum_{\omega}\int\frac{d^3\boldsymbol{k}}{(2\pi)^3}\left(-\partial_n^2\frac{1}{i\hbar\omega-\xi_k}\right)\frac{1}{(i\hbar\omega+\xi_k)^2(i\hbar\omega-\xi_k)}\\
&= gT\sum_{n}\frac{|\Delta\boldsymbol{x}|^2}{2}\nabla_n^2\Delta(\boldsymbol{x})\sum_{\omega}\int\frac{d^3\boldsymbol{k}}{(2\pi)^3}\left(\frac{2\frac{\hbar^2}{m}k_n\frac{\hbar^2}{m}k_n}{(i\hbar\omega-\xi_k)^3}+\frac{\frac{\hbar^2}{m}}{(i\hbar\omega-\xi_k)^2}\right)\frac{1}{(i\hbar\omega+\xi_k)^2(i\hbar\omega-\xi_k)}\\
&= gT\sum_{n}\frac{|\Delta\boldsymbol{x}|^2}{2}\nabla_n^2\Delta(\boldsymbol{x})\sum_{\omega}\left\{\int\frac{d^3\boldsymbol{k}}{(2\pi)^3}\frac{2}{(i\hbar\omega+\xi_k)^2(i\hbar\omega-\xi_k)^4}\frac{\hbar^2}{m}k_n\frac{\hbar^2}{m}k_n\right\}
\end{aligned}
$$

$$
\begin{aligned}
&= gT\frac{|\Delta\boldsymbol{x}|^2}{2}\nabla^2\Delta(\boldsymbol{x})\sum_\omega \frac{4\hbar^2}{3m}\int\frac{d^3\boldsymbol{k}}{(2\pi)^3}\frac{(\xi_k+\mu)(i\hbar\omega+\xi_k)^2}{(i\hbar\omega+\xi_k)^4(i\hbar\omega-\xi_k)^4}\\
&= gT\frac{|\Delta\boldsymbol{x}|^2}{2}\nabla^2\Delta(\boldsymbol{x})\sum_\omega \frac{4\hbar^2}{3m}\int\frac{d^3\boldsymbol{k}}{(2\pi)^3}\frac{(\xi_k+\mu)(-\hbar^2\omega^2+\xi_k^2+i\xi_k\hbar\omega)}{(i\hbar\omega+\xi_k)^4(i\hbar\omega-\xi_k)^4}\\
&= gT\frac{4\hbar^2}{3m}\mu\mathcal{N}(0)\frac{|\Delta\boldsymbol{x}|^2}{2}\nabla^2\Delta(\boldsymbol{x})\sum_\omega\int d\xi\frac{(-\hbar^2\omega^2+\xi^2)}{(\hbar^2\omega^2+\xi^2)^4}\\
&= gT\frac{4\hbar^2}{3m}\mu\mathcal{N}(0)\frac{|\Delta\boldsymbol{x}|^2}{2}\nabla^2\Delta(\boldsymbol{x})\sum_\omega\frac{1}{|\hbar\omega|^5}\underbrace{\int_{-\infty}^{\infty}d\xi\frac{(x^2-1)}{(x^2+1)^4}}_{-\pi/4}\\
&= gT\frac{4\hbar^2}{3m}\mu\mathcal{N}(0)\frac{|\Delta\boldsymbol{x}|^2}{2}\nabla^2\Delta(\boldsymbol{x})\left(-\frac{\pi}{4}\right)\frac{2}{(2\pi T)^5}31\zeta(5)
\end{aligned}
$$

$$
\boxed{I_{4b}=-\frac{g\mathcal{N}(0)}{3}\hbar^2v_f^2\frac{93\zeta(5)}{128\pi^4T_c^4}\frac{2}{9}\frac{|\Delta\boldsymbol{x}|^2}{2}\nabla^2\Delta(\boldsymbol{x})} \tag{B.21}
$$

The integral (B.16).

$$
\begin{aligned}
I_{5b} &= -gT\sum_\omega\int\prod_{j=1}^{3}d^3z_jK_b(\{\boldsymbol{z}\}_3)\Delta(\boldsymbol{x})\Delta^*(\boldsymbol{x})\frac{(\boldsymbol{z}_3\cdot\boldsymbol{\nabla})^2}{2!}\Delta(\boldsymbol{x})\\
&= -gT\sum_n\frac{|\Delta\boldsymbol{x}|^2}{2}\nabla_n^2\Delta(\boldsymbol{x})\sum_\omega\int\frac{d^3\boldsymbol{k}}{(2\pi)^3}\frac{1}{(i\hbar\omega-\xi_k)^2(i\hbar\omega+\xi_k)}\left(-\partial_n^2\frac{1}{i\hbar\omega+\xi_k}\right)\\
&= gT\sum_n\frac{|\Delta\boldsymbol{x}|^2}{2}\nabla_n^2\Delta(\boldsymbol{x})\sum_\omega\int\frac{d^3\boldsymbol{k}}{(2\pi)^3}\left(\frac{2\frac{\hbar^2}{m}k_n\frac{\hbar^2}{m}k_n}{(i\hbar\omega+\xi_k)^3}-\frac{\frac{\hbar^2}{m}}{(i\hbar\omega-\xi_k)^2}\right)\frac{1}{(i\hbar\omega-\xi_k)^2(i\hbar\omega+\xi_k)}\\
&= gT\sum_n\frac{|\Delta\boldsymbol{x}|^2}{2}\nabla_n^2\Delta(\boldsymbol{x})\sum_\omega\left\{\int\frac{d^3\boldsymbol{k}}{(2\pi)^3}\frac{2}{(i\hbar\omega-\xi_k)^2(i\hbar\omega+\xi_k)^4}\frac{\hbar^2}{m}k_n\frac{\hbar^2}{m}k_n\right\}\\
&= gT\frac{|\Delta\boldsymbol{x}|^2}{2}\nabla^2\Delta(\boldsymbol{x})\sum_\omega \frac{4\hbar^2}{3m}\int\frac{d^3\boldsymbol{k}}{(2\pi)^3}\frac{(\xi_k-\mu)(i\hbar\omega+\xi_k)^2}{(i\hbar\omega+\xi_k)^4(i\hbar\omega-\xi_k)^4}\\
&= gT\frac{|\Delta\boldsymbol{x}|^2}{2}\nabla^2\Delta(\boldsymbol{x})\sum_\omega \frac{4\hbar^2}{3m}\int\frac{d^3\boldsymbol{k}}{(2\pi)^3}\frac{(\xi_k+\mu)(-\hbar^2\omega^2+\xi_k^2-i\xi_k\hbar\omega)}{(i\hbar\omega+\xi_k)^4(i\hbar\omega-\xi_k)^4}\\
&= gT\frac{4\hbar^2}{3m}\mu\mathcal{N}(0)\frac{|\Delta\boldsymbol{x}|^2}{2}\nabla^2\Delta(\boldsymbol{x})\sum_\omega\int d\xi\frac{(-\hbar^2\omega^2+\xi^2)}{(\hbar^2\omega^2+\xi^2)^4}\\
&= gT\frac{4\hbar^2}{3m}\mu\mathcal{N}(0)\frac{|\Delta\boldsymbol{x}|^2}{2}\nabla^2\Delta(\boldsymbol{x})\sum_\omega\frac{1}{|\hbar\omega|^5}\underbrace{\int_{-\infty}^{\infty}d\xi\frac{(x^2-1)}{(x^2+1)^4}}_{-\pi/4}\\
&= gT\frac{4\hbar^2}{3m}\mu\mathcal{N}(0)\frac{|\Delta\boldsymbol{x}|^2}{2}\nabla^2\Delta(\boldsymbol{x})\left(-\frac{\pi}{4}\right)\frac{2}{(2\pi T)^5}31\zeta(5)
\end{aligned}
$$

$$
\boxed{I_{5b}=-\frac{g\mathcal{N}(0)}{3}\hbar^2v_f^2\frac{93\zeta(5)}{128\pi^4T_c^4}\frac{2}{9}\frac{|\Delta\boldsymbol{x}|^2}{2}\nabla^2\Delta(\boldsymbol{x})\frac{|\Delta\boldsymbol{x}|^2}{2}} \tag{B.22}
$$

Finally calculate of integral (B.17)

$$I_{6b} = -gT\sum_{\omega}\int\prod_{j=1}^{3} d^3 z_j G_{\omega}^{(0)}(-\boldsymbol{z}_1)\bar{G}_{\omega}^{(0)}(\boldsymbol{z}_1-\boldsymbol{z}_2)G_{\omega}^{(0)}(\boldsymbol{z}_2-\boldsymbol{z}_3)\bar{G}_{\omega}^{(0)}(\boldsymbol{z}_3)\Delta(\boldsymbol{x})\frac{(\boldsymbol{z}_2\cdot\boldsymbol{\nabla})^2}{2!}\Delta^*(\boldsymbol{x})\Delta(\boldsymbol{x})$$

$$\begin{aligned}(\boldsymbol{z}_2\cdot\boldsymbol{\nabla})^2 &= \sum_{n,m} z_{2n}z_{2m}\nabla_n\nabla_m \to \sum_n z_{2n}^2\nabla_n^2\\ &= \sum_n (z_{2n}-z_{3n}+z_{2^n})^2\nabla_n^2\\ &= \sum_n\{(z_{2n}-z_{3n})^2+z_{3n}^2+2(z_{2n}-z_{3n})z_{3n}\}\nabla_n^2\end{aligned}$$

here have three integrals to solve

$$\begin{aligned}I_{6b}^{(a)} &= -gT\sum_n\Delta^2(\boldsymbol{x})\frac{\nabla_n^2\Delta(\boldsymbol{x})}{2!}\sum_{\omega}\int\prod_{j=1}^{3} d^3 z_j G_{\omega}^{(0)}(-\boldsymbol{z}_1)\bar{G}_{\omega}^{(0)}(\boldsymbol{z}_1-\boldsymbol{z}_2)(z_{2n}-z_{3n})^2G_{\omega}^{(0)}(\boldsymbol{z}_2-\boldsymbol{z}_3)\bar{G}_{\omega}^{(0)}(\boldsymbol{z}_3),\\ I_{6b}^{(b)} &= -gT\sum_n\Delta^2(\boldsymbol{x})\frac{\nabla_n^2\Delta(\boldsymbol{x})}{2!}\sum_{\omega}\int\prod_{j=1}^{3} d^3 z_j G_{\omega}^{(0)}(-\boldsymbol{z}_1)\bar{G}_{\omega}^{(0)}(\boldsymbol{z}_1-\boldsymbol{z}_2)G_{\omega}^{(0)}(\boldsymbol{z}_2-\boldsymbol{z}_3)z_{3n}^2\bar{G}_{\omega}^{(0)}(\boldsymbol{z}_3),\\ I_{6b}^{(a)} &= -gT\sum_n\Delta^2(\boldsymbol{x})\nabla_n^2\Delta(\boldsymbol{x})\sum_{\omega}\int\prod_{j=1}^{3} d^3 z_j G_{\omega}^{(0)}(-\boldsymbol{z}_1)\bar{G}_{\omega}^{(0)}(\boldsymbol{z}_1-\boldsymbol{z}_2)(z_{2n}-z_{3n})G_{\omega}^{(0)}(\boldsymbol{z}_2-\boldsymbol{z}_3)\boldsymbol{z}_3\bar{G}_{\omega}^{(0)}(\boldsymbol{z}_3).\end{aligned}$$

$$\begin{aligned}I_{6b}^{(a)} &= -gT\sum_n\Delta^2(\boldsymbol{x})\frac{\nabla_n^2\Delta(\boldsymbol{x})}{2!}\sum_{\omega}\int\frac{d^3\boldsymbol{k}}{(2\pi)^3}\frac{1}{(i\hbar\omega-\xi_k)(i\hbar\omega+\xi_k)^2}\left(-\partial_n^2\frac{1}{i\hbar\omega-\xi_k}\right),\\ I_{6b}^{(b)} &= -gT\sum_n\Delta^2(\boldsymbol{x})\frac{\nabla_n^2\Delta(\boldsymbol{x})}{2!}\sum_{\omega}\int\frac{d^3\boldsymbol{k}}{(2\pi)^3}\frac{1}{(i\hbar\omega-\xi_k)^2(i\hbar\omega+\xi_k)}\left(-\partial_n^2\frac{1}{i\hbar\omega+\xi_k}\right),\\ I_{6b}^{(a)} &= -gT\sum_n\Delta^2(\boldsymbol{x})\nabla_n^2\Delta(\boldsymbol{x})\sum_{\omega}\int\frac{d^3\boldsymbol{k}}{(2\pi)^3}\frac{1}{(i\hbar\omega-\xi_k)(i\hbar\omega+\xi_k)}\left(-\partial_n^2\frac{1}{i\hbar\omega-\xi_k}\right)\left(-\partial_n^2\frac{1}{i\hbar\omega+\xi_k}\right).\end{aligned}$$

the solution is similar to previously resolved integrals, the result is:

$$\begin{aligned}I_{6b}^{(a)} &= -g\mathcal{N}(0)\frac{2}{9}\hbar^2v_f^2\Delta^2(\boldsymbol{x})\boldsymbol{\nabla}^2\Delta^*(\boldsymbol{x})\frac{93\zeta(5)}{128\pi^4T_c^4},\\ I_{6b}^{(b)} &= -g\mathcal{N}(0)\frac{2}{9}\hbar^2v_f^2\Delta^2(\boldsymbol{x})\boldsymbol{\nabla}^2\Delta^*(\boldsymbol{x})\frac{93\zeta(5)}{128\pi^4T_c^4},\\ I_{6b}^{(c)} &= g\mathcal{N}(0)\frac{\hbar^2v_f^2}{3}\Delta^2(\boldsymbol{x})\boldsymbol{\nabla}^2\Delta^*(\boldsymbol{x})\frac{93\zeta(5)}{128\pi^4T_c^4}.\end{aligned}$$

such that

$$\boxed{I_{6b} = I_{6b}^{(a)} + I_{6b}^{(b)} + I_{6b}^{(c)} = -g\mathcal{N}(0)\frac{\hbar^2 v_f^2}{3}\frac{93\zeta(5)}{128\pi^4 T_c^4}\frac{2}{9}\Delta^2(\boldsymbol{x})\boldsymbol{\nabla}^2\Delta^*(\boldsymbol{x})} \tag{B.23}$$

APPENDIX B.3 - Coefficient of the Term Coming with $K_c(\boldsymbol{x}, \{y\}_5)$

$$I_c = \int \prod_{j=1}^{5} d\boldsymbol{y}_j K_c(\boldsymbol{x}, \{\boldsymbol{y}\}_5)\Delta(\boldsymbol{y}_1)\Delta^*(\boldsymbol{y}_2)\Delta(\boldsymbol{y}_3)\Delta^*(\boldsymbol{y}_4)\Delta(\boldsymbol{y}_5)$$

We need all contributions up to the order $\tau^{5/2}$. As the leading-order term in the order parameter is proportional to $\tau^{1/2}$, it is possible to neglect the contribution of the spatial derivatives of the order parameter and limit ourselves only to the local contribution given by

$$\begin{aligned}
I_c &= -gT\Delta(\boldsymbol{x})|\Delta(\boldsymbol{x})|^4 \sum_\omega \int \prod_{j=1}^{5} d\boldsymbol{y}_j G_\omega^{(0)}(\boldsymbol{x}, \boldsymbol{y}_1)\bar{G}_\omega^{(0)}(\boldsymbol{y}_1, \boldsymbol{y}_2)G_\omega^{(0)}(\boldsymbol{y}_2, \boldsymbol{y}_3)\bar{G}_\omega^{(0)}(\boldsymbol{y}_3, \boldsymbol{y}_4)G_\omega^{(0)}(\boldsymbol{y}_4, \boldsymbol{y}_5)\bar{G}_\omega^{(0)}(\boldsymbol{y}_5, \boldsymbol{x}) \\
&= -gT\Delta(\boldsymbol{x})|\Delta(\boldsymbol{x})|^4 \sum_\omega \int \frac{d^3\boldsymbol{k}}{(2\pi)^3}\frac{1}{(i\hbar\omega - \xi_k)^3(i\hbar\omega - \xi_k)^3} \\
&= gT\Delta(\boldsymbol{x})|\Delta(\boldsymbol{x})|^4 \sum_\omega \int \frac{d^3\boldsymbol{k}}{(2\pi)^3}\frac{1}{(\hbar^2\omega^2 + \xi_k^2)^3} \\
&= gT\mathcal{N}(0)\Delta(\boldsymbol{x})|\Delta(\boldsymbol{x})|^4 \sum_\omega \frac{1}{|\hbar\omega|^5} \underbrace{\int_{-\infty}^{\infty} d\xi \frac{1}{(x^2+1)^3}}_{3\pi/8} \\
&= gT\mathcal{N}(0)\Delta(\boldsymbol{x})|\Delta(\boldsymbol{x})|^4 \frac{2}{(2\pi T)^5} 31\zeta(5)\frac{3\pi}{8}
\end{aligned}$$

$$\boxed{I_c = g\mathcal{N}(0)\frac{93\zeta(5)}{128\pi^4 T_c^4}\Delta(\boldsymbol{x})|\Delta(\boldsymbol{x})|^4.} \tag{B.24}$$

APPENDIX C - Calculation $\mathfrak{g}^{(0)}$ and $\mathfrak{g}^{(0)}$

According to the equations (8.9) and (8.10) the solution to the zero order

$$\begin{aligned} g^{(0)} &= \frac{(\mathfrak{B} - H_c^{(0)})^2}{8\pi} + f^{(0)} \qquad (\text{C.1}) \\ &= \frac{(H_c^{(0)})^2}{8\pi}\left(\frac{\mathfrak{B}}{H_c^{(0)}} - 1\right)^2 + a|\Psi|^2 + \frac{b}{2}|\Psi|^4 + \mathcal{K}|\mathfrak{D}\Psi|^2, \qquad (\text{C.2}) \end{aligned}$$

and to the first order

$$\begin{aligned} g^{(1)} &= \frac{(\mathfrak{B} - H_c^{(0)})(\mathfrak{b} - H_c^{(1)})}{8\pi} + f^{(1)} \qquad (\text{C.3}) \\ &= \underbrace{\frac{(\mathfrak{B} - H_c^{(0)})\mathfrak{b}}{8\pi}}_{I} - \underbrace{\frac{(\mathfrak{B} - H_c^{(0)})H_c^{(1)}}{8\pi}}_{II} + \underbrace{f^{(1)}}_{III} \qquad (\text{C.4}) \end{aligned}$$

- I.

$$\begin{aligned} I = \frac{(\mathfrak{B} - H_c^{(0)})\mathfrak{b}}{8\pi} &= \int dr \frac{(\mathfrak{B} - H_c^{(0)})\mathbf{rot}\mathfrak{a}}{8\pi} = \int dr \frac{(\mathfrak{B}_i - H_{c,i}^{(0)})\varepsilon_{ijk}\partial_j \mathfrak{a}_k}{8\pi} \\ &= \int dr \left[\partial_j \left(\frac{(\mathfrak{B}_i - H_{c,i}^{(0)})\varepsilon_{ijk}\mathfrak{a}_k}{8\pi}\right) - \partial_j \left(\frac{(\mathfrak{B}_i - H_{c,i}^{(0)})}{8\pi}\right)\varepsilon_{ijk}\mathfrak{a}_k\right] \\ &= \underbrace{\int dr \partial_j \left(\frac{(\mathfrak{B}_i - H_{c,i}^{(0)})\varepsilon_{ijk}\mathfrak{a}_k}{8\pi}\right)}_{=0} - \int dr \varepsilon_{ijk}\mathfrak{a}_k \partial_j \left(\frac{(\mathfrak{B}_i - H_{c,i}^{(0)})}{8\pi}\right) \\ &= \int dr \frac{\mathfrak{a}\mathrm{rot}\mathfrak{B}}{8\pi} \end{aligned}$$

- II.

$$II = \int dr \frac{(\mathfrak{B} - H_c^{(0)})H_c^{(1)}}{8\pi} = \int dr \frac{H_c^{(0)}}{4\pi}\left(\frac{\mathfrak{B}}{H_c^{(0)}} - 1\right)H_c^{(0)} = \int dr \frac{(H_c^{(0)})^2}{4\pi}\left(\frac{\mathfrak{B}}{H_c^{(0)}} - 1\right)\frac{H_c^{(1)}}{H_c^{(0)}}$$

how $\frac{H_c^{(1)}}{H_c^{(0)}} = -\left(\frac{1}{2} + \frac{ac}{3b^2}\right)$ (eq. 41), then

$$II = -\int dr \frac{(H_c^{(0)})^2}{4\pi} \left(\frac{\mathfrak{B}}{H_c^{(0)}} - 1\right)\left(\frac{1}{2} + \frac{ac}{3b^2}\right)$$

- III

$$III = \int dr f^{(1)} = \int dr (f_1^{(1)} + f_2^{(1)})$$

then

$$\int d\mathbf{r} f_1^{(1)} = \int dr \left\{(a + b|\Psi|^2)(\Psi^*\psi + c.c.) + \mathcal{K}[(\mathfrak{D}\Psi \cdot \mathfrak{D}^*\psi^* + c.c.) - \mathfrak{a}\cdot\mathfrak{i}]\right\}$$

$$\begin{aligned}
\mathfrak{D}\Psi \cdot \mathfrak{D}^*\psi^* &= e^{-\alpha}\mathfrak{D}(e^{\alpha}\Psi)e^{\alpha}\mathfrak{D}(e^{-\alpha}\psi_1^*) \\
&= \mathfrak{D}(e^{-\alpha}\mathfrak{D}(e^{\alpha}\Psi)e^{\alpha}\psi^* e^{-\alpha}) - \mathfrak{D}(e^{-\alpha}\mathfrak{D}(e^{\alpha}\Psi))(e^{\alpha}\Psi^* e^{-\alpha}) \\
&= \mathfrak{D}(e^{-\alpha}\mathfrak{D}(e^{\alpha}\Psi)e^{\alpha}\psi^* e^{-\alpha}) - \mathfrak{D}^2\Psi\psi^*
\end{aligned}$$

$$\begin{aligned}
\int d\mathbf{r} f_2^{(1)} &= \left\{(a + b|\Psi|^2)(\Psi^*\psi + c.c.) + \mathcal{K}[\mathfrak{D}(e^{-\alpha}\mathfrak{D}(e^{\alpha}\Psi)e^{\alpha}\psi^* e^{-\alpha}) - \mathfrak{D}^2\Psi\psi^* - \mathfrak{a}\cdot\mathfrak{i}]\right\} \\
&= \int dr \underbrace{[a\Psi + b|\Psi|^2\Psi - \mathcal{K}\mathfrak{D}^2\Psi + c.c.]}_{=0}\Psi^* + \int dr\mathcal{K}\mathfrak{D}(e^{-\alpha}\mathfrak{D}(e^{\alpha}\Psi)e^{\alpha}\psi^* e^{-\alpha}) - \int dr\mathcal{K}\mathfrak{a}\cdot\mathfrak{i} \\
&= -\int dr\mathcal{K}\mathfrak{a}\cdot\mathfrak{i}
\end{aligned}$$

$$\begin{aligned}
\mathfrak{g} = &\int dr \left(\frac{(H_c^{(0)})^2}{8\pi}\left(\frac{\mathfrak{B}}{H_c^{(0)}} - 1\right)^2 + a|\Psi|^2 + \frac{b}{2}|\Psi|^4 + \mathcal{K}|\mathfrak{D}\Psi|^2\right) + \\
&\int dr \frac{\mathfrak{a}\mathrm{rot}\mathfrak{B}}{8\pi} - \int dr \frac{(H_c^{(0)})^2}{4\pi}\left(\frac{\mathfrak{B}}{H_c^{(0)}} - 1\right)\left(\frac{1}{2} + \frac{ac}{3b^2}\right) - \int dr\mathcal{K}\mathfrak{a}\cdot\mathfrak{i} \\
&+ \int d\mathbf{r}\left\{\frac{a}{2}|\Psi|^2 + 2\mathcal{K}|\mathfrak{D}\Psi|^2 + b|\Psi|^4 + \frac{b}{36}\frac{e^2\hbar^2}{m^2\boldsymbol{c}}\mathfrak{B}^2|\Psi|^2.\right. \\
&- \mathcal{Q}\left\{|\mathfrak{D}^2\Psi|^2 + \frac{1}{3}(\mathrm{rot}\mathfrak{B}\cdot\mathfrak{i}) + \frac{4e^2}{\hbar^2\boldsymbol{c}^2}\mathfrak{B}^2|\Psi|^2\right\} \\
&\left.- \frac{\mathcal{L}}{2}\left\{8|\Psi|^2|\mathfrak{D}\Psi|^2 + [\Psi^2(\mathfrak{D}^*\Psi^*)^2 + c.c]\right\} - \frac{c}{3}|\psi|^6\right\}
\end{aligned}$$

The Maxwell equation ($\mathrm{rot}\mathfrak{B} = \frac{4\pi}{\boldsymbol{c}}\boldsymbol{j}$) in the zero$^{\mathrm{th}}$ order and $\boldsymbol{j} = \mathfrak{j} + \tau\mathbf{j}$ where $\mathfrak{j} = \mathcal{K}c\mathfrak{i}$, then, $\mathrm{rot}\mathfrak{B} = \frac{4\pi}{\boldsymbol{c}}\mathfrak{j} = \mathcal{K}\mathfrak{i}$

$$\int dr \frac{\mathfrak{a}\mathrm{rot}\mathfrak{B}}{4\pi} - \int dr \mathcal{K}\mathfrak{a}\cdot\mathfrak{i} = \int dr(\mathrm{rot}\mathfrak{B} - \mathcal{K}\mathfrak{i})\mathfrak{a} = 0.$$

To proceed further, it is convenient to introduce the following dimensionless quantities:

$$\begin{aligned}
&\widetilde{\boldsymbol{r}} = \frac{\boldsymbol{r}}{\sqrt{2}\lambda}, \quad \widetilde{\mathfrak{A}} = \kappa\frac{\mathfrak{A}}{H_c^{(0)}\lambda}, \quad \widetilde{\mathfrak{B}} = \kappa\sqrt{2}\frac{\mathfrak{B}}{H_c^{(0)}}, \quad \widetilde{\Psi} = \sqrt{-\frac{b}{a}}\Psi \\
&\widetilde{\mathfrak{D}} = \sqrt{2}\lambda\mathfrak{D}, \qquad \widetilde{\mathfrak{i}} = 4\pi\frac{\mathcal{K}\lambda}{H_c^{(0)}}, \quad \mathfrak{g} = \frac{(H_c^{(0)})^2}{4\pi}\widetilde{\mathfrak{g}} \quad \mathcal{G} = \frac{(H_c^{(0)})^2(\sqrt{2}\lambda)^3}{4\pi}\widetilde{G}
\end{aligned} \tag{C.5}$$

$$\begin{aligned}
\widetilde{G} = \int d^3r \Bigg[&-\frac{1}{2}\left(\frac{\mathfrak{B}}{\kappa\sqrt{2}} - 1\right) - |\widetilde{\Psi}| + \frac{1}{2\kappa^2}|\widetilde{\mathfrak{D}}\widetilde{\Psi}|^2 \\
&+ \left(\frac{\widetilde{\mathfrak{B}}}{\kappa\sqrt{2}} - 1\right)\left(\frac{1}{2} + \frac{ac}{3b^2}\right) - \frac{1}{2}|\widetilde{\Psi}|^2 + |\widetilde{\Psi}|^4 + \frac{ca}{3b^2}|\widetilde{\Psi}|^6 + \frac{1}{\kappa^2}|\widetilde{\mathfrak{D}}\widetilde{\Delta}|^2 \\
&+ \frac{\mathcal{Q}a}{\mathcal{K}^2}\frac{1}{4\kappa^4}\left(|\widetilde{\mathfrak{D}}^2\widetilde{\Psi}|^2 + \frac{1}{3}\mathrm{rot}\widetilde{\mathfrak{B}}\cdot\widetilde{\mathfrak{i}} + \widetilde{\mathfrak{B}}|\widetilde{\Psi}|^2\right) \\
&+ \frac{\mathcal{L}a}{\mathcal{K}b}\frac{1}{4\kappa^2}\left(8|\widetilde{\Psi}|^2|\widetilde{\mathfrak{D}}\widetilde{\Psi}|^2 + \widetilde{\Psi}^{*2}(\widetilde{\mathfrak{D}}\widetilde{\Psi})^2 + \widetilde{\Psi}^2(\widetilde{\mathfrak{D}}^*\widetilde{\Psi}^*)^2\right)\Bigg]
\end{aligned}$$

the Gibbs energy difference becomes

$$\mathfrak{g}^{(0)} = \frac{1}{2}\left(\frac{\mathfrak{B}}{\kappa\sqrt{2}} - 1\right) - |\widetilde{\Psi}|^2 + \frac{1}{2}|\widetilde{\Psi}|^4 + \frac{1}{2\kappa^2}|\widetilde{\mathfrak{D}}\widetilde{\Psi}|^2 \tag{C.6}$$

$$\mathfrak{g}^{(1)} = \left(\frac{\widetilde{\mathfrak{B}}}{\kappa\sqrt{2}} - 1\right)\left(\frac{1}{2} + \frac{ac}{3b^2}\right) - \frac{1}{2}|\widetilde{\Psi}|^2 + |\widetilde{\Psi}|^4 + \frac{ca}{3b^2}|\widetilde{\Psi}|^6 + \frac{1}{\kappa^2}|\widetilde{\mathfrak{D}}\widetilde{\Delta}|^2 \tag{C.7}$$

$$+ \frac{\mathcal{Q}a}{\mathcal{K}^2}\frac{1}{4\kappa^4}\left(|\widetilde{\mathfrak{D}}^2\widetilde{\Psi}|^2 + \frac{1}{3}\mathrm{rot}\widetilde{\mathfrak{B}}\cdot\widetilde{\mathfrak{i}} + \widetilde{\mathfrak{B}}|\widetilde{\Psi}|^2\right) \tag{C.8}$$

$$+ \frac{\mathcal{L}a}{\mathcal{K}b}\frac{1}{4\kappa^2}\left(8|\widetilde{\Psi}|^2|\widetilde{\mathfrak{D}}\widetilde{\Psi}|^2 + \widetilde{\Psi}^{*2}(\widetilde{\mathfrak{D}}\widetilde{\Psi})^2 + \widetilde{\Psi}^2(\widetilde{\mathfrak{D}}^*\widetilde{\Psi}^*)^2\right) \tag{C.9}$$

APPENDIX D - Bogomolnyi Equations

Our starting point is the standard GL equations

$$\Psi(1-|\Psi|^2)+\mathbf{D}^2\Psi=0, \quad \mathbf{rotB}=\mathbf{i}. \tag{D.1}$$

A magnetic field is set along the z axis, $\mathbf{B}=(0,0,B)$, so that the system is homogeneous along this axis and the order parameter is independent of z.

$$\mathbf{B}=(0,0,B) \quad \Rightarrow \mathbf{A}=(A_x,A_y,0)$$

we introduce the new gauge invariant gradients

$$D_\pm = D_x \pm iD_y \tag{D.2}$$

that satisfy the identity

$$\begin{aligned}
\mathbf{D}^2 &= D_x^2+D_y^2\\
D_+D_- &= D_x^2+D_y^2+i[D_y,D_x]\\
[D_x,D_y] &= [\partial_y+iA_y,\partial_x+iA_x]\\
&= \cancelto{0}{[\partial_y,\partial_x]}+i[A_y,\partial_x]+i[\partial_y,A_x]+\cancelto{0}{i^2[A_x,A_y]}\\
&= i(A_y\partial_x-\partial_xA_y)+i(\partial_yA_x-A_x\partial_y)\\
&= i(\partial_yA_x-\partial_xA_y)\\
&= -i\mathbf{B}
\end{aligned}$$

$$D_+D_- = D_x^2+D_y^2+B \quad \Rightarrow \quad \mathbf{D}^2=D_+D_- - \mathbf{B}$$

Let us assume that a solution to the GL formalism satisfies the first order equation

$$D_-\Psi=0, \quad \text{the first of the Bogomolnyi equation}$$

$$\begin{aligned}\Psi - \Psi|\Psi|^2 + (D_+D_- - \mathbf{B})\Delta = 0 \\ \Pi^-\Delta = 0, \quad 1 - |\Delta|^2 = \mathbf{B}\end{aligned}$$

then

$$\mathbf{B} = 1 - |\Psi|^2, \quad \text{which is know as the second Bogomolnyi equation.}$$

Taking into account that rot$\mathbf{B} = (\partial_y B, -\partial_x B, 0)$, one can find from the second GL equation that

$$\begin{aligned}
&\text{rot}\mathbf{B} = 2\text{Im}[\Psi \mathbf{D}^* \Psi^*] \\
&\partial_y B = (\Psi D_x^* \Psi^* - \Psi^* D_x \Psi); \quad -\partial_x B = (\Psi D_y^* \Psi^* - \Psi^* D_y \Psi); \\
&\partial_y B = (\Psi(\partial_x + iA_x)^* \Psi^* - \Psi^*(\partial_x + iA_x)\Psi); \quad -\partial_x B = (\Psi(\partial_y + iA_y)^* \Psi^* - \Psi^*(\partial_y + iA_y)\Psi); \\
&\partial_y B = (\Psi \partial_x \Psi^* - \Psi^* \partial_x \Psi - i2A_x|\Psi|^2); \quad -\partial_x B = (\Psi \partial_y \Psi^* - \Psi^* \partial_y \Psi - i2A_y|\Psi|^2); \\
&\partial_y B = (\Psi \partial_x \Psi^* - \Psi^* \partial_x \Psi - i2A_x|\Psi|^2); \quad -i\partial_x B = (\Psi i\partial_y \Psi^* - \Psi^* i\partial_y \Psi + 2A_y|\Psi|^2); \\
&\partial_y B = (\partial_x|\Psi|^2 - 2\Psi^* \partial_x \Psi - i2A_x|\Psi|^2); \quad -i\partial_x B = (i\partial_y|\Psi|^2 - 2\Psi^* i\partial_y \Psi + 2A_y|\Psi|^2); \\
&(\partial_y B + i\partial_x B) = \partial_x|\Psi|^2 - i\partial_y|\Psi|^2 - 2\Psi^*(\partial_x + iA_x)\Psi - 2\Psi^*(i\partial_y - A_y)\Psi \\
&(\partial_y B + i\partial_x B) = \partial_x|\Psi|^2 - i\partial_y|\Psi|^2 - 2\underbrace{(\Psi^*(\partial_x + iA_x)\Psi - i\Psi^*(\partial_y + iA_y)\Psi)}_{\Psi^*(D_-\Psi)=0}
\end{aligned}$$

$$(\partial_y B + i\partial_x B) = (\partial_x - i\partial_y)|\Psi|^2$$

and by $D_-\Psi = 0$

$$(\partial_y + i\partial_x)\Psi = (A_x - iA_y)\Psi$$

so, the Bogomonlyi equation are reduced to self-duality Bogomolnyi equation

$$\begin{aligned}B = 1 - |\Psi|^2 \\ (\partial_y + i\partial_x)\Psi = (A_x - iA_y)\Psi\end{aligned}$$

APPENDIX E - Scientific Works Produced During this Ph.D. Course

- W. Y. Córdoba-Camacho, R. M. da Silva, A. Vagov, A. A. Shanenko, and J. Albino Aguiar. *Between types I and II: Intertype flux exotic states in thin superconductors.* **Phys. Rev. B**, 94:054511, 2016.

PHYSICAL REVIEW B **94**, 054511 (2016)

Between types I and II: Intertype flux exotic states in thin superconductors

W. Y. Córdoba-Camacho,[1] R. M. da Silva,[2] A. Vagov,[3] A. A. Shanenko,[1] and J. Albino Aguiar[1,2]
[1]*Departamento de Física, Universidade Federal de Pernambuco, Avenida Jorn. Aníbal Fernandes, s/n, Cidade Universitária 50740-560 Recife, PE, Brazil*
[2]*Programa de Pós-Graduação em Ciência de Materiais, Universidade Federal de Pernambuco, Avenida Jorn. Aníbal Fernandes, s/n, Cidade Universitaria 50740-560 Recife, PE, Brazil*
[3]*Institut für Theoretische Physik III, Bayreuth Universität, Bayreuth 95440, Germany*

(Received 27 April 2016; revised manuscript received 13 July 2016; published 15 August 2016)

The Bogomolnyi point separates superconductivity types I and II while itself hiding infinitely degenerate magnetic flux configurations, including very exotic states (referred to here as flux "monsters"). When the degeneracy is removed, the Bogomolnyi point unfolds into a finite, intertype domain in the phase diagram between types I and II. One can expect that in this case the flux monsters can escape their "prison" at the Bogomolnyi point, occupying the intertype domain and shaping its internal structure. Our calculations reveal that such exotic flux distributions are indeed stable in the intertype regime of thin superconductors made of a type-I material, where the Bogomolnyi degeneracy is removed by stray magnetic fields. They can be classified into three typical patterns that are qualitatively different from those in types I and II: superconducting islands separated by vortex chains; stripes/worms/labyrinths patterns; and mixtures of giant vortices and vortex clusters. Our findings shed light on the problem of the interchange between types I and II, raising important questions on the completeness of the textbook classification of the superconductivity types.

DOI: 10.1103/PhysRevB.94.054511

- W. Y. Córdoba-Camacho, R. M. da Silva, A. Vagov, A. A. Shanenko, and J. Albino Aguiar. *Quasi-One-Dimensional Vortex Matter in Superconducting Nanowires.* **Submitted to Phys. Rev. Lett.**

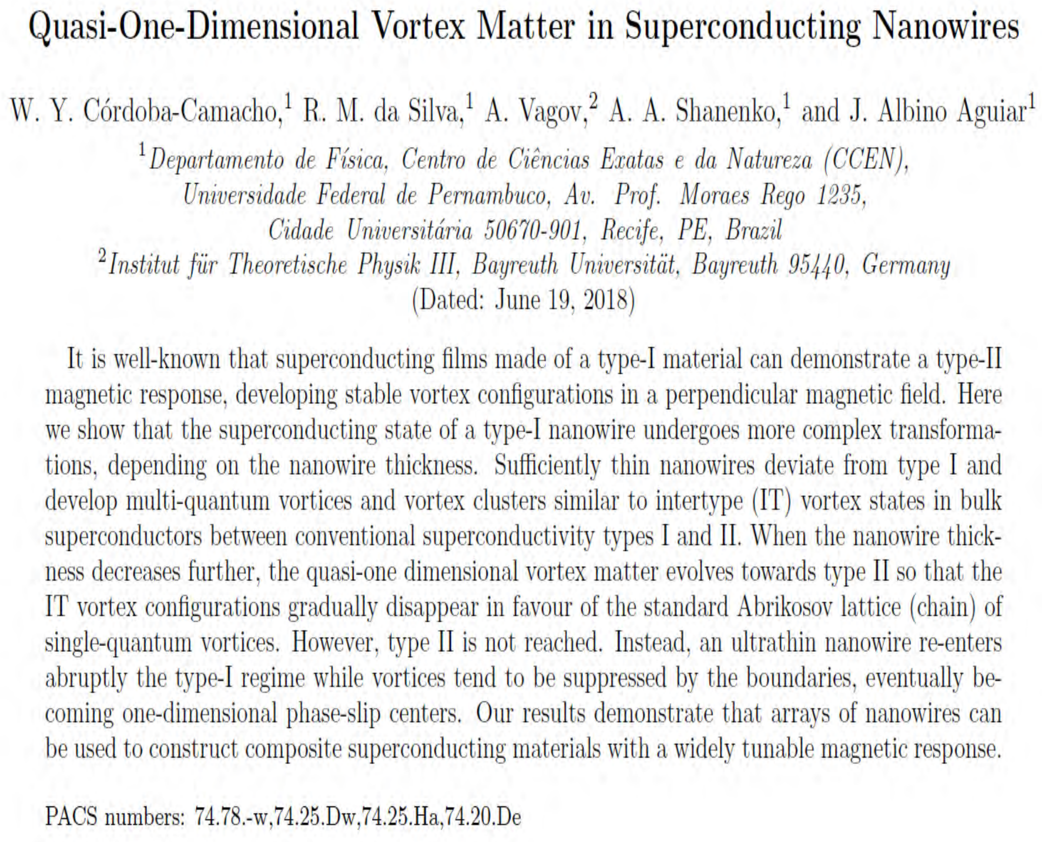

Quasi-One-Dimensional Vortex Matter in Superconducting Nanowires

W. Y. Córdoba-Camacho,[1] R. M. da Silva,[1] A. Vagov,[2] A. A. Shanenko,[1] and J. Albino Aguiar[1]
[1]*Departamento de Física, Centro de Ciências Exatas e da Natureza (CCEN),*
Universidade Federal de Pernambuco, Av. Prof. Moraes Rego 1235,
Cidade Universitária 50670-901, Recife, PE, Brazil
[2]*Institut für Theoretische Physik III, Bayreuth Universität, Bayreuth 95440, Germany*

(Dated: June 19, 2018)

It is well-known that superconducting films made of a type-I material can demonstrate a type-II magnetic response, developing stable vortex configurations in a perpendicular magnetic field. Here we show that the superconducting state of a type-I nanowire undergoes more complex transformations, depending on the nanowire thickness. Sufficiently thin nanowires deviate from type I and develop multi-quantum vortices and vortex clusters similar to intertype (IT) vortex states in bulk superconductors between conventional superconductivity types I and II. When the nanowire thickness decreases further, the quasi-one dimensional vortex matter evolves towards type II so that the IT vortex configurations gradually disappear in favour of the standard Abrikosov lattice (chain) of single-quantum vortices. However, type II is not reached. Instead, an ultrathin nanowire re-enters abruptly the type-I regime while vortices tend to be suppressed by the boundaries, eventually becoming one-dimensional phase-slip centers. Our results demonstrate that arrays of nanowires can be used to construct composite superconducting materials with a widely tunable magnetic response.

PACS numbers: 74.78.-w,74.25.Dw,74.25.Ha,74.20.De

Scientific works under preparation

1. Exotic Vortices States in Superconducting Bilayer type-II/N/type-I.
2. Stray Field Contribution to Vortex Interaction in Thin Films: Extended Ginzburg-Landau Analysis.